MODELING AND CHARACTERIZATION OF THE ELASTIC BEHAVIOR OF INTERFACES IN NANOSTRUCTURED MATERIALS: FROM AN ATOMISTIC DESCRIPTION TO A CONTINUUM APPROACH

A Dissertation
Presented to
The Academic Faculty

by

Rémi Dingreville

In Partial Fulfillment
of the Requirements for the Degree
Doctor of Philosophy in the
School of Mechanical Engineering

Georgia Institute of Technology
December 2007

MODELING AND CHARACTERIZATION OF THE ELASTIC BEHAVIOR OF INTERFACES IN NANOSTRUCTURED MATERIALS: FROM AN ATOMISTIC DESCRIPTION TO A CONTINUUM APPROACH

Approved by:

Dr. Jianmin Qu, Advisor
GWW School of Mechanical Engineering
Georgia Institute of Technology

Dr. Mo Li
School of Materials Science & Engineering
Georgia Institute of Technology

Dr. David L. McDowell
GWW School of Mechanical Engineering
Georgia Institute of Technology

Dr. Elisa Riedo
School of Physics
Georgia Institute of Technology

Dr. Min Zhou
GWW School of Mechanical Engineering
Georgia Institute of Technology

Date Approved: July 24th, 2007

To my wife Stephani, my family and my friends.

ACKNOWLEDGEMENTS

This work is the accomplishment of both an individual and collective effort to find a path in the world of "*nano*" and the meanders of interface theory. If one had to find the roots of this journey, I would probably cite two particular events. The first one would be the reading of an essay by Gleiter on nanocrystalline materials in Progress in Materials Science during my Masters study in France. I discovered a whole new world made of nanotubes and nanoribbons, a world ruled by abnormal behaviors. It seemed to me there were many interesting things to discover and issues to tackle. The second event occurred a few months earlier during an internship at Georgia Tech in the summer of 2000. That was the meeting of Professor Jianmin Qu who gave me the opportunity later on to join his research group for this work. The fact that, many years later, this dissertation reflects the achievements of our collaborative work on nanostructured materials, constitute for me a great honor and pride. But I also see this as a sign that, fundamental research is first and foremost a question of time and interpersonal relationships. I owe therefore a great deal of appreciation to Jianmin Qu who gave me the freedom to direct this research project according to my own observations and ideas, developing in me the ability to think creatively and independently. I also would like to thank him for his guidance, advice and patience especially in moments when disappointment might have overcome my enthusiasm.

My thanks and gratitude then go Dr. Dave McDowell, Dr. Min Zhou, Dr. Mo Li and Dr. Elisa Riedo who serve as the members of my Ph.D. thesis reading committee and

have the task of reviewing this work. My interaction with some of them over the past several years have undoubtfully added to the quality and relevance of this research.

There are a number of people at Georgia Tech who also have contributed greatly to my experiences over the course of my doctorate. I would like to thank Douglas Spearot for introducing me to the "joys" of Molecular Dynamics and the technical explanations on the MD software WARP and PARADYN. Thank you also to Ambarish Kulkarni for introducing me to the "joys" of ionic systems and ZnO nanobelts. Even though we unsuccessfully spent many hours working on these systems, our collaboration greatly contributed to the quality of this work. I thank him for his enthusiasm, his availability and cheerful spirit. I would also like to stress the essential role of the other members of this research group who directly or indirectly contributed to this work by their availability, sense of humor, sense of welcome or own skills. Thanks to Marie Blanche Cornil, Jason Mayeur, Narashiman Swaminathan, Min Pei, Janine Johnson, and many others. Thank you also to Cecilia Jones the administrative assistant of this group.

On a lighter note, I would like to thank my friends for their cheerful support over the years, may they be oversea or in the building next door on campus. Therefore thank you to the "manioules" Baptiste Anti, Sébastien Doulet, Marcel Raybaud, Laurent Licht, Shane Elipot, Sylvain Rigal; my high school friends Joffrey and Stéphanie Desrousseaux, Geoffrey Denans, Guillaume Poignet, Frédéric Olech; and the "French GT mafia" Matthieu Masquelet, Diane de Zelicourt, Franklin Genin, Léon Phan, Gilles Eggenspieler, Frédéric Bouygue, Rémy Prosper Magnier, Kaoruko Magnier Watanabe, Igor "Butchy" Vilfan and all the others I forgot.

Finally, I do not forget my parents, Philippe and Annie, my grand-parents, Jacques and Muguette, my families, the Dingrevilles, the Stephens and the Swanns, and my wife Stephani whose patience and support were tested many times. Thank you to all of you from the bottom of my heart.

TABLE OF CONTENTS

	Page
ACKNOWLEDGEMENTS	iv
LIST OF TABLES	xi
LIST OF FIGURES	xiii
NOMENCLATURE	xvii
SUMMARY	xxvi
1 INTRODUCTION	1
1.1 Motivations	1
1.2 Dissertation Objectives and Goals	7
1.3 Dissertation Structure	13
2 ATOMISTIC SIMULATIONS	19
2.1 Introduction	19
2.2 Nuts and Bolts of Atomistic Simulation	22
2.2.1 Periodic Boundary Conditions	22
2.2.2 Control of the System: Role of Statistical Ensembles	24
2.3 Molecular Statics	27
2.4 Interatomic Potentials	30
2.4.1 Interatomic Potentials for F.C.C metals: the Embedded Atom Method (EAM)	31
3 ELASTIC DESCRIPTION OF BULK PHASES	37
3.1 Introduction	37
3.2 Definition of the Elastic Constants	39
3.2.1 Elastic Strain and Complementary Energy Representations	39

3.2.2 Second and Third Order Elastic Constants of Cubic Crystals 41

3.2.3 Second and Third Order Elastic Constants of Isotropic Materials 43

3.3 A Method of Computing the Elastic Constants 44

3.4 Elastic Constants for Single Crystals 48

3.5 Elastic Constants of Isotropic Aggregates 51

3.5.1 Voigt and Reuss-type Estimates of the Elastic Constants of an Isotropic Aggregate 51

3.5.2 Semi Consistent Estimates of the Elastic Constants of an Isotropic Aggregate 54

3.6 Summary and Conclusions 56

4 ELASTIC DESCRIPTION OF FREE SURFACES AND INTERFACES 65

4.1 Introduction 66

4.2 Surface Free Energy and Surface Stress 70

4.2.1 Dividing Surface 70

4.2.2 Definition of Interfacial Excess Energy 72

4.2.3 Surface Stress and Surface Strain 77

4.2.4 Surface Elasticity, Generalized Shuttleworth Relation 77

4.2.5 Isotropic Bimaterials 79

4.3 Semi-analytical Method to Evaluate Surface Properties 83

4.3.1 Free Surface 84

4.3.2 Bicrystal Interface 88

4.3.2.1 Atomic Level Mapping 89

4.3.2.2 Total Energy of the Atomic Assembly 90

4.3.2.3 Atomic Level Stress 91

4.3.2.4 Finding the Internal Relaxations 92

4.3.2.5 Interface Elastic Properties 93

4.4 Surface Elastic Properties of Cu, Ni, Ag and Pd Free Surfaces 95

4.4.1 Computational Framework and Results 95

4.4.2 Surface Elastic Properties of Transition Metals 98

4.4.3 Surface Relaxation 101

4.5 Surface Elastic Properties for Grain Boundaries in Cu Bicrystals 103

4.5.1 Computational Framework and Results 103

4.5.2 Atomic Level Moduli for Grain Boundaries 105

4.5.3 Interface Internal Relaxation 108

4.6 Summary and Conclusions 111

5 FROM AN ATOMISTIC DESCRIPTION TO A CONTINUUM FRAMEWORK: SIZE-DEPENDENT ELASTICITY 138

5.1 Introduction 138

5.2 Effective Modulus of Nanoparticle 140

5.2.1 Special Cases 146

5.2.1.1 Thin Films 146

5.2.1.2 Thin Wire of Square Cross-section 149

5.2.1.3 Spherical Particles 151

5.2.2 Atomistic Calculation for Computing the Effective Elastic Constants of Nanoparticles 152

5.2.3 Numerical Results for Thin Films, Nanowires and Nanospheres 156

5.2.4 Influence of Non-Linear Elastic Behavior of the Bulk Core and Surface Elasticity 159

5.2.4.1 Parameters Influencing the Size-Dependence of Nanowires 161

5.2.4.2 Parameters Influencing the Size-Dependence of Thin Films 162

5.3 Eshelby nano-inclusion problem 164

5.3.1 Interphase vs. Interface 164

5.3.2 Mesoscopic Interfacial Conditions 166

5.3.2.1 Kinematic Interfacial Conditions: Displacement Fields Near the Interphase 167

5.3.2.2 Kinetic Interfacial Conditions: Traction Across the Interface 171

5.3.3 Inhomogeneity problem 172

5.4 Summary and Conclusions 176

6 CONCLUSIONS AND RECOMMENDATIONS 196

6.1 Summary of Significant Contributions 196

6.2 Recommendations for Future Work 204

APPENDIX A: TAYLOR EXPANSION OF THE EAM POTENTIAL 207

APPENDIX B: "T" STRESS DECOMPOSTION 210

APPENDIX C: ATOMIC LEVEL STRESS AND INTERNAL RELAXATION 213

APPENDIX D: COORDINATE TRANSFORMATION 221

APPENDIX E: BULK AND SURFACE ELASTICITY TENSORS 223

APPENDIX F: EFFECTIVE ELASTIC PROPERTIES OF NANOPARTICLES: SPECIAL CASES 225

REFERENCES 229

LIST OF TABLES

Page

Table 2.1: Elastic constants (in 100 GPa) and surface energy for (111), (100) and (110) surfaces (in $J.m^{-2}$) from EAM potential validation 36

Table 3.1: Interatomic lattice spacing (in Å) 60

Table 3.2: Second order elastic constants for single crystals (in 100 GPa) 60

Table 3.3: Third order elastic constants for single crystals (in 100 GPa) calculated from analytical method 61

Table 3.4: Elastic constants of single crystals calculated by the strain meshing of the energy (in 100GPa) 62

Table 3.5: Voigt estimates of the SOEC and TOEC for isotropic polycrystalline aggregates (in 100 GPa) 62

Table 3.6: Reuss estimates of the SOEC and TOEC for isotropic polycrystalline aggregates (in 100 GPa) 63

Table 3.7: Hill estimates of the SOEC and TOEC for isotropic polycrystalline aggregates (in 100 GPa) 63

Table 3.8: Self-Consistent estimates of the SOE and TOE constants for isotropic polycrystalline aggregates (in 100 GPa) 64

Table 4.1: Calculated surface elastic properties of low-index surfaces for several FCC metals. The unit used is $J.m^{-2}$ 131

Table 4.2: Surface elastic properties of (100) surfaces for several FCC metals calculated by the strain meshing of the energy. The unit used is $J.m^{-2}$ 132

Table 4.3: Bulk lattice constant (λ) and bulk cohesive energy (E_c) 132

Table 4.4: Surface relaxation for several FCC metals (in %) 133

Table 4.5: Calculated surface elastic properties of low-index unrelaxed surfaces for several FCC metals. The unit used is $J.m^{-2}$ 134

Table 4.6: Crystallographic characteristics of the symmetric tilt grain boundaries studied in this work 135

Table 4.7: Calculated interface elastic properties of low-CSL symmetric tilt grain boundaries for copper 136

Table 4.8: Calculated interface elastic properties of low-CSL symmetric tilt grain boundaries for copper without the effect of internal relaxation 137

LIST OF FIGURES

Page

Figure 1.1: Hall-Petch plot of the effect of grain size d on the flow stress σ of Cu at 300K from Conrad (2003) 17

Figure 1.2: The dependence of the Young's modulus of silver and aluminum films on the film thickness *d* from Mizubayashi *et al.* (1999) 17

Figure 1.3: Thickness dependence of Young's moduli for [001], [110], and [111] nanowires from Liang *et al.* (2005) 18

Figure 2.1: Principle of Periodic Boundary Conditions 35

Figure 3.1: Scheme representing the equivalent inclusion method 57

Figure 3.2: TOEC for single crystals of the transitions metals in groups 10 – 11 and aluminum 58

Figure 3.3: TOEC for isotropic aggregates of cubic crystals 59

Figure 4.1: (a) Flat interface of a bimaterial, (b) Interface excess energy as a function of the distance away from the interface 114

Figure 4.2: Semi-infinite crystal and its free surface 115

Figure 4.3: Schematic of the strain meshing process to calculate the surface excess energy and surface elastic constants 116

Figure 4.4: Surface atomic packing density of basal FCC surfaces 117

Figure 4.5: Layer decomposition of the intrinsic surface energy Γ_0 and surface stress Γ_{11} of Ag for a (100) surface orientation. The sum over half the thickness for Γ_0 is 0.703 J/m^2 and for Γ_{11} is 0.816 J/m^2 118

Figure 4.6: Intrinsic surface energy in reduced units (Surface energy/(surface packing density × bulk cohesive energy) for several metals. The (111) surface (filled circles), has the lowest energy compared to the (100) surface (plain circle) and the (110) surface (triangle) 119

Figure 4.7: Internal surface stress (at zero surface strain) in reduced units (Surface energy/(surface packing density × bulk cohesive energy) for several metals. The (111) surface (filled circles), has the lowest residual stresses compared to the (100) surface (plain circle) and the (110) surface (triangle) 120

Figure 4.8: Tensile surface elasticity coefficients in reduced units (Surface elastic coefficient/(lattice constant × bulk elastic constant) 121

Figure 4.9: Shear surface elasticity coefficients in reduced units (Surface elastic coefficient/(lattice constant × bulk elastic constant) 122

Figure 4.10: Possible displacements of atoms near the surface of a crystal. The dotted lines indicate the positions of the planes at an ideal lattice structure 123

Figure 4.11: Effects of the surface relaxation on the elastic properties of low-index surfaces for several FCC metals such as (a) intrinsic surface energy density, (b) intrinsic surface stress, (c) surface biaxial modulus and (d) the surface shear modulus 124

Figure 4.12: Comparison of the interfacial excess energy as a function of the applied tensile stress calculated from full blown MD calculations and from the semi-analytical method of section 4.3 for the symmetric tilt grain boundary Σ5[100]/(310) 125

Figure 4.13: Bicrystal interface structures for copper interfaces (a) Σ5 [100]/(310) symmetric tilt grain boundary (b) Σ5 [100]/(210) symmetric tilt grain boundary (c) Σ3 [110]/(111) symmetric tilt grain boundary 126

Figure 4.14: Layer decomposition of (a) the surface energy Γ_0 and (b) residual surface stress $\pi^s_{\alpha\alpha}$ for Σ5 [001]/(310), Σ5 [001]/(210) and Σ3 [110]/(210) symmetric tilt grain boundaries in copper 127

Figure 4.15: Normalized diagonal elements of the tensor of the atomic elastic moduli for Σ5 [001]/(310), Σ5 [001]/(210) and Σ3 [110]/(210) symmetric tilt grain boundaries in copper, (a) $C^{s,n}_{1111}/C^{s,bulk}_{1111}$, (b) $C^{s,n}_{2222}/C^{s,bulk}_{2222}$, (c) $M^{t,n}_{3333}/M^{t,bulk}_{3333}$ 128

Figure 4.16: Effects of the interface internal relaxation on the elastic properties of low-CSL symmetric tilt grain boundary in copper 129

Figure 4.17: Layer decomposition of the transverse internal relaxtion $\tilde{\varepsilon}^{t,n}_3$ for different loading configuration: (a) transverse loading (b) biaxial stretching $\varepsilon^s = \varepsilon^s{}_{11} = \varepsilon^s{}_{22}$ for Σ5 [001]/(310), Σ5 [001]/(210) and Σ3 [110]/(210) symmetric tilt grain boundaries in copper 130

Figure 5.1: A particle is created by removing it from a bulk crystal 179

Figure 5.2: An ellipsoidal particle 179

Figure 5.3: A single crystal thin film 180

Figure 5.4: A thin wire of square cross-section 180

Figure 5.5: Atomistic structures and the crystallographic orientations used in the simulation cells. Periodic boundary conditions are applied in the longitudinal directions (X_3 axis in the case of nanowires, X_1 and X_2 axis in the case of thin films). The transversal directions are kept traction free 181

Figure 5.6: (a) Strain energy density meshing as a function of in-plane strains for Cu thin film (b) Comparison of the in-plane uniaxial Young's modulus of Cu films between meshing method and continuum model presented in section 5.2.1 182

Figure 5.7: Self Equilibrium strain of nickel nanowires as a function of the nanowires thickness for different crystallographic orientations calculated using the EAM potential after energy minimization and compared with self equilibrium strain calculated from (5.24) 183

Figure 5.8: Self Equilibrium strain of silver thin films as a function of the films thickness for different crystallographic orientations calculated using the EAM potential after energy minimization and compared with self equilibrium strain calculated from equation (5.24) 184

Figure 5.9: Effective longitudinal Young's modulus of silver nanowires as a function of the nanowires thickness calculated using the semi analytical method and compared to the effective longitudinal Young's modulus calculated from equation (5.43) 185

Figure 5.10: Effective biaxial Young's modulus of copper thin films as a function of the film thickness calculated using the semi analytical method and compared to the effective longitudinal Young's modulus calculated from equation (5.38) 186

Figure 5.11: Poisson's ratio for the films and the wires of various sizes 187

Figure 5.12: Comparison of elastic responses of nanowires and thin films for Cu, Ni, Ag and Pd; (a) Effective longitudinal Young's modulus of nanowires, (b) Effective biaxial Young's modulus of thin films and (c) Effective uniaxial Young's modulus of thin films as a function of the film thickness for various orientations for the studied materials. Atomistic calculation results are compared to the effective longitudinal Young's modulus calculated from section 5.2.1 188

Figure 5.13: Relative effects of surface elasticity and third order elastic constants for copper nanowires 189

Figure 5.14: Relative effects of the surface elasticity and third order elastic constants for nickel thin films on the biaxial modulus 190

Figure 5.15: Relative effects of the surface elasticity and third order elastic constants for copper thin films on the uniaxial Young's modulus 191

Figure 5.16: Comparison of the effects of surface elasticity on (a) uniaxial Young's modulus of nanowires, (b) biaxial Young's modulus of thin films and (c) uniaxial Young's modulus of thin films as a function of the film thickness and orientation for Cu, Ni, Ag, and Pd 192

Figure 5.17: Comparison of the effects of core elasticity on (a) uniaxial Young's modulus of nanowires, (b) biaxial Young's modulus of thin films and (c) uniaxial Young's modulus of thin films as a function of the film thickness and orientation for Cu, Ni, Ag, and Pd 193

Figure 5.18: Interphase vs. interface: different views based on different length scales 194

Figure 5.19: Schematic of the inhomogeneity problem 195

NOMENCLATURE

Molecular Dynamics / Interatomic potentials

$\mathbf{r}^i$	Atomic position vector for the i^{th} atom
$\mathbf{F}^i$	Force vector on an atom i
U	Potential energy of an atomic assembly
N	Total number of atoms in an atomic assembly
V	Total volume of an assembly
P	Pressure of an assembly
T	Temperature of an assembly
R_c	Interatomic potentials cut-off distance
Θ	Arbitrary physical quantity
$\Phi(t)$	Phase space coordinate
t_N	Final time step of the calculation
$\mathbf{v}$	Velocity vector
Δt	Time step
m	Mass of an atom
k	Boltzmann's constant
ζ	Isothermal time-dependent frictional term in NVT calculations
v_T	Thermostating rate
P_o	Control pressure used in NPT calculations
$\boldsymbol{\eta}$	Isobaric friction coefficient in NPT calculations
$\mathbf{h}$	Boundary vector in NPT calculation
v_P	Constant pressure damping coefficient in NPT calculations

$\mathbf{\Pi}^{\alpha\beta}$	Virial stress
$\mathbf{F}_{ij}$	Force between atom *i* and atom *j*
$\mathbf{r}_{ij}$	Interatomic distance between atoms *i* and *j*
$\mathbf{p}_{(i)}$	Residual in Conjugate Gradient Method
$\mathbf{d}_{(i)}$	Search direction in Conjugate Gradient Method
α_i	Scalar minimizing the potential energy in the search direction
$\beta_{(i+1)}$	Orthogonality scalar in Conjugate Gradient Method
Φ_{LJ}	Lennard Jones potential
E_n	Total energy of an atom *n*
E_n^G	Embedding energy of an atom *n*
E_n^V	Pair interaction energy at atom *n*
G_n	Embedding function
$V(r^{mn})$	Pair interaction potential between atom *m* and atom *n*
$\overline{\rho}_n$	Local background electron density induced at atom *n*

Atomistic Models / Semi-Analytical Methods

r^{mn}	Scalar distance between the atom *m* and atom *n*
u_i^{mn}	Displacement vector between the atom *m* and atom *n*
F_{ij}^{mn}	Deformation gradient tensor
ε_{ij}	Symmetric second order tensor representing pure deformation
ω_{ij}	Antisymmetric second order tensor representing rigid body rotation

Ω_n	Atomic volume
$A^{(n)}$	0^{th}-order coefficient of the Taylor expansion of total energy E^n of atom n
$A_{ij}^{(n)}$	1^{st}-order coefficient of the Taylor expansion of total energy E^n of atom n
$A_{ijkl}^{(n)}$	2^{nd}-order coefficient of the Taylor expansion of total energy E^n of atom n
$A_{ijkluv}^{(n)}$	3^{rd}-order coefficient of the Taylor expansion of total energy E^n of atom n
$C_{ijkl}^{(n)}$	Atomic-level elastic stiffness tensor in homogeneous field
$\mathbf{D}^{-1}$	Traction-free boundary conditions matrix
$B_{\alpha\beta}^{(n)}$	In-plane residual stress of an atom n with traction-free boundary conditions
$B_{\alpha\beta\kappa\lambda}^{(n)}$	In-plane stiffness tensor of an atom n with traction-free boundary conditions
$\tilde{\varepsilon}_{ij}^{m}$	"Inner" relaxation of atom m
$A_{ij\alpha\beta}^{\pm}$	Mixed mode elastic tensor of the homogeneous behavior of a semi-crystal
$B_{ijk}^{\pm}$	Mixed mode elastic tensor of the homogeneous behavior of a semi-crystal
$A_{i\alpha\beta}^{mn}$	Mixed mode elastic tensor between atom m and atom n in a bicrystal
B_{ik}^{mn}	Mixed mode elastic tensor between atom m and atom n in a bicrystal
w^n	Atomic energy of an atom n
E	Total strain energy of an atomic assembly
$\overline{A}_{\alpha\beta}^{(1)}$	First order homogeneous in-plane tensor
$\overline{B}_{k}^{(1)}$	First order homogeneous transverse tensor
$\overline{A}_{\alpha\beta\kappa\lambda}^{(2)}$	Second order homogeneous in-plane tensor
$\overline{B}_{ij}^{(2)}$	Second order homogeneous transverse tensor
$\overline{Q}_{\alpha\beta i}$	In-plane-transverse coupling tensor

K_{ij}^{n}	First order perturbation tensor
$D_{ij\alpha\beta}^{n}$	Second order in-plane perturbation tensor
G_{ijk}^{n}	Second order transverse perturbation tensor
L_{ijkl}^{mn}	Second order perturbation coupling tensor
σ_{ij}^{n}	Atomic level stress
τ_{ij}^{n}	Atomic level residual stress
$\bar{C}_{ij\alpha\beta}^{s,n}$	Homogeneous atomic level stiffness tensor
$\bar{M}_{kij}^{t,n}$	Homogeneous atomic level compliance tensor
T_{ijkl}^{nm}	Atomic level relaxation coupling stiffness tensor
$\tilde{\varepsilon}_{\alpha\beta}^{s,n}$	Atomic level in-plane relaxation
$\eta_{\alpha\beta}^{s,n}$	Atomic level residual in-plane relaxation
$M_{i\alpha\beta}^{s,n}$	Atomic level in-plane modified compliance tensor
$Q_{\alpha\beta\kappa\lambda}^{s,n}$	Atomic level in-plane modified stiffness tensor
$\tilde{\varepsilon}_{i}^{t,n}$	Atomic level transverse relaxation
$\eta_{i}^{t,n}$	Residual transverse relaxation
$M_{3j3k}^{t,n}$	Atomic level transverse compliance tensor
$\sigma_{\alpha\beta}^{s,n}$	Atomic level in-plane stress
$\pi_{\alpha\beta}^{n}$	Atomic level in-plane residual stress
$C_{\alpha\beta\kappa\lambda}^{s,n}$	Atomic level in-plane stiffness tensor
$Q_{i\alpha\beta}^{n}$	Atomic level Poisson's effect tensor

$d_{(hkl)}$	Surface atomic packing density

Interface Elasticity

Γ	Surface / Interface excess energy
$\hat{\Gamma}_s$	"Traditional" interfacial *free* energy
γ_n	Excess energy of an atom *n*
A	Area in a deformed configuration
A_0	Area in an undeformed configuration
$w(x_3)$	Elastic strain energy densities
h	Thickness of the interfacial region
$\boldsymbol{\varepsilon}^s$	In-plane strain tensor
$\boldsymbol{\sigma}^t$	Transverse stress tensor
η_{ij}	Arbitrary second order tensor
$\hat{c}_0$	Intrinsic energy at a point in space $\boldsymbol{x}$
$\hat{\boldsymbol{\tau}}^s$	Residual in-plane stresses at a point in space $\boldsymbol{x}$
$\mathbf{C}^s$	In-plane elastic stiffness tensor at a point in space $\boldsymbol{x}$
$\mathbf{M}$	Transverse elastic compliance at a point in space $\boldsymbol{x}$
$\boldsymbol{\Sigma}^s$	Interfacial excess stress
Γ_0	Intrinsic surface energy
$\boldsymbol{\Gamma}^{(1)}$	Residual surface stresses
$\boldsymbol{\Gamma}^{(2)}$	Interface's in-plane elasticity stiffness tensor
$\mathbf{H}$	Interface Poisson's effect tensor
$\boldsymbol{\Delta}^t$	Transverse interfacial excess strain tensor

$\mathbf{\Lambda}^{(1)}$	Residual transverse interfacial deformation tensor
$\mathbf{\Lambda}^{(2)}$	Interfacial transverse compliant tensor
$\lambda_{\pm}$	Lamé constant
$\mu_{\pm}$	Lamé constant
K_S	In-plane bi-axial bulk modulus of an interface
μ_S	In-plane shear modulus of an interface
μ_T	Transverse shear modulus of an interface
E_T	Transverse Young's modulus of an interface
ν_S	Interface Poisson's ratio
Y_{bulk}	Bulk biaxial modulus
Y_{surf}	Surface biaxial modulus
G_{bulk}	Bulk shear modulus
G_{surf}	Surface shear modulus

Continuum Models

δ_{ij}	Kronecker symbol
e_{ijk}	Ricci tensor of alternation
I_{ijkl}	Fourth-order identity tensor
ε_{ij}	Lagrangian strain tensor
σ_{ij}	Symmetric Piola-Kirchhoff II stress tensor
C_{ijkl}	Second order elastic stiffness constants
C_{IJ}	Second order elastic stiffness constants in Voigt notation

$C^{(3)}_{ijklmn}$	Third order elastic stiffness constants
C_{IJK}	Third order elastic stiffness constants in Voigt notation
M_{ijkl}	Second order elastic compliance constants
M_{IJ}	Second order elastic compliance constants in Voigt notation
$M^{(3)}_{ijklmn}$	Third order elastic compliance constants
M_{IJK}	Third order elastic compliance constants in Voigt notation
L	Third order isotropic elastic constant
M	Third order isotropic elastic constant
N	Third order isotropic elastic constant
U	Elastic strain energy
U_c	Complementary elastic strain energy
$A^{(3)}_{ijklmn}$	Arbitrary sixth order tensor
C^{V}_{ijkl}	Voigt estimate of the second order elastic stiffness constants
C^{V}_{ijklmn}	Voigt estimate of the third order elastic stiffness constants
M^{R}_{ijkl}	Reuss estimate of the second order elastic compliance constants
M^{R}_{ijklmn}	Reuss estimate of the third order elastic compliance constants
C^{H}_{ijkl}	Hill estimate of the second order elastic stiffness constants
C^{H}_{ijklmn}	Hill estimate of the third order elastic stiffness constants
ε^{*}_{ij}	Eigenstrain
$\bar{E}_{ij}$	Far-field applied strain
$\bar{\Sigma}_{ij}$	Far-field applied stress

$\overline{S}_{ijlk}$	Eshelby inclusion tensor
$\overline{T}_{ijlk}$	Strain localization tensor
$\overline{H}_{ijlk}$	Stress localization tensor
$\overline{C}_{ijlk}$	Effective second order elastic stiffness constants
$\overline{C}^{(3)}_{ijklmn}$	Effective third order elastic stiffness constants
$\overline{M}_{ijlk}$	Effective second order elastic compliance constants
$\overline{M}^{(3)}_{ijklmn}$	Effective third order elastic compliance constants
Ω	Ellipsoidal region
V_0	Initial Volume
S_0	Surface area
$t_{\alpha i}$	Transformation tensor
U_{bulk}	Total strain energy in the bulk of a given particle
$U_{surface}$	Total surface free energy on the entire particle surface
τ_{ij}	Residual surface stress tensor on a given particle
Q_{ijkl}	Surface rigidity tensor of a given particle
P_{ijklmn}	Third order rigidity tensor of a given particle
a	Smallest of the three semi-axes of an ellipsoid particle
$\hat{\varepsilon}_{ij}$	Self-equilibrium strain tensor
$\overline{C}_{ijkl}$	Effective stiffness tensor of an ellipsoidal particle
$\overline{E}_{X_i}$	In-plane unidirectional Young's modulus in the X_i direction
κ	Combined surface / core coefficient

χ	Combined surface / core coefficient
$\overline{Y}_b$	Thin film in-plane biaxial Young's modulus
$\overline{\nu}_b$	Effective biaxial Poisson's ratio
$\overline{K}$	Sphere effective bulk modulus
$\overline{\mu}$	Sphere effective shear modulus
D	Radius of curvature of an interface / particle length parameter
d	Atomic spacing length parameter
h	Thickness of the interphase
$F(x_1, x_2, x_3)$	Mathematical description of interface geometry
$\boldsymbol{\kappa}$	Curvature tensor of an interface
$\mathbf{g}$	Metric tensor
$\left\{ \begin{matrix} i \\ k \quad j \end{matrix} \right\}$	Christofell tensor of the second kind
$\mathbf{n}$	Normal of an interface
$\mathbf{P}$	Surface projection tensor
∇_s	Surface gradient operator
$\mathrm{div}_s(\ )$	Surface divergence operator
$[\![.]\!]$	Jump operator
$\langle . \rangle$	Average operator

SUMMARY

Steady technological progresses in all fields of nanoscale technology and probe technology have enabled the synthesis, the assembly, the development, the characterization and the improvement of nanostructured materials. The lack of understanding of their macroscopic behavior is a major roadblock for inserting these materials into engineering applications. Partially due to these rapid advances in nano-scale and nano-structured materials, there has been a resurgence of interest in surface elastic properties such as surface energy, surface stresses, and surface elastic stiffness. Because of the large surface-to-volume ratio in nano-materials, surface elastic properties become more prominent. They have strong influence on the overall thermo-mechanical behavior of the nano-materials.

In this dissertation, an innovative approach combining continuum mechanics and atomistic simulations is exposed to develop a nanomechanics theory for modeling and predicting the macroscopic behavior of nanomaterials. This nanomechanics theory exhibits the simplicity of the continuum formulation while taking into account the discrete atomic structure and interaction near surfaces/interfaces. There are four primary objectives to this dissertation. First, theory of interfaces is revisited to better understand its behavior and effects on the overall behavior of nanostructures. Second, atomistic tools are provided in order to efficiently determine the properties of free surfaces and interfaces. Interface properties are reported in this work, with comparison to both theoretical and experimental characterizations of interfaces. Specifically, we report surface elastic properties of groups 10 – 11 transition metals as well as properties for

low-CSL grain boundaries in copper. Third, we propose a continuum framework that casts the atomic level information into continuum quantities that can be used to analyze, model and simulate macroscopic behavior of nanostructured materials. In particular, we study the effects of surface free energy on the effective modulus of nano-particles, nano-wires and nano-films as well as nanostructured crystalline materials and propose a general framework valid for any shape of nanostructural elements / nano-inclusions (integral forms) that characterizes the size-dependency of the elastic properties. This approach bridges the gap between discrete systems (atomic level interactions) and continuum mechanics. Finally this continuum outline is used to understand the effects of surfaces on the overall behavior of nano-size structural elements (particles, films, fibers, etc.) and nanostructured materials. More specifically we will discuss the impact of surface relaxation, surface elasticity and non-linearity of the underlying bulk on the properties nanostructured materials.

In terms of engineering applications, this approach proves to be a useful tool for multi-scale modeling of heterogeneous materials with nanometer scale microstructures and provides insights on surface properties for several material systems; these will be very useful in many fields including surface science, tribology, fracture mechanics, adhesion science and engineering, and more. It will accelerate the insertion of nano-size structural elements, nano-composite and nanocrystalline materials into engineering applications.

CHAPTER 1

INTRODUCTION

This chapter introduces the research presented in this document. First, we discuss the motivations and past works from other scientists that lead to the research covered in this dissertation. We next present a synopsis of the primary objectives and goals of this work to set out clearly the research intended and the methods to be used. Finally, we explain the structure of this dissertation in order to facilitate the reading of this document.

1.1 Motivations

On December 29th 1959, Richard P. Feynman gave a famous talk *"There's Plenty of Room at the Bottom"* at the annual meeting of the American Physical Society at the California Institute of Technology (Caltech) on the problem of manipulating and controlling things on a small scale. Since 1959, the fields of nanostructure science and nanostructured materials (NsM) have been growing explosively and nanomaterials, such as nanocrystalline materials and nanocomposites, have shown promising new and exciting properties. Steady technological progress in all fields of nanoscale technology and probe technology has enabled the synthesis, the assembly, the development, the characterization and the improvement of nanostructured materials. While considerable progress has been made in the basic understanding of making these nano-structured materials, the shift from basic science to technological applications has yet to occur. For example, there has been extensive research on the microstructure and unique properties of carbon nano-tubes (Iijima, 1992; Iijima and Ichihashi, 1993; Gamaly and Ebbesen, 1995; Palaci *et al.*, 2005). Developing applications that take full advantage of the

properties of carbon nanotubes will be the next important step towards their potential industrial use and economic impact. However, up to now, only a very small number of engineering applications of carbon nano-tubes exists (Collins *et al.*, 2001). Even among those applications, very few have taken full advantage of the unique properties that the carbon nano-tubes can provide.

Besides the difficulties of making bulk forms of nano-structured materials, the lack of understanding of their macroscopic behavior is a major roadblock for inserting these materials in engineering applications. Innovative ways of testing and modeling the thermomechanical behavior of nanomaterials must be developed before one can take full advantage of the unique properties that these materials can offer. In other words, in order to bring material science knowledge to material engineering applications, one needs an engineering science-based methodology to bridge the gap between atomic (nano) level understanding and macroscopic material behavior. Very few studies of nano-structured materials have successfully attempted this. For example, requirements for increased fuel economy in motor vehicles demand the use of new, lightweight materials. Nanocomposites, consisting of traditional polymers reinforced by nanometer-scale particles dispersed throughout, may prove to be an economical candidate for metal replacement. In theory, nanocomposites can be easily extruded or molded to near-final shape, provide stiffness and strength approaching that of metals, and reduce weight. Corrosion resistance, noise dampening, parts consolidation, and recyclability all would be improved. However, before such nanocomposites can be used in commercial vehicles, their macroscopic mechanical behaviors, such as effective modulus, fracture toughness, fatigue and creep resistance, etc., must be well understood so that the vehicles can be designed with sufficient reliability and durability.

Continuum mechanics-based micromechanics theories have been used extensively and very successfully in the past to model the macroscopic mechanical behavior of conventional polycrystalline and composite materials. The basic length scale (grain size

or particle size) for such conventional materials is on the order of micrometers or above. At this length scale, the assumption of continuum is valid. In other words, each crystal (or each particle in composite materials) can be treated as a continuous medium and, therefore, continuum mechanics equations can be used to describe the deformation of conventional polycrystalline and composite materials. Nano-structured materials, on the other hand, are characterized by its microstructure with a length scale in the order of nanometers (typically less than 100nm). Because of such fine microstructure, nanomaterials exhibit a wide range of new properties and behavior (Gleiter, 1989; Morris, 1998) that cannot be modeled or explained by the conventional continuum mechanics-based micromechanics theories. For example, it is well known for conventional polycrystalline metals that the yield strength and hardness increase with reduction of grain size, as defined by the Hall-Petch relationship

$$\sigma_{yield} = \sigma_0 + k_y d^{-n} \quad , \tag{1.1}$$

where n is a positive constant (typically $0<n<1$) and d is the grain size. The Hall-Petch relationship was derived based on the continuum theory of dislocation pile-up. Clearly, such a relationship cannot be extrapolated to fine grain size. From a pure mathematical standpoint, this equation would predict infinite strength, certainly as high as the ideal material strength, as grain sizes approaches the nano-scale. Physically, however, the nano-size grains may not have enough space for creating a pile-up of even only two dislocations. In fact, it has been observed by several investigators (Gryaznov *et al.*, 1989; Gryaznov *et al.*, 1990; Nieh and Wadsworth, 1991) that below a certain critical grain size, the yield strength actually decreases with decreasing grain size. This phenomenon, shown in Figure 1.1 from Conrad (2003), is called the Hall-Petch "breakdown" or inverse Hall-Petch. Other mechanical properties, such as the melting point (Alymov and Shorshorov, 1999), toughness and fatigue behavior (Morris, 1998), have also been observed to vary with grain (or particle) size in ways different between nano- and conventional materials.

Another example is the elastic constants (e.g., Young's modulus, Poisson's ratio). It has been reported in the literature that the surface stresses could increase by about 15 to 25% the apparent in-plane bi-axial modulus of a Cu (100) free standing film of 2 nm thick (Banerjea, 1987; Cammarata, 1989; Kosevich, 1989; Nix, 1998). Some experimental work (Catlin, 1960) seems to indicate that the modulus enhancement could be as much as 50%, although it has been pointed out by later studies (Itozaki, 1982; Baker, 1993) that such a large enhancement might be due to experimental errors. When the thickness reduces to below 5 nm, modulus enhancement/reduction of 20% was also predicted (Cammarata, 1989; Streitz, 1994; Streitz, 1994) and confirmed experimentally for several multilayered metal films such as Cu-Nb (Fartash, 1991). As an example, Figure 1.2 shows dependence of the Young's modulus of silver and aluminum films on the film thickness *d* from Mizubayashi *et al.* (1999). More recently, Miller and Shenoy (Shenoy, 1998; Miller, 2000) developed a simple model to incorporate surface stress in determining the size-dependent elastic modulus of plates and rods. In a recent paper, Zhou and Huang (Zhou, 2004) used molecular dynamics simulations to show that depending upon the crystallographic orientations, the effective elastic modulus of a thin free-standing film can either increase or decrease as the film thickness decreases.

Another relevant area of research is the investigation of elastic properties of grain boundaries. A number of publications have suggested that the elastic moduli in the grain boundary domain may differ significantly from those of the bulk. Wolf and co-workers (Wolf, 1989; Wolf, 1989; Kluge, 1990; Wolf, 1990), who studied superlattices of (001) twist boundaries, as well as Adams et al. (Adams, 1989), who examined the $\Sigma 5$ twist boundary in a thin film of copper, have found an increase of the Young's modulus perpendicular to the boundary plane and a substantial decrease of the shear modulus in the boundary plane in the atomic layers adjacent to the boundary. Bassani and co-workers (Alber, 1992; Bassani, 1992; Vitek, 1994; Marinopoulos, 1998) defined the local atomic elastic modulus tensor and determined the values of the local elastic modulus

tensor near grain boundaries in several face center cubic metals using molecular dynamic simulations. They also found that the local elastic moduli are significantly different for atoms near the grain boundaries. Since grain boundaries have distinct elastic properties, the effective modulus of polycrystalline materials should also be dependent on its grain size since the interface (grain boundary) to volume ratio is inversely proportional to the grain size. Existing literature shows mixed results on the dependency of modulus on grain sizes. Some have reported reduction of elastic modulus by as much as 30% (Korn, 1988; Gleiter, 1989; Suryanarayana, 1995) for nano-structured materials. Others (Nieman, 1991; Krstic, 1993; Fougere, 1995) argued that such reduction is purely due to porosities. However, careful molecular dynamic simulations of copper polycrystal (Schiøtz, 1998) have shown that the Young's modulus is indeed reduced by over 25% when the grain size is reduced to 5 nm, even when the polycrystal is fully dense. Similar reduction is seen in simulations where the nanocrystalline metal is grown from a molten phase (Phillot, 1995). Clearly, more experimental work is needed to confirm the relationship between elastic modulus and grain size.

A related issue is the effective properties of composite materials. Specifically, the effective modulus of a conventional composite material, where particles or fibers are measured in μm, is independent of the size of the particles (or fibers), according to the conventional continuum mechanics-based micromechanics theories (Mura, 1987). For example, the well-known Mori-Tanaka formula states that the effective shear modulus for a particulate reinforced composite is given by

$$\bar{\mu} = \mu_0 \left\{ 1 + \frac{f(\mu_1 - \mu_0)}{\mu_0 + 2(4-5\nu_0)(1-f)(\mu_1 - \mu_0)/15(1-\nu_0)} \right\} , \qquad (1.2)$$

where f is the particle volume fraction, ν_0 the Poisson's ratio of the matrix and μ_0 and μ_1 the shear modulus of the particle and matrix, respectively. What this formula tells us is that the effective shear modulus of the composite is the same, as long as the volume fraction of the reinforcement particles remains the same, regardless the size of the

particles. Extensive studies (both theoretical and experimental) have shown that the Mori-Tanaka prediction (as well as predictions from many other conventional continuum mechanics-based micromechanics theories) is quite accurate for composites with micron-size particles. However, the validity of this prediction is questionable when applied to nano-composites. Several studies of nano-laminates already showed the dependency of effective modulus on the layer thickness (Streitz *et al.*, 1994).

Geometrically speaking, the only difference between the nano- and conventional materials is the characteristic length (grain or particle size) of the microstructure. If each phase is assumed continuum, as it is done in the continuum mechanics theory, the overall properties of the material shall be independent of the characteristic length of the microstructure. This is because the characteristic length can be used to re-scale other dimensions in the context of continuum mechanics. In order to take into account the characteristic length of the microstructure, modifications to the continuum assumption must be made and physical characteristics of the nano-composites must be taken into consideration.

Physically speaking, one of the obvious differences between nano- and conventional materials is the amount of grain boundaries (or particle/matrix interfaces in case of composites) per unit volume. The volume fraction of material in the grain boundaries, considered negligible for conventional polycrystalline materials, can in fact become significant for nanomaterials. The fraction of grain boundary material (Mütschele and Kirchheim, 1987) can be assessed as $f=3\delta/d$, where δ is the grain boundary thickness and d the grain size. Thus, 30% of matter is found in grain boundaries for nanomaterials of grain size 5 nm if the grain boundary is considered to be 0.5 nm thick, but only 3% when the grain size is increased to 50 nm. Since the properties of grain boundaries are very different from those of bulk crystals, it is conceivable that the dramatic decrease in grain boundaries will inevitably alter the overall macroscopic behavior of the material.

The distinction between nano- and conventional materials is the characteristic length of the material studied, which dictates the amount of interfacial area per unit volume of the composite. To characterize the amount of interfacial area per unit volume, we introduce the specific interfacial area to volume ratio

$$S_V = \frac{\text{total interfacial area} \times \text{interface thickness}}{\text{volume}} = \frac{S \times \text{t}}{d} \quad . \tag{1.3}$$

It is seen from the above that, when the characteristic size d is reduced from 10 μm (typical of conventional materials) to 10 nm, the corresponding interfacial area to volume ratio of a materials (for example a polycrystalline materials with an average grain size size d) increases by a factor of 1000 for the same given interface thickness. Such dramatic increase in the mount of interfacial area necessitates the consideration of interfacial properties in modeling and predicting the macroscopic behavior of the materials. Such considerations inevitably lead us to the discrete atomic level microstructure of the interface between a nano-size particle and its surrounding environment. In other words, any theory to model and predict the macroscopic behavior of nanostructured materials must be based on the discrete nature of the particle interfaces.

1.2 Dissertation Objectives and Goals

Obviously, one way to account for the behavior of atoms at a surface or an interface is to use quantum mechanics to describe the interaction among atoms on the free surface or the grain boundaries. However, direct use of such theories to model and predict the macroscopic behavior of nanomaterials for engineering applications may not be computationally feasible.

One fundamental issue that needs to be addressed in modeling macroscopic mechanical behavior of nano-structured materials based on their atomic structure is

therefore the large difference in time and length scales. On the opposite ends of the time and length scale spectrum are atomistic calculations and continuum mechanics, each of which consists of highly developed and reliable modeling methods. Atomistic calculation models, such as Molecular Dynamics for example, predict atomic interactions based on discrete atomic properties, while continuum mechanics models predict the macroscopic mechanical behavior of materials idealized as continuous media based on known bulk material properties. However, a corresponding model does not exist in the intermediate range of time and length scales. Even though there is a long history of modeling bulk properties of materials based on atomic level properties, a simple link between the firmly established disciplines of atomistic modeling and continuum mechanics has not been established.

In this dissertation: we propose an innovative approach that combines continuum mechanics and atomistic calculations to develop a nanomechanics theory for modeling and predicting the macroscopic behavior of nanomaterials. This nanomechanics theory exhibits the simplicity of the continuum formulation while taking into account the discrete atomic structure and interaction near surfaces/interfaces. In other words, it uses the atomic level information in a continuum mechanics framework that can be used to analyze, model and simulate macroscopic behavior of nano-structure materials. This approach bridges the gap between discrete system (atomic level interactions) and continuum mechanics. It is a step towards bringing nano-science, where the focus is on atomic interaction, to nano-technology where the interest is in the macroscopic behavior of nano-structured materials in an engineering system.

There are four main objectives to this dissertation: (i) to understand the general behavior of interfaces considered as a dividing surface; (ii) to provide atomistic tools in order to efficiently determine the behavior of interfaces and surfaces; (iii) to develop, a continuum framework that accounts for the interface effects by casting the atomic level information into continuum quantities and that can be used to analyze, model and

simulate macroscopic behavior of nanostructured materials; (iv) to understand the effects of surfaces on the overall behavior of nano-size structural elements (particles, films, fibers, etc.) and nanostructured materials.

First, this thesis addresses the formulation of the surface and interface elastic behavior. The reduced coordination of atoms near a free surface or near an interface induces a corresponding redistribution of electronic charge, which alters the binding situation (Sander, 2003). As a result, the equilibrium position and energy of these atoms will, in general, be different from their bulk positions and bulk energies. Thus, the elastic moduli of the surface region may differ from those of the bulk. Inspired by the works of Gibbs (1928) on the concept of a dividing surface and surface energy, those of Shuttleworth (1950) on surface tension and finally those of Nozières and Wolf (1988) who introduced the concept of surface strain, we clearly formulate the surface free energy, the surface excess energy, the surface stress and strains and the surface elastic constants. We capture the surface atomistic structure and interactions and cast it into surface free energy, a thermodynamic quantity of continuum that will subsequently be used in a continuum framework.

Second, a semi-analytical methodology is developed to quantify the interface elastic behavior. Because of their significant effects on material behavior, surface properties have attracted tremendous attention. Many approaches have been proposed and used to experimentally measure or theoretically predict surface properties. Among the various experimental techniques, contact angle measurement and zero creep method are well-known techniques commonly used to measure surface energy (Digilov *et al.*, 1976; Tyson and Miller, 1977; de Boer *et al.*, 1988; Qu, 2003). Theoretical predictions of surface elastic properties have been made using a variety of different techniques. Among them, first principle calculations, molecular dynamics (MD) and molecular static (MS) simulations have been extensively used. As early as 1986, Ackland and Finnis (1986, 1987) presented calculations of surface tension for body-centered cubic (BCC)

and face-centered-cubit (FCC) metals using simple empirical N-body potentials. Their results yield satisfactory agreement with available experimental data. Needs (Needs and Godfrey, 1990; Mansfield and Needs, 1991; Needs *et al.*, 1991) performed first principle calculations of surface stresses and surface energy for different materials and different surface orientations, and investigated the role that surface stress may play in surface reconstructions. Todd and Lynden-Bell (1993) investigated surface properties and some bulk properties of metals using the Sutton-Chen potential in order to gain microscopic insights into surface phenomena. Others, like Schmid and coworkers (1995), have studied stresses and surface elasticity using effective-medium theory potentials which allow them to probe the stresses and elasticity of individual layers. Daw and Baskes (1983, 1984, 1992), as well as Mishin and coworkers (1999, 2001), evaluated the ability of the embedded-atom method (EAM) potentials to predict energies and stability of non-equilibrium structures. Shenoy (2005), using MS simulations of a slab in conjunction with the EAM potential, calculated several crystal faces of some FCC metals. His method requires multiple MS simulations at different levels of stretching of the slab. Tartaglino (2001) presented a calculation of the change of free energy of a solid surface upon bending of the solid. It is based on extracting the surface stress through a molecular dynamics simulation of a bent slab by using a generalized stress theorem formula, and subsequent integration of the stress with respect to the strain as a function of bending curvature.

Concerning the interfacial energy, Wolf (1990) and Rittner (Rittner and Seidman, 1996) performed energy minimization calculations to reproduce the grain boundary interface energy as a function of misorientation angle for <110> symmetric tilt interfaces. Surprisingly enough, there is limited atomistic simulation work in the literature that directly addresses interfacial stresses and interface elasticity (Streitz, 1994; Streitz *et al.*, 1994; Schmid *et al.*, 1995; Shenoy, 2005). Most of the existing methods of computing surface elastic properties are rather complicated to perform and are computationally

intensive, particularly if the surface stress as a function of surface deformation is the main interest. This work represents an advancement over previous calculations of interface and surface elastic properties of crystalline materials. Using this method, surface elastic properties, such as the intrinsic surface energy density, intrinsic surface stress and surface elastic stiffness, are given analytically in terms of the inter-atomic potentials of the material. To evaluate these analytical expressions for the relaxed surfaces, one needs to know only the equilibrium (or relaxed) positions of the atoms near the free surface, which are obtained by conducting a standard energy minimization calculation of the interface structure (Spearot, 2005). In comparison with existing methods, the semi-analytical method developed here reduces the amount of computation significantly, and conceivably increases the accuracy of the computation. More importantly, because of the analytical and explicit nature of the method, it provides us with a much better tool to understand the surface characteristics.

Third we focus on developing a continuum framework that incorporates the surface free energy into the analysis of the macroscopic deformation of nanostructured materials. In particular, we study the effects of surface free energy on the effective modulus of nano-particles, nano-wires and nano-films as well as nanostructured crystalline materials. The effect of free surfaces on the elastic properties of thin films and nanowires has been studied intensively by atomistic simulation (Cammarata and Sieradzki, 1989; Wolf, 1991; Streitz, 1994; Cammarata, 2000; Diao, 2004; Liang *et al.*, 2005). For example, Liang *et al.* (2005) found a decrease of the Young's modulus of [100] copper nanowires when decreasing the cross-sectional area and they qualitatively attribute the decrease of Young's modulus to the non-linear elasticity of the core of nanowires (see Figure 1.3). In a similar study Diao et al. study the effects of the surfaces and edges on the structure and elastic properties of gold (Au) nanowires. They found that when the thickness of a gold nanowire is less than a critical value, the surface stresses induce a phase transformation and result in a new structure for the nanowire. Wolf

(1991) examined elastic properties of thin films along different crystallographic orientations. He found that the Young's modulus in the (100) direction for (100) oriented Cu and Au films decreases when decreasing the thickness of the film while the Young's modulus in the (110) or (112) direction for (111) oriented Cu and Au films is found to be increasing when decreasing the film thickness.

Nevertheless, few researchers have proposed a model incorporating the surface behavior into a continuum model. Cammarata and Sieradzki (1989) proposed a simple surface stress model that explicitly introduced surface energy and surface stress into the equations for equilibrium of a thin film. They showed that depending on the sign of surface stress (tensile or compressive), surface stress causes a thin film to contract or expand in the plane of the film upon relaxation from its bulk atomic positions. The resulting equilibrium strain with respect to the unrelaxed configuration is given by

$$\varepsilon^* = -2\frac{f_0}{\lambda_0 Y_\infty} \quad , \tag{1.4}$$

where f_0 is the surface stress, λ_0 is the initial unrelaxed thickness of the film, and Y_∞ is the biaxial modulus of the bulk. The effective biaxial modulus of the relaxed film is then evaluated as

$$Y^* = Y_\infty + 2\frac{f_0}{\lambda_0}\left(B_\infty + 2\eta - 3 + \frac{f'}{f_0}\right) \quad , \tag{1.5}$$

where B_∞ is the coefficient of first-order term in the Taylor expansion of the biaxial modulus of bulk as a function of the biaxial strain, η is some sort of a Poisson's ratio, and f' is the first derivative of the surface energy with respect to the surface strain. This model neglects the change of the film thickness caused by the surface relaxations and is specifically tailored to a very specific type of nanostructural elements.

Concerning nanostructured materials, there is a very limited and recent work in the literature (Sharma and Ganti, 2003; Sharma and Ganti, 2004; Duan *et al.*, 2005; Huang, 2006) that addresses the size dependence of nanostructured materials and

nanocomposites. All of these works revisited the Eshelby solution including the surface energy and interfacial stresses assuming that the same relationship between surface energy (or interfacial energy in this case) and surface stress exist for free surfaces and bicrystal surfaces.

In comparison with the existing models, the work presented here clearly distinguishes free surfaces and interfaces. It incorporates the surface properties in a general framework valid for any shape of nanostructural elements / nano-inclusions (integral forms) and characterizes the size-dependency of the elastic properties. Such a formulation clearly constitutes a tool that will enable the integration of those types of materials into engineering applications and a basis to develop more advanced composite materials.

1.3 Dissertation Structure

This dissertation is the synthesis of several years of personal research at Georgia Tech but also refers to collaborative work with some of my colleagues. This research led to five publications in scientific journals and several presentations at various conferences. The writing of these memoirs had been carried out with the concern of details and precision, in the hope that this manuscript might become a useful working tool for the ones who would like to get inspired from the results obtained and the methods developed. Therefore, some sections might be redundant but each chapter can be read independently and does not require the reader to know all the subtleties of the previous chapters.

Chapter 2 is relatively short and presents the theory of atomistic simulation. First, we outline the fundamentals and the role of atomistic simulation. Next the basic assumptions and simplifications used in the basic atomistic "machinery" are discussed. This includes the use of periodic boundary conditions to mimic medium of infinite extent

of thin films for examples, and the different type of statistical mechanics ensembles considered to control the evolution of the atomistic system. Next, we present the mathematical details of the molecular statics and energy minimization algorithm used throughout this work. The most probable configuration of nanostructure in their relaxed state is necessary to be able to describe their elastic properties. Finally, we close this chapter with a discussion of the fundamentals of interatomic potentials in section 2.4 with an emphasis on the embedded-atom method for F.C.C metals and the pair-wise potentials for ionic solids. Detailed explanations regarding the interatomic potentials used for this work (Daw and Baskes, 1984; Foiles *et al.*, 1986; Wolf *et al.*, 1999) are given.

Chapter 3 is devoted to the elastic properties of bulk phases. Following the axiom "nanostructure = bulk + surface", a clear understanding of the properties of the bulk is a necessary first step in the description of nanostructure. In this chapter we first recall some useful fundamental concepts and definitions used to describe the elastic behavior of bulk phases. More specifically, we will recall definitions of stress, strain and elastic energy as well as the elastic constant. Next we focus and present an easy and simple analytical method of calculating the full set of second and third order elastic (TOE) constants for single crystal materials based on their interatomic potentials. This method is based on the expansion of an interatomic potential about the equilibrium state of the bulk. It has the advantage of significantly reducing the computation time and is inherently accurate. The method is analytical in that it involves only numerical evaluation of the interatomic potential and its derivatives. To illustrate this methodology, we present the TOE constants Cu, Ni, Au, Ag, Pt, Pd and Al single crystals. We close this chapter by presenting homogenization techniques to calculate the effective TOE constants of the corresponding polycrystals. The estimates of the effective TOEC for isotropic aggregates of cubic crystals are of greater interest when calibrating experiments measuring anharmonicity properties of the studied materials. Results are presented for

Cu, Ni, Au, Ag, Pt, Pd and Al polycrystalline isotropic aggregates of single cubic crystals.

Chapter 4 presents the elastic description of surfaces and interfaces. In this chapter, the concept of interfacial excess energy is first reformulated from the continuum mechanics perspective. This approach considers a single dividing surface separating the two homogeneous phases (as opposed to the interface considered as an interphase). The interface contribution to the thermodynamic properties is defined as the excess over the values that would obtain if the bulk phases retained their properties constant up to an imaginary surface (of zero thickness) separating the two phases. Such a new formulation allows us to then determine interfacial excess energy using a semi-analytical method. The cases of free surfaces and interfaces are distinguished. To illustrate this methodology we subsequently present numerical examples of calculated free surface elastic properties, such as the intrinsic surface energy density, intrinsic surface stress and surface elastic stiffness for low-index surfaces (111), (100) and (110) of face-centered cubic metals copper (Cu), nickel (Ni), silver (Ag), and palladium (Pd). The properties of these surfaces are discussed in terms of "reduced units" in order to compare the different materials and understand the origin of these coefficients. Numerical examples of calculated interfacial excess energy are finally given for grain boundaries in Cu bicrystals to close this chapter.

Chapter 5 discusses nanomechanics theories modeling the macroscopic behavior of nano-structured materials. First, existing methods in the literature designed to account for the size-effect in material behavior are briefly reviewed. We then propose and develop a framework to incorporate the surface free energy into the continuum theory of mechanics. Based on this approach, it is demonstrated that the overall elastic behavior of structural elements (such as particles, wires, films) is size-dependent. Although such size-dependency is negligible for conventional structural elements, it becomes significant when at least one of the dimensions of the element shrinks to nanometers. Numerical

examples are given to illustrate quantitatively the effects of surface free energy on the elastic properties of nano-size particles, wires and films for several materials. These results are then compared with a semi-analytical method based on interatomic potential to compute and study the elasticity of nanowires and thin films grown along (001), (110), and (111) crystallographic directions for group 10-11 transition metals. The comparison with the continuum model clearly shows the influence of the third order elastic constants on the effective elastic stiffness of the nanostructural elements. The softening induced by the surface elasticity in all three directions is accentuated or compensated by the non-linear response of the core of the element depending on the orientation. A decomposition of the interatomic potential gives insights on the origins of the effective elastic response of the nanostructural elements. We finally close this chapter by revisiting boundary conditions of the classical formulation of Eshelby (1957) for embedded inclusions and modifying it by incorporating the previously excluded surface/interface stresses, tension and energies. Unlike the classical result, our modified formulation will eventually renders the elastic state of an embedded inclusion size-dependent making possible the extension of Eshelby's original formalism to nano-inclusions. The theory developed combines continuum mechanics and atomistic simulation for modeling and predicting the macroscopic properties of nanomaterials. Such nanomechanics theory exhibits the simplicity of the continuum formulation while takes into account the discrete atomic structure and interaction near surfaces/interfaces. In other words, it uses the atomic level information in a continuum mechanics framework that can be used to analyze, model and simulation macroscopic behavior of nano-structure materials. This approach bridges the gap between discrete system (atomic level interactions) and continuum mechanics.

Chapter 6 summarizes the significant contributions of this research and provides recommendations and suggestions for future work directions based on the results of this thesis.

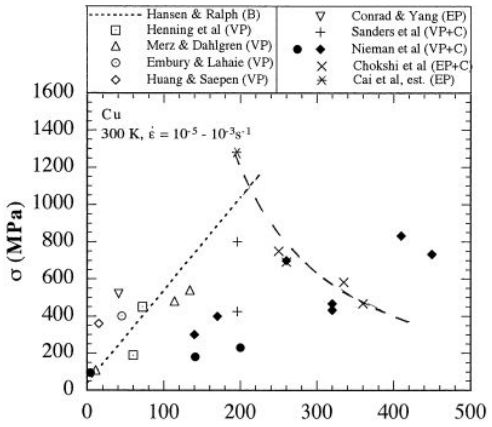

Figure 1.1 Hall-Petch plot of the effect of grain size d on the flow stress σ of Cu at 300K from Conrad (2003)

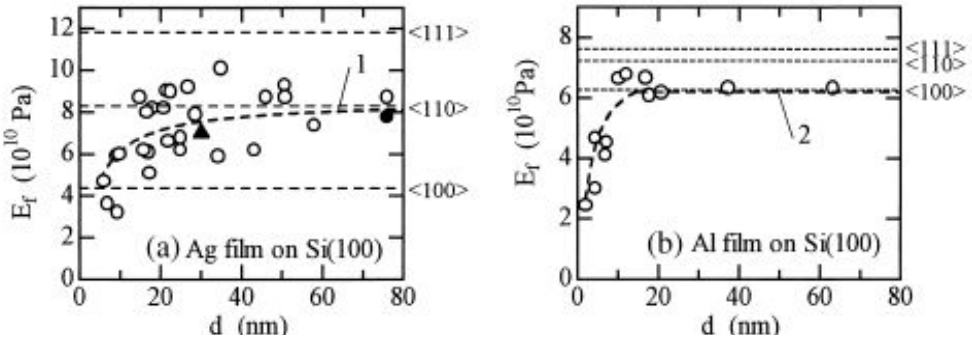

Figure 1.2 The dependence of the Young's modulus of silver and aluminum films on the film thickness *d* from Mizubayashi *et al.* (1999)

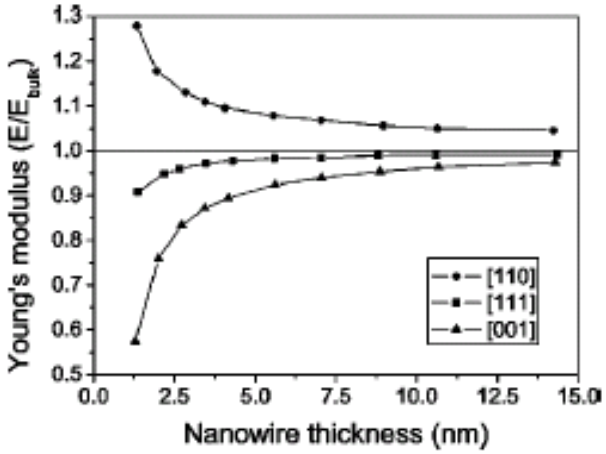

Figure 1.3 Thickness dependence of Young's moduli for [001], [110], and [111] nanowires from Liang *et al.* (2005)

CHAPTER 2

ATOMISTIC SIMULATIONS

This chapter presents the theory of atomistic simulation. First, we outline the fundamentals of atomistic simulation and its limitations. We next discuss the main assumptions and simplifications used in the basic "machinery". This includes the role of periodic boundary conditions and the different types of statistical mechanics ensembles considered. In the following section the mathematical algorithm details of molecular statics calculations used for this work are presented. Finally, the fundamentals of interatomic potentials with an emphasis on the embedded-atom method close this chapter. No attempt is made to address advanced topics in atomistic calculations and we recommend the reading of more detailed and comprehensive reviews in books by Haile (1992) or Rapaport (1995) for examples.

2.1 Introduction

Many physical problems of great interest fall outside the realm of "special cases" that can be treated with theoretical models. Among them, we could mention the physics and chemistry of surfaces and interfaces, the characterization of clusters of atoms or the anharmonic properties of materials, which all involve to a large extent, disorder, asymmetry and a considerable amount of degrees of freedom. With the advent of high speed computers, computational material science became a scientific field in its own right, enabling the setup of computer experiments to investigate complex and realistic systems. For instance, as early as 1957, the introduction of the monstrous IBM 704, allowed Alder and Wainwright (1957) to investigate the phase diagram of hard sphere

systems and to perform their calculations for a 108-atom system. Many important insights concerning the behavior of simple liquids emerged from their studies. Nowadays atomistic simulations complement most fields of materials science and engineering. For example, former colleague Douglas Spearot used Molecular Dynamics (MD) simulations to study the fundamental failure processes that occur at a bicrystal interface in Cu and Al as a result of a mechanical deformation (Spearot, 2005).

Atomistic simulation refers to a family of computational techniques used to model the interaction and configuration of a system of atoms. These simulation models include energy minimization, Molecular Dynamics, Monte Carlo and lattice Monte Carlo method. The energy minimization method seeks to reduce the net force acting on the atoms by moving the atoms to lower energy configurations. This process is ideal for determining lowest energy structures at zero Kelvin. The Molecular Dynamics model imitates the vibrations of atoms by solving Newton's equation of motion. Through this process, systems are simulated at finite temperatures. The Monte Carlo method involves the random sampling of a system's states. This method is useful in determining equilibrium structures and properties at finite temperatures. Finally, the lattice Monte Carlo method is useful to model systems over long time periods. This method ignores atomic vibrations and considers events that involve atomic motion from one lattice site to another. In this research we principally dealt with energy minimization and Molecular Dynamics.

In atomistic simulations, the goal is to understand and model the motion of each atom in the material. The collective behavior of the atoms allows the understanding of how the material undergoes deformation, phase changes or other phenomena, providing links between the atomic scale and meso/macro phenomena. In the atomistic framework, each atom is represented as a point mass in space. The force acting upon each atom is derived from energy functionals of the positions of the atomic nuclei. This simplification bypasses the treatment of the motion and interaction of the individual electrons. The

conservation law of total energy implies that the force $\mathbf{F}^i$ on a given atom *i* derives from the gradient of the potential energy *U*,

$$\mathbf{F}^i = -\frac{\partial U\left(\mathbf{r}^1,\cdots,\mathbf{r}^i,\cdots,\mathbf{r}^N\right)}{\partial \mathbf{r}^i} \quad , \tag{2.1}$$

where $\mathbf{r}^i$ is the atomic position vector for the i^{th} atom. Detailed information concerning the interatomic potential used for calculations in this research is presented in section 2.4. Traditional atomistic simulations follow the classical laws of mechanics and evaluate the atomic positions, velocities and forces of a set of interacting atoms. This is a deterministic technique: given initial conditions, the subsequent evolution is in principle completely determined. The conversion of this microscopic information to macroscopic observables such as pressure, stress tensor, energy, etc… requires theories and strategies developed in the realm of statistical mechanics. According to statistical physics, physical quantities are represented by averages following the ergodicity principle (ensemble average = time average). Trajectories in the phase space calculated by atomistic simulation provide such configurations, and therefore measurement of physical quantities is simply obtained through arithmetic averaging.

Typical atomistic simulations can be performed on systems containing thousands, maybe millions of atoms, for a simulation time ranging a few picoseconds to several nanoseconds. Simulations are therefore limited by the relaxation time and the characteristic length of the quantities of interest. As discussed later in this chapter, there is a solution for solving the scaling problem (ability to treat more atoms in the system studied), although no solution exists for the time scale dilemma (limitation in the time scale range). As a consequence, we need to be very careful while considering its range of validity and interpret with caution the results.

2.2 Nuts and Bolts of Atomistic Simulation

In this thesis work we used two atomistic codes called PARADYN and WARP, initially written by Dr. Steve Plimpton at Sandia National Laboratories / Albuquerque, NM. The code is written in FORTRAN90 and performs parallel calculations with a domain-decomposition technique. We used a MD code modified by former student Douglas Spearot who implemented in parallel the capability to perform molecular statics (energy minimization) calculations. In addition, we made a number of small modifications to the code that are critical to the analysis provided in this thesis, such as the implementation of algorithms to identify various characteristics of nanoscale configurations. This section discusses some important aspects of atomistic simulations performed throughout this research.

2.2.1 Periodic Boundary Conditions

As briefly discussed in the previous section, an inherent problem associated with atomistic simulations is the limited number of atoms or equivalently the degrees of freedom that can be treated. No matter how large the simulated system is, its total number of atoms N, is still negligible compared with the number of atoms contained in "macroscopic chunks" of materials (for example in the order of 10^{11} atoms for a 1mm-long wire with a cross section of 5 nm). While the study of atomic surface effects is particularly important, in this research we want to study and characterize the macroscopic behavior of surfaces and interfaces as well as realistic nanostructures. In order to have a realistic modeling of those physical systems we can use *Periodic Boundary Conditions* (PBCs). This methodology virtually replicates to infinity the calculation box containing the studied geometry by rigid translation in all the three Cartesian directions. Figure 2.1 illustrates this principle in a 2-D case.

If one particle of the calculation box is located at a position vector $\mathbf{r}$, then it is assume that this particle actually represents an infinite set of particle located at,

$$\left\{\mathbf{r} + l\mathbf{a} + m\mathbf{b} + n\mathbf{c}\right\} \quad , \; l,m,n = \left(-\infty, +\infty\right) \quad , \tag{2.2}$$

where l, m, n are integers ranging from minus infinity to plus infinity, and with **a**, **b**, and **c** being the three axis vectors of the calculation box. All of these "image" cells are subjected to the same forces, but only one of them is explicitly represented in the atomistic methods. Not only does each particle i in the calculation cell interact with other particles in the box, but also with their images in the surrounding images cells. One can easily see that periodic boundaries virtually remove surface effects from the system and that the position of the box boundary has no consequence.

As an effect of the PBCs, the number of interactions increases tremendously. Nevertheless, in practice, the interatomic potentials used have a finite range for interaction and particles do not interact with each other if they are separated by a distance larger than a defined cutoff distance R_c. By making sure that the box size is at least 2 R_c, we can simplify even more the PBCs by keeping the closest image cells. This is known as the minimum image criterion.

Even though, the purpose of PBCs is to eliminate surface effects, in this work we are also interested in situations where we want to have free surfaces. Free surfaces are generally simulated by defining a thick slab delimited by 2 free surfaces. PBC in the direction perpendicular to the free surfaces is removed while it is retained in the in-plane directions. There is therefore no replication in the perpendicular direction. The slab is taken to be thick enough so that one can expect that the core would be similar to the bulk of the material. The top and bottom surface can then be considered as decoupled and independent. In these conditions the system can be considered to behave as a semi-infinite medium. Similarly if one leaves PBCs along one direction only, we can simulate a wire, with the wire axis along the PBC direction.

2.2.2 Control of the System: Role of Statistical Ensembles

In an atomistic calculation, the system could be in a state characterized by a certain density, energy, temperature, and/or pressure. From a statistical mechanics point of view, different ensembles can be considered to describe isolated or partially isolated systems. These considerations are particularly important when performing atomistic simulations. Different boundary types lead to different ensembles.

If the system is completely isolated from its surroundings with a fixed number of atoms, volume and constant total energy, this corresponds to a microcanonical (NVE) ensemble (Greiner *et al.*, 1995). The microcanonical average of a physical quantity Θ is obtained as the time average on the trajectory

$$\langle \Theta \rangle_{NVE} = \frac{1}{t_N} \sum_{t=1}^{t_N} \Theta\left(\Phi(t)\right) \quad , \tag{2.3}$$

where $\Phi(t)$ is the phase space coordinate of the system (3N positions and 3N velocities), and t_N is the final time step of the calculation.

To carry out calculations in the NVE ensemble, the Verlet leapfrog scheme (Verlet, 1967) is commonly used. It generates trajectories in the NVE ensemble in which the total energy (kinetic plus potential energy) is conserved. If this property drifts or fluctuates significantly in the course of a simulation it indicates that the time step is too large or the potential cutoffs too small. The algorithm requires for each atom, that values be obtained for the position vector $\mathbf{r}$ and the force vector $\mathbf{F}$ at time t while the velocity vector $\mathbf{v}$ is half a time step behind. The first step is to advance the velocity to $t + 1/2\,\Delta t$ by integrating the force

$$\mathbf{v}(t + \frac{1}{2}\Delta t) = \mathbf{v}(t - \frac{1}{2}\Delta t) + \Delta t \frac{\mathbf{F}(t)}{m} \quad , \tag{2.4}$$

where m is the mass of the atom and Δt is the time step. The positions are then evaluated at the next time step using the new velocity

$$\mathbf{r}(t+\Delta t) = \mathbf{r}(t) + \Delta t\, \mathbf{v}(t+\frac{1}{2}\Delta t) \quad . \tag{2.5}$$

Atomistic simulations normally require properties that depend on position and velocity to be evaluated at the same time. The velocity at time t is therefore obtained from averaging the velocities at time $t+1/2\,\Delta t$ and $t-1/2\,\Delta t$

$$\mathbf{v}(t) = \frac{1}{2}\left[\, \mathbf{v}(t+\frac{1}{2}\Delta t) + \mathbf{v}(t-\frac{1}{2}\Delta t)\right] \quad . \tag{2.6}$$

If the system is allowed to interact with its surrounding environment through either thermal or physical constraints then depending on the equations of motion that describe the system of atoms, this may correspond to the canonical (NVT or NPT) ensemble (Greiner *et al.*, 1995). The basic idea is to integrate other equations in place of Newton's equations in such a way that the sampling is performed in another statistical ensemble.

To carry out calculations in the NVT, the method developed by Nosé and Hoover (Nosé, 1984; Hoover, 1985) is generally used. It introduces a time-dependent frictional term ζ to the equation of motions, whose time evolution is driven by the imbalance between the instantaneous kinetic energy and the average kinetic energy $(3N/2)k_BT$. The velocity of each atom is calibrated to the control temperature T_o through

$$\begin{aligned} \dot{\mathbf{v}}(t) &= \frac{\mathbf{F}(t)}{m} - \zeta\, \mathbf{v}(t) \\ \dot{\zeta} &= v_T^2\left(\frac{T(t)}{T_o} - 1\right) \end{aligned} \quad , \tag{2.7}$$

where the 'dot' represents the first derivative with respect to time, T is the temperature at time t, and v_T is the thermostating rate. We use this type of system control in this research when performing studies of the tensile behavior of nanostructures (such as thin films or nanowires) or grain boundary interfaces.

To carry out calculations in the NPT an additional degree of freedom representing the volume of the calculation box is introduced, and all the particle coordinates are given in units relative to the box. Several schemes for isobaric ensembles have been developed by Andersen (1980), Parrinello and Rahman (1981) or Hoover (1985). Each of these methods allows the volume of the calculation cell to change its size, driven by the imbalance between the internal and desired system pressures or stresses. Similar to the NVT ensemble, the Nosé-Hoover (1985) constant pressure equations of motion calibrate the velocity of each atom to the control pressure P_o through

$$\begin{aligned} \dot{\mathbf{v}}(t) &= \mathbf{F}(t) - \boldsymbol{\eta}\mathbf{v}(t) \\ \dot{\boldsymbol{\eta}} &= \frac{v_P^2}{NkT_o} V(t)\left(\boldsymbol{\Pi} - \mathbf{P}_o\right) \quad , \\ \dot{\mathbf{h}} &= \boldsymbol{\eta}\mathbf{h} \end{aligned} \tag{2.8}$$

where $\boldsymbol{\eta}$ is the isobaric friction coefficient, v_P is the constant pressure damping coefficient, k is the Boltzmann's constant and $V(t)$ is the volume of the calculation box at time t. The boundaries of the calculation box are defined by a set of three vectors $\mathbf{h}$ along the edges of the periodic unit cell, $\mathbf{h}$. The internal system stress $\boldsymbol{\Pi}$ is calculated using the virial definition,

$$\boldsymbol{\Pi}^{\alpha\beta} = \frac{1}{\Omega}\left(-\sum_i m_i \mathbf{v}_i^{\alpha} \mathbf{v}_i^{\beta} + \frac{1}{2}\sum_{j \neq i} \mathbf{F}_{ij}^{\alpha} \mathbf{r}_{ij}^{\beta} \right) \quad . \tag{2.9}$$

where Ω is the volume of the system, m_i and $\mathbf{v}_i$ the mass and velocity of the atom i, $\mathbf{F}_{ij}$ is the force between atoms i and j, $\mathbf{r}_{ij}$ is the distance between atoms i and j, and the subscripts α and β denote the Cartesian components. In this work, we use this control scheme when performing equilibration studies of the nanostructures and grain boundary interfaces in order to get the relaxed states.

More complete reviews of ensembles used in atomistic calculation are provided in textbooks by Haile (1992).

2.3 Molecular Statics

In this work, molecular statics (MS) calculations are used to compute the minimum energy of nanostructures such as films and nanowires as well as the most probable configurations of interface structures. It is critical that the relaxed states of interfaces and nanostructures are depicted accurately to enable us to draw unambiguous conclusions regarding the surface and interface properties or the mechanical behavior of the nanostructures studied. A nonlinear conjugate gradient method is used to calculate the atomic configuration (relaxed positions of the atoms) associated with the minimum potential energy of the system considered. The following is a brief overview of the algorithms implemented with Douglas Spearot in the WARP code. The MD code PARADYN already had a built-in conjugate gradient algorithm to minimize the energy of the system to a certain tolerance. A more complete review of steepest decent, linear and nonlinear conjugate gradient methods is provided in Shewchuk (1994).

The conjugate gradients (CG) method is a well-known iterative method used to solve sparse systems of linear equations. The basic idea behind this method is to used the gradient $f'(x)$ of smooth enough continuous function $f(x)$ to find the minimum of this function since by definition, the gradient vector points in the direction of the greatest increase of a given function.

The starting point of the CG method in atomistic simulation is taken from equation (2.1) where the force is defined as the negative of the gradient of the potential energy U. Therefore, since the force vector points in the direction of greatest decrease in the potential energy, the minimum of the potential energy is found by setting the gradient equal to zero and solving for the appropriate values of $\{\mathbf{r}^1,\cdots,\mathbf{r}^N\}$.

The minimum potential energy of a system (most probable configuration) is obtained through an iteration process. For the i^{th} iteration step, the first step is to define

the residual $\mathbf{p}_{(i)}$ as the negative of the gradient of the potential energy which is also by definition the force

$$\mathbf{p}_{(i)} = -\frac{\partial U\left(\mathbf{r}^1, \cdots, \mathbf{r}^N\right)}{\partial \mathbf{r}_{(i)}} \quad , \tag{2.10}$$

where $\mathbf{r}_{(i)}$ represents the position vector at the i^{th} iteration step. The position is then updated at the next step using search direction $\mathbf{d}_{(i)}$ such that

$$\mathbf{r}_{(i+1)} = \mathbf{r}_{(i)} + \alpha_i \mathbf{d}_{(i)} \quad , \tag{2.11}$$

where α_i is a scalar that minimizes the potential energy in the search direction for this iteration step.

The choice of step direction is different depending on the minimization technique chosen. For example, the method of steepest decent (SD) sets the search direction equal to the residual at each iteration step. Thus, successive search directions will always be orthogonal. Unfortunately, the method of steepest decent is inefficient, as the algorithm will often search in the same direction a number of times during energy minimization. Linear and nonlinear conjugate gradient methods use the residual to define the initial search direction such as,

$$\mathbf{d}_{(0)} = \mathbf{p}_{(0)} = -\frac{\partial U\left(\mathbf{r}^1, \cdots, \mathbf{r}^N\right)}{\partial \mathbf{r}_{(0)}} \quad . \tag{2.12}$$

Using equation (2.12) and an appropriate step size α_0, the positions of the atoms are updated. Once the new atomic positions are obtained, the new search direction, $\mathbf{d}_{(i+1)}$, is built from the new residual, $\mathbf{p}_{(i+1)} = -\partial U / \partial \mathbf{r}_{(i+1)}$, and the last search direction,

$$\mathbf{d}_{(i+1)} = \mathbf{p}_{(i+1)} + \beta_{i+1} \mathbf{d}_{(i)} \quad , \tag{2.13}$$

where the scalar $\beta_{(i+1)}$ is calculated by requiring that successive search directions are *U*-orthogonal meaning conjugate,

$$\mathbf{d}_{(i+1)}^{T} U \mathbf{d}_{(i)} = 0 \quad . \tag{2.14}$$

Due to convergence criteria for non-linear problems, the minimization algorithm implemented in WARP calculates the scaling parameter β using the Polak-Ribière formula,

$$\beta_{(i+1)} = \max\left\{ \frac{\mathbf{p}_{(i+1)}^{T}\left(\mathbf{p}_{(i+1)} - \mathbf{p}_{(i)}\right)}{\mathbf{p}_{(i)}^{T}\mathbf{p}_{(i)}}, 0 \right\} \quad , \tag{2.15}$$

Convergence is guaranteed in the Polak-Ribière method by requiring that β be non-negative (Shewchuk, 1994). Setting $\beta = 0$ essentially results in reinitializing the minimization calculation, as the search direction is then equal to the residual of the potential energy.

Once the search direction is determined, we finally need to evaluate the scalar α_i before using equation (2.11) to calculate the new atomic positions associated with the minimum potential energy of the system. To solve for α_i, the CG method requires that the gradient of the potential energy at the point $\mathbf{r}_{(i+1)}$ be orthogonal to the search direction,

$$\left[U'\left(\mathbf{r}_{(i+1)}\right)\right]^{T} \mathbf{d}_{(i)} = \left[U'\left(\mathbf{r}_{(i)} + \alpha_i \mathbf{d}_{(i)}\right)\right]^{T} \mathbf{d}_{(i)} = 0 \quad . \tag{2.16}$$

A line search algorithm is used to solve the above expression. Two common algorithms are the Newton-Raphson method and the secant method. Both require that the second derivative of the potential energy exist and be continuous. The Newton-Raphson method requires the explicit evaluation of the second derivative of the potential and is computational expensive, therefore the implemented algorithm employs the secant method which is simpler and less computationally demanding. The secant method does not directly compute $U''\left(\mathbf{r}_{(i)}\right)$; it evaluates the first derivative (negative of the force vector) at various points around $U'\left(\mathbf{r}_{(i)}\right)$. With this methodology,

$$\alpha_i = -\mu \frac{\left[U'\left(\mathbf{r}_{(i)}\right)\right]^T \mathbf{d}_{(i)}}{\left[U'\left(\mathbf{r}_{(i)} + \mu \mathbf{d}_{(i)}\right)\right]^T \mathbf{d}_{(i)} - \left[U'\left(\mathbf{r}_{(i)}\right)\right]^T \mathbf{d}_{(i)}} \quad , \tag{2.17}$$

where μ is a small, nonzero number. The choice of μ is arbitrary during the first iteration of the secant method. For each subsequent iteration, the value of μ is set equal to the negative of the previous value of α_{n}, i.e.,

$$\mu_{n+1} = -\alpha_n \quad . \tag{2.18}$$

In equation (2.18), *n* denotes the number of iterations taken in the secant method, which should not be confused with the number of iterations in the conjugate gradient routine, *i*. The combination of properly chosen search directions and step sizes avoids repeated searches by stepping the 'correct' distance in each search direction on every CG iteration step.

Nevertheless, nonlinear CG methods, applied to nonlinear functions such as the potential energy of system of atoms, does not guarantee the convergence toward the global minimum of the system every time but rather a local minimum. To improve convergence, the CG algorithm routine is restarted every few iterations, especially in problems that involve small numbers of atoms.

In order to verify the CG algorithm, we modeled a F.C.C lattice of copper with the lattice spacing slightly different from its bulk value in one of the three directions. After applying PBCs in the three directions, and letting the system relax using the CG routine in a NVT ensemble, the resulting structure reached after equilibration, was exactly the bulk configuration.

2.4 Interatomic Potentials

The interatomic potentials are at the heart of atomistic simulations. In classical atomistic simulations, the atoms are represented by mass-points in space interacting

through many-body interactions potential. The complex description of electrons dynamics is abandoned and an effective depiction is taken. In this picture, the interatomic interaction and internal degrees of freedom are completely defined by a set of parameters and functions which depend on the positions of the atoms in the system.

2.4.1 Interatomic Potentials for F.C.C metals: the Embedded Atom Method (EAM)

Among all of the interatomic potentials, the EAM method is a very efficient technique for modeling realistic descriptions of metallic cohesion. Pair-wise potentials, like Lennard-Jones (LJ) potentials (Lennard-Jones, 1924a, 1924b) presented in equation (2.19) fail to adequately describe all the properties of metals.

$$\Phi_{LJ}(r) = 4\varepsilon\left[\left(\frac{\sigma}{r}\right)^{6} - \left(\frac{\sigma}{r}\right)^{12}\right] . \tag{2.19}$$

For example, the LJ potential imposes the Cauchy relation $C_{12}=C_{44}$ on the elastic constants. This relation proves to be wrong for most metals. Pair-wise potential also fails to estimate accurately the relaxation and reconstruction around point defects such as vacancies or interstitial sites.

By introducing many-body potentials, we can go beyond the pair interaction. Daw and Baskes (1983; 1984) developed the embedded atom method (EAM) potential to describe atomic bonding in face-centered cubic (FCC) metallic systems. The EAM is a semi-empirical approach that uses multi-atom potential for modeling the interatomic forces. In this scheme all atoms are treated in a unified way. The method is so called "embedded" because it views each atom individually as if it was embedded in a host lattice comprising all other atoms. It has the important benefit of keeping the computational scaling on the order of magnitude of N (if N is the number of particle composing the system) whereas more complex and thorough many-body potential scale on the order of magnitude N^3 (for instance, Density Functional Theory). For example the

EAM potential requires only 2 to 5 times the computing time of pair potential (Voter, 1994). In the EAM framework, the total energy of an atom is expressed as the sum of the contribution from the energy of two-body interactions and the embedding energy incorporating the complex nature of metallic cohesion

$$E_n = E_n^G + E_n^V = G_n(\bar{\rho}_n) + \frac{1}{2}\sum_{m \neq n} V(r^{mn}) \quad , \tag{2.20}$$

where E_n^G and E_n^V represent, respectively, the embedding energy of atom *n* and the pair interaction potential between atoms *m* and *n*. . In the above expressions, r^{mn} is the scalar distance between atoms *m* and *n* and $\bar{\rho}_n$ is the local background electron density induced at atom *n* by the rest of the atoms in the system calculated as a linear superposition of the contributions from all neighboring atoms. The density contribution of each atom is assumed to be spherically symmetric, implying that bond orientation is neglected in such potentials.

$$\bar{\rho}_n \equiv \sum_{\mathrm{m} \neq \mathrm{n}} \rho^m \left(r^{mn} \right) \quad . \tag{2.21}$$

This summation is performed over the neighboring atoms within a specified cut-off distance and typically includes at least first and second nearest neighbors.

According to Density Functional Theory, it can be demonstrated that (i) the energy of a system of atoms can be exactly determined by a function of its electronic density (Carlsson, 1990) and (ii) the energy change due to the embedding of an atom into a host matrix of atoms can be also given by a function of the electronic density of the host matrix prior to embedding an atom (Daw and Baskes, 1984). A parameterized functional form is determined empirically by fitting the predicted results to experimental values or values obtained from more precise ab-initio techniques. These include physical properties such as the equilibrium lattice parameter, cohesive energy, sublimation energy, elastic constants C_{11}, C_{12} and C_{44} and vacancy-formation energy (Daw and Baskes, 1984; Foiles *et al.*, 1986). Interatomic potentials developed more recently are fit to additional

structural properties, such as the energies of hexagonal close-packed (HCP), body-centered cubic (BCC) and diamond cubic structures, the phonon energies or the stacking fault energy (Mishin, 1999; 2001).

In this work we used two types of potential to study metallic surfaces and interfaces. For free surfaces the Foiles *et al.* (1986) EAM interatomic potential for copper, nickel, palladium and silver was used. This potential is satisfactory when studying basal free surfaces since it is fitted to bulk elastic constants and surface energy. To partially validate these EAM potentials and the molecular dynamics codes used, we performed two sets of simulations to calculate the elastic constants (C_{11}, C_{12}) and surface energy in the [100], [110] and [111] crystallographic directions (more detailed results and discussion on these subjects are presented in chapter 3 and chapter 4).

The first set of simulations is designed to compute the elastic constants. We first created the initial assembly using the given material properties (atomic weight, lattice spacing, material EAM potential, etc.). A typical computation cell contains 1000 atoms. PBCs in all three directions are applied in order to simulate a crystal of infinite extent. We then performed a strain meshing of the calculation cell in all three directions with strains ranging from -1% to 1% and a strain increment of ±0.01% using a NVT ensemble. The crystal was therefore stretched by independently varying the lattice constants along the three principal directions of the calculation cell. The total energy density u of the system was then calculated for each triplet (ε_{11}, ε_{22}, ε_{33}). The elastic constants were then determined by fitting a polynomial to the bulk energy density–strain curve such as,

$$u = U_0 + U_{ii}\varepsilon_{ii} + \frac{1}{2}U_{iijj}\varepsilon_{ii}\varepsilon_{jj} \quad . \tag{2.22}$$

Through this curve fitting, the coefficients C_{11} and C_{12} can be directly determined. In the second series of calculations, the initial assembly is created and oriented in the desired crystallographic orientation. Periodic boundary conditions are used in the two planar directions with free surfaces in the vertical direction to mimic an infinite plane. The slab

thickness must be chosen to be thick enough to avoid interaction between the two surfaces. A conjugate gradient method is used to minimize the total energy of the system using a NVT ensemble such that atoms in the vertical direction can fully relax. Numerical results for the elastic constant surface energy calculations are shown in Table 2.1 and compared to experimental values. As expected, results show good agreement with the experimental values.

When studying interfaces, The Mishin *et al*. EAM interatomic potential for copper (2001) is used in this work. Spearot (2005) showed in his work that the EAM interatomic potential of Mishin *et al.* (2001) for copper is in fact the most appropriate choice to accurately model the formation and structure of dislocations in FCC metals, as well as the structure of grain boundaries. Indeed this potential gives better estimates for both the intrinsic and unstable stacking fault energies compared to Foiles *et al.* (1986) potential.

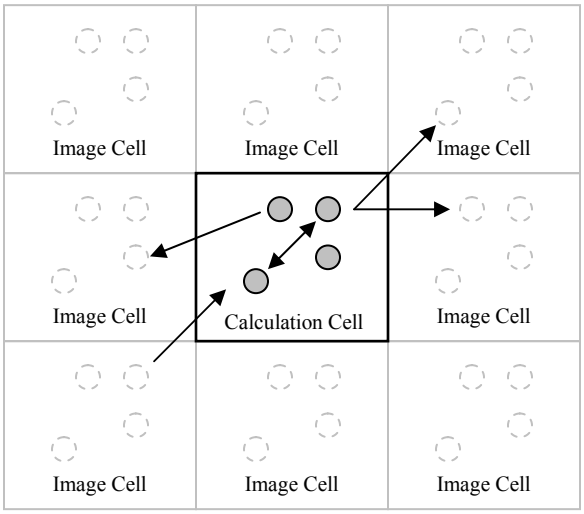

Figure 2.1 Principle of Periodic Boundary Conditions

Table 2.1 Elastic constants (in 100 GPa) and surface energy for (111), (100) and (110) surfaces (in $J.m^{-2}$) from EAM potential validation

	Ni	**Cu**	**Pd**	**Ag**	**Ag**
C_{11}	2.331 (2.500)[b]	1.674 (1.661)[b]	1.984 -	1.289 1.222)[b]	1.289 1.222)[b]
C_{12}	1.544 (1.5)[b]	1.241 (1.199)[a]	1.707 -	0.911 (0.907)[a]	0.911 (0.907)[a]
Γ_0 (111)	1.436 (1.45)[c]	1.181 (1.17)[c]	1.224 (1.22)[c]	0.620 (0.62)[c]	0.620 (0.62)[c]
Γ_0 (100)	1.572 (1.58)[c]	1.288 (1.28)[c]	1.377 (1.37)[c]	0.703 (0.705)[c]	0.703 (0.705)[c]
Γ_0 (110)	1.721 (1.73)[c]	1.413 (1.40)[c]	1.482 (1.49)[c]	0.768 (0.77)[c]	0.768 (0.77)[c]

[a] Reference (Hiki and Granato, 1966) ; [b] Reference (Landolt-Bornstein, 1979)
[c] Reference (Foiles *et al.*, 1986)

CHAPTER 3

ELASTIC DESCRIPTION OF BULK PHASES

In this chapter we recall useful fundamental concepts and definitions used to describe the elastic behavior of bulk phases. More specifically, we recall definitions of stress, strain and elastic energy as well as the elastic constant. A particular emphasis focus on an easy and simple analytical method of calculating the full set of third order elastic (TOE) constants for single crystal materials based on their interatomic potentials. The method is analytical in that it involves only numerical evaluation of the interatomic potential and its derivatives. The TOE constants of single crystal Cu, Ni, Au, Ag, Pt, Pd and Al were calculated using this method. The effective TOE constants of their corresponding polycrystals were also obtained from their single crystal data using a self-consistent method as well as Voigt and Reuss-type estimates. The results show good agreement with existing experimental data.

3.1 Introduction

Second order elastic (SOE) constants and third order elastic (TOE) constants respectively appear in the quadratic and cubic representation of strain energy density. SOE constants describe the linear elastic response of a material. They are commonly the only parameters used in engineering to characterize the elastic properties of a material. TOE constants are of interest in solid state physics because they characterize the anharmonicity properties of materials (non-linearity of the atomic displacements) such as thermal expansion, Grüneisen parameters, specific heat, interactions of thermal and acoustic phonons, and defects' properties of crystals or the equation of state. If higher

order elastic constants are known, many of these anharmonic properties can be calculated or estimated. For example, the speeds and propagation modes of sound waves in statically stressed and damaged materials are different from those in unstressed and undamaged specimens(Seeger and Buck, 1960). In the presence of small damages at the beginning of a fatigue cycle, non-linear effects are important, and thus the knowledge of the higher-order elastic constants. The deviation from the linear behavior can be expressed in terms of the TOE constants. For the reasons cited above it is important to determine the higher order elastic constants in crystals.

While data for SOE constants can be found in any given book of undergraduate Mechanical Engineering class, there are few experimental and theoretical data available in the literature concerning the third order elastic constants. Experimentally, TOE constants can be determined from velocity measurements (Thurston and Brugger, 1964; Brugger, 1965; Hiki and Granato, 1966; Salama and Alers, 1967; Riley and Skove, 1973) of small amplitude sound waves in statically stressed media. The difference in speed and propagation modes from the unstressed media is expressed as a function of the TOE constants. An alternative experimental technique is to measure the TOEC statically (Seeger and Buck, 1960; Powell and Skove, 1968) by observing the deviations of the second order elastic constants (SOEC) from the Hooke's law in materials under hydrostatic pressure. However there is a large discrepancy in the measured values principally due to the accuracy of these experiments and the structure sensitivity of the TOE constants. Furthermore these experimental procedures are exceedingly laborious.

Analytical methods have also been used to estimate the TOE constants. Micromechanics formulations (Barsh, 1968; Hamilton and Parrott, 1968; Lubarda, 1997) have been applied to calculate the effective TOE constants of isotropic aggregates of cubic crystals. Çağin (Çağin and Ray, 1988) and Ray (Ray and Moody, 1985) presented a fluctuation formula allowing them to calculate the third-order elastic constants of solids, using molecular-dynamics computer simulation. Srinivasan (Srinivasan, 1966)

derived expressions for the third-order elastic constants of non-primitive lattices from lattice theory by the method of homogeneous deformation.

In the literature, there are few, sometimes incomplete, reported experimental and theoretical measurements for single crystals and polycrystalline materials and there is a large discrepancy of results among them. In this chapter, along with the reminder of fundamental concepts used in the description of elastic properties, we present an analytical method of computing the second and third order elastic constants of groups 10 – 11 transition metals using the interatomic potentials directly without any atomistic simulations and tabulate the results for single crystals as well as isotropic aggregates of cubic crystals. It is of interest to determine the higher order elastic constants in a homologous series of metals because the nature of the binding forces in metals is very different from that in ionic or covalent crystals but should be very similar in the homologous series. Specifically, we calculate the full set of elastic constants for Cu, Ni, Au, Ag, Pt, Pd but also for Al. The calculated elastic coefficients are consistent with the few existing data.

3.2 Definition of the Elastic Constants

3.2.1 Elastic Strain and Complementary Energy Representations

One way to introduce the elastic constants is through the Taylor expansion of the total strain energy density at the state of zero strain and stress (Martin, 1975),

$$U = \frac{1}{2} C_{ijkl} \varepsilon_{ij} \varepsilon_{kl} + \frac{1}{6} C^{(3)}_{ijklmn} \varepsilon_{ij} \varepsilon_{kl} \varepsilon_{mn} + \dots \quad , \tag{3.1}$$

where ε_{ij} is the Lagrangian strain measured from the perfect lattice of an undeformed crystal of infinite extent, C_{ijkl} is a fourth order tensor consists of second order elastic

constants, and $C^{(3)}_{ijklmn}$ is a sixth order tensor consisting of the third order elastic constants of the solid. All are defined in the reference configuration, or the initial stress-free configuration. Since the strain energy is expressed as a function of the strains, it can be easily shown that the following symmetry conditions must be met by these tensors,

$$C_{ijkl} = C_{jikl} = C_{klij} \quad , \tag{3.2}$$

$$C^{(3)}_{ijklmn} = C^{(3)}_{jiklmn} = C^{(3)}_{klmnij} = C^{(3)}_{mnijkl} = C^{(3)}_{ijmnkl} = C^{(3)}_{mnklij} = C^{(3)}_{klijmn} \quad . \tag{3.3}$$

Instead of the tensorial notation, it is convenient in certain cases to use the notation introduced by Voigt (contracted) for these tensors defined as a mapping of pair indices *ij* to a single index *α*. The general rules to contract the indices are $(11) \Leftrightarrow (1)$, $(22) \Leftrightarrow (2)$, $(33) \Leftrightarrow (3)$, $(23) \Leftrightarrow (4)$, $(13) \Leftrightarrow (5)$, $(12) \Leftrightarrow (6)$. Of course, the symmetry properties of the elasticity tensor remain in their contracted form, e.g., $C_{12} = C_{21}$ and $C_{123} = C_{312}$.The number of independent SOE constants varies from 21 to 2 while the number of independent TOE constants(Fumi, 1951; Jarić and Kuzmanović, 2001) varies from 56 to 3. For crystal with higher symmetry, the number is in its reduced form.

The symmetric Piola-Kirchhoff stress is the gradient of the strain energy with respect to the (Lagrangian) strain

$$\sigma_{ij} = \frac{\partial U}{\partial \varepsilon_{ij}} = C_{ijkl}\varepsilon_{kl} + \frac{1}{2} C^{(3)}_{ijklmn}\varepsilon_{kl}\varepsilon_{mn} \quad . \tag{3.4}$$

Similarly, the elastic compliance constants M_{ijkl} and $M^{(3)}_{ijklmn}$ are defined from the complementary strain energy U_c, the Legendre transform of the strain energy U. The complementary strain energy density of an elastic solid can also be expanded in a Taylor series about the state of zero strain and stress as,

$$U_c = \frac{1}{2} M_{ijkl}\sigma_{ij}\sigma_{kl} + \frac{1}{6} M^{(3)}_{ijklmn}\sigma_{ij}\sigma_{kl}\sigma_{mn} + \dots \quad , \tag{3.5}$$

The second and third order elastic moduli and compliances are related by(Barsh, 1968),

$$M_{ijkl} = C^{-1}_{ijkl} \quad , \tag{3.6}$$

$$M^{(3)}_{ijklmn} = -M_{ijpq} C^{(3)}_{pqrsuv} M_{rskl} M_{uvmn} \quad . \tag{3.7}$$

3.2.2 Second and Third Order Elastic Constants of Cubic Crystals

The invariant constants of cubic crystals can be obtained from the symmetries of the crystal structure. The principal cubic axis vectors **a**, **b** and **c** are orthonormal and each one of them is a two-fold axes of rotation. The atomic array is unchanged by inversion about the plane defined any of the three principal axes. Furthermore the atomic array should be invariant under 120º rotation about its principal axes. Therefore there are at most three independent SOE constants and six independent TOE constants.

Written with respect to the principal cubic axes, the corresponding second order elastic stiffness tensor is

$$C_{ijkl} = C_{12}\delta_{ij}\delta_{kl} + 2C_{44} I_{ijkl} + (C_{11} - C_{12} + 2C_{44}) A_{ijkl} \quad , \tag{3.8}$$

where δ_{ij} is the Kronecker symbol, I_{ijkl} is the fourth-order unit tensor and $A_{ijkl} = a_i a_j a_k a_l + b_i b_j b_k b_l + c_i c_j c_k c_l$ is the principal cubic axes tensor. Therefore for solids with cubic symmetry, the three independent non-zero second order elastic constants are

$$C_{11} = C_{22} = C_{33}\,, \quad C_{12} = C_{13} = C_{23}\,, \quad C_{44} = C_{55} = C_{66} \quad . \tag{3.9}$$

Similarly the second order elastic compliance tensor has the form

$$M_{ijkl} = M_{12}\delta_{ij}\delta_{kl} + 2M_{44} I_{ijkl} + (M_{11} - M_{12} + 2M_{44}) A_{ijkl} \quad , \tag{3.10}$$

with the relation

$$M_{11} = \frac{C_{11} + C_{12}}{(C_{11} - C_{12})(C_{11} + 2C_{12})}, \quad M_{11} = \frac{-C_{12}}{(C_{11} - C_{12})(C_{11} + 2C_{12})}, \quad M_{44} = \frac{1}{4C_{44}} \quad . \tag{3.11}$$

The inversion of symbol *C* and *M* gives the relationship expressing the second order elastic stiffness tensor as a function of the second order compliance tensor.

As for the corresponding third order elastic stiffness tensor we have

$$
\begin{aligned}
C^{(3)}_{ijlkmn} = {} & \lambda_1\delta_{ij}\delta_{kl}\delta_{mn} + \lambda_2\left(\delta_{ij}\delta_{kl}\delta_{ln} + \delta_{ij}\delta_{kn}\delta_{lm} + \delta_{im}\delta_{kl}\delta_{jn} + \delta_{in}\delta_{kl}\delta_{jm} + \right. \\
& \left. \delta_{ik}\delta_{jl}\delta_{mn} + \delta_{il}\delta_{jk}\delta_{mn}\right) + \lambda_3\left(\delta_{ik}\delta_{jm}\delta_{ln} + \delta_{ik}\delta_{jn}\delta_{lm} + \delta_{il}\delta_{jm}\delta_{kn} + \right. \\
& \left. \delta_{il}\delta_{km}\delta_{jn} + \delta_{im}\delta_{jk}\delta_{ln} + \delta_{im}\delta_{jl}\delta_{kn} + \delta_{in}\delta_{km}\delta_{jl} + \delta_{in}\delta_{jm}\delta_{kl}\right) + \\
& \lambda_4 A^{(3)}_{ijklmn} + \lambda_5\left(\delta_{ij}A_{klmn} + \delta_{kl}A_{ijmn} + \delta_{mn}A_{ijkl}\right) + \lambda_6\left(a_i a_j b_k b_l c_m c_n + \right. \\
& a_i a_j c_k c_l b_m b_n + b_i b_j a_k a_l c_m c_n + b_i b_j c_k c_l a_m a_n + c_i c_j b_k b_l a_m a_n + \\
& \left. c_i c_j a_k a_l b_m b_n\right)
\end{aligned}
\quad , \tag{3.12}
$$

where $A^{(3)}_{ijklmn}$ is introduced as the following quantity

$$
A_{ijkl} = a_i a_j a_k a_l a_m a_n + b_i b_j b_k b_l b_m b_n + c_i c_j c_k c_l c_m c_n \quad . \tag{3.13}
$$

It follows that for crystals with cubic symmetry, the six independent TOE constants are given by

$$
\begin{gathered}
C_{111} = C_{222} = C_{333}, \\
C_{112} = C_{113} = C_{122} = C_{133} = C_{223} = C_{233}, \\
C_{123}, \\
C_{144} = C_{255} = C_{366}, \\
C_{155} = C_{166} = C_{244} = C_{266} = C_{344} = C_{355}, \\
C_{456} \quad .
\end{gathered}
\quad . \tag{3.14}
$$

Using equation (3.7), the components of the sixth-order elastic compliance tensor for a cubic crystal $M^{(3)}_{ijklmn}$ rewritten in the Voigt notation are therefore given by

$$
M_{111} = -\left(M_{11}^3 + 2M_{12}^3\right)C_{111} - 6M_{12}\left(M_{11}^2 + M_{11}M_{12} + M_{12}^2\right)C_{112} - 6M_{11}M_{12}^2 C_{123} \quad , \tag{3.15}
$$

$$
\begin{aligned}
M_{112} = {} & -M_{12}\left(M_{11}^2 + M_{11}M_{12} + M_{12}^2\right)\left(C_{111} + 2C_{123}\right) \\
& -\left(M_{11}^3 + 3M_{11}^2 M_{12} + 9M_{11}M_{12}^2 + 5M_{12}^3\right)C_{112}
\end{aligned}
\quad , \tag{3.16}
$$

$$
\begin{aligned}
M_{123} = {} & -3M_{11}M_{12}^2 C_{111} - 6M_{12}\left(M_{11}^2 + M_{11}M_{12} + M_{12}^2\right)C_{112} \\
& -\left(M_{11}^3 + 3M_{11}M_{12}^2 + 2M_{12}^3\right)C_{123}
\end{aligned}
\quad , \tag{3.17}
$$

$$
M_{144} = -4M_{44}^2\left(M_{11}C_{144} + 2M_{12}C_{155}\right) \quad , \tag{3.18}
$$

$$
M_{155} = -4M_{44}^2\left(M_{12}C_{144} + \left(M_{11} + M_{12}\right)C_{155}\right) \quad , \tag{3.19}
$$

$$M_{456} = -8M_{44}^{3}C_{456} \quad . \tag{3.20}$$

The inverse relationships expressing the third order stiffness moduli in terms of the third order compliance moduli can be obtained by simply interchanging the compliance moduli by the stiffness moduli in equations (3.15) – (3.20). Once the elastic constants are known, their corresponding compliance can be calculated.

3.2.3 Second and Third Order Elastic Constants of Isotropic Materials

An isotropic tensor is a tensor which retains its components unchanged when subjected to any proper orthogonal transformation of rectangular Cartesian coordinates. The isotropic tensors of second and third order (or higher order) can be constructed by only using Kronecker delta tensors δ_{ij} and Ricci tensor of alternation e_{ijk}. Any isotropic tensor can be represented by a linear combination of these two tensors. For isotropic materials, the representation of the SOE stiffness tensor becomes quite simple:

$$C_{ijkl} = C_{12}\delta_{ij}\delta_{kl} + 2C_{44}I_{ijkl} \quad . \tag{3.21}$$

And the TOE stiffness tensor is expressed as

$$\begin{aligned} C^{(3)}_{ijklmn} = {} & C_{123}\delta_{ij}\delta_{kl}\delta_{mn} + 6C_{144}\left(\delta_{ij}I_{klmn} + \delta_{kl}I_{ijmn} + \delta_{mn}I_{ijkl}\right) + \\ & 8C_{456}\left(\delta_{in}I_{jmkl} + \delta_{jn}I_{imkl} + \delta_{im}I_{jnkl} + \delta_{jm}I_{inkl}\right) \end{aligned} \quad . \tag{3.22}$$

Like the Lame's constants for isotropic solids, these constants are sometimes referred to as *universal constants* for isotropic materials.

In the next section, we will present an easy and simple method of calculating the full set of second and third order elastic constants for single crystal materials based on their interatomic potentials.

3.3 A Method of Computing the Elastic Constants

The interaction between atoms in crystalline metals can be well characterized by the interatomic potential. A generic interatomic potential function for the atom *n* an infinite crystal can be written formally as

$$E_n = E\left(r^{mn}\right) \quad , \tag{3.23}$$

,where $r^{mn} = \sqrt{\left(r_1^{mn}\right)^2 + \left(r_2^{mn}\right)^2 + \left(r_3^{mn}\right)^2}$ is the scalar distance between atom *m* and atom *n*. The form of the potential function in equation (3.23) implies central symmetry of the interatomic forces, i.e. the potential is a function of scalar distance r^{mn} between atoms, rather than the vector components r_i^{mn} of the interatomic distance. In other words, bond orientation is neglected in the description of such potentials. This assumption is reasonably good for f.c.c metals, but not so appropriate for materials with oriented bonding such as b.c.c or hexagonal closed-packed (h.c.p.) crystals.

For small displacements, a Taylor expansion of E_n yields

$$\begin{aligned} E_n = \sum_m E\left(r^{mn}\right)\Big|_{r^{mn}=\hat{r}^{mn}} &+ \left.\frac{\partial E\left(r^{mn}\right)}{\partial \mathrm{r}_j^{mn}}\right|_{r^{mn}=\hat{r}^{mn}} \mathrm{u}_j^{mn} \\ &+ \frac{1}{2}\left.\frac{\partial^2 E\left(r^{mn}\right)}{\partial \mathrm{r}_j^{mn}\partial \mathrm{r}_l^{mn}}\right|_{r^{mn}=\hat{r}^{mn}} \mathrm{u}_j^{mn}\mathrm{u}_l^{mn} + \cdots \end{aligned} \quad , \tag{3.24}$$

where $\hat{r}^{mn}$ is the scalar distance between the atom *m* and atom *n* in the undeformed or referenced configuration, r_i^{mn} is the Cartesian component of the vector $\mathbf{r}^{mn}$ and the component of the displacement vector is $u_i^{mn} = r_i^{mn} - \hat{r}_i^{mn}$. For a homogeneous and uniform deformation, the nine components of the deformation gradient tensor F_{ij}^{mn} relative to the undeformed configuration are given by

$$r_i^{mn} - \hat{r}_i^{mn} = F_{ij}^{mn}\hat{r}_j^{mn} = (\varepsilon_{ij} + \omega_{ij})\hat{r}_j^{mn} \quad , \tag{3.25}$$

where, the summation convention is implied for the subscripts, but not superscripts. In equation (3.25), ω_{ij} is an antisymmetric second order tensor representing rigid body rotation while ε_{ij} is the usual strain tensor. Note that for homogeneous deformation the deformation gradient is constant therefore independent of *n*. It then follows that the Taylor expansion (Johnson, 1972; Johnson, 1973; Oh and Johnson, 1988) of (3.23) with respect to perfect lattice configuration can be written as,

$$E_n = A^{(n)} + A_{ij}^{(n)}\varepsilon_{ij} + \frac{1}{2}A_{ijkl}^{(n)}\varepsilon_{ij}\varepsilon_{kl} + \frac{1}{6}A_{ijklmn}^{(n)}\varepsilon_{ij}\varepsilon_{kl}\varepsilon_{mn} \quad , \tag{3.26}$$

with the quantities $A^{(n)}$, $A_{ij}^{(n)}$, $A_{ijkl}^{(n)}$ and $A_{ijklmn}^{(n)}$ defined by,

$$A^{(n)} = E_n\left(\hat{r}^{mn}\right) \quad , \tag{3.27}$$

$$A_{ij}^{(n)} = \sum_{p\neq n}\left.\frac{\hat{r}_j^{pn}\partial E_n\left(r^{mn}\right)}{\partial r_i^{pn}}\right|_{r^{mn}=\hat{r}^{mn}} \quad , \tag{3.28}$$

$$A_{ijkl}^{(n)} = \sum_{p\neq n}\sum_{q\neq n}\left.\frac{\hat{r}_j^{pn}\hat{r}_l^{qn}\partial^2 E_n\left(r^{mn}\right)}{\partial r_i^{pn}\partial r_k^{qn}}\right|_{r^{mn}=\hat{r}^{mn}} , \; A_{ijkluv}^{(n)} = \sum_{p\neq n}\sum_{q\neq n}\sum_{s\neq n}\left.\frac{\hat{r}_j^{pn}\hat{r}_l^{qn}\hat{r}_v^{sn}\partial^3 E_n\left(r^{mn}\right)}{\partial r_i^{pn}\partial r_k^{qn}\partial r_u^{sn}}\right|_{r^{mn}=\hat{r}^{mn}} \quad . \tag{3.29}$$

The equalities presented in equations (3.27) and (3.29) are valid as long as the potential is a smooth enough function of the interatomic distance r^{mn}. The equilibrium condition for a perfect lattice with this energy function is that energy is independent of terms linear with in the strain parameter with equivalently translate mathematically by

$$\left.\frac{\partial E_n}{\partial \varepsilon_{ij}}\right|_{r^{mn}=\hat{r}^{mn}} = 0 = A_{ij}^{(n)} \quad . \tag{3.30}$$

Equilibrium with respect to pure rotation ω_{ij} only requires that $A_{ij}^{(n)}$ be positive, while equilibrium with respect to pure deformation leads directly to equation (3.30).

We can now consider a representative volume element (RVE) of volume Ω that contains *N* number of atoms. When subjected to uniform strain ε_{ij}, the stored elastic strain energy density averaged over the RVE is thus given by

$$U = \frac{1}{N}\sum_{n=1}^{N}\frac{1}{\Omega_n}\left(E_n - A^{(n)}\right) = \frac{1}{N}\sum_{n=1}^{N}\frac{1}{\Omega_n}\left(\frac{1}{2}A^{(n)}_{ijkl}\varepsilon_{ij}\varepsilon_{kl} + \frac{1}{6}A^{(n)}_{ijklmn}\varepsilon_{ij}\varepsilon_{kl}\varepsilon_{mn}\right) \quad , \qquad (3.31)$$

where Ω_n is the atomic volume of atom n. For a large enough crystal (i.e. N is considerably large), equation (3.31) is independent of the definition of the atomic volume Ω_n. Comparison of equation (3.31) with equation (3.1) leads to identification of the elastic constants tensors

$$C_{ijkl} = \frac{1}{N}\sum_{n=1}^{N}\frac{1}{\Omega_n}A^{(n)}_{ijkl} = \frac{1}{N}\sum_{n=1}^{N}\sum_{p\neq n}\sum_{q\neq n}\frac{1}{\Omega_n}\left.\frac{\hat{r}_j^{pn}\hat{r}_l^{qn}\partial^2 E_n\left(r^{mn}\right)}{\partial r_i^{pn}\partial r_k^{qn}}\right|_{r^{mn}=\hat{r}^{mn}} \quad , \qquad (3.32)$$

$$C^{(3)}_{ijklmn} = \frac{1}{N}\sum_{n=1}^{N}\frac{1}{\Omega_n}A^{(n)}_{ijklmn} = \frac{1}{N}\sum_{n=1}^{N}\sum_{p\neq n}\sum_{q\neq n}\sum_{s\neq n}\frac{1}{\Omega_n}\left.\frac{\hat{r}_j^{pn}\hat{r}_l^{qn}\hat{r}_v^{sn}\partial^3 E_n\left(r^{mn}\right)}{\partial r_i^{pn}\partial r_k^{qn}\partial r_u^{sn}}\right|_{r^{mn}=\hat{r}^{mn}} \quad . \qquad (3.33)$$

Certain papers related to the thermodynamics of elasticity theory (Brugger, 1965) argue that the Lagrangian strains $\eta_{ij} = \varepsilon_{ij} + \frac{1}{2}F_{ik}F_{kj}$ should be used rather than ε_{ij}, but the same results are obtained with either choice of deformation parameter. It is seen that the coefficients $A^{(n)}$, $A^{(n)}_{ij}$, $A^{(n)}_{ijkl}$, and $A^{(n)}_{ijklmn}$ only depend on the interatomic potential used. We note that, once the potential E_n is given, its derivatives can be calculated and evaluated numerically as long as the interatomic spacing $\hat{r}^{mn}$ is known for the crystal in its fully relaxed state (ideal crystal of infinite extent), which is available for most metallic crystals. It thus follows from (3.32) – (3.33) that, one can easily calculate the elastic constants C_{ijkl} and $C^{(3)}_{ijklmn}$ for a given interatomic potential. Such calculation involves only numerical evaluation of the derivatives of the potential function. Obviously, the choice of the interatomic potential function is important.

In this work, the interactions between atoms are modeled using Embedded Atom Method (EAM) potentials(Daw and Baskes, 1983; Daw and Baskes, 1984) is used in equations (3.32) and (3.33) to calculate the SOE and TOE constants. As explained in

chapter 2, the embedded atom method is a semi-empirical approach modeling the interatomic forces. It has the important benefit of being a multi-atom potential. In this scheme all atoms are treated in a unified way. This method is so called "embedded" because it views each atom individually as if it was embedded in a host lattice constituted of all other atoms. The total energy of an atom is the sum of the energy from the two-body interactions and the embedding energy given by

$$E_n = E_n^G + E_n^V \quad , \tag{3.34}$$

where,

$$E_n^G = G_n(\bar{\rho}_n) \text{ and } E_n^V = \frac{1}{2}\sum_{m \neq n} V(r^{mn}) \quad , \tag{3.35}$$

represent, respectively, the embedding energy of atom *n* and the pair interaction potential between atom *m* and atom *n*. In the above expressions, $\bar{\rho}_n$ is the local background electron density induced at atom *n* by the rest of atoms in the system. The electron density $\bar{\rho}_n$ at atom *n* is taken as a linear superposition of the contributions from all neighboring atoms which are assumed to be spherically symmetric, i.e.,

$$\bar{\rho}_n = \sum_m \rho_n(r^{mn}) \quad . \tag{3.36}$$

The functions $V(r)$, $G(r)$ and $\rho(r)$ are central function (i.e. function of unique scalar *r* rather than components of the coordinates of the interatomic distance) material dependent. The derivatives of (3.32) and (3.33) have been calculated and their expressions are listed in the Appendix A.

Before closing this section, we mention that, one can neglect the kinetic energy term. The free energy involves contributions from both the internal energy of the crystal and the product of the entropy and absolute temperature. The latter contribution vanishes at 0K temperature. Configurational and thermal sources of entropy can be ignored. The atomic rearrangements in the bulk of the crystal are regular and smooth enough to be ignored. It is well known that, as far as the elastic properties are concerned, the thermally

activated atomic vibrations in the interior of the crystal are negligible at low and room temperature. In fact, our calculations have confirmed that the kinetic energy for copper at 100K is only about 3% of the total energy. When the temperature rises to 1200K, the kinetic energy constitutes about 10% of the total energy. The elastic modulus decrease approximately linearly with increasing temperature (Chen and Chen, 2005; Wu, 2006), with a decrease of up to 10% over a temperature range of 0 to 400 K for copper for example Therefore the zero temperature internal energy constitutes a fair measure of the free energy at low moderate temperature. The choice of the potential function is important because it influences the final results. Among all of the interatomic potentials, the many-body EAM potential gives a realistic description of metallic cohesion.

3.4 Elastic Constants for Single Crystals

The method presented above has been used to calculate the second and third order elastic constants of single crystals of the transitions metals in groups 10 – 11 as well as aluminum. As discussed in the previous section, the interatomic spacing for a single crystal of infinite extent is needed for calculating the elastic constants. The interatomic spacings of the materials studied are presented in Table 3.1.

To simulate an infinite crystal, we constructed a rectangular cell and used periodic boundary conditions in all directions to mimic a crystal of infinite extend (see chapter 2 Section 2.2.1 for more details). A typical calculation cell contains 500 atoms. A bigger calculation sample is not necessary since the dimension of the calculation box are chosen to be at least twice as big as the cut-off distance of the interatomic potential. The interactions between atoms are modeled using Embedded Atom Method (EAM) potentials(Daw and Baskes, 1983; Daw and Baskes, 1984) and calculated up to the third nearest neighbor by truncating the potential at the appropriate distance. More details on

the interatomic potentials are presented in chapter 2. The next step is to compute the derivatives of the potential function and evaluate them numerically according to (3.32) and (3.33). The numerical values of the SOE constants and TOE constants for single crystal calculated according to the analytical method presented in this chapter are given in Table 3.2 and Table 3.3. Shown in parentheses are the corresponding experimental data with their references indicated by the superscripts. In comparing the results among them, for more readability a graphical representation of the TOEC for the single crystals studied are presented in Figure 3.2.

It is seen from our results that the SOE constants are very close to the literature values. This comes with no surprise because the EAM potentials are fitted with the SOE constants. The methodology used here is merely a reverse procedure to back calculate them. As for the TOE constants, the comparison with existing experimental data varies. We find a good agreement between the theoretical calculations and the experimental data for copper, silver and gold. Agreement in the case of aluminum and nickel is less satisfactory. This should not be a surprise neither, for some of the experimental data on TOE constants differ among themselves by an order of magnitude as observed in Table 3.3. Disagreement might be due to the accuracy of the experimental processes. Other factors like the grain structure, purity of the sample, or the presence of impurities might also affect the experimental measurements. Despite some literature research, we are not aware of any experimental method that can definitively asses the accuracy of these experimental data. However, it is reasonable to assume that the EAM potentials that are fitted to the lattice constant, the cohesive energy, the elastic constants, the vacancy formation energy, phonon frequencies and the intrinsic stacking fault energy would provide an accurate prediction of the TOE constants. In other words, the theoretical values computed using the EAM potential should be considered more accurate than some of the experimental data, considering the accuracy of the experimental methods, and the wide range of variability of the materials used in the experiments. So, even though, we

are not aware of experimental data on the TOE of platinum and palladium single crystals, we believe the values predicted here are reliable.

In order to verify those calculations, we have also performed a strain meshing of the calculation cell with strains in the three directions ranging from -1% to 1% and incremented by ±0.01% strain steps. The calculation cell is stretched by independently varying the lattice constants along the three directions. This state corresponds to the energy state of the cell in the $\varepsilon_{xx}, \varepsilon_{yy}, \varepsilon_{zz}$ strain space.

The procedure just described yields to a strain mesh of the total strain energy of the sample with respect to the reference configuration. The general steps of the calculation can be outlined as follows:

(a) Create the initial assembly using the given material properties (atomic weight, lattice spacing, EAM potential, crystallographic orientation, etc…).

(b) Apply a small strain field, ε_{ii}, to the assembly.

(c) Compute the energy density corresponding to this given strain field.

(d) Increase the magnitude of ε_{ii} and repeat steps (b) and (c)

After repeating steps (b) – (d) a sufficient number of times, we obtain a mesh of *U* as a function of the strains, ε_{ii}. A numerical interpolation of the energy density was performed to evaluate the elastic constants. The results obtained for a few tested materials are shown in Table 3.4.

These results are in good agreement with the results obtained using the analytical method presented in this section. Nevertheless, the "strain meshing" method has the disadvantages of only giving an incomplete set of elastic constants since the energy meshing is limited to the stretching domain $\varepsilon_{xx}, \varepsilon_{yy}, \varepsilon_{zz}$ (no shear strains) and of being computationally not as efficient as the analytical method presented in section 3.3.

3.5 Elastic Constants of Isotropic Aggregates

The estimates of the effective TOEC for isotropic aggregates of cubic crystals are of greater interest when calibrating experiments measuring anharmonicity properties of the studied materials. For polycrystalline aggregates consisting of randomly oriented single crystals, the effective elastic properties can be obtained through homogenization methods. In the following section we present several analytical schemes to determine the TOE constants of isotropic aggregates of single cubic crystals.

3.5.1 Voigt and Reuss-type Estimates of the Elastic Constants of an Isotropic Aggregate

One of the simplest homogenization methods is the "rule of mixture", or the Voigt and Reuss estimates. According to the Voigt estimate, when a polycrystalline aggregate is subjected to an overall uniform strain, the individual crystals are assumed to be in the same state of strain. It thus follows that the effective elastic constants of a polycrystalline aggregate are simply the geometric averages of these of the single crystal, i.e.,

$$C^V_{ijkl} = \frac{1}{8\pi^2}\int_\Omega C_{ijlk}\, d\Omega \quad , \tag{3.37}$$

$$C^V_{ijklmn} = \frac{1}{8\pi^2}\int_\Omega C_{ijlkmn}\, d\Omega \quad , \tag{3.38}$$

where $d\Omega = \sin\theta d\varphi d\theta d\psi$, and φ , θ , and ψ are the Euler angles.

By carrying out the integrals in equation (3.37) we arrived at,

$$C^V_{ijkl} = \frac{1}{5}\left(C_{11} + 4C_{12} - 2C_{44}\right)\delta_{ij}\delta_{kl} + \frac{2}{5}\left(C_{11} - C_{12} + 3C_{44}\right) I_{ijkl} \quad . \tag{3.39}$$

The two Voigt estimates of the effective second-order elastic moduli for a polycrystalline aggregate are thus,

$$C_{12}^{V}=\frac{1}{5}\left(C_{11}+4C_{12}-2C_{44}\right),\ C_{44}^{V}=\frac{1}{5}\left(C_{11}-C_{12}+3C_{44}\right)\ . \tag{3.40}$$

Similarly, the integration of equation (3.38) leads to the effective third-order elastic moduli for a polycrystalline aggregate its estimates of the three TOE constants of the isotropic polycrystal

$$C_{123}^{V}=\frac{1}{35}\left(C_{111}+18C_{112}+16C_{123}-30C_{144}-12C_{244}+16C_{456}\right)\ , \tag{3.41}$$

$$C_{144}^{V}=\frac{1}{35}\left(C_{111}+4C_{112}-5C_{123}+19C_{144}+2C_{244}-12C_{456}\right)\ , \tag{3.42}$$

$$C_{456}^{V}=\frac{1}{35}\left(C_{111}-3C_{112}+2C_{123}-9C_{144}+9C_{244}+9C_{456}\right)\ . \tag{3.43}$$

Similarly, when a polycrystalline aggregate is subjected to an overall uniform stress, the Reuss estimate assumed that the individual crystals are also in the same state of stress. The effective elastic compliant constants of the polycrystalline aggregate are then given by the directional averages of the single crystal compliant constants, i.e.,

$$M_{ijkl}^{R}=\left(C_{ijkl}^{R}\right)^{-1}=\frac{1}{8\pi^{2}}\int_{\Omega}M_{ijlk}d\Omega\ , \tag{3.44}$$

$$M_{ijklmn}^{R}=\frac{1}{8\pi^{2}}\int_{\Omega}M_{ijlkmn}d\Omega\ , \tag{3.45}$$

By carrying out the integrals in equations (3.44) and (3.45), similar expressions for the Reuss estimates of the compliance constants can be obtained. Substitution of these expressions into (3.6) and (3.7) yields the Reuss estimates for the elastic constants,

$$C_{12}^{R}=-\frac{M_{12}^{R}}{2M_{44}^{R}\left(3M_{12}^{R}+2M_{44}^{R}\right)}\ , \tag{3.46}$$

$$C_{44}^{R}=\frac{1}{4M_{44}^{R}}\ , \tag{3.47}$$

$$\begin{aligned}C_{123}^{R}=&-\left(3C_{12}^{R}+2C_{44}^{R}\right)^{3}M_{123}^{R}-6C_{12}^{R}\left(3C_{12}^{R}+2C_{44}^{R}\right)\left(3C_{12}^{R}+4C_{44}^{R}\right)M_{144}^{R}\\&-24\left(C_{12}^{R}\right)^{2}\left(3C_{12}^{R}+2C_{44}^{R}\right)M_{456}^{R}\end{aligned}\ , \tag{3.48}$$

$$C_{144}^{R} = -4\left(C_{44}^{R}\right)^{2}\left[\left(3C_{12}^{R} + 2C_{44}^{R}\right)M_{144}^{R} + 4C_{12}^{R}M_{456}^{R}\right] \quad , \tag{3.49}$$

$$C_{456}^{R} = -8\left(C_{44}^{R}\right)^{3} M_{456}^{R} \quad . \tag{3.50}$$

It is well known that the Voigt estimate is the upper bound for the SOE constants, while the Reuss estimates upper bound (Hill, 1952) for the second order compliance constants (or equivalently lower bound for the SOE constants).

Since the Voigt approximation assumes that the material is in a state of homogeneous strain and the Reuss approximation assumes it is in a state of homogeneous stress, these assumptions corresponds to two extreme configurations. It is often expected that the real polycrystalline aggregate will have its elastic properties in somewhere in between these two bounds. Consequently, the arithmetic mean of these two bounds gives a "better" approximation of the values of the elastic moduli. It is sometimes referred to as the Voigt-Reuss-Hill estimates. According to common knowledge the arithmetic mean is defined as,

$$C_{ijkl}^{H} = \frac{1}{2}\left(C_{ijkl}^{V} + C_{ijkl}^{R}\right) \quad , \quad C_{ijklmn}^{H} = \frac{1}{2}\left(C_{ijklmn}^{V} + C_{ijklmn}^{R}\right) \quad . \tag{3.51}$$

Results for the Voigt, Reuss and Hill estimates are presented in Table 3.6 and Table 3.7. The only possible comparison with experimental and reported values is made with the available data from Lubarda (1997) and Hamilton (Hamilton and Parrott, 1968) who evaluated the effective TOEC for isotropic aggregates of cubic crystals using the Voigt and Reuss approximation. To our knowledge no values have been reported for platinum and palladium at the time of the writing of this dissertation. As noted previously, the elastic constants of real polycrystalline aggregates is somewhere in between the Voigt and Reuss bounds. We find satisfactory agreement with the few reported values. The discrepancy and scatter in the results might be attributed to the precision of experimental techniques used, and to the fact that analytical estimates are not based on the same estimates for the single crystal SOEC and TOEC values.

3.5.2 Semi Consistent Estimates of the Elastic Constants of an Isotropic Aggregate

Another improved homogenization technique for estimating the effective elastic properties of aggregates of cubic crystals is the self-consistent method(Lubarda, 1997; Qu and Cherkaoui, 2006) . This method was initially developed for SOE constants. In what follows, we will briefly outline how it can be extended to TOE constants. In the self consistent approach, we consider a polycrystal, consisting of randomly oriented and shaped single crystals as an infinite isotropic homogenized domain *D* containing an embedded ellipsoidal inclusion Ω uniform eigenstrain ε_{ij}^{*}. The term eigenstrain defines a stress free strain. In other words an eigenstrain is a strain that would not create any stress in the inclusion if it was not embedded in a matrix. Phase transformation and thermal expansion are two examples of eigenstrains. When this method is applied to calculate the effective elastic properties (SOE and TOE constants), the approaches using the strain energy and the complementary energy are self-consistent with respect to the SOE constants but not the TOE constants. This is why it is referred to as "semi-consistent".

From the classical Eshelby problem (Eshelby, 1957), using an equivalent inclusion method (see Figure 3.1) in the framework of linear elasticity, the total strain (and the stress as well) inside the ellipsoidal inclusion is uniform and proportional to the far-field applied strain.

In the framework of this work, the total strain in a single crystal *r* of a polycrystal is therefore proportional to the applied strain by,

$$\varepsilon_{ij}^{(r)} = [I_{ijkl} + \overline{S}_{ijpq}\overline{M}_{pqrs}(C_{rskl}^{(r)} - \overline{C}_{rskl})]^{-1}\overline{E}_{kl} = \overline{T}_{ijkl}\overline{E}_{kl} \quad , \tag{3.52}$$

where $\overline{S}_{ijlk}$ is the Eshelby inclusion tensor, $\overline{C}_{ijlk}$ and $\overline{M}_{ijlk}$ are the stiffness and compliance tensors respectively of the homogenized matrix, $C_{ijkl}^{(r)}$ and I_{ijlk} is the identity tensor and $\overline{E}_{ij}$ is the far-field applied strain. The tensor $\overline{T}_{ijlk}$ is called the strain localization tensor. This is still a simplification of the problem since a non linear

relationship should relate $\varepsilon_{ij}^{(r)}$ with $\overline{E}_{ij}$ with the addition of a quadratic term in $\overline{E}_{ij}$ of the form $\overline{T}_{ijklmn}\overline{E}_{kl}\overline{E}_{mn}$ to the right-hand side of (3.52).

If an individual cubic crystal is considered as a spherical anisotropic inhomogeneity embedded in an effective isotropic matrix of the polycrystal, the effective elastic constants of a polycrystalline aggregate are simply given by,

$$\overline{C}_{ijkl} = \frac{1}{8\pi^2}\int_{\Omega} C_{ijmn}\overline{T}_{mnkl}\,d\Omega \quad , \tag{3.53}$$

$$\overline{C}^{(3)}_{ijklmn} = \frac{1}{8\pi^2}\int_{\Omega} C^{(3)}_{ijpqrs}\overline{T}_{pqkl}\overline{T}_{rsmn}\,d\Omega \quad . \tag{3.54}$$

Similarly one can adopt a dual formulation. In the dual formulation, one assumes that the state of stress in an ellipsoidal inhomogeneity within a homogenized isotropic matrix subjected to a far field uniform stress is also uniform. The total stress in a single crystal *r* of a polycrystal is therefore proportional to the applied stress by,

$$\sigma_{ij}^{(r)} = C_{ijmn}^{(r)}[I_{mnpq} + \overline{S}_{mnrs}\overline{M}_{rsuv}(C_{uvpq}^{(r)} - \overline{C}_{uvpq})]^{-1}\overline{M}_{pqkl}\Sigma_{kl} = \overline{H}_{ijkl}\overline{\Sigma}_{kl} \quad , \tag{3.55}$$

where $\overline{\Sigma}_{ij}$ is the far-field applied stress. If an individual cubic crystal is considered as a spherical anisotropic inhomogeneity embedded in an effective isotropic matrix of the polycrystal, the effective third order compliance tensor of the polycrystal is then,

$$\overline{M}^{(3)}_{ijklmn} = \frac{1}{8\pi^2}\int_{\Omega} M^{(3)}_{ijpqrs}\overline{H}_{pqkl}\overline{H}_{rsmn}\,d\Omega \quad . \tag{3.56}$$

The second order elastic constants calculated using the strain energy approach or the complementary approach, are identical in both calculations and therefore self consistent with that regard. The two estimates of the TOE constants calculated based on the semi consistent approach may not coincide, therefore the arithmetic mean of the two self-consistent estimates of the TOE constants is expected to give a more realistic idea of the effective third order elastic properties of the polycrystalline. Results for the self-consistent estimates are presented in Table 3.8. When comparing the different bounds in Figure 3.3, one can notice that the self-consistent estimates falls in between the Voigt and

Reuss estimates and therefore correlate with the fact the real polycrystalline aggregate will have its elastic properties in somewhere in between these two bounds (state of homogeneous strain versus state of homogeneous stress). Nevertheless, nothing guarantees that the so called self-consistent method is an upper or lower bound since the two estimates of the TOE constants calculated based on the semi consistent approach may not coincide.

3.6 Summary and Conclusions

The main purpose of this chapter is to report a full set of third order elastic of the transition metals in groups 10 – 11 for single crystals and isotropic aggregates. Although some data are available in the open literature, we are not aware of a simple unified analytical method to evaluate TOE constant and for single crystals and isotropic aggregates. The comparison of our results with available literature data shows satisfactory agreement.

An analytical method has been developed for evaluating the elastic properties. The method developed here requires the construction of the crystal of interest. Once the atomic coordinates of the atoms are known, higher order elastic properties can be expressed analytically based on the interatomic potential and its spatial derivatives. Furthermore, although EAM was used in the present work, the methodology can be applied to any interatomic potential.

As noted when presenting the self-consistent method to evaluate the estimate of the elastic constants of polycrystals, several extensions of the presented analysis should be undertaken. Some efforts should address the variational estimates and derivation of possible bounds for the TOEC. The existing results for nonlinear heterogeneous solids, already considered in the literature (Willis, 1990), may be of significant help.

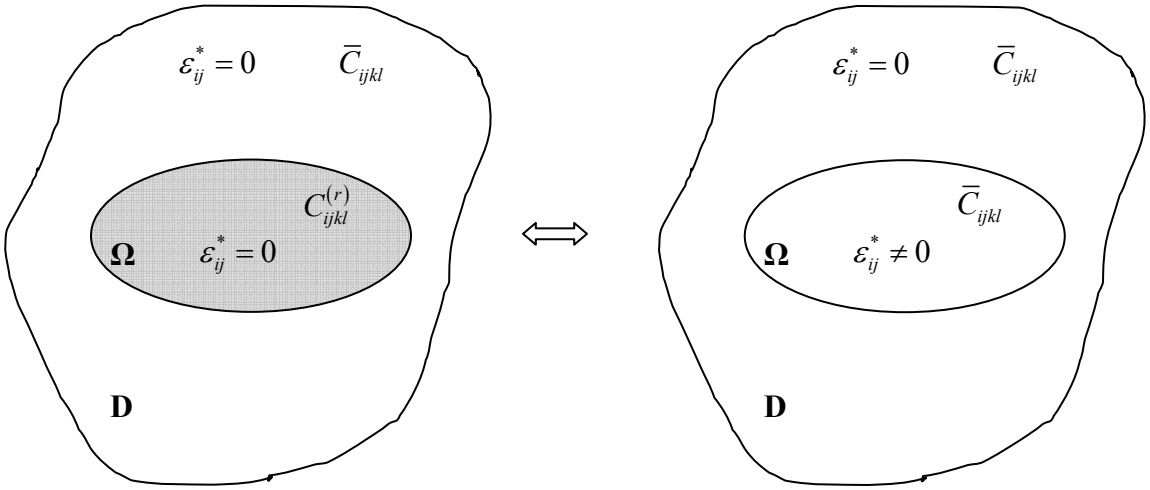

Figure 3.1 Scheme representing the equivalent inclusion method

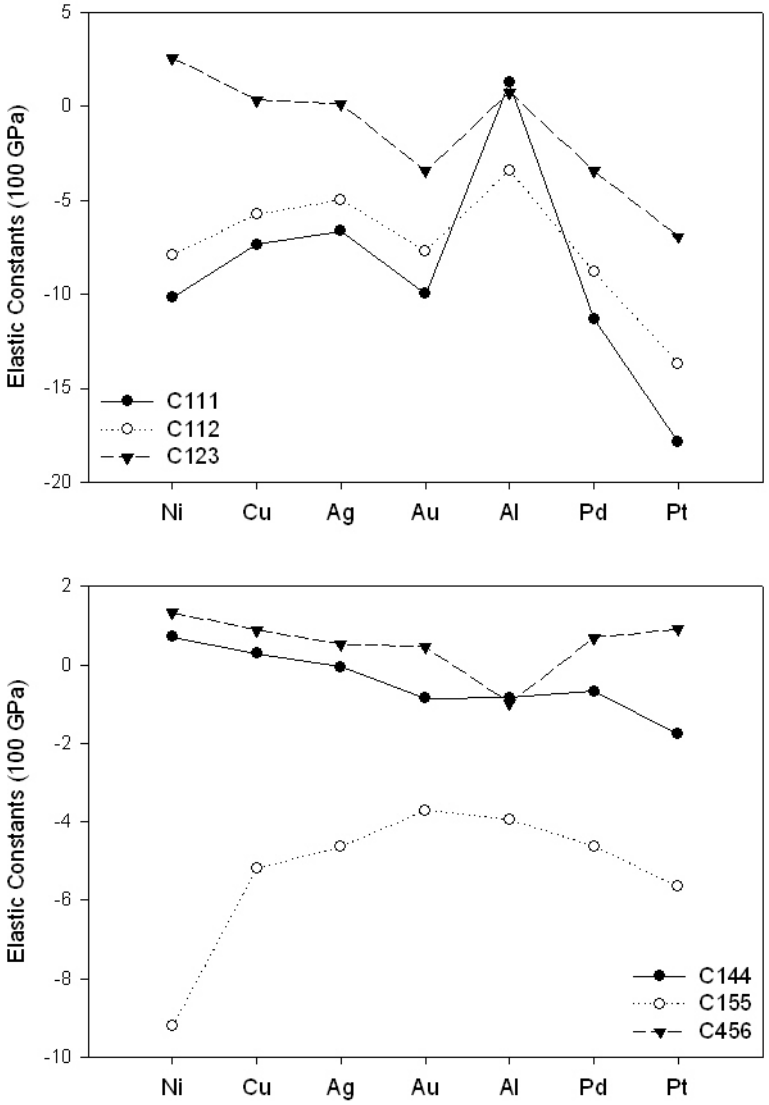

Figure 3.2 TOEC for single crystals of the transitions metals in groups 10 – 11 and aluminum

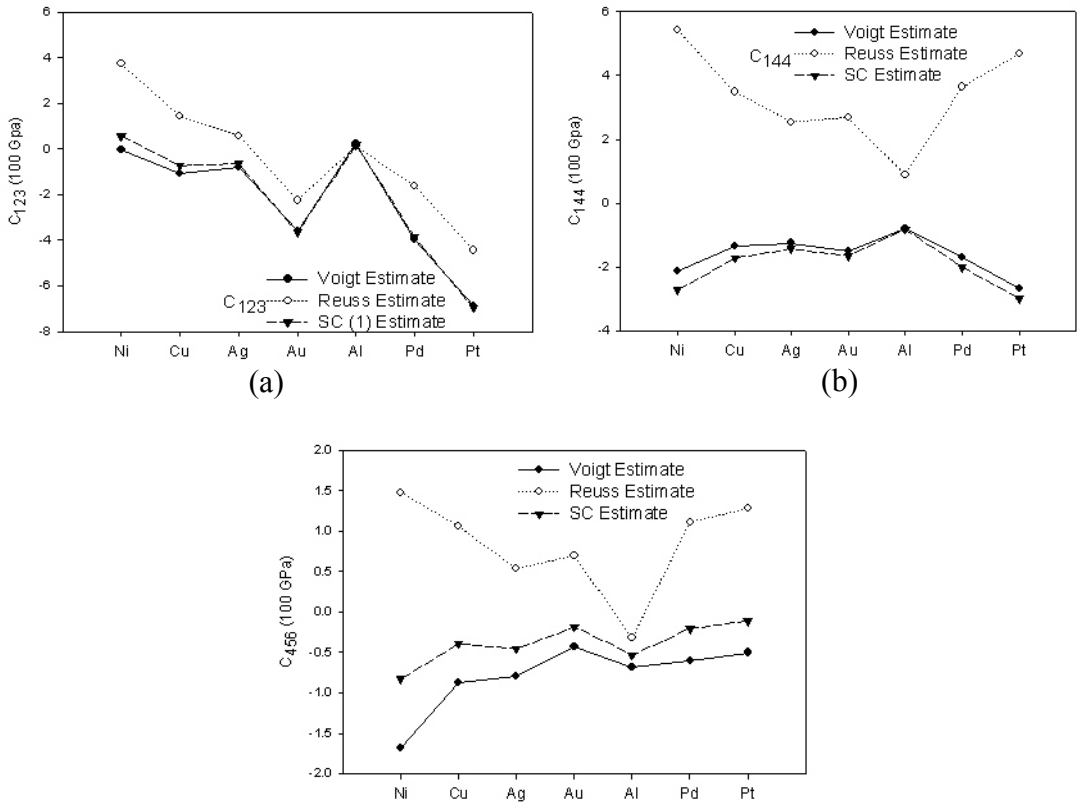

Figure 3.3 TOEC for isotropic aggregates of cubic crystals

Table 3.1 Interatomic lattice spacing (in Å)

	Cu	**Ni**	**Ag**	**Au**	**Al**	**Pd**	**Pt**
$\hat{r}^{mn}$ **(Å)**	3.615	3.52	4.09	4.08	4.032	3.89	3.92

Table 3.2 Second order elastic constants for single crystals (in 100 GPa)

	Cu	**Ni**	**Ag**	**Au**	**Al**	**Pd**	**Pt**
C_{11}	1.671 (1.661)[a]	2.329 (2.5)[c]	1.289 (1.222)[a]	1.831 (1.929)[a]	1.180 (1.08)[b]	1.983	3.317
C_{12}	1.240 (1.199)[a]	1.541 (1.5)[c]	0.909 (0.907)[a]	1.587 (1.638)[a]	0.622 (0.62)[b]	1.704	2.942
C_{44}	0.764 (0.756)[a]	1.275 (1.2)[c]	0.567 (0.454)[a]	0.447 (0.415)[a]	0.367 (0.283)[b]	0.580	0.769

[a] Reference (Hiki and Granato, 1966) ; [b] Reference (Landolt-Bornstein, 1979)
[c] Reference (Riley and Skove, 1973)

Table 3.3 Third order elastic constants for single crystals (in 100 GPa) calculated from analytical method

	Cu	Ni	Ag	Au	Al	Pd	Pt
C_{111}	-7.375 (-12.71±0.22) [a] (-15.00±1.50) [f]	-10.179 (-20.40±0.4) [c]	-6.630 (-8.43±0.37) [a]	-9.984 (-17.29±0.21) [a]	1.247 (-10.80±0.30) [b]	-11.295	-17.884
C_{112}	-5.758 (-8.14±0.09) [a] (-8.50±1.00) [f]	-7.898 (-10.30±0.30) [c]	-4.976 (-5.29±0.18) [a]	-7.701 (-9.22±0.12) [a]	-3.405 (-3.15±0.10) [b]	-8.817	-13.674
C_{123}	0.3221 (-0.50±0.18) [a] (-6.70±1.80) [d] (-2.50±1.00) [f]	2.545 (-2.10±0.50) [c]	0.119 (1.89±0.37) [a]	-3.460 (-2.33±0.49) [a]	0.732 (0.36±0.15) [b] (-0.39±0.17) [e]	-3.440	-6.941
C_{144}	0.284 (-0.03±0.09) [a] (1.75±2.07) [d] (-1.35±0.15) [f]	0.724 (-1.40±0.60) [c]	-0.057 (0.56±0.26) [a]	-0.854 (-0.13±0.32) [a]	-0.828 (-0.23±0.15) [b] (1.24±0.04) [e]	-0.670	-1.761
C_{155}	-5.189 (-7.80±0.05) [a] (-6.45±0.10) [f]	-9.213 (-9.20±0.30) [c]	-4.632 (-6.37±0.13) [a]	-3.708 (-6.48±0.17) [a]	-3.940 (-3.40±0.10) [b]	-4.622	-5.651
C_{456}	0.886 (-0.95±0.87) [a] (-3.98±0.05) [d] (-0.16±0.1) [f]	1.336 (-0.7±0.30) [c]	0.530 (0.83±0.08) [a]	0.469 (-0.12±0.16) [a]	-0.971 (-0.30±0.30) [b] (0.86±0.01) [e]	0.694	0.913

[a] Reference (Hiki and Granato, 1966) ; [b] Reference (Landolt-Bornstein, 1979)
[c] Reference (Riley and Skove, 1973) ; [d] Reference (Seeger and Buck, 1960)
[e] Reference (Wasserbach, 1990) ; [f] Reference (Salama and Alers, 1967)

Table 3.4 Elastic constants of single crystals calculated by the strain meshing of the energy (in 100GPa)

	Cu	**Ni**	**Au**	**Pt**
C_{11}	1.6739	2.331	1.833	3.034
C_{12}	1.241	1.544	1.588	2.733
C_{111}	-8.320	-12.020	-10.168	-17.037
C_{112}	-6.219	-8.177	-7.625	-13.358
C_{123}	0.306	2.282	-3.488	-6.418

Table 3.5 Voigt estimates of the SOEC and TOEC for isotropic polycrystalline aggregates (in 100 GPa)

	Ni	**Cu**	**Ag**	**Au**	**Al**	**Pd**	**Pt**
C_{12}^V	1.189	1.021	0.758	1.457	0.587	1.528	2.710
C_{44}^V	0.923	0.544	0.416	0.317	0.332	0.404	0.536
C_{123}^V	-0.040	-1.084 (-2.51 [a])	-0.815 (-0.01 [b])	-3.609 (-4.02 [b])	0.236 (-0.54 [a])	-3.954	-6.852
C_{144}^V	-2.148	-1.361 (-1.36 [a])	-1.252 (-1.46 [b])	-1.508 (-1.61 [b])	-0.800 (-0.94 [a])	-1.704	-2.674
C_{456}^V	-1.680	-0.878 (-1.94 [a])	-0.796 (-1.25 [b])	-0.436 (-1.50 [b])	-0.681 (-0.91 [a])	-0.602	-0.501

[a] Reference (Lubarda, 1997) ; [b] Reference (Hamilton and Parrott, 1968)

Table 3.6 Reuss estimates of the SOEC and TOEC for isotropic polycrystalline aggregates (in 100 GPa)

	Ni	Cu	Ag	Au	Al	Pd	Pt
C_{12}^R	1.355	1.132	0.825	1.524	0.591	1.626	2.839
C_{44}^R	0.673	0.378	0.316	0.216	0.326	0.256	0.343
C_{123}^R	3.724	1.448 (0.449 [a])	0.577 (2.17 [b])	-2.260 (-1.81 [b])	0.109 (-0.49 [a])	-1.604	-4.440
C_{144}^R	5.435	3.486 (-3.92 [a])	2.541 (-3.33 [b])	2.686 (-3.31 [b])	0.896 (-0.98 [a])	3.643	4.671
C_{456}^R	1.480	1.055 (0.513 [a])	0.537 (0.510 [b])	0.697 (-0.17 [b])	-0.323 (-0.86 [a])	1.116	1.279

[a] Reference (Lubarda, 1997) ; [b] Reference (Hamilton and Parrott, 1968)

Table 3.7 Hill estimates of the SOEC and TOEC for isotropic polycrystalline aggregates (in 100 GPa)

	Ni	Cu	Ag	Au	Al	Pd	Pt
C_{12}^H	1.272	1.076	0.791	1.490	0.589	1.577	2.774
C_{44}^H	0.798	0.461	0.366	0.266	0.329	0.330	0.440
C_{123}^H	1.842	0.182	-0.119	-2.934	0.173	-2.779	-5.646
C_{144}^H	1.644	1.063	0.644	0.589	0.048	0.969	0.999
C_{456}^H	-0.010	0.088	-0.129	0.131	-0.502	0.257	0.389

Table 3.8 Self-Consistent estimates of the SOE and TOE constants for isotropic polycrystalline aggregates (in 100 GPa)

	Ni	**Cu**	**Ag**	**Au**	**Al**	**Pd**	**Pt**
C_{12}^{Self}	1.264	1.070	0.788	1.485	0.588	1.570	2.761
C_{44}^{Self}	0.809	0.471	0.372	0.275	0.329	0.339	0.460
$C_{123}^{Self(1)}$	0.569	-0.730	-0.653	-3.643	0.180	-3.880	-6.968
$C_{123}^{Self(2)}$	-9.628	-13.168	-8.168	-52.529	0.179	-56.889	-126.88
C_{123}^{SC}	-4.530	-6.949	-4.410	-28.086	0.180	-30.384	-66.923
$C_{144}^{Self(1)}$	-2.780	-1.707	-1.463	-1.538	-0.845	-1.829	-2.636
$C_{144}^{Self(2)}$	-2.673	-1.756	-1.396	-1.786	-0.802	-2.206	-3.365
C_{144}^{SC}	-2.727	-1.732	-1.430	-1.662	-0.824	-2.017	-3.000
$C_{456}^{Self(1)}$	-0.4927	-0.210	-0.291	-0.0981	-0.519	-0.943	-0.0310
$C_{456}^{Self(2)}$	-1.163	-0.580	-0.619	-0.273	-0.548	-0.318	-0.197
C_{456}^{SC}	-0.827	-0.395	-0.455	-0.186	-0.533	-0.206	-0.114

CHAPTER 4

ELASTIC DESCRIPTION OF FREE SURFACES AND INTERFACES

In this chapter, we discuss essential concepts and definitions relative to the elastic description of surfaces and interfaces. The concept of surface / interfacial excess energy is first reformulated from the continuum mechanics point of view by considering a single dividing surface separating the two homogeneous phases (as opposed to the interface considered as an interphase). It is shown that the well-known Shuttleworth relationship between the interfacial excess energy and interfacial excess stress is valid only when the interface is free of transverse stresses. To account for the transverse stress, a new relationship is derived between the interfacial excess energy and interfacial excess stress. At the same time, the concept of transverse interfacial excess strain is also introduced, and a complementary Shuttleworth equation is derived that relates the interfacial excess energy to the newly introduced transverse interfacial excess strain. This new formulation of interfacial excess stress and excess strain naturally leads to the definition of an in-plane interfacial stiffness tensor, a transverse interfacial compliance tensor, and a coupling tensor that accounts for the Poisson's effect of the interface. These tensors fully describe the elastic behavior of a coherent interface upon deformation. A semi-analytical method is subsequently presented to calculate the interfacial elastic properties. The cases of free surfaces and interfaces are distinguished. As an illustration, we present numerical examples for low-index surfaces (111), (100) and (110) of face-centered cubic transition metals. Numerical examples for grain boundaries in Cu bicrystals of the so called “low-order CSL boundaries” will finally close this chapter.

Note: In what follows, the term *surface* is used interchangeably when describing either a free surface or a bicrystal interface.

4.1 Introduction

The reduced coordination of atoms near a surface induces a corresponding redistribution of electronic charge, which alters the binding situation (Sander, 2003). As a result, the equilibrium position and energy of these atoms will, in general, be different from their bulk positions and bulk energies. Thus, the elastic moduli of the surface region (typically very thin, only a few atomic layers) may differ from those of the bulk. It is thus perfectly acceptable to neglect the surface region and to use the bulk modulus of a structural element as its overall modulus, when the size of the element is in micrometers or larger. For nano-sized structural elements and nanostructured materials, however, the surface to volume ratio is much higher and the surface region can no longer be neglected when considering the overall elastic behavior of nanostructured materials.

Because interfaces and grain boundaries present a different atomic structure than their bulk counterparts, interfacial physical and chemical properties are generally different from the ones of the surrounding bulk crystals. These peculiar properties often control the overall behavior of materials. Because of their significant effects on material behavior, surface properties have attracted tremendous attention and research activity allowing a better understanding of the stress effects on surface physics. For example, the equilibrium shape of a body (Wulf, 1901; Mullins, 1959) is governed by the minimization of its surface free energy (in other words, the minimization of its total free energy at constant bulk energy). Mullins has also shown that the surface energy drives the mass transport from regions of high curvatures to regions of lower curvature until the chemical potential of the whole material is equilibrated. Surface phase transition is another example illustrating the effects of surface elasticity. Alymov (Alymov and Shorshorov, 1999) established the role of surface stresses and size dependence of the melting temperature of ultrafine particles. In the context of a bottom-up approach in the fabrication process of nanostructural elements, surface elasticity is used as a tool for self-

organization. Proville (2001) for example describes the self-organization of domains on a solid surface and finds that the morphology of the adsorbed phase depends on the coverage and the surface elastic constants of the substrate.

For these reasons theoretical and atomistic studies have been carried out for many years to investigate the structure and energetics of grain boundaries and bicrystal interfaces.

On one hand, the main idea behind the majority of the theoretical studies is to set up a thermodynamic framework to characterize the behavior of the interface. Gibbs (1928) was the first one to formulate the thermodynamics of a fluid interface through the use of interfacial free energy. In his original idea, a single dividing surface is used to separate the two homogeneous phases, and the interface contribution to the thermodynamic properties is defined as the excess over the values that would be obtained if the bulk phases retained their properties constant up to an imaginary surface (of zero thickness) separating the two phases. Gibbs showed that various combinations of the interfacial excess quantities can yield physically meaningful and experimentally measurable variables which are independent of the dividing surface position. Gibbs' work was followed by substantial efforts made by many researchers (Herring, 1950; Shuttleworth, 1950; Mullins, 1959) to extend this Gibbsian description of fluid-fluid interfaces to solid-solid interfaces and to associate a "surface stress" with the change of in interfacial energy upon deformation. Later on, Larché and Cahn (Larché and Cahn, 1978; Cahn and Larché, 1982) derived conditions for the thermomechanical equilibrium of single phase crystalline solids and two-phase crystalline solids for planar interfaces in which surface properties were ignored. They allow for both coherent and incoherent interfaces but neglect the surface contribution. Gurtin (1998) developed a self-consistent framework treating the mechanical deformation of curved material surfaces while Nozières and Wolf (1989) considered a general thermodynamics of surfaces that includes the concept of transversal surface strains. Unfortunately all these schemes fail to explore

the elastic behavior of interfaces in mixed modes (in-plane deformation and transversal loading).

On the other hand, the main objective of the experiments (actual experiments and computer/atomistic experiments) is to investigate and characterize the atomic structure and energetics of grain boundaries and bicrystal interfaces. Many approaches have been proposed and used to experimentally measure or theoretically predict surface properties. Among the various experimental techniques, contact angle measurement is a well-known method commonly used to measure surface energy (Tyson and Miller, 1977; de Boer *et al.*, 1988; Qu, 2003). Unfortunately, this technique is not capable of measuring the surface stress. One of the techniques to measure the surface stress is the zero creep method (Digilov *et al.*, 1976). This technique is based on the fact that creep deformation under very small load can be prevented by surface stress. Therefore, by observing the point when creep deformation stops, one can estimate the surface stress.

Theoretical predictions of surface elastic properties have been made using a variety of different techniques. Among them, first principle calculations, molecular dynamics (MD) and molecular static (MS) simulations have been extensively used. As early as 1986, Ackland and Finnis (Ackland and Finnis, 1986; Ackland *et al.*, 1987) presented calculations of surface tension for body-centered cubic (BCC) and face-centered-cubit (FCC) metals using simple empirical N-body potentials. Their results yield satisfactory agreement with available experimental data. Needs (Needs and Godfrey, 1990; Mansfield and Needs, 1991; Needs *et al.*, 1991) performed the first principle calculations of surface stresses and surface energy for different materials and different surface orientations, and investigated the role that surface stress may play in surface reconstructions. Todd and Lynden-Bell (1993) investigated surface and some bulk properties of metals using the Sutton-Chen potential in order to gain microscopic insights into surface phenomena. Others, like Schmid and coworkers (1995), have studied stresses and surface elasticity using effective-medium theory potentials which

allow them to probe the stresses and elasticity of individual layers. Daw and Baskes (Daw and Baskes, 1983; Daw and Baskes, 1984; Baskes, 1992), as well as Mishin and coworkers (Mishin, 1999; Mishin *et al.*, 1999; Mishin, 2001), evaluated the ability of the embedded-atom method (EAM) potentials to predict energies and stability of non-equilibrium structures. Shenoy (2005), using MS simulations of a slab in conjunction with the EAM potential, calculated several crystal faces of some FCC metals. His method requires conducting multiple MS simulations at different levels of stretching of the slab. Tartaglino (Tartaglino *et al.*, 2001) presented a calculation of the change of free energy of a solid surface upon bending of the solid. It is based on extracting the surface stress through a molecular dynamics simulation of a bent slab by using a generalized stress theorem formula, and subsequent integration of the stress with respect to the strain as a function of bending curvature.

The examination of elastic properties of grain boundaries has also been studied by a certain number of researchers. While some researchers like Sutton and Vitek (Lee and Aaronson, 1980; Sutton and Vitek, 1983; Sutton and Vitek, 1983; Sutton and Vitek, 1983; Sutton and Balluffi, 1987; Gilmore and Provenzano, 1990; Streitz *et al.*, 1994; Vitek *et al.*, 1994; Leo and Schwartz, 2000; Borchers and Bormann, 2005; Yang *et al.*, 2005) focused more on the dominant structural features that characterize grain boundaries, a number of research works have suggested that the elastic moduli in the grain boundary domain may differ significantly from those of the bulk. Wolf and co-workers (Wolf, 1989; Kluge *et al.*, 1990; Wolf, 1990; Wolf, 1990), who studied superlattices of (001) twist boundaries, as well as Adams *et al* (1989), who examined the $\Sigma = 5(001)$ twist boundary in a thin film of copper, have found an increase of the Young's modulus perpendicular to the boundary plane and a substantial decrease of the shear modulus in the boundary plane in the atomic layers adjacent to the boundary. Bassani and co-workers (Alber *et al.*, 1992; Bassani *et al.*, 1992; Vitek, 1994; Marinopoulos *et al.*, 1998) defined the local elastic modulus tensor and determined the

values of the local elastic modulus tensor near grain boundaries in several face center cubic metals using molecular dynamic simulations. They, too, found that the local elastic moduli are significantly different for atoms near the grain boundary.

In materials with fine-scale microstructures, measurements of the macroscopic elastic constants can lead to eloquent experimental values on the evaluation and interpretation of the orientational averages of interfaces elastic constants.

4.2 Surface Free Energy and Surface Stress

4.2.1 Dividing Surface

There are different ways in which the properties of the surface can be defined and introduced. For example, if one considers an "interface" separating two otherwise homogeneous phases, the interfacial property may be defined either in terms of an *inter-phase*, or by introducing the concept of a *dividing surface*. In the first approach, the system is considered to be one in which there are three phases present – the two bulk phases and an inter-phase; the boundaries of the inter-phase are somewhat arbitrary and are usually chosen to be at locations at which the properties are no longer varying significantly with position. The inter-phase then has a finite volume and may be assigned thermodynamic properties in the normal way (Capolungo *et al.*, 2005). In the second approach where a single dividing surface is used to separate the two homogeneous phases, the interface contribution to the thermodynamic properties is defined as the excess over the values that would obtain if the bulk phases retained their properties constant up to an imaginary surface (of zero thickness) separating the two phases. In this work, we adopt this second approach.

These concepts of surface free energy Γ and surface stress $\boldsymbol{\Sigma}^s$, ever since being introduced by Gibbs (1928), have been widely used in physics and chemistry, e.g., (Mullins, 1959; Blakely, 1973; Gurtin and Murdoch, 1975; Gurtin, 1978; Cahn and Larché, 1982; Nozières and Wolf, 1988; Adams *et al.*, 1989; Cammarata, 1989; Wolf and Lutsko, 1989; Needs *et al.*, 1991; Cammarata and Sieradzki, 1994; Cammarata, 1997; Alymov and Shorshorov, 1999; Cammarata, 2000; Sanfeld, 2000; Sander, 2003; Müller and Saúl, 2004; Zhou, 2004). In a liquid, where the atomic mobility is sufficiently high, atoms from the bulk will come to the surface when the surface is stretched. This way the microscopic configuration of the surface is preserved following deformation, i.e., the surface free energy density remains invariant to the surface strain. Consequently, the surface free energy is numerically equal to surface stress, i.e., $\boldsymbol{\Sigma}^s = \Gamma \mathbf{I}$. This is perhaps why surface free energy has also been historically called surface tension. For a solid, it might not be possible in any reasonable experimental time to keep constant the local configuration around any particular atom in the surface region where the deformation takes place. This is due to the long range correlation in atomic positions and low atomic mobility in solids. In other words, when a solid crystal deforms, its surface area may change. Such change of surface area is not accomplished by adding (or subtracting) mass to the surface. Instead, the change of surface area is accompanied by the change of surface free energy density. Consequently, the surface free energy density becomes a function of the surface strain $\boldsymbol{\varepsilon}^s$. In a Lagrangian formulation, it has been shown (Shuttleworth, 1950; Dingreville *et al.*, 2005) that the surface stress is related to the surface free energy through

$$\boldsymbol{\Sigma}^s = \frac{\partial \Gamma}{\partial \boldsymbol{\varepsilon}^s} \quad , \tag{4.1}$$

This is known as the Shuttleworth equation (Shuttleworth, 1950). Although derived only for free surfaces, the Shuttleworth equation has been used extensively for solid-solid interfaces such as grain boundaries, e.g., (Cammarata, 1989; Cammarata and Sieradzki,

1994; Cammarata, 1997; Cammarata, 2000; Sharma, 2003; Sharma *et al.*, 2003). Even though there are many similarities between a free surface and an interface in elastic solid, there is one key difference between them, namely, in addition to in-plane deformation, an interface may be subjected to transverse (normal to the interface) stress. Such transverse stress and the corresponding transverse deformation also contribute to the interfacial excess (Andreev and Kosevich, 1981; Nozières and Wolf, 1988). It is therefore questionable that the original Shuttleworth equation can be directly applied to interfaces in elastic solids. Nozières and Wolf (Nozières and Wolf, 1988) recognized the necessity of including the transverse deformation of the interface in computing the interfacial excess energy, but did not give an expression of the contribution from the transverse stress.

4.2.2 Definition of Interfacial Excess Energy

The surface free (excess) energy, w_n, of a near surface atom is defined by the difference between its total energy and that of an atom deep in the interior of a large bicrystal. Clearly, w_n depends on the location of the atom. For the bicrystal interface shown in Figure 4.1(a), the x_3-dependence of w_n is schematically shown in Figure 4.1(b), i.e., it reaches its maximum value on the interface and tends to zero deep into the crystal. In addition, w_n is a function of the intrinsic bicrystal interface properties, as well as a function of the relative surface deformation. If there are *N* atoms surrounding an area *A* in the deformed configuration, see Figure 4.1(a), then the total surface free energy associated with area *A* is given by $\sum_{n=1}^{N} w_n$. Thus, the Gibbs surface free energy density is defined by

$$\Gamma = \frac{1}{A}\sum_{n=1}^{N} w_n \quad . \tag{4.2}$$

Note that the above definition is in the deformed configuration. It can be viewed as the Eulerian description of the surface free energy density. For solid crystal surfaces, the Lagrange description of the surface free energy density can be defined by

$$\Gamma = \frac{1}{A_0}\sum_{n=1}^{\infty} w_n = \frac{1}{A_0}\sum_{n=1}^{\infty}(E^{(n)} - E^{(0)}) \quad , \tag{4.3}$$

where $E^{(n)}$ is the total energy of the atom *n* surrounding the area A_0, and $E^{(0)}$ is the total energy of an atom in a perfect lattice far away from the free surface. A_0 is the area originally occupied in the undeformed configuration by the same atoms that occupy the area A in the deformed configuration. It can be easily shown that the two areas are related through

$$A = A_0(1 + \varepsilon^s_{\eta\eta}) \quad , \tag{4.4}$$

where, $\varepsilon^s_{\alpha\beta}$ is the Lagrange surface strain relative to the undeformed crystal lattice. Continuity of the strain field requires, for example, in the particular coordinate system shown in Figure 4.1(a),

$$\varepsilon^s_{\alpha\beta} = \varepsilon_{\alpha\beta}\Big|_{x_3=0} \quad , \quad \alpha,\beta = 1,2 \quad , \tag{4.5}$$

where ε_{ij} is the bulk Lagrange strain of the crystal under a given external loading. In the above and in the rest of this chapter, Roman indices range from 1 to 3 and Greek indices range from 1 to 2, unless other wise indicated. For future reference, the Lagrangian strain measure will be used in this chapter. Although the sum in (4.3) involves an infinite number of atoms, the difference $E^{(n)} - E^{(0)}$ is non-zero only for atoms within a few atomic layers near the interface. So, in practice, the sum in (4.3) only involves a very limited number of terms. It should also be pointed out that the surface energy density calculated from (4.3) contains contributions not only from atoms on the surface, but from all atoms near the interface.

Now, let us consider a flat interface between two dissimilar elastic solids. For convenience, let the interface be located at $x_3 = 0$ in a Cartesian coordinate system, see Figure 4.1. Both constituent materials are assumed to be semi-infinite and are perfectly bonded together along the interface. Furthermore, we assume that the interface is homogeneous in its own plane (not necessarily normal to its plane).

Let the bimaterial be subjected to a homogeneous traction and displacement boundary condition at infinity so that far away from the interface the deformation can be assumed homogeneous, and the (second Piola–Kirchhoff) stress and the (Lagrangian) strain tensors in the upper ($x_3 > 0$) and lower ($x_3 < 0$) materials are given by $\boldsymbol{\sigma}_{\pm}$ and $\boldsymbol{\varepsilon}_{\pm}$, respectively. It has been shown that such homogeneous deformation can be easily constructed in a bimaterial (Qu and Bassani, 1993) by adding the so called "T" stress. Both bulk phases are being strained by the same amount in the plane of the interface. Although the deformation far away from the interface is homogeneous, the stress and strain fields near the interface are disturbed by the presence of the interface. Therefore, the actual total fields in the bimaterial are generally different from the remote fields. To distinguish them, we use $\boldsymbol{\sigma}$ and $\boldsymbol{\varepsilon}$ to denote the actual stress and strain tensors, respectively. Clearly, $\boldsymbol{\sigma}$ and $\boldsymbol{\varepsilon}$ depend on the distance from the interface and approach their corresponding remote values far away from the interface, respectively, i.e.,

$$\lim_{x_3 \to \pm\infty} \boldsymbol{\sigma} = \boldsymbol{\sigma}_{\pm} \quad , \quad \lim_{x_3 \to \pm\infty} \boldsymbol{\varepsilon} = \boldsymbol{\varepsilon}_{\pm} \quad . \tag{4.6}$$

Next, we can consider the interfacial excess energy. If we limit ourselves to mechanical energy only, the standard Gibbs definition of the interfacial excess energy per unit undeformed area is given by

$$\Gamma = \int_0^{\infty} \left[w(x_3) - w_+ \right] dx_3 + \int_{-\infty}^{0} \left[w(x_3) - w_- \right] dx_3 \quad , \tag{4.7}$$

where, following Appendix B and equation (B.10),

$$w(x_3) = \hat{c}_0 + \hat{\boldsymbol{\tau}}^s : \boldsymbol{\varepsilon}^s + \frac{1}{2}\boldsymbol{\varepsilon}^s : \mathbf{C}^s : \boldsymbol{\varepsilon}^s + \frac{1}{2}\boldsymbol{\sigma}^t : \mathbf{M} : \boldsymbol{\sigma}^t \quad , \tag{4.8}$$

$$w_{\pm} = \frac{1}{2}\boldsymbol{\varepsilon}^s_{\pm} : \mathbf{C}^s_{\pm} : \boldsymbol{\varepsilon}^s_{\pm} + \frac{1}{2}\boldsymbol{\sigma}^t_{\pm} : \mathbf{M}_{\pm} : \boldsymbol{\sigma}^t_{\pm} \quad , \tag{4.9}$$

are the elastic strain energy densities (in the undeformed configuration) corresponding to the total and remote fields, respectively. Specifically, $\boldsymbol{\varepsilon}^s$ and $\boldsymbol{\sigma}^t$ are, respectively, the in-plane strain and transverse stress tensors as defined by Appendix B, equation (B.4). Note that, although not explicitly indicated, all the terms on the right hand side of (4.8) may depend on x_3. Even though the range of integration in (4.7) is infinite, the convergence of the integral is expected because of (4.6). In fact, extensive data (experimental and numerical) have shown that $w(x_3)$ differs from $w_{\pm}$ only within a very small distance from the interface so that the integral needs to be carried out only over the thickness of the interfacial region, $h_+ + h_-$, see, Figure 4.1(b).

To further simplify (4.7) into a form that is tractable for numerical evaluation, we introduce the following decomposition of a second order tensor η_{ij} into an in-plane portion and a transverse portion, i.e.,

$$\eta_{ij} = \eta^s_{ij} + \eta^t_{ij} \quad , \tag{4.10}$$

where, written in a matrix form we have,

$$\boldsymbol{\eta}^s = \begin{pmatrix} \eta_{11} & \eta_{12} & 0 \\ \eta_{12} & \eta_{22} & 0 \\ 0 & 0 & 0 \end{pmatrix} \quad , \quad \boldsymbol{\eta}^t = \begin{pmatrix} 0 & 0 & \eta_{13} \\ 0 & 0 & \eta_{23} \\ \eta_{13} & \eta_{23} & \eta_{33} \end{pmatrix} \quad . \tag{4.11}$$

It can be easily show that the decomposition is orthogonal, i.e., $\boldsymbol{\eta}^s : \boldsymbol{\eta}^t = 0$.

Making use of the coherence of the interface leads to

$$\boldsymbol{\varepsilon}^s = \boldsymbol{\varepsilon}^s_+ = \boldsymbol{\varepsilon}^s_- \quad . \tag{4.12}$$

This clearly represents the stretching of the interface caused by uniform traction at $x_1 = \pm\infty$, and/or $x_2 = \pm\infty$. $\boldsymbol{\varepsilon}^s = \boldsymbol{\varepsilon}^s_+ = \boldsymbol{\varepsilon}^s_-$. It is conceivable that all interfacial excess

quantities should be expressible in terms of $\boldsymbol{\sigma}^t_{\pm}$ and $\boldsymbol{\varepsilon}^s$ since they are independent bulk thermodynamic variables and therefore completely characterize the elastic state of the interface.

We will now consider and define the surface stress and surface strain. It then follows from (4.7) – (4.9) that the interfacial excess energy can be re-rewritten as

$$\Gamma = \Gamma_0 + \boldsymbol{\Gamma}^{(1)} : \boldsymbol{\varepsilon}^s + \frac{1}{2}\boldsymbol{\varepsilon}^s : \boldsymbol{\Gamma}^{(2)} : \boldsymbol{\varepsilon}^s + \frac{1}{2}\boldsymbol{\sigma}^t_+ \cdot \boldsymbol{\Lambda}^{(2),+} \cdot \boldsymbol{\sigma}^t_+ + \frac{1}{2}\boldsymbol{\sigma}^t_- \cdot \boldsymbol{\Lambda}^{(2),-} \cdot \boldsymbol{\sigma}^t_- \quad , \tag{4.13}$$

where

$$\Gamma_0 = \int_{-\infty}^{\infty} \hat{w}_0(x_3)dx_3 \quad , \quad \boldsymbol{\Gamma}^{(1)} = \int_{-\infty}^{\infty} \hat{\boldsymbol{\tau}}^s(x_3)dx_3 \quad , \tag{4.14}$$

$$\boldsymbol{\Gamma}^{(2)} = \int_0^{\infty} \left[\mathbf{C}^s(x_3) - \mathbf{C}^s_+\right]dx_3 + \int_{-\infty}^{0} \left[\mathbf{C}^s(x_3) - \mathbf{C}^s_-\right]dx_3 \quad , \tag{4.15}$$

$$\boldsymbol{\Lambda}^{(2)} = \boldsymbol{\Lambda}^{(2),+} + \boldsymbol{\Lambda}^{(2),-} = \int_0^{\infty} \left[\mathbf{M}(x_3) - \mathbf{M}_+\right]dx_3 + \int_{-\infty}^{0} \left[\mathbf{M}(x_3) - \mathbf{M}_-\right]dx_3 \quad . \tag{4.16}$$

A more convenient way of writing (4.13) is to use the average transverse stress $\left\langle \boldsymbol{\sigma}^t \right\rangle = \frac{1}{2}\left(\boldsymbol{\sigma}^t_+ + \boldsymbol{\sigma}^t_-\right)$ and the relative transverse stress discontinuity $\left[\!\left[\boldsymbol{\sigma}^t \right]\!\right] = \boldsymbol{\sigma}^t_+ - \boldsymbol{\sigma}^t_-$ such that,

$$\begin{aligned} \Gamma = \Gamma_0 + \boldsymbol{\Gamma}^{(1)} : \boldsymbol{\varepsilon}^s + \frac{1}{2}\boldsymbol{\varepsilon}^s : \boldsymbol{\Gamma}^{(2)} : \boldsymbol{\varepsilon}^s + \frac{1}{2}\left\langle \boldsymbol{\sigma}^t \right\rangle \cdot \boldsymbol{\Lambda}^{(2)} \cdot \left\langle \boldsymbol{\sigma}^t \right\rangle + \frac{1}{8}\left[\!\left[\boldsymbol{\sigma}^t \right]\!\right] \cdot \boldsymbol{\Lambda}^{(2),} \cdot \left[\!\left[\boldsymbol{\sigma}^t \right]\!\right] \\ + \frac{1}{2}\left\langle \boldsymbol{\sigma}^t \right\rangle \cdot \mathbf{K} \cdot \left[\!\left[\boldsymbol{\sigma}^t \right]\!\right] \end{aligned} \quad , \tag{4.17}$$

where,

$$\mathbf{K} = \boldsymbol{\Lambda}^{(2),+} - \boldsymbol{\Lambda}^{(2),-} \quad . \tag{4.18}$$

Equation (4.17) gives the interfacial excess energy as an explicit function of the in-plane strain and transverse stress tensors.

4.2.3 Surface Stress and Surface Strain

Next, we define the (second Piola–Kirchhoff) interfacial excess stress by

$$\boldsymbol{\Sigma}^s = \int_0^{\infty} \left[\boldsymbol{\sigma}^s(x_3) - \boldsymbol{\sigma}_+^s \right] dx_3 + \int_{-\infty}^{0} \left[\boldsymbol{\sigma}^s(x_3) - \boldsymbol{\sigma}_-^s \right] dx_3 \quad . \tag{4.19}$$

It follows from Appendix B and equation (B.8) that,

$$\boldsymbol{\Sigma}^s = \boldsymbol{\Gamma}^{(1)} + \boldsymbol{\Gamma}^{(2)} : \boldsymbol{\varepsilon}^s + \left\langle \boldsymbol{\sigma}^t \right\rangle \cdot \mathbf{H} + \frac{1}{2} \left[\!\left[\boldsymbol{\sigma}^t \right]\!\right] \cdot \left(\mathbf{H}^+ - \mathbf{H}^- \right) \quad , \tag{4.20}$$

where,

$$\mathbf{H} = \mathbf{H}^+ + \mathbf{H}^- = \int_0^{\infty} \left[\boldsymbol{\gamma}(x_3) - \boldsymbol{\gamma}_+ \right] dx_3 + \int_{-\infty}^{0} \left[\boldsymbol{\gamma}(x_3) - \boldsymbol{\gamma}_- \right] dx_3 \quad . \tag{4.21}$$

Similarly if we consider the "excess" strain, the (Lagrange) transverse interfacial excess strain is defined by

$$\boldsymbol{\Delta}^t = \int_0^{\infty} \left[\boldsymbol{\varepsilon}^t(x_3) - \boldsymbol{\varepsilon}_+^t \right] dx_3 + \int_{-\infty}^{0} \left[\boldsymbol{\varepsilon}^t(x_3) - \boldsymbol{\varepsilon}_-^t \right] dx_3 \quad . \tag{4.22}$$

Making use of Appendix B and equation (B.6) we have

$$\boldsymbol{\Delta}^t = \boldsymbol{\Lambda}^{(1)} + \boldsymbol{\Lambda}^{(2)} \cdot \left\langle \boldsymbol{\sigma}^t \right\rangle + \frac{1}{2} \mathbf{K} \cdot \left[\!\left[\boldsymbol{\sigma}^t \right]\!\right] - \mathbf{H} : \boldsymbol{\varepsilon}^s \quad , \tag{4.23}$$

where,

$$\boldsymbol{\Lambda}^{(1)} = -\int_{-\infty}^{\infty} \mathbf{M}(x_3) \cdot \boldsymbol{\tau}^t(x_3) dx_3 \quad . \tag{4.24}$$

4.2.4 Surface Elasticity, Generalized Shuttleworth Relation

Comparing (4.13) with (4.20) and (4.23) leads to, respectively,

$$\boldsymbol{\Sigma}^s = \left(\frac{\partial \Gamma}{\partial \boldsymbol{\varepsilon}^s} \right)_{\boldsymbol{\sigma}^t} + \left\langle \boldsymbol{\sigma}^t \right\rangle \cdot \mathbf{H} + \frac{1}{2} \left[\!\left[\boldsymbol{\sigma}^t \right]\!\right] \cdot \left(\mathbf{H}^+ - \mathbf{H}^- \right) \quad , \tag{4.25}$$

$$\boldsymbol{\Delta}^t - \boldsymbol{\Lambda}^{(1)} = \left(\frac{\partial \Gamma}{\partial \left\langle \boldsymbol{\sigma}^t \right\rangle} \right)_{\boldsymbol{\varepsilon}^s} - \mathbf{H} : \boldsymbol{\varepsilon}^s \quad . \tag{4.26}$$

Equation (4.25) relates the interfacial excess stress to the interfacial excess energy. It reduces to the original Shuttleworth equation (4.1) only when $\left\langle \boldsymbol{\sigma}^t \right\rangle = \mathbf{0}$. Therefore, we will call equation (4.25) the generalized Shuttleworth equation. For $\left\langle \boldsymbol{\sigma}^t \right\rangle \neq \mathbf{0}$, it is seen from (4.20) that interfacial excess stress $\boldsymbol{\Sigma}^s$ consists of three terms. The first term $\boldsymbol{\Gamma}^{(1)}$ is a two-dimensional second order tensor representing the internal excess stress of the interface. It is the part of interfacial stress that exists when the surface strain and transverse stress are absent. The second term is related to the two-dimensional fourth order tensor $\boldsymbol{\Gamma}^{(2)}$ that represents the interface's in-plane elasticity, while the third term is related to a third order tensor $\mathbf{H}$ that measures the Poisson's effect of the interface.

Analogously, the transverse interfacial excess strain tensor $\boldsymbol{\Delta}^t$ measures the interfacial excess deformation in the direction transverse to the interface. Therefore, equation (4.26) can be viewed as the complimentary Shuttleworth equation. It is seen from (4.23) that $\boldsymbol{\Delta}^t$ also consists of three terms. The first term $\boldsymbol{\Lambda}^{(1)}$ represents the part of transverse interfacial deformation that exists even when $\left\langle \boldsymbol{\sigma}^t \right\rangle = \mathbf{0}$ and $\boldsymbol{\varepsilon}^s = \mathbf{0}$ (i.e., when the remote traction the in-plane strain vanishes). Therefore, $\boldsymbol{\Lambda}^{(1)}$ is called the interfacial "relaxation" tensor. The fourth order tensor $\boldsymbol{\Lambda}^{(2)}$ representing the transverse compliance of the interface is called the interfacial transverse compliant tensor. It should be pointed out that although $\boldsymbol{\Lambda}^{(1)}$ and $\mathbf{H}$ affect the in-plane interfacial excess stress and transverse interfacial excess strain, they do not explicitly appear in the interfacial excess energy. Furthermore, although $\boldsymbol{\Delta}^t$ is referred to as the transverse interfacial excess "strain", it has a dimension of length. In fact, it actually represents the intrinsic “width” of the interface accounting for the relative movement between the top and bottom "surfaces" of the

interfacial region.

It is clear from the foregoing discussions that the interfacial tensors $\mathbf{\Gamma}^{(1)}$, $\mathbf{\Gamma}^{(2)}$, $\mathbf{\Lambda}^{(1)}$, $\mathbf{\Lambda}^{(2)}$ and $\mathbf{H}$ are intrinsic properties of the interface. They can be calculated analytically for a given bimaterial with known interatomic potentials as shown later on in this chapter. Once these tensors are known, the elastic behavior of the interface is fully characterized.

Before closing this sub-section, it is worthwhile to clarify certain terms. Since the term "surface free energy" was originally introduced to fluid surfaces, the traditional surface free energy, or surface energy consists of only $\hat{\Gamma}_s = \Gamma\big|_{\boldsymbol{\sigma}^t=\mathbf{0},\boldsymbol{\varepsilon}^s=\mathbf{0}} = \Gamma_0$. The surface free energy $\hat{\Gamma}_s$ by and large is an intrinsic material property. However, if the remote loading $\boldsymbol{\varepsilon}^s$ and/or $\boldsymbol{\sigma}^t$ is applied, the total interfacial excess energy is given by (4.7) which is no longer an intrinsic material property. It also depends on the applied load. To distinguish them, we name $\hat{\Gamma}_s$ the interfacial *free* energy, which is an intrinsic material property, while the Γ as given by (4.13) will be called interfacial *excess* energy, which represents the "extra" energy associated with the interface subjected to $\boldsymbol{\varepsilon}^s$ and/or $\boldsymbol{\sigma}^t$. In traditional continuum mechanics, neither $\hat{\Gamma}_s$ nor Γ appears in the formulation. In the classic work on elastic interfaces (Gurtin and Murdoch, 1975; Gurtin, 1978; Gurtin, 1998), only the in-plane part $\Gamma\big|_{\boldsymbol{\sigma}^t=0}$ was considered.

4.2.5 Isotropic Bimaterials

The formulation presented above is valid for elastic materials with arbitrary anisotropy. In this section, we consider a special case where the interface is flat and therefore traction continuity is assured ($\boldsymbol{\sigma}^t = \boldsymbol{\sigma}^t_+ = \boldsymbol{\sigma}^t_-$) and both constituents of the bimaterial are elastically isotropic with Lamé constants $\lambda_\pm$ and $\mu_\pm$. In this case, it is

perceivable that the interface will be transversely isotropic with its axis of symmetry being perpendicular to the interface. In the coordinate shown in Figure 4.1, the interfacial matrices defined by (4.14) – (4.21) can be calculated formally from Appendix B and equations (B.17) – (B.18)

$$\Gamma^{(2)}_{\alpha\beta\kappa\lambda} = (K_S - \mu_S)\delta_{\alpha\beta}\delta_{\kappa\lambda} + \mu_S\left(\delta_{\alpha\kappa}\delta_{\beta\lambda} + \delta_{\alpha\lambda}\delta_{\beta\kappa}\right) \quad , \tag{4.27}$$

$$\Lambda^{(2)}_{ij} = (\frac{1}{E_T} - \frac{1}{\mu_T} - \frac{4K_S\nu_S^2}{E_T^2})\delta_{3i}\delta_{3j} + \frac{1}{\mu_T}\delta_{ij} \quad , \tag{4.28}$$

$$H_{i\alpha\beta} = \frac{2K_S\nu_S}{E_T}\delta_{3i}\delta_{\alpha\beta} \quad , \tag{4.29}$$

where

$$\mu_S = \int_0^\infty (\mu - \mu_+)dx_3 + \int_{-\infty}^0 (\mu - \mu_-)dx_3 \quad , \tag{4.30}$$

$$K_S = \mu_S + \int_0^\infty \left(\frac{2\lambda\mu}{\lambda + 2\mu} - \frac{2\lambda_+\mu_+}{\lambda_+ + 2\mu_+}\right)dx_3 + \int_{-\infty}^0 \left(\frac{2\lambda\mu}{\lambda + 2\mu} - \frac{2\lambda_-\mu_-}{\lambda_- + 2\mu_-}\right)dx_3 \quad , \tag{4.31}$$

$$\frac{1}{\mu_T} = \int_0^\infty \left(\frac{1}{\mu} - \frac{1}{\mu_+}\right)dx_3 + \int_{-\infty}^0 \left(\frac{1}{\mu} - \frac{1}{\mu_-}\right)dx_3 \quad , \tag{4.32}$$

$$\frac{2K_S\nu_S}{E_T} = \int_0^\infty \left(\frac{\lambda}{\lambda + 2\mu} - \frac{\lambda_+}{\lambda_+ + 2\mu_+}\right)dx_3 + \int_{-\infty}^0 \left(\frac{\lambda}{\lambda + 2\mu} - \frac{\lambda_-}{\lambda_- + 2\mu_-}\right)dx_3 \quad , \tag{4.33}$$

$$\frac{1}{E_T} - \frac{4K_S\nu_S^2}{E_T^2} = \int_0^\infty \left(\frac{1}{\lambda + 2\mu} - \frac{1}{\lambda_+ + 2\mu_+}\right)dx_3 + \int_{-\infty}^0 \left(\frac{1}{\lambda + 2\mu} - \frac{1}{\lambda_- + 2\mu_-}\right)dx_3 \quad . \tag{4.34}$$

The physical meaning of these five parameters K_S, μ_S, μ_T, E_T and ν_S will become clear next. Substituting equations (4.27) – (4.29) into (4.20) gives

$$\Sigma^s_{\alpha\beta} = \Gamma^{(1)}_{\alpha\beta} + (K_S - \mu_S)\delta_{\alpha\beta}\varepsilon^s_{\kappa\kappa} + 2\mu_S\varepsilon^s_{\alpha\beta} + \frac{2K_S\nu_S}{E_T}\sigma^t_3\delta_{\alpha\beta} \quad , \tag{4.35}$$

where

$$\Gamma^{(1)}_{\alpha\beta} = \int_{-\infty}^{\infty} \hat{\tau}_{\alpha\beta}(x_3)dx_3 = \int_{-\infty}^{\infty}\left[\tau^s_{\alpha\beta}(x_3) - \frac{\lambda(x_3)\tau^t_3(x_3)}{\lambda(x_3) + 2\mu(x_3)}\delta_{\alpha\beta}\right]dx_3 \tag{4.36}$$

is the in-plane interfacial excess stress when no external load is applied while the in-plane strain (measured from the undeformed crystal lattice) remains zero. The in-plane biaxial "hydrostatic" stress is thus given by $\Sigma^s_{\alpha\alpha}/2$, where

$$\Sigma^s_{\alpha\alpha} = \Gamma^{(1)}_{\alpha\alpha} + 2K_S\varepsilon^s_{\kappa\kappa} + \frac{4K_S\nu_S}{E_T}\sigma^t_3 \quad . \tag{4.37}$$

Clearly, K_S is the in-plane bi-axial bulk modulus of the interface. The individual components of the interfacial excess stress tensor are

$$\Sigma^s_{11} = \Gamma^{(1)}_{11} + (K_S - \mu_S)\varepsilon^s_{\kappa\kappa} + 2\mu_S\varepsilon^s_{11} + \frac{2K_S\nu_S}{E_T}\sigma^t_3 \quad , \tag{4.38}$$

$$\Sigma^s_{22} = \Gamma^{(1)}_{22} + (K_S - \mu_S)\varepsilon^s_{\kappa\kappa} + 2\mu_S\varepsilon^s_{22} + \frac{2K_S\nu_S}{E_T}\sigma^t_3 \quad , \tag{4.39}$$

$$\Sigma^s_{12} = \Gamma^{(1)}_{12} + 2\mu_S\varepsilon^s_{12} \quad . \tag{4.40}$$

It is seen from (4.40) that μ_S is the in-plane shear modulus of the interface.

The transverse interfacial excess strain follows from making use of Appendix (B.17) – (B.18) in (4.23)

$$\Delta^t_i = \Lambda^{(1)}_i + (\frac{1}{E_T} - \frac{1}{\mu_T} - \frac{4K_S\nu_S^2}{E_T^2})\delta_{3i}\sigma^t_3 + \frac{1}{\mu_T}\sigma^t_i - \frac{2K_S\nu_S}{E_T}\delta_{3i}\varepsilon^s_{\kappa\kappa} \quad , \tag{4.41}$$

where

$$\Lambda^{(1)}_i = \int_{-\infty}^{\infty}\left[\frac{\lambda+\mu}{(\lambda+2\mu)\mu}\delta_{3i}\tau^t_3 - \frac{1}{\mu}\tau^t_i\right]dx_3 \tag{4.42}$$

is the transverse relaxation of the interface when no external load is applied while the in-plane strain (measured from the undeformed crystal lattice) remains zero. By making use of (4.37) in (4.41), one can write Δ^t_i in terms of the stresses,

$$\Delta^t_i = \Lambda^{(1)}_i + (\frac{1}{E_T} - \frac{1}{\mu_T})\sigma^t_3\delta_{3i} + \frac{1}{\mu_T}\sigma^t_i - \frac{2\nu_S}{E_T}(\Sigma^s_{\alpha\alpha} - \Gamma^{(1)}_{\alpha\alpha})\delta_{3i} \quad . \tag{4.43}$$

Specifically,

$$\Delta_1^t = \Lambda_1^{(1)} + \frac{1}{\mu_T}\sigma_1^t \quad , \quad \Delta_2^t = \Lambda_2^{(1)} + \frac{1}{\mu_T}\sigma_2^t \quad , \tag{4.44}$$

$$\Delta_3^t = \Lambda_3^{(1)} + \frac{1}{E_T}\left[\sigma_3^t - \nu_S(\Sigma_{\alpha\alpha}^s - \Gamma_{\alpha\alpha}^{(1)})\right] \quad . \tag{4.45}$$

It is seen that E_T is the transverse Young's modulus of the interface, and ν_S is the Poisson's ratio associated with the contraction of the interface in the transverse (thickness) direction when the interface is stretched by in-plane stress.

Finally, we note that in the special case when $\sigma_j^t = 0$, the interfacial excess stress (4.37) reduces to

$$\Sigma_{\alpha\beta}^s = \Gamma_{\alpha\beta}^{(1)} + \lambda_S \delta_{\alpha\beta}\varepsilon_{\kappa\kappa}^s + 2\mu_S \varepsilon_{\alpha\beta}^s \quad , \tag{4.46}$$

where $\lambda_S = K_S - \mu_S$ can be viewed as one of the two-dimensional Lamé constants of the interface. Equation (4.46) is identical to the classical form of interfacial excess stress derived in (Gurtin and Murdoch, 1975; Murdoch, 1976; Gurtin, 1978; Gurtin, 1998).

In all the preceding discussions, we have intentionally limited ourselves to continuum media. Therefore, there is not microstructure, thus no characteristic length involved, and the interface is a mathematical surface with zero-thickness. For realistic bimaterials, there typically exist two distinctive length parameters, namely, the atomic spacing (lattice parameter) *d*, and the radius of curvature of the interface *D*, where *D* is generally several order of magnitude greater than *d* for most of the problems of engineering interest. More detailed discussions about the surface elastic properties and their effects on nano-scaled materials can be found in chapter 5. It is shown the size-dependence effect on the elastic properties of nanostructures and the contribution made by the surface elastic behavior.

4.3 Semi-analytical Method to Evaluate Surface Properties

In this section, a semi-analytic method is developed to compute the surface elastic properties of crystalline materials. The method presented in this section is based on the idea of expanding the atomic energy and atomic stress into power series of surface strains and transverse stresses. The roots of this approach has been used to successfully compute bulk properties (Johnson, 1988; Johnson and Oh, 1989) and to fit various interatomic potentials (Foiles *et al.*, 1986). For an atomic ensemble in equilibrium, the energy of each atom can be written as a function of the atomic position and the elastic constants can be extracted assuming homogeneous deformation (Born and Huang, 1954). As pointed out by Shenoy (2005), direct application of such an approach in calculating surface properties fails to account for the internal relaxation. The approach used in this work relies on the expansion of the energy and stress of each atom into a power series of surface strains and transverse stresses relative to the relaxed configuration. The appropriate use of the equilibrium and traction conditions across the interface enables us to solve and account for the inner relaxation. The theoretical framework for interfaces presented in the previous section helps us to subsequently formulate analytical expressions for the interface elastic properties. These quantities are explicit functions of the interatomic potentials and atomic positions.

Now, let us consider a given interface between two crystals. Because of the reduced coordination, atoms near the interface relaxed, i.e., they moved away from their perfect lattice position when the interface was created. If this relaxed, or self-equilibrium, state of the bicrystal is regarded as an intermediate configuration in the deformation process, the total strain measured from the perfect crystal lattice can be written as,

$$\boldsymbol{\varepsilon} = \hat{\boldsymbol{\varepsilon}} + \overline{\boldsymbol{\varepsilon}} \quad , \tag{4.47}$$

where $\hat{\boldsymbol{\varepsilon}}$ is the strain at the relaxed state of the bicrystal measured from the perfect crystal lattice, and $\overline{\boldsymbol{\varepsilon}}$ is the relative strain measured from the relaxed state of the bicrystal. The relative strain can also be interpreted as the applied strain imposed upon the relaxed state of the bicrystal. Since the in-plane interface coherent strain $\boldsymbol{\varepsilon}^s$ is also measured from the perfect crystal lattice, continuity of the strain field near the interface, leads to

$$\boldsymbol{\varepsilon}^s\Big|_{x_3=0} = \left(\overline{\boldsymbol{\varepsilon}}^s + \hat{\boldsymbol{\varepsilon}}^s\right)\Big|_{x_3=0} = \boldsymbol{\varepsilon}^s \quad . \tag{4.48}$$

Let us then consider a bimaterial system containing N equivalent atoms. The total energy E^n of atom n in the bimaterial is a generic inter-atomic potential functional given by,

$$\begin{aligned} E^{(n)} = E_0 + \sum_{m\neq n} E\left(r^{nm}\right) + \frac{1}{2!}\sum_{m\neq n}\sum_{p\neq n} E\left(r^{nm}, r^{np}\right) + \dots \\ + \frac{1}{N!}\sum_{m\neq n}\sum_{p\neq n}\cdots\sum_{q\neq n} E\left(r^{nm}, r^{np}, \dots, r^{nq}\right) \end{aligned} \quad , \tag{4.49}$$

where,

$$r^{mn} = \sqrt{\left(r_1^{mn}\right)^2 + \left(r_2^{mn}\right)^2 + \left(r_3^{mn}\right)^2} \tag{4.50}$$

is the scalar distance between atom m and atom n. Note that the generic form of (4.49) may include pair potentials such as the Lennard-Jones potential as well as multi-body potentials such as the EAM potentials used in the numerical examples in this work.

4.3.1 Free Surface

Let us first consider a flat free surface of a given single crystal. Let $\hat{r}^{mn}$ be the scalar distance between the atom m and atom n at the relaxed configuration of the assembly. If $\mathbf{r}^{mn}$ is the position vector between atom m and atom n in a uniform strain

field superimposed on the relaxed configuration, then the strain tensor relative to the relaxed configuration is the same for all atoms and can be written as

$$r_i^{mn} - \hat{r}_i^{mn} = F_{ij}^{mn}\hat{r}_j^{mn} = F_{ij}\hat{r}_j^{mn} \quad , \tag{4.51}$$

The nine independent strains F_{ij} can be written as six symmetric parameters

$$\overline{\varepsilon}_{ij} = \frac{1}{2}\left(F_{ij} + F_{ji}\right) \quad , \tag{4.52}$$

corresponding to the pure deformation and three anti-symmetric parameters

$$\omega_{ij} = \frac{1}{2}\left(F_{ij} - F_{ji}\right) \quad , \tag{4.53}$$

corresponding to pure rotation. The method presented in this paper only considers pure deformation. Note also that such a procedure is simple in a centrosymmetric crystal, since all the interatomic vectors in this case transform through $\overline{\varepsilon}_{ij}$ as in (4.52). This is the case of the basal surfaces studied in the following of this section, however, in the case of non-centrosymmetric crystals, which is the case of atomic assemblies containing interfaces or for non-basal free surfaces, internal relaxation occurs. This situation will be treated separately in section 4.3.2.

It then follows from references(Johnson, 1972; Johnson, 1973; Ackland and Finnis, 1986; Johnson, 1988) and equations (4.52) that for a uniform and homogeneous deformation the Taylor expansion of (4.49) with respect to the relaxed configuration can be written as

$$E^{(n)} = A^{(n)} + A_{ij}^{(n)}\overline{\varepsilon}_{ij} + \frac{1}{2}A_{ijkl}^{(n)}\overline{\varepsilon}_{ij}\overline{\varepsilon}_{kl} \quad , \tag{4.54}$$

where the uniform strain field $\overline{\varepsilon}_{ij}$ is measured from the equilibrium (relaxed) state of the semi-infinite crystal and the coefficients $A^{(n)}$, $A_{ij}^{(n)}$, and $A_{ijkl}^{(n)}$ are related to the energy of atom *n* by

$$A^{(n)} = E^{(n)}\Big|_{r^{mn}=\hat{r}^{mn}} \quad , \tag{4.55}$$

$$A_{ij}^{(n)} = \left[\sum_{p \neq n} \hat{r}_i^{pn} \left. \frac{\partial E^{(n)}}{\partial r_j^{pn}} \right|_{r^{mn} = \hat{r}^{mn}} \right]_{<i,j>} , \tag{4.56}$$

$$A_{ijkl}^{(n)} = \left[\sum_{p \neq n} \sum_{q \neq n} \left. \frac{\hat{r}_i^{pn} \hat{r}_k^{qn} \partial^2 E^{(n)}}{\partial r_j^{pn} \partial r_l^{qn}} \right|_{r^{mn} = \hat{r}^{mn}} \right]_{<i,j>,<k,l>} , \tag{4.57}$$

where the notation in subscript means taking the symmetric part of the base tensor, e.g.,

$$\left[u_{i,j} \right]_{<i,j>} = \frac{1}{2} \left[u_{i,j} + u_{j,i} \right] . \tag{4.58}$$

Note that, once the inter-atomic potential $E^{(n)}$ is given, the coefficients $A^{(n)}$, $A_{ij}^{(n)}$, and $A_{ijkl}^{(n)}$ can be computed analytically from (4.55) – (4.57). The explicit expressions of (4.55) – (4.57) for the EAM potentials are derived in Appendix A.

For an atom deep inside the semi-infinite crystal (or, equivalently, an atom in an infinite crystal), the local elastic stiffness tensor can be defined as(Alber *et al.*, 1992; Bassani *et al.*, 1992; Marinopoulos *et al.*, 1998),

$$C_{ijkl}^{(n)} = \frac{1}{\Omega^{(n)}} A_{ijkl}^{(n)} , \tag{4.59}$$

where $\Omega^{(n)}$ is the volume of the Voronoi polyhedron associated with atom *n*. The atomic-level elastic stiffness tensor $C_{ijkl}^{(n)}$ can be interpreted as describing the homogeneous elastic response at individual atomic sites.

For atoms near the free surface, however, the atomic level elastic stiffness tensor can no longer be given simply by (4.59). To derive the elastic properties of free surfaces, let us consider a semi-infinite crystal subjected to an applied uniform strain field $\bar{\varepsilon}_{ij}$. The free surface at $x_3 = 0$ requires,

$$\sigma_{13} = \sigma_{23} = \sigma_{33} = 0 \text{ at } x_3 = 0 . \tag{4.60}$$

It then follows from Hooke's law that any uniform strain field that is compatible with the traction-free boundary conditions (4.60) should satisfy

$$2\overline{\varepsilon}_{13} = -D_{1j}C_{j3\alpha\beta}\overline{\varepsilon}_{\alpha\beta}\,,\;\; 2\overline{\varepsilon}_{23} = -D_{2j}C_{j3\alpha\beta}\overline{\varepsilon}_{\alpha\beta}\,,\;\; \overline{\varepsilon}_{33} = -D_{3j}C_{j3\alpha\beta}\overline{\varepsilon}_{\alpha\beta}\;\;, \tag{4.61}$$

where C_{ijkl} is the elastic stiffness tensor of the perfect crystal lattice, and the 3×3 matrix D_{ij} is given by

$$\mathbf{D}^{-1} = \begin{bmatrix} C_{1313} & C_{1323} & C_{1333} \\ C_{2313} & C_{2323} & C_{2333} \\ C_{3313} & C_{3323} & C_{3333} \end{bmatrix}\;. \tag{4.62}$$

Making use of (4.61) into (4.54) yields

$$E^{(n)} = A^{(n)} + B^{(n)}_{\alpha\beta}\overline{\varepsilon}_{\alpha\beta} + \frac{1}{2}B^{(n)}_{\alpha\beta\kappa\lambda}\overline{\varepsilon}_{\alpha\beta}\overline{\varepsilon}_{\kappa\lambda}\;\;, \tag{4.63}$$

where

$$B^{(n)}_{\alpha\beta} = A^{(n)}_{\alpha\beta} - A^{(n)}_{i3}D_{ij}C_{j3\alpha\beta}\;\;, \tag{4.64}$$

$$B^{(n)}_{\alpha\beta\kappa\lambda} = A^{(n)}_{\alpha\beta\kappa\lambda} + A_{i3j3}D_{ip}D_{jq}C_{p3\alpha\beta}C_{q3\kappa\lambda} - A_{i3\kappa\lambda}D_{iq}C_{q3\alpha\beta} - A_{\alpha\beta j3}D_{jp}C_{p3\kappa\lambda}\;\;, \tag{4.65}$$

Substituting (4.63) into (4.2) yields

$$\Gamma = \frac{1}{A_0}\sum_{n=1}^{\infty}\left[\left(A^{(n)} - A^{(0)}\right) + \left(B^{(n)}_{\alpha\beta} - B^{(0)}_{\alpha\beta}\right)\overline{\varepsilon}_{\alpha\beta} + \frac{1}{2}\left(B^{(n)}_{\alpha\beta\kappa\lambda} - B^{(0)}_{\alpha\beta\kappa\lambda}\right)\overline{\varepsilon}_{\alpha\beta}\overline{\varepsilon}_{\kappa\lambda}\right]\;\;, \tag{4.66}$$

where $A^{(0)}$, $B^{(0)}_{\alpha\beta}$ and $B^{(0)}_{\alpha\beta\kappa\lambda}$ are calculated from (4.55), (4.64) and (4.65), respectively, for an atom far away from the surface embedded in the bulk of the semi-infinite crystal. For the free surface at $x_3 = 0$ in Figure 4.2, it follows from (4.12) that uniform strain tensor $\overline{\varepsilon}_{\alpha\beta}$ in (4.66) can be replaced with the surface strain tensor $\varepsilon^s_{\alpha\beta}$. Thus, comparing (4.66) with (4.13) when $\boldsymbol{\sigma}^t = \mathbf{0}$ leads to the expressions for the elastic properties of the free surface

$$\Gamma_0 = \frac{1}{A_0}\sum_{n=1}^{\infty}\left(A^{(n)} - A^{(0)}\right)\;\;, \tag{4.67}$$

$$\Gamma^{(1)}_{\alpha\beta} = \frac{1}{A_0}\sum_{n=1}^{\infty}\left(B^{(n)}_{\alpha\beta} - B^{(0)}_{\alpha\beta}\right)\;\;, \tag{4.68}$$

$$\Gamma^{(2)}_{\alpha\beta\kappa\lambda} = \frac{1}{A_0}\sum_{n=1}^{\infty}\left(B^{(n)}_{\alpha\beta\kappa\lambda} - B^{(0)}_{\alpha\beta\kappa\lambda}\right) \quad , \tag{4.69}$$

These are the analytical expressions of the intrinsic surface energy density, intrinsic surface stress and the surface elastic stiffness tensor, respectively. Note that there is an important difference between (4.67) – (4.69) and similar results in the literature (Johnson, 1972; Johnson, 1973; Ackland and Finnis, 1986; Johnson, 1988; Johnson and Oh, 1989; Feibelman, 1991). In these existing solutions, as noted by Shenoy (2005), surface relaxation is not accounted for, while (4.67) – (4.69) are derived for the relaxed surface.

Before closing this section, it should be mentioned that, for a given inter-atomic potential function $E^{(n)}$, numerical evaluation of the analytical expressions (4.67) – (4.69) requires knowledge of the inter-atomic spacing $\hat{r}^{mn}$ at the relaxed state of the surface. To obtain $\hat{r}^{mn}$, a molecular static simulation may be conducted. This is why we called the method developed here semi-analytical. Note also that only one Molecular Static simulation is needed for each surface orientation. In contrast, existing methods (Zhou and Huang, 2004; Shenoy, 2005) evaluating the surface properties require multiple simulations for each surface.

4.3.2 Bicrystal Interface

To evaluate the elastic properties of a given interface from a discrete medium point of view, we consider now a given flat interface between two crystals. Given equation (4.49), the total energy of this ensemble containing *N* such atoms is $E = \sum_{n=1}^{N} E^{(n)}$. If we consider a single crystal of infinite extent subjected to a macroscopically uniform strain field ε_{ij} it has been demonstrated by Johnson (1972) that the elastic stiffness tensor of the bulk crystal is given by,

$$C_{ijkl} = \frac{1}{N}\sum_{n=1}^{N}\sum_{p\neq n}\sum_{q\neq n}\frac{1}{\Omega_n}\frac{\partial^2 E^{(n)}}{\partial r_i^{pn}\partial r_k^{qn}}\bigg|_{r^{mn}} r_j^{pn} r_l^{qn} \quad . \tag{4.70}$$

However, when considering an atomic ensemble containing non-equivalent atoms (which is the case for systems containing grain boundaries and interfaces) subjected to a macroscopically uniform deformation, internal relaxations occur (Martin, 1975) and equation (4.70) can be interpreted as a description of the homogeneous elastic response of the ensemble.

4.3.2.1 Atomic Level Mapping

In order to account for the inner displacements, we first define an atomic level mapping between the undeformed and deformed configurations by,

$$r_i^m - \hat{r}_i^m = \left(\overline{\varepsilon}_{ij}^{\pm} + \tilde{\varepsilon}_{ij}^m\right)\hat{r}_j^m \quad , \tag{4.71}$$

where $\overline{\varepsilon}_{ij}^{\pm}$ corresponds to a homogeneous deformation of atom *m* and $\tilde{\varepsilon}_{ij}^m$ describes the "inner" relaxation (or additional "non-homogeneous" deformation) of atom *m* with respect to a homogeneous deformation. The positive (or negative) sign should be selected if atom *m* is in the upper (or lower) crystal. The atomic position of atom *m* is measured from a fixed reference point. The homogeneous deformation of the bicrystal assembly can be described by an in-plane deformation $\varepsilon_{\alpha\beta}^s$ and a transverse loading σ_i^t ("T" stress). Derivations and detailed expressions are presented in Appendix B. The homogeneous deformation is expressed as a function of these two global variables such that (4.71) transforms into,

$$r_i^m - \hat{r}_i^m = \left(A_{ij\alpha\beta}^{\pm}\varepsilon_{\alpha\beta}^s + B_{ijk}^{\pm}\sigma_k^t\right)\hat{r}_j^m + \tilde{\varepsilon}_{ij}^m\hat{r}_j^m \quad , \tag{4.72}$$

with,

$$A_{ij\alpha\beta}^{\pm} = \delta_{i\alpha}\delta_{j\beta} - \frac{1}{2}\left(\gamma_{j\alpha\beta}^{\pm}\delta_{3i} + \gamma_{i\alpha\beta}^{\pm}\delta_{3j}\right) \quad , \tag{4.73}$$

$$B_{ijk}^{\pm} = \frac{1}{2}\left(M_{jk}^{\pm}\delta_{3i} + M_{ik}^{\pm}\delta_{3j}\right) \quad , \tag{4.74}$$

where $\gamma_{j\alpha\beta}^{\pm}$ and $M_{jk}^{\pm}$ are given in Appendix B. Note that $A_{ij\alpha\beta}^{\pm}$ and $B_{ijk}^{\pm}$ are known tensors and characterize the homogeneous behavior of the bicrystal.

The difference in position of two atoms near their relaxed state is therefore given by,

$$r_i^{mn} - \hat{r}_i^{mn} = A_{i\alpha\beta}^{mn}\varepsilon_{\alpha\beta}^{s} + B_{ik}^{mn}\sigma_k^{t} + \left(\tilde{\varepsilon}_{ij}^{m}\hat{r}_j^{m} - \tilde{\varepsilon}_{ij}^{n}\hat{r}_j^{n}\right) \quad , \tag{4.75}$$

where,

$$A_{i\alpha\beta}^{mn} = \left(A_{ij\alpha\beta}^{\pm,m} + A_{ij\alpha\beta}^{\pm,n}\right)\hat{r}_j^{mn} - \left(A_{ij\alpha\beta}^{\pm,n}\hat{r}_j^{m} - A_{ij\alpha\beta}^{\pm,m}\hat{r}_j^{n}\right) \quad , \tag{4.76}$$

and,

$$B_{ik}^{mn} = \left(B_{ijk}^{\pm,m} + B_{ijk}^{\pm,n}\right)\hat{r}_j^{mn} - \left(B_{ijk}^{\pm,n}\hat{r}_j^{m} - B_{ijk}^{\pm,m}\hat{r}_j^{n}\right) \quad . \tag{4.77}$$

4.3.2.2 Total Energy of the Atomic Assembly

Next let us consider the atomic energy of an atom *n*. As reported by Johnson (1972), one can expand the energy density of an atom *n* about its equilibrium configuration.

$$\begin{aligned} w^n = \frac{1}{\Omega_n}\sum_{\substack{m=1 \\ m\neq n}}^{N}\Bigg[& E^{(n)}\left(r^{nm}\right)\Big|_{r^{nm}=\hat{r}^{nm}} + \left.\frac{\partial E^{(n)}}{\partial r_i^{nm}}\right|_{r^{nm}=\hat{r}^{nm}}\left(r_i^{nm} - \hat{r}_i^{nm}\right) \\ & + \frac{1}{2}\sum_{\substack{p=1 \\ p\neq n}}^{N}\left.\frac{\partial E^{(n)}}{\partial r_i^{nm} r_k^{np}}\right|_{r^{nm}=\hat{r}^{nm}}\left(r_i^{nm} - \hat{r}_i^{nm}\right)\left(r_k^{np} - \hat{r}_k^{np}\right) + \cdots\Bigg] \end{aligned} \quad , \tag{4.78}$$

The total strain energy density of the system, *E*, is defined by the sum $\sum_n w^n$. Substituting equation (4.75) into equation (4.78) yields for the total strain energy of the atomic assembly,

$$\begin{aligned} E = E_0 + \bar{A}_{\alpha\beta}^{(1)}\varepsilon_{\alpha\beta}^{s} + \bar{B}_k^{(1)}\sigma_k^{t} + \frac{1}{2}\bar{A}_{\alpha\beta\kappa\lambda}^{(2)}\varepsilon_{\alpha\beta}^{s}\varepsilon_{\kappa\lambda}^{s} + \frac{1}{2}\bar{B}_{ij}^{(2)}\sigma_i^{t}\sigma_j^{t} + \bar{Q}_{\alpha\beta u}\varepsilon_{\alpha\beta}^{s}\sigma_i^{t} \\ + \sum_{n=1}^{N-1}\left(K_{ij}^{n} + D_{ij\alpha\beta}^{n}\varepsilon_{\alpha\beta}^{s} + G_{ijk}^{n}\sigma_k^{t}\right)\tilde{\varepsilon}_{ij}^{n} + \frac{1}{2}\sum_{n=1}^{N-1}\sum_{m=1}^{N-1}L_{ijkl}^{mn}\tilde{\varepsilon}_{ij}^{n}\tilde{\varepsilon}_{kl}^{m} \end{aligned} \quad , \tag{4.79}$$

where $\overline{A}^{(1)}_{\alpha\beta}$, $\overline{B}^{(1)}_{k}$, $\overline{A}^{(2)}_{\alpha\beta\kappa\lambda}$, $\overline{B}^{(2)}_{ij}$ and $\overline{Q}_{\alpha\beta i}$ describe the homogeneous behavior of the assembly upon a deformation configuration $\left(\varepsilon^{s}_{\alpha\beta},\ \sigma^{t}_{k}\right)$ while, K^{n}_{ij}, $D^{n}_{ij\alpha\beta}$, G^{n}_{ijk} and L^{mn}_{ijkl} represent the components of perturbation response of the system introduced by the non-equivalency of the atomic ensemble such as in grain boundaries or multi-species compounds and account for the accommodation of internal relaxations upon a deformation configuration $\left(\varepsilon^{s}_{\alpha\beta},\ \sigma^{t}_{k}\right)$.

4.3.2.3 Atomic Level Stress

After defining the total energy of the system and the atomic level mapping, we then look at the atomic level stress associated with an atom *n*. The virial stress on atom *n* is given by,

$$\sigma^{n}_{ij} = \frac{1}{2\Omega_{n}} \sum_{\substack{m=1 \\ m\neq n}}^{N} \frac{\partial E}{\partial r^{mn}_{i}} r^{mn}_{j} \quad . \tag{4.80}$$

Expanding the atomic level stress σ^{n}_{ij} with respect to r^{mn}_{i} near $\hat{r}^{mn}_{i}$, where $\hat{r}^{mn}_{i}$ is the equilibrium configuration of the bi-crystal, gives

$$\sigma^{n}_{ij} = \sigma^{n}_{ij}\Big|_{r^{mn}=\hat{r}^{mn}} + \sum_{\substack{m=1 \\ m\neq n}}^{N} \left.\frac{\partial \sigma^{n}_{ij}}{\partial r^{mn}_{k}}\right|_{r^{mn}=\hat{r}^{mn}} \left(r^{mn}_{k} - \hat{r}^{mn}_{k}\right) \ , \tag{4.81}$$

where

$$\left.\frac{\partial \sigma^{n}_{ij}}{\partial r^{mn}_{k}}\right|_{r^{mn}=\hat{r}^{mn}} = \frac{1}{2\Omega_{n}} \sum_{\substack{p=1 \\ p\neq n}}^{N} \frac{\partial}{\partial r^{mn}_{k}} \left(\frac{\partial E}{\partial r^{pn}_{i}} r^{pn}_{j} \right)\Bigg|_{r^{pn}=\hat{r}^{pn}} \quad . \tag{4.82}$$

After substituting the mapping of equation (4.75),we obtain for the atomic level stress,

$$\sigma^{n}_{ij} = \tau^{n}_{ij} + \overline{C}^{s,n}_{ij\alpha\beta}\varepsilon^{s}_{\alpha\beta} + \overline{M}^{t,n}_{kij}\sigma^{t}_{k} + \sum_{m=1}^{N-1} T^{nm}_{ijkl}\tilde{\varepsilon}^{m}_{kl} \quad , \tag{4.83}$$

where, τ_{ij}^{n}, $\bar{C}_{ij\alpha\beta}^{s,n}$, $\bar{M}_{kij}^{t,n}$ and T_{ijkl}^{nm} are known constants given in terms of the interatomic potential E and its partial derivative with respect to the interatomic distance r. Derivations and expressions of these tensors are given in Appendix C.

4.3.2.4 Finding the Internal Relaxations

The conditions of mechanical equilibrium and traction continuity across the interface yield,

$$\sigma_{j}^{t,n} = \sigma_{j}^{t} \quad . \tag{4.84}$$

Substituting equation (4.84) into equation (4.83) gives a system of 3N equations for the 6N unknowns $\tilde{\varepsilon}_{ij}^{n}$.

$$\sigma_{i}^{t} = \tau_{i}^{t,n} + \bar{C}_{3i\alpha\beta}^{s,n}\varepsilon_{\alpha\beta}^{s} + \bar{M}_{k3i}^{t,n}\sigma_{k}^{t} + \sum_{m=1}^{N-1} T_{3ikl}^{nm}\tilde{\varepsilon}_{kl}^{m} \quad . \tag{4.85}$$

Using equation (4.85), one can express the transverse relaxation $\tilde{\varepsilon}_{i}^{t,n}$ as a function of the in-plane relaxation $\tilde{\varepsilon}_{\alpha\beta}^{s,n}$, in the in-plane homogeneous strains $\varepsilon_{\alpha\beta}^{s}$ and the transverse stretching σ_{i}^{t}.

$$\tilde{\varepsilon}_{i}^{t,n} = \varsigma_{i}^{t,n} + X_{ij}^{n}\sigma_{j}^{t} - Y_{i\alpha\beta}^{n}\varepsilon_{\alpha\beta}^{s} - \sum_{m=1}^{N-1} Z_{i\alpha\beta}^{nm}\tilde{\varepsilon}_{\alpha\beta}^{s,m} \quad , \tag{4.86}$$

with $\varsigma_{i}^{t,n}$, X_{ij}^{n}, $Y_{i\alpha\beta}^{n}$ and $Z_{i\alpha\beta}^{nm}$ given in Appendix C. Note that equation (4.86) implicitly accounts for the traction condition across the interface and therefore uniquely defines the relationship between the in-plane and transverse internal relaxation.

In order to solve for the 6N unknowns of equation (4.85), we furthermore need to consider that the application of a prescribed "mixed" loading configuration (in-plane prescribed deformation and transverse prescribed traction) to the bicrystal produces a finite strain and a minimization of strain energy density by internal relaxation. In other words, once we substitute the transverse relaxation from Equation (4.86) into equation

(4.79), the total strain energy must be minimum with respect to any arbitrary spontaneous in-plane relaxation, i.e.,

$$\frac{\partial E}{\partial \tilde{\varepsilon}^{s,n}_{\alpha\beta}} = 0 \quad ; \quad \forall n \in \Omega \quad , \tag{4.87}$$

where Ω is the total bicrystal assembly. It is seen that Equation (4.87) is now a system of $3N$ equations for the $3N$ unknowns $\tilde{\varepsilon}^{s,n}_{\alpha\beta}$. Then, we solve for the internal in-plane relaxation,

$$\tilde{\varepsilon}^{s,n}_{\alpha\beta} = \eta^{s,n}_{\alpha\beta} - M^{s,n}_{i\alpha\beta}\sigma^{t}_{i} + Q^{s,n}_{\alpha\beta\kappa\lambda}\varepsilon^{s}_{\kappa\lambda} \quad , \tag{4.88}$$

with $\eta^{s,n}_{\alpha\beta}$, $M^{s,n}_{i\alpha\beta}$ and $Q^{s,n}_{\alpha\beta\kappa\lambda}$ given in Appendix C. Substituting equation (4.88) back into equation (4.86) leads to the internal transverse relaxation,

$$\tilde{\varepsilon}^{t,n}_{i} = \eta^{t,n}_{i} + M^{t,n}_{ij}\sigma^{t}_{j} - Q^{t,n}_{i\alpha\beta}\varepsilon^{s}_{\alpha\beta} \quad , \tag{4.89}$$

with $\eta^{t,n}_{i}$, $M^{t,n}_{3j3k}$ and $Q^{n}_{i\alpha\beta}$ given in Appendix C.

4.3.2.5 Interface Elastic Properties

When applying in-plane deformations $\varepsilon^{s}_{\alpha\beta}$ and transversal (out-of-plane) stresses σ^{t}_{j} to the atomic ensemble of interest, the atomic level in-plane stress $\sigma^{s,n}_{\alpha\beta}$ is given by,

$$\sigma^{s,n}_{\alpha\beta} = \pi^{n}_{\alpha\beta} + C^{s,n}_{\alpha\beta\kappa\lambda}\varepsilon^{s}_{\kappa\lambda} + Q^{n}_{i\alpha\beta}\sigma^{t}_{i} \quad , \tag{4.90}$$

While the transversal relaxation $\tilde{\varepsilon}^{t,n}_{k}$ is given by equation (4.89).

The derivations and detailed expressions for $\pi^{n}_{\alpha\beta}$, $C^{s,n}_{\alpha\beta\kappa\lambda}$, and $Q^{n}_{i\alpha\beta}$ are presented in Appendix C. Note that the in-plane atomic level modified stiffness tensor $C^{s,n}_{\alpha\beta\kappa\lambda}$ accounts for the transverse effects and should not be confused with the in-plane components of the atomic level stiffness tensor $\overline{C}^{s,n}_{\alpha\beta\kappa\lambda}$ of equation (4.83).

Similarly, far away from the interface region, when in-plane deformations $\varepsilon_{\alpha\beta}^{s}$ and transversal (out-of-plane) stresses σ_j^t are applied to an atomic ensemble (which can be considered as a perfect crystal), the bulk in-plane stress $\sigma_{\alpha\beta}^{bulk,s}$ is determined by,

$$\sigma_{\alpha\beta}^{bulk,s} = \left(C_{\alpha\beta\kappa\lambda}^{bulk} - C_{\alpha\beta 3j}^{bulk} S_{3i3j}^{bulk} C_{3i\kappa\lambda}^{bulk}\right)\varepsilon_{\kappa\lambda}^{s} + C_{\alpha\beta 3j}^{bulk} S_{3i3j}^{bulk} \sigma_i^t \quad , \tag{4.91}$$

where the derivations and detailed expressions for C_{ijkl}^{bulk}, and S_{i3j3}^{bulk} are presented in Appendix B.

With equations (4.90) – (4.91), we are now ready to evaluate the interfacial stress $\mathbf{\Sigma}^s$ and interfacial strain $\mathbf{\Delta}^t$. Combining equations (4.90) with (4.91) leads to the "excess" in-plane stress for an atom *n*,

$$\begin{aligned}\sigma_{\alpha\beta}^{s,n} - \sigma_{\alpha\beta}^{\pm s} = \pi_{\alpha\beta}^{n} &+ \left[C_{\alpha\beta\kappa\lambda}^{s,n} - \left(C_{\alpha\beta\kappa\lambda}^{\pm} - C_{\alpha\beta 3j}^{\pm} S_{3i3j}^{\pm} C_{3i\kappa\lambda}^{\pm}\right)\right]\varepsilon_{\kappa\lambda}^{s} \\ &+ \left[Q_{i\alpha\beta}^{n} - C_{\alpha\beta 3k}^{\pm} S_{3i3k}^{\pm}\right]\sigma_i^t\end{aligned} \quad . \tag{4.92}$$

In all these expressions, the positive (or negative) sign should be selected if atom *n* is in the upper (or lower) crystal. The interfacial excess in-plane stress is thus determined by,

$$\Sigma_{\alpha\beta}^{s} = \frac{1}{A_0}\sum_{n=1}^{N}\Omega_n\left(\sigma_{\alpha\beta}^{s,n} - \sigma_{\alpha\beta}^{\pm s}\right) = \Gamma_{\alpha\beta}^{(1)} + \Gamma_{\alpha\beta\kappa\lambda}^{(2)}\varepsilon_{\kappa\lambda}^{s} + H_{i\alpha\beta}\sigma_i^t \quad , \tag{4.93}$$

where A_0 is the area of the interface concerned, and

$$\Gamma_{\alpha\beta}^{(1)} = \frac{1}{A_0}\sum_{n=1}^{N}\Omega_n\pi_{\alpha\beta}^{n} \quad , \tag{4.94}$$

$$\Gamma_{\alpha\beta\kappa\lambda}^{(2)} = \frac{1}{A_0}\sum_{n=1}^{N}\Omega_n\left[C_{\alpha\beta\kappa\lambda}^{s,n} - \left(C_{\alpha\beta\kappa\lambda}^{\pm} - C_{\alpha\beta 3j}^{\pm} S_{3i3j}^{\pm} C_{3i\kappa\lambda}^{\pm}\right)\right] \quad , \tag{4.95}$$

$$H_{i\alpha\beta} = \frac{1}{A_0}\sum_{n=1}^{N}\Omega_n\left[Q_{i\alpha\beta}^{n} - C_{\alpha\beta 3k}^{\pm} S_{3i3k}^{\pm}\right] \quad . \tag{4.96}$$

Similarly if we consider the transverse excess strain given by (4.89), the interfacial excess transverse strain is given by,

$$\Lambda_k^t = \frac{1}{A_0}\sum_{n=1}^{N}\Omega_n\tilde{\varepsilon}_i^{t,n} = \Lambda_k^{(1)} + \Lambda_{kj}^{(2)}\sigma_j^t - H_{k\alpha\beta}\varepsilon_{\alpha\beta}^s \quad , \tag{4.97}$$

where

$$\Lambda_k^{(1)} = -\frac{1}{A_0}\sum_{n=1}^{N}\Omega_n\eta_j^{t,n} \quad , \tag{4.98}$$

$$\Lambda_{kj}^{(2)} = \frac{1}{A_0}\sum_{n=1}^{N}\Omega_n M_{3j3k}^{t,n} \quad . \tag{4.99}$$

These are the analytical expressions of the interfacial elastic properties. Note that, for a given inter-atomic potential function $E^{(n)}$, numerical evaluation of the analytical expressions (4.94) – (4.99) requires knowledge of the relaxed state of the interface. To obtain $\hat{r}^{mn}$, a preliminary molecular static simulation may be conducted. This is why we called the method developed here semi-analytical.

4.4 Surface Elastic Properties of Cu, Ni, Ag and Pd Free Surfaces

In this section, the surface elastic properties of Cu, Ni, Ag and Pd are computed using the semi-analytical method developed in the previous section. The EAM of Daw and Baskes(Daw and Baskes, 1983; Daw and Baskes, 1984) was used in the computation. Explicit expressions of $A^{(n)}$, $A_{ij}^{(n)}$, and $A_{ijkl}^{(n)}$ for this EAM are given in Appendix A.

4.4.1 Computational Framework and Results

To obtain the inter-atomic spacing $\hat{r}^{mn}$ at the relaxed state, a MS simulation was conducted. The initial unrelaxed configuration was constructed by rotating a perfect crystal lattice about an axis by a proper angle to arrive at the desired surface orientation in a rectangular simulation cell with the top surface of the cell being $x_3 = 0$. In the plane

of the surface of interest, periodic boundary conditions have been used to mimic an infinite surface. In the direction perpendicular to the surface, the slab is made sufficiently thick (more than 40 layers) to ensure that the results are independent of the thickness of the computational cell. The interactions between atoms are calculated up to the third nearest neighbor by truncating the EAM potential at the appropriate distance. The reduced coordination of atoms near the free surface induces a redistribution of electronic charges, which alters the binding situation. Consequently, atoms near the surface relaxed, i.e., they have moved away from the perfect crystal lattice and changed their energy. By minimizing the potential energy of the system, the most probable (relaxed) configuration can be obtained, which yields $\hat{r}^{mn}$. A nonlinear conjugate gradient method(Fletcher and Reeves, 1964) was used to minimize the energy of the system.

Once $\hat{r}^{mn}$ is known, the coefficients $A^{(n)}$, $A_{ij}^{(n)}$, and $A_{ijkl}^{(n)}$ can be evaluated from (A3) – (A5). Subsequently, the intrinsic surface energy density, intrinsic surface stress and surface elastic tensors can be easily obtained from (4.67) – (4.69). Following these steps, three low-index surfaces, (100), (110), and (111) of Cu, Ni, Ag and Pd were considered and their surface properties are presented in Table 4.1. Previously published results (Daw and Baskes, 1984; Ackland and Finnis, 1986; Ackland *et al.*, 1987; Gumbsch and Daw, 1991; Mansfield and Needs, 1991; Needs *et al.*, 1991; Fiorentini *et al.*, 1993; Feibelman, 1995) on Γ_0 and $\Gamma_{11}^{(1)}$ (referred to as the surface energy and surface stress, respectively, in the literature) are also listed next to ours. Our results seem to agree with those available in the open literature, although it is not clear whether the existing data are expressed in the Lagrangian or Eulerian frame. Schmid (1995) and Shenoy (2005) appear to be the only ones referring to surface elasticity in a somewhat different way.

In order to verify those calculations, we have also performed a strain meshing of the calculation cell with strains in the two planar directions ranging from -1% to 1% and

incremented by ±0.01% strain steps. The initial simulation cell consists of two horizontal planes oriented in the desired direction as shown in Figure 4.3(a). Periodic boundary conditions are used in the two planar directions with free surfaces in the vertical direction to mimic an infinite plane.

The atomic interaction is prescribed through the EAM potential. By varying the number of layers of atoms in the vertical direction we can represent thin films of different thicknesses. The slab thickness must be chosen to be thick enough to avoid interaction between the two surfaces. The film is stretched by independently varying the lattice constants along the two planar directions, while atoms in the third direction can fully relax. A conjugate gradient method is used to minimize the total energy of the system. For each calculation, strains along the horizontal directions are fixed and atoms are fully relaxed under this constraint. Prior to any deformation, the first step of the calculation is to determine the self equilibrium state of the films. This state corresponds to the lowest energy state of the film in the $\varepsilon_{11} - \varepsilon_{22}$ strain space. The self equilibrium state serves as a reference configuration for the nanoplate.

The procedure just described yields to a mesh of the total strain energy of the sample with respect to the reference configuration. The surface free energy, w_n, of a near surface atom is obtained by taking the difference between its total energy and that of an atom deep in the interior of a large crystal following equation (4.2). The general steps of the calculation can be outlined as follows:

(a) Create the initial assembly using the given material properties (atomic weight, lattice spacing, EAM potential, crystallographic orientation, etc.).

(b) Equilibrate the assembly to find the self equilibrium state.

(c) Apply a small strain field, $\varepsilon^s_{\alpha\beta}$, to the assembly and re-equilibrate.

(d) Compute the surface energy density corresponding to this given strain field.

(e) Increase the magnitude of $\varepsilon^s_{\alpha\beta}$ and repeat steps (c) and (d).

After repeating steps (c) – (d) a sufficient number of times, we obtain a mesh of Γ as a function of surface strains, $\varepsilon^s_{\alpha\beta}$ as seen in Figure 4.3(b.1) and Figure 4.3(b.2). Through curve fitting, the coefficients $\Gamma^{(0)}$, $\Gamma^{(1)}_{\alpha\beta}$, $\Gamma^{(2)}_{\alpha\beta\kappa\lambda}$ ... can be determined. Results obtained using this "meshing" method are in good agreement with the semi-analytical method presented in section 4.3.1 as seen from Table 4.2.

4.4.2 Surface Elastic Properties of Transition Metals

For discussion in terms of properties of the potentials and comparison of materials, we used reduced units for the surface elastic constants which are defined as the ratio of surface energy to the bulk cohesive energy(E_c) multiplied by the surface atomic packing density ($d_{(hkl)}$) in the case of the intrinsic surface energy and surface stress (Γ_0, $\Gamma_{\alpha\beta}$), and defined as the surface elastic modulus of interest divided by the corresponding bulk elastic modulus multiplied by the lattice constant. Figure 4.4 and Table 4.3 summarize the atomic surface density and constants used.

For tensile elastic properties we define the biaxial modulus for the bulk as,

$$Y_{bulk} = \frac{1}{2}\left(\frac{\partial^2 E}{\partial \varepsilon^2}\right)\Bigg|_{\varepsilon_{11}=\varepsilon_{22}=\varepsilon,\sigma_3=0} = \frac{1}{2}\left(C_{1111} + C_{2222} + 2C_{1122}\right) \quad . \tag{4.100}$$

And the respective biaxial modulus for the surface is defined as,

$$Y_{surf} = \frac{1}{2}\left(\frac{\partial^2 \Gamma}{\partial \varepsilon^2}\right)\Bigg|_{\varepsilon_{11}=\varepsilon_{22}=\varepsilon,\sigma_3=0} = \frac{1}{2}\left(\Gamma_{1111} + \Gamma_{2222} + 2\Gamma_{1122}\right) \quad . \tag{4.101}$$

For the in-plane shear elastic properties we define the shear modulus for the bulk as,

$$G_{bulk} = \frac{1}{2}\left(\frac{\partial^2 E}{\partial \varepsilon_{12}{}^2}\right)\Bigg|_{\varepsilon_{13}=\varepsilon_{23}=0} = 2C_{1212} \quad . \tag{4.102}$$

And the respective shear modulus for the surface is defined as,

$$G_{surf} = \frac{1}{2}\left(\frac{\partial^2 \Gamma}{\partial \varepsilon_{12}{}^2}\right) = 2\Gamma_{1212} \quad . \tag{4.103}$$

In all the figures the materials are ordered according to their atomic number. Data presented in this way are useful to qualitatively compare different metals and observe general trends.

As mentioned earlier and shown as an example for silver in Figure 4.5, the first point to note is that surface energy and surface stresses are not only localized at the surface layer but rather continue for several layers near the surface (this is also true for the higher order surface elastic constants). The surface has therefore a physical thickness that extends up to the point where the excess quantity considered vanishes. The concept of dividing surface casts these discrete "layered" quantities (it can be either the surface energy or the surface elastic constants) into one single thermodynamic quantity located at a dividing surface of zero thickness. The method presented above has the advantage of calculating the average quantity individually (for each atom *n*) and evaluating separately the average quantity considered for each layer. Most of the surface excess quantity is found to reside in the top layer of atoms, with approximately 10 to 15 percent in the second layer and a few percent (1 to 3%) in the third layer.

The results for surface energy are presented in Figure 4.6. For all the modeled materials, the close-packed (111) surfaces have the lowest intrinsic energy Γ_0, followed by the (100) and the (110) surfaces. The order of magnitude of the surface energy can be estimated from the number of nearest neighbors. Atoms in the first layer have 9, 8 and 7 neighbors for (111), (100) and (110) surfaces. The (111) surface is the most close-packed of the three basal planes for FCC crystals. The (110) surface is the most open of the three basal planes for FCC.

When a perfect crystal lattice is cut to create a free surface, the resulting unrelaxed surface is stressed both in the perpendicular direction and in the in-plane direction; while the perpendicular stresses are eliminated by inward relaxation of the

surface, residual in-plane stresses still reside on the surface. As shown in Figure 4.7, all the surfaces, are subjected to a tensile stress (stresses are positive) and do not bear any shear stress at equilibrium (the Γ_{12} coefficients are equal to zero). The residual surface stresses respect the symmetry of the surface orientation. Surface stress increases with "openness" of the surface. As a general trend, we can notice that the (110) surfaces present the highest surface stress while the (111) seem to sustain the lowest stresses.

Upon deformation, a surface will respond differently from its bulk counterpart. The surface response will increase or decrease the amount of surface stresses stored. As we can see in Figure 4.8, the biaxial surface modulus is always weaker/softer than its corresponding bulk. The (110) surface has a negative biaxial surface modulus. This does not contradict our common knowledge of classical elasticity. Given equation (4.69), the surface elastic constants can in principle be negative. In the particular case of the (110) surface, the surface stresses tend to decrease as tensile strains are applied. This is a direct consequence of the through-and-ridge structure of the (110) surfaces, which reduces its resistance in the transverse direction ([100] close-packed direction) to the rows of atoms. Another interesting remark concerns the more close-packed surfaces. Figure 4.8 clearly shows that, in the case of palladium and silver, close-packed surfaces have nearly zero surface elasticity compared to the bulk, which means in consequence that the stress/strain ratio of the surface is the same as the bulk.

Similar to tensile deformation, when a surface is sheared, its elastic response will differ from the bulk. The surface shear moduli in reduced units for the modeled materials are presented in Figure 4.9. We should note that, for all surface orientations, as the surface is sheared, surface shear stresses decrease. This comment is the most compelling for (110) surfaces.

4.4.3 Surface Relaxation

A surface that is formed at low temperatures, by cleavage for example, may essentially retain its bulk configuration with small displacements or relaxations as the atoms in the vicinity of the surface move away from the ideal surface positions of a perfect mono-atomic crystal lattice as indicated in Figure 4.10.

It is expected that the displacement of the layers near the surface will decrease rapidly with depth into the crystal. Our calculations show in fact that the surface relaxation extends about 3 layers underneath the surface. The results obtained from the equilibration process are summed up in Table 4.4.

The general trend of the results is that the surface layer is displaced by a few percent and the displacement rapidly decreases with the layer number. Note that the smallest relaxation strains are measured for the most closely packed surfaces. For all the (111) and (100) surfaces, the total relaxation is relatively small and close to zero, while the (110) surfaces exhibit a total relaxation ranging from 1 to almost 4 percent and a relaxation of the first interlayer ranging from 2 to 12 percent. On all the (110) surfaces, an alternation of the relaxation has been observed, with a contraction of the first and third interlayer and an expansion of the second interlayer.

This has already been widely observed in the literature(Ackland and Finnis, 1986; Ackland *et al.*, 1987; Todd and Lynden-Bell, 1993). Comparison with available results shows that a good qualitative agreement is obtained for all the materials studied. However, self-equilibrium calculations always predict a smaller relaxation than the compared results. This is mainly because Todd and coworkers used the Sutton-Chen potentials which have a longer range part. These results might change when it comes to the reconstruction phenomenon. All the results presented in this paper are for unreconstructed surfaces, but it has been reported for example that clean (111) oriented Pt surfaces reconstruct above 0.65 T_m, where T_m is the melting temperature (Sandy *et al.*, 1992). A $23 \times \sqrt{3}$ reconstruction has been observed in Au(111) that can be described as

an insertion of an extra row every 23 rows on the surface (Harten *et al.*, 1985; Needs, 1991). The stability of these reconstructions has not been investigated in the scope of this work.

In order to study the effects of relaxation on the surface elastic constants, we used the semi-analytical method presented in section 4.3.1 to calculate the surface elastic properties, such as the intrinsic surface energy density, intrinsic surface stress and surface elastic stiffness for unrelaxed surfaces. The results are presented in Table 4.5.

We can observe from Figure 4.11(a) that for all the studied materials and all three crystallographic orientations, the additional surface relaxations do not affect the value of the intrinsic surface energy Γ_0 in a significant manner. For copper, nickel and silver the change in surface energy when the surface relaxation strains are neglected is less than one percent. This can mainly be explained by the fact that the intrinsic surface energy is much more influenced by the local atomic configuration rather than by the electron redistribution.

The intrinsic surface stresses seem to follow the same trend for the close packed surfaces. As seen from Figure 4.11(b), the initial values of the Γ_{ii} do not change significantly when the surface relaxation is neglected and remain positive (tensile stress). But the surface relaxation seems to have some consequences on the intrinsic surface stresses of the (110) surfaces regarding the material considered. We observe a change of up to 40% in the magnitude in the case of silver. The reason for this is that the inward relaxation of the outer layers increases the local electron density towards the optimum (higher) value which is reached in the bulk and thus reduces the attractive part of the interaction forces between the atoms. Nevertheless the fact that residual stresses do not vary significantly indicates that these in-plane stresses are mainly due to the bonds within the top layer which do not change length upon relaxation.

Although the relaxations do not have a major effect on the surface energy and the intrinsic stresses (at least for the close-pack surfaces), they profoundly affect the surface

elastic stiffness properties. As seen from Figure 4.11(c), the most convincing case would be for palladium where the elastic constants change from 10 to 300% depending on the orientation. We note that the more closely packed the surface the less change in coefficients. Looking at the values of the elastic constants in detail, we can make an interesting observation by noting that the elastic constants Γ_{iiii} seem to be the most sensitive to relaxation for all three directions.

It has been clearly uncovered from these results the importance of accounting for the surface relaxation and its impact on the surface elastic properties. It is found that on one hand the relaxation effects do not or moderately affect the intrinsic surface energy and intrinsic surface stresses. On the other hand the elastic constants are strongly influenced by the relaxation.

4.5 Surface Elastic Properties for Grain Boundaries in Cu Bicrystals

In this section, the interfacial elastic properties of a couple of the so called "low-order CSL boundaries" (Kluge *et al.*, 1990; Wolf, 1990) for copper are computed using the semi-analytical method developed in section 4.3.

4.5.1 Computational Framework and Results

The procedure described in section 4.3.2 and in Appendix C allows us to evaluate exactly the elastic moduli of any coherent interface for any type of material/bimaterial interface. However, this method first requires the knowledge of the inter-atomic spacing $\hat{r}^{mn}$ at the relaxed state of the assembly. Molecular statics calculations with a nonlinear conjugate gradient algorithm are used to refine the initial interface structures. The tilt bicrystal interface model used in the energy minimization calculations is shown in Figure

4.1(a). The bicrystal containing the studied grain boundary is constructed using the geometrical rules of the Coincident Site Lattice (CSL). The interface misorientation is created by a symmetric tilt rotation of opposing lattice regions around a misorientation axis (Kluge *et al.*, 1990; Wolf, 1990). A certain number of initial starting positions are considered by parallel and perpendicular shifting to the interface plane to increase the probability of reaching the global minimum energy configuration of the interfacial structure studied (Kluge *et al.*, 1990). Periodic boundary conditions are prescribed in all directions. The in-plane periodicity is imposed by the CSL rules and relaxation of the structure occurs only in the direction perpendicular to the boundary plane. Therefore in the relaxed configuration, the transversal stress (in the sense of perpendicular to the boundary plane) is null. Note that the use of periodic boundary conditions in the transverse direction implicitly introduces a second interface at the edge of the calculation box with an identical structure as the interface at the center of atomic assembly. Calculations in this work are focused on the so called "low-order CSL boundaries" ($\Sigma 3$ and $\Sigma 5$). More specifically, we have studied symmetric tilt grain boundaries with the [100] and [110] rotation axis. The corresponding crystallographic parameters are summarized in Table 4.6. The interatomic used is a copper embedded-atom method (EAM) potential of Mishin *et al* (Mishin *et al.*, 1999; Mishin, 2001). For accuracy purposes, interface structures were compared with high resolution transmission microscopy micrographs of the studied grain boundary to ensure the correctness of the atomic structure. Following these steps, the surface properties of tilt interfaces with low-order CSL are presented in Table 4.7.

In order to partially validate those calculations, a comparison of the evolution of the excess interfacial energy upon transverse loading (no in-plane stretching) is made with full blown MD calculations performed by colleague Douglas Spearot. Results obtained by MD agree well with the semi-analytical method up to a critical threshold

stress corresponding to an elastic structural transition (see below) as seen from Figure 4.12.

4.5.2 Atomic Level Moduli for Grain Boundaries

The definition of the atomic level stress and the atomic level elastic constants introduced in section 4.3.2, naturally leads to the description of a heterogeneous medium composed of N different phases identified with each single atom of the atomic assembly. It therefore grants us a local map of the elastic properties in the interphase region.

As with the observations made for the free surfaces, we can remark in Figure 4.14 that the surface energy and surface stresses are not only localized at the interface plane between the two crystals but rather extend for several layers of atoms near the interface, hence reflecting the impact of the atomic rearrangement and internal relaxations. It is interesting to note that, although the interface "continuum" residual stresses are positive in the rotation axis X_1 while negative in the normal in-plane axis X_2, this is no longer the case at the atomic level where some atoms present a tensile state of stress while others present a compressive state of stress. This can be purely attributed to the local atomic arrangement and is highly dependent on both the atomic position and the internal relaxations acting on a specific atom.

In agreement with previous work by Nazarov and Sutton (Sutton and Vitek, 1983; Bachurin *et al.*, 2003), the interface structures of both Σ5 boundaries and the Σ3 are presented in Figure 4.13. While the Σ5 [100]/(310) and the Σ3 [110]/(111) boundaries have perfect symmetric structures after the energy minimization (see energy profile in Figure 4.14), the Σ5 [100]/(210) boundary is slightly asymmetric after energy minimization which is obvious in Figure 4.14(a), as the atoms in the layer directly below the interface ($h/\lambda>0$) have a slightly higher excess energy than the atoms in the layer directly above the interface ($h/\lambda<0$). Figure 4.13(b) shows this asymmetry in the

interface structure, as there is a lateral shift of the opposing atomic planes across the boundary. As confirmed in Figure 4.15, it is therefore expected to observe symmetry conditions in the interfacial properties of the Σ5 [100]/(310) and the Σ3 [110]/(111) and to observe no specific symmetry conditions in the case of the Σ5 [100]/(210) interface.

The diagonal elements of the tensor of the atomic level in-plane moduli, $C^{s,n}_{\alpha\beta\kappa\lambda}$ and transverse compliance $M^{t,n}_{3i3j}$ for the different boundaries studied here are displayed in Figure 4.15. The Voigt notation is adopted to represent the elastic moduli tensors and is normalized by the corresponding moduli in the bulk (ideal lattice configuration). It is seen that far away from the boundary, the atomic level moduli correspond to their bulk values, while they have significantly different values near the boundary region compared to those in the bulk. It is important to bear in mind that, although the elastic constants tensor in the ideal bulk configuration is characterized by only three elastic components (in the case of FCC metals), atoms lying in the grain boundary interphase do not necessarily present the same characteristics as their bulk counterparts and can display a general anisotropy therefore having twenty-one distinct components. Thus, the interphase region is generally not symmetric and the variation of the off diagonal terms can be significant. As already observed by Alber and Bassani, most of the elastic moduli are positive definite, i.e. the strain energy will always be positive at every strained point in the deformed body, but for a limited number of atoms the moduli are not positive definite, i.e. the local stability of the atomic structure may be stable for small perturbations but are unstable for larger perturbations and lead to lower energy structures by internal relaxation. This is consistent with the results from Spearot (Capolungo *et al.*, 2007) who observed an elastic structural transition upon transverse loading for the Σ5 (310) symmetric tilt grain boundary initiating at a critical threshold transverse stress (see Figure 4.12).

For discussion and comparison in terms of the properties of the different grain boundaries studied, as it is seen from Table 4.7, the first thing to be observed is that the lower the intrinsic surface energy Γ_0 (i.e. as the structure of an interface gets more similar to its bulk structure), the lower the magnitude of the interface properties.

When two perfect semi-infinite crystal lattices are put together to create a given interface, while the perpendicular stresses are eliminated by transverse inward relaxation of the surface, the resulting relaxed surface is stressed in both in-plane directions and leads to in-plane residual stresses $\Gamma_{\alpha\beta}^{(1)}$ residing on the interface plane. As shown in Table 4.7, all the studied interfaces are subjected to a tensile stress (stresses are positive) in the rotation axis and a compressive stress in the other in-plane direction. They do not bear any residual shear stress at equilibrium (the $\Gamma_{12}^{(1)}$ coefficients are equal to zero). Residual surface stress increases as the surface structure differs from its bordering bulk counterparts. Thus, it is with no surprise that we can observe that the Σ3 [110]/(111) have almost no residual surface stresses.

Upon deformation, an interface (considered as a dividing surface) will respond differently from its bulk counterpart. The surface response will increase or decrease the amount of surface stresses and surface strain stored in the interface. As we can see from Table 4.7, the in-plane moduli and transverse moduli are always weaker/softer than their adjoining bulk moduli. Although some of these moduli are negative, this does not contradict our common knowledge of classical elasticity. If we look closely at equations (4.14) – (4.24), the surface elastic constants can, in principle, be negative. In the particular case of both Σ5 tilt grain boundaries, the surface stresses would tend to decrease as tensile strains are applied (no transverse loading). Physically, this negative change in the surface stresses of both Σ5 tilt interfaces signifies that the interface structure relaxes as it is stretching in its plane. We hypothesize that this observation is a result of the special geometric constraints on the atomic structure of the Σ5(310) and

Σ5(210) interfaces which are entirely composed of either B' or C structural units (Sutton and Vitek, 1983). As indicated by the Poisson's effect tensor in Table 4.7, when the interface is stretched in its plane, the interface tends to internally relax and thus reduces its the interfacial stresses.

Comparable to tensile deformation, when an interface is sheared, its elastic respond will differ from the bulk. We should just note that, for all grain boundaries studied here, the surface shear moduli are always weaker/softer than their corresponding bulk moduli.

4.5.3 Interface Internal Relaxation

While the analysis in section 4.5.3 provides a wealth of information regarding the discrete elastic moduli in the interphase region, we did not cover information regarding the influence of the internal relaxation and its changes as a function of the applied loading. The definition of the atomic level internal relaxation introduced in section 4.3.2, confers on us a local mapping of the relaxation across the interphase region and a useful tool to quantitatively measure its impact on the interface properties.

Before presenting the above mentioned results, several points need to be mentioned first. As already confirmed by full blown MD calculations performed by Spearot (Capolungo *et al.*, 2007), no local in-plane relaxation is to be observed in the grain boundaries studied in this work. Only transverse internal relaxation occurs as the interface is deformed. Also, although it will not be discussed in the rest of this section, the interfacial in-plane shear modulus is not affected by the transverse internal relaxations. This comes from the fact that the in-plane shear components of the local Poisson's effect tensor $Q^n_{i\alpha\beta}$ are equally null.

When applying a macroscopically uniform loading $\left(\varepsilon^s_{\alpha\beta}, \sigma^t_i\right)$, the displacement of atoms in the atomic assembly studied can be divided to the homogeneous ones which are

linearly related to $\left(\varepsilon^{s}_{\alpha\beta}, \sigma^{t}_{i}\right)$ and to the inhomogeneous displacements resulting from the internal relaxations. If no internal displacement takes place, as, for example, in centro-symmetric structures, or if the internal relaxations are neglected, the methodology presented in section 4.3.2 can still be used to calculate the interface properties of interest. In order to study the effects of relaxation on the surface elastic constants, we used this semi-analytical method to calculate the surface elastic properties, such as the intrinsic surface energy density, intrinsic surface stress and surface elastic stiffness while ignoring the contribution of the internal relaxations. The results are presented in Table 4.8 and Figure 4.16.

As clearly shown in Figure 4.16, the internal transverse relaxations have a significant impact on the surface elastic properties regardless of the interface considered. In the case of the Σ5[100]/(310) and Σ5[100]/(210) tilt boundaries, we can observe that the omission of the internal relaxations renders the interface stiffer than it actually is when those are accounted for. While this stiffening is moderate in the case of the Σ5[100]/(310) interface, we observe a greater sensitivity on the interfacial properties of the Σ3[100]/(310) interface with a change up to 120% in magnitude in the case of biaxial surface modulus (introduced earlier in equation (4.101)). The reason for this can be mainly attributed to the fact that the Σ5[100]/(210) interface has an asymmetric structure. Looking at Figure 4.17 and the evolution of the internal relaxation upon biaxial stretching with no transverse loading, one can notice that the Σ5[100]/(210) interface tends to flatten out as it stretches and thus the boundary evolves toward a more symmetric configuration. Contrary to the Σ5 boundaries, the internal relaxations tend to stiffen the uniaxial behavior of the Σ3 (111) interface. A physical explanation could be attributed to the fact that this grain boundary has a structure really close to the bulk structure and therefore any atomic rearrangement can be seen as a stiffening mechanism rather than a relaxation mechanism.

While internal relaxations clearly play a role in the stiffening or softening of the elastic properties, a closer look at their variation on the atomic level gives a better understanding of the evolution of the interface structure during deformation. Figure 4.17 shows the internal relaxation profile for different loading configurations. Two loading configurations are considered. Figure 4.17(a) shows the evolution of the internal relaxations across the boundary upon pure transverse loading (no in-plane strains) and Figure 4.17(b) presents the evolution of the internal relaxation across the boundary upon a biaxial stretching (both in-plane directions are stretched equally, while no transverse loading is applied).

In the case of pure transverse loading, as seen in Figure 4.17, but also as suggested by the coefficients $\Lambda_{33}^{(2)}$ presented in Table 4.7, the average internal relaxation decreases as the transverse stress increases in the case of the Σ5[100]/(210) and the Σ3[110]/(111) interfaces while it is increasing in the case of the Σ5[100]/(310) boundary. Physically speaking, this simply means that the thickness of the Σ5 (310) increases upon transverse stretching with it tends to die out in the cases the Σ5 (210) and Σ3 (111). Interestingly enough, when examining the amplitude of the internal relaxation, one can notice that in all three cases it is decreasing as the load increases. It is especially relevant in the case of the Σ5[100]/(210) boundary as the internal relaxation across the interface tends to be more symmetric as the load increases.

Looking at the behavior of the interface upon pure biaxial loading, although it is not really obvious in Figure 4.17, but as it is suggested by the coefficients $H_{3\alpha\alpha}$ presented in Table 4.7, for all the boundaries studied, as the interface is stretched biaxially, its thickness is likely to die out (in the sense of reducing the internal relaxation). Similarly, when monitoring the amplitude of the internal relaxation, we can notice that, in the case of both Σ5, the amplitude increase as the interface is stretched, while it decreases in the case of the Σ3 grain boundary. This is simply due to the "near-

bulk-structure" of the Σ3 interface, since the stretching has a tendency to flatten its structural units.

4.6 Summary and Conclusions

The main purpose of this chapter revolves around the properties of interfaces considered as a single dividing surface (as opposed to an interphase with finite thickness).

We derived a new relationship between the interfacial excess energy and interfacial excess stress for coherent interfaces that is applicable to interfaces in elastic solids under general loading conditions. It is shown that the well-known Shuttleworth relationship between the interfacial excess energy and interfacial excess stress is valid only when the interface is free of transverse stresses. The new formulation accounts for both in-plane and transverse deformation of the interface, and naturally introduces the interfacial stiffness and compliance tensors, as well as the transverse interfacial excess strain. At the same time, the concept of transverse interfacial excess strain is also introduced, and a complementary Shuttleworth equation is derived that relates the interfacial excess energy to the newly introduced transverse interfacial excess strain. This new formulation of interfacial excess stress and excess strain naturally leads to the definition of an in-plane residual stresses tensor $\boldsymbol{\Gamma}^{(1)}$, an in-plane interfacial stiffness tensor $\boldsymbol{\Gamma}^{(2)}$, a transverse interfacial compliance tensor $\boldsymbol{\Lambda}^{(2)}$, and a coupling tensor $\mathbf{H}$ that accounting for the Poisson's effect of the interface, and that fully characterize the elastic behavior of coherent solid bimaterial interfaces upon deformation. It was shown that when both constituents of the bimaterial are isotropic, the interface is transversely isotropic. Explicit expressions of the interfacial tensors were derived for such transversely isotropic interface in terms of five elastic constants of the interface. The

consequences of this generalized Shuttleworth relationship allow us to establish the relationship between microscopic properties and mesoscopic properties of the interface.

Based on the idea of expanding the atomic energy and atomic stresses into power series of surface strains and transverse stresses and accounting for internal relaxation by appropriately incorporating the equilibrium and traction conditions across the interface, we presented semi-analytical methods to evaluate and calculate interfacial elastic properties. The theoretical framework of the generalized Shuttleworth relationship helps us to subsequently obtain analytical expressions for the interface elastic properties, such as the surface density, intrinsic surface stress and surface elastic stiffness and compliance. Basal free surfaces and low order CSL grain boundaries have been studied using this method in a uniform manner without modifications to the formulation. These methods are so called semi-analytical because they require knowledge of the relaxed configuration of the atomic assembly of interest in order to evaluate the interface properties.

In comparison with other existing methods, the semi-analytical methods developed here present several advantages compared with classical full blown atomistic calculations. They reduce the amount of computation significantly (~95% reduction in CPU time as compared to full blown atomistic techniques). They also directly give the full set of elastic properties and can be applied to any inter-atomic potential. More importantly, because of the analytical nature of these methods, they provide a much better understanding of the interface characteristics, providing a wealth of information on the connection between the atomic level and the continuum level, and they enable us to analytically evaluate the elastic response of any given interface under any given load without any further computation.

Finally by applying this tool to the unrelaxed structure we were able to quantitatively measure the impact of relaxation on the interface/surface properties. We have clearly uncovered from this analysis the importance of accounting for the surface

relaxation and its impact on the surface elastic properties. It is found that, as a general rule, relaxation softens the interface.

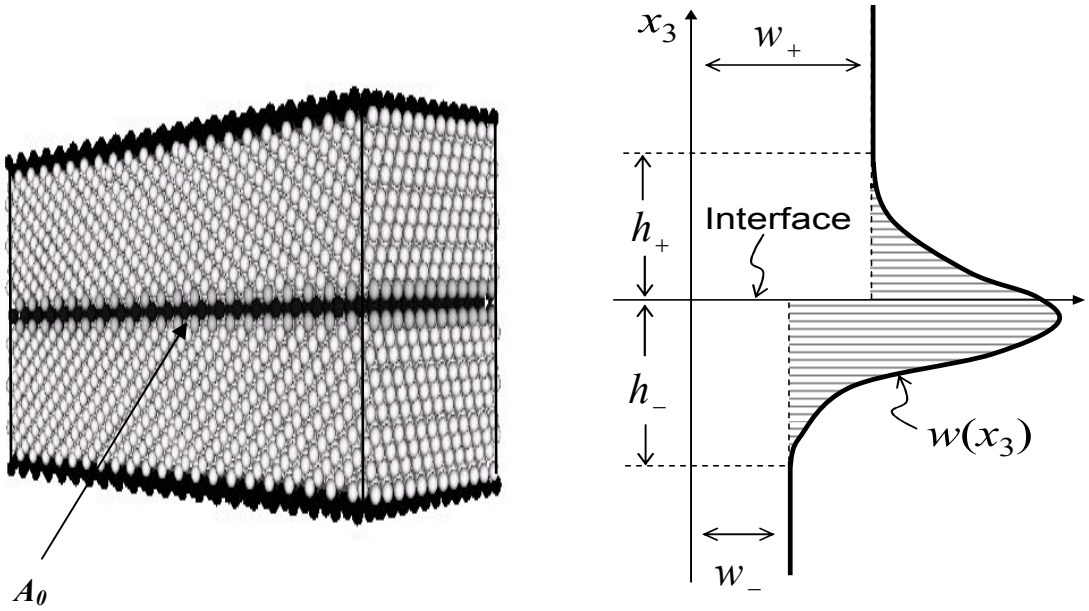

(a) (b)

Figure 4.1 (a) Flat interface of a bimaterial, (b) Interface excess energy as a function of the distance away from the interface

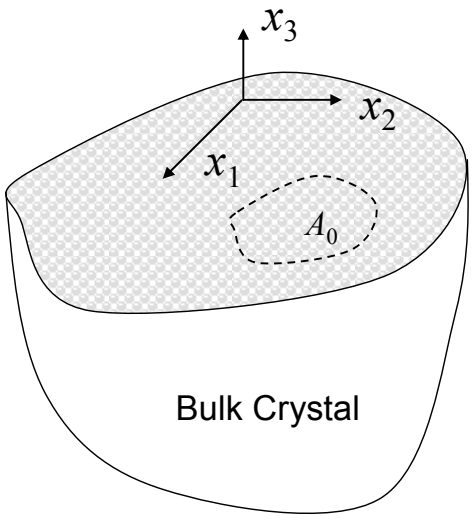

Figure 4.2 Semi-infinite crystal and its free surface

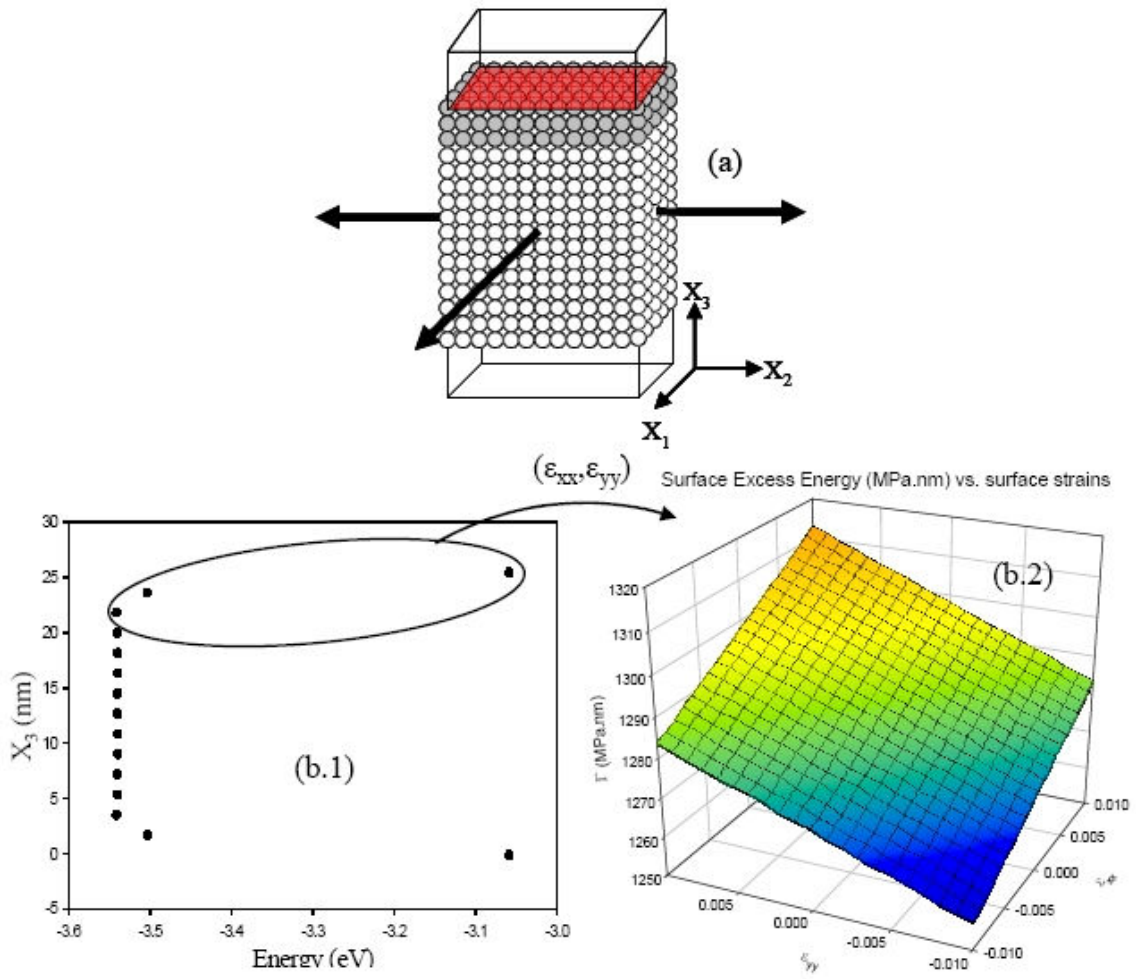

Figure 4.3 Schematic of the strain meshing process to calculate the surface excess energy and surface elastic constants

(111) **(100)** **(110)**

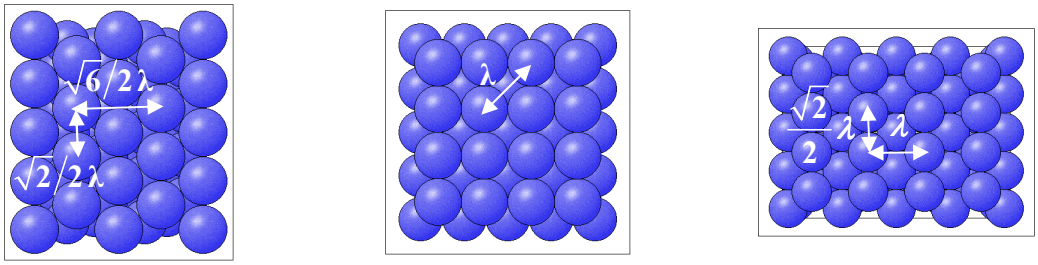

$$S_{(111)} = \frac{\sqrt{3}}{2}\lambda^2 \qquad S_{(100)} = \lambda^2 \qquad S_{(110)} = \frac{\sqrt{2}}{2}\lambda^2$$

$$d_{(111)} = \frac{4}{\sqrt{3}\lambda^2} \qquad d_{(100)} = \frac{2}{\lambda^2} \qquad d_{(110)} = \frac{\sqrt{2}}{\lambda^2}$$

Figure 4.4 Surface atomic packing density of basal FCC surfaces

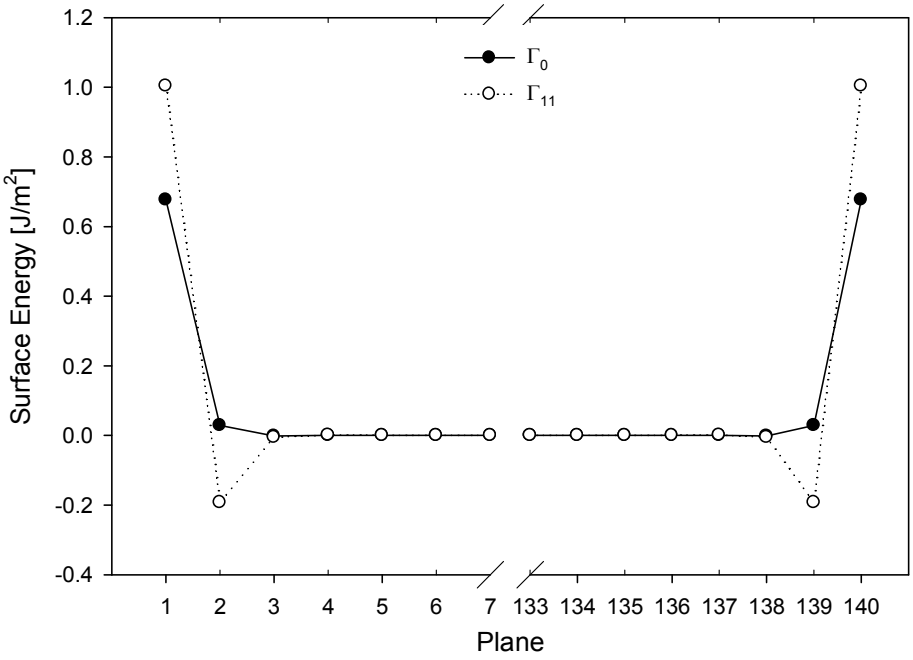

Figure 4.5 Layer decomposition of the intrinsic surface energy Γ_0 and surface stress Γ_{11} of Ag for a (100) surface orientation. The sum over half the thickness for Γ_0 is 0.703 J/m^2 and for Γ_{11} is 0.816 J/m^2

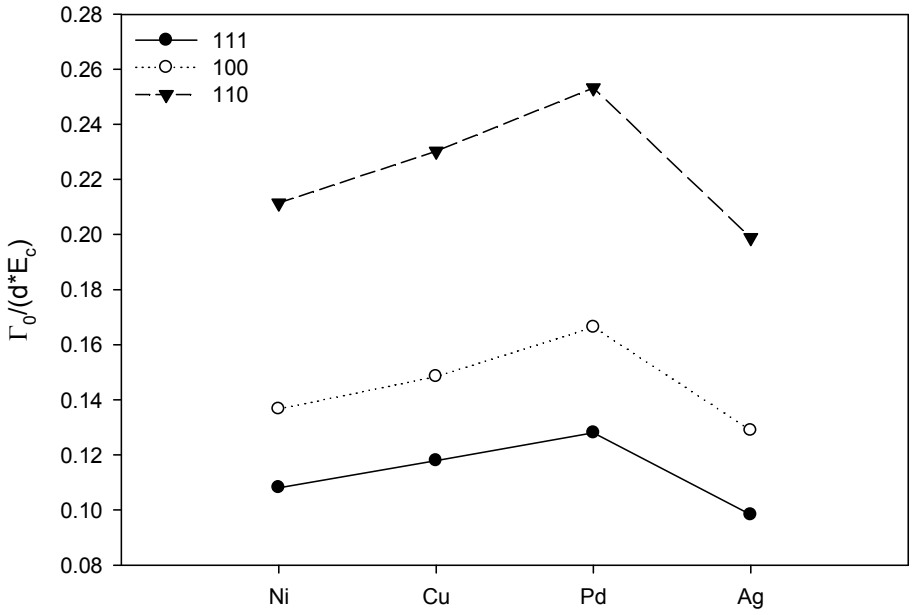

Figure 4.6 Intrinsic surface energy in reduced units (Surface energy/(surface packing density × bulk cohesive energy) for several metals. The (111) surface (filled circles), has the lowest energy compared to the (100) surface (plain circle) and the (110) surface (triangle)

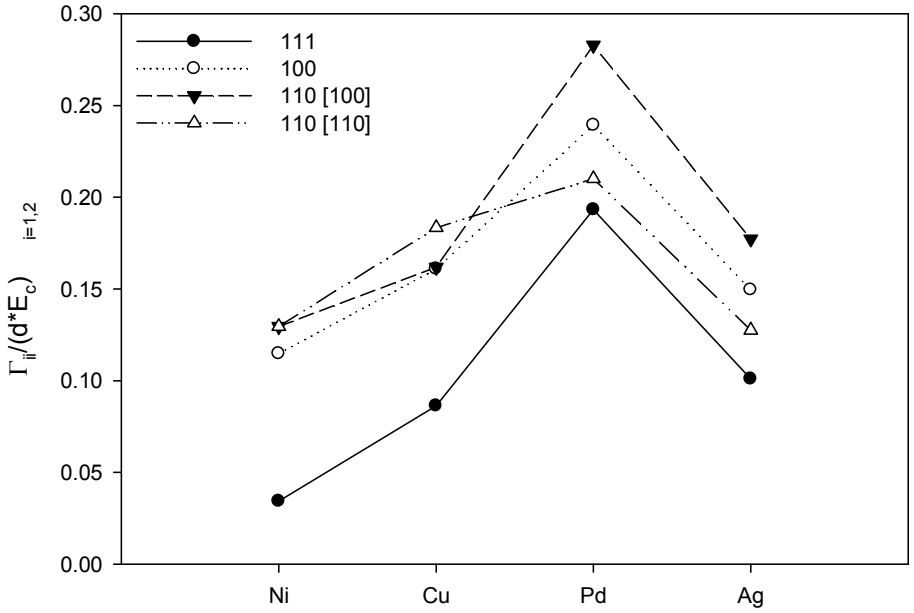

Figure 4.7 Internal surface stress (at zero surface strain) in reduced units (Surface energy/(surface packing density × bulk cohesive energy) for several metals. The (111) surface (filled circles), has the lowest residual stresses compared to the (100) surface (plain circle) and the (110) surface (triangle)

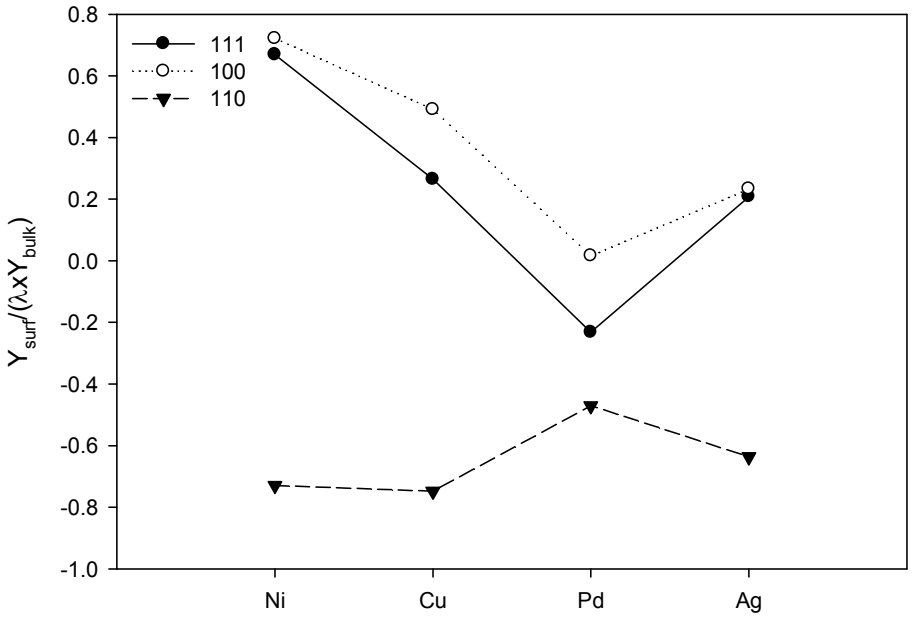

Figure 4.8 Tensile surface elasticity coefficients in reduced units (Surface elastic coefficient/(lattice constant × bulk elastic constant)

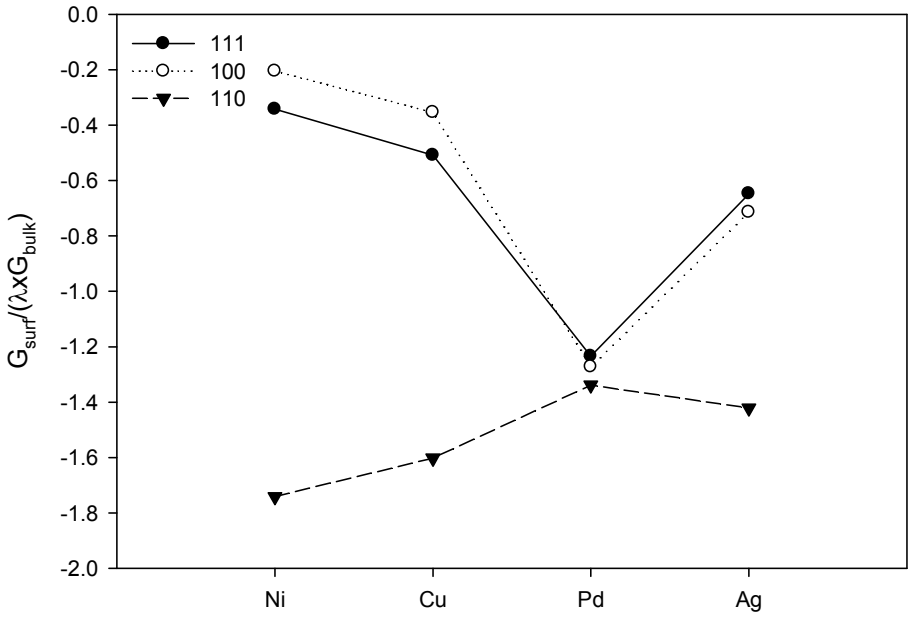

Figure 4.9 Shear surface elasticity coefficients in reduced units (Surface elastic coefficient/(lattice constant × bulk elastic constant)

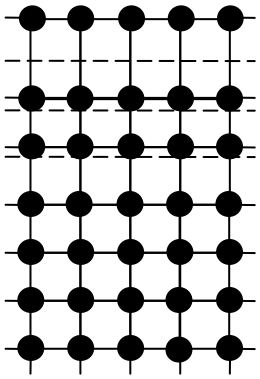

Figure 4.10 Possible displacements of atoms near the surface of a crystal. The dotted lines indicate the positions of the planes at an ideal lattice structure

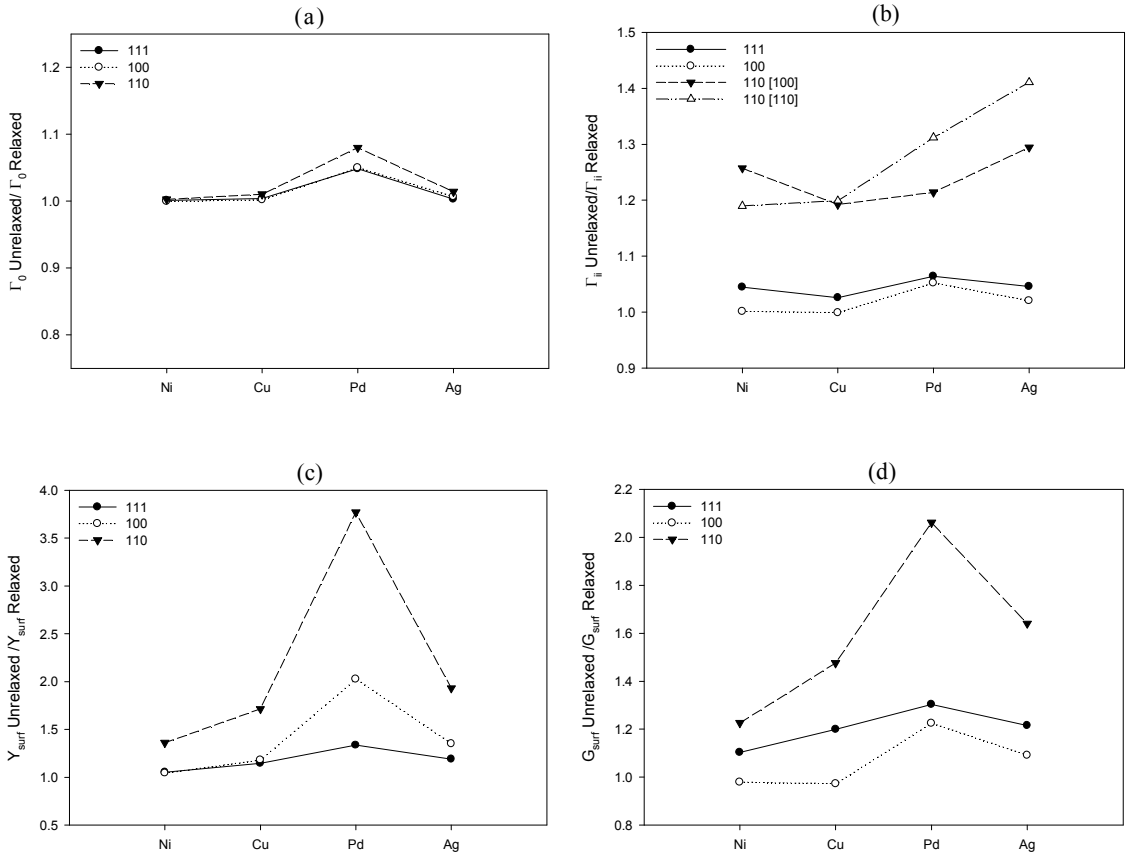

Figure 4.11 Effects of the surface relaxation on the elastic properties of low-index surfaces for several FCC metals such as (a) intrinsic surface energy density, (b) intrinsic surface stress, (c) surface biaxial modulus and (d) the surface shear modulus

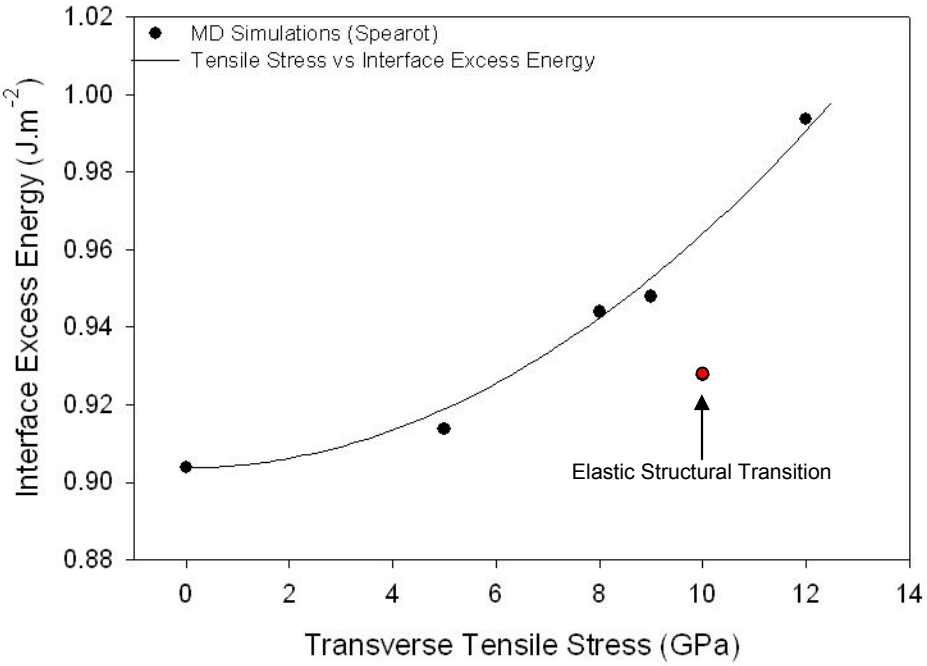

Figure 4.12 Comparison of the interfacial excess energy as a function of the applied tensile stress calculated from full blown MD calculations and from the semi-analytical method of section 4.3 for the symmetric tilt grain boundary Σ5 [100]/(310)

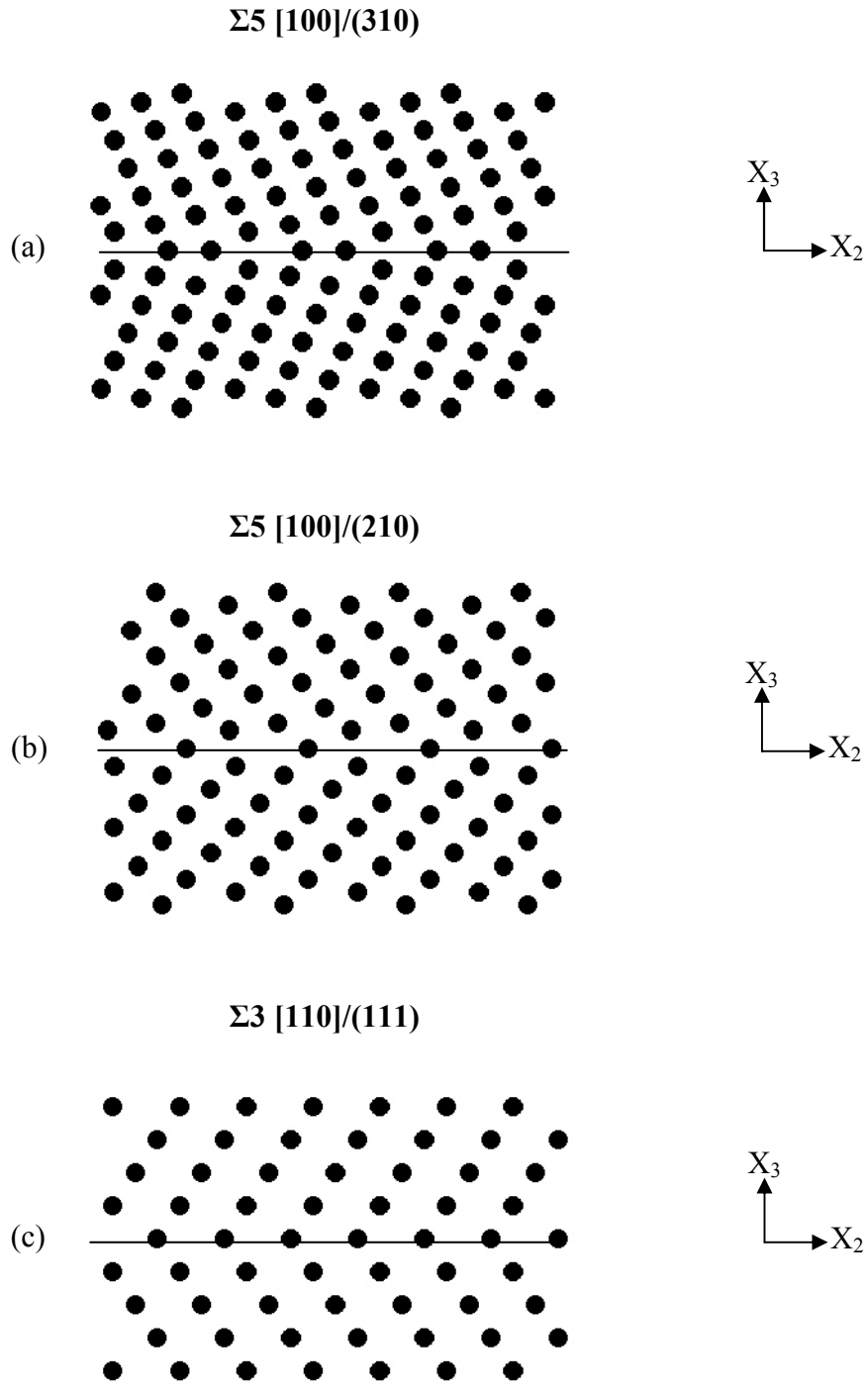

Figure 4.13 Bicrystal interface structures for copper interfaces (a) Σ5 [100]/(310) symmetric tilt grain boundary (b) Σ5 [100]/(210) symmetric tilt grain boundary (c) Σ3 [110]/(111) symmetric tilt grain boundary

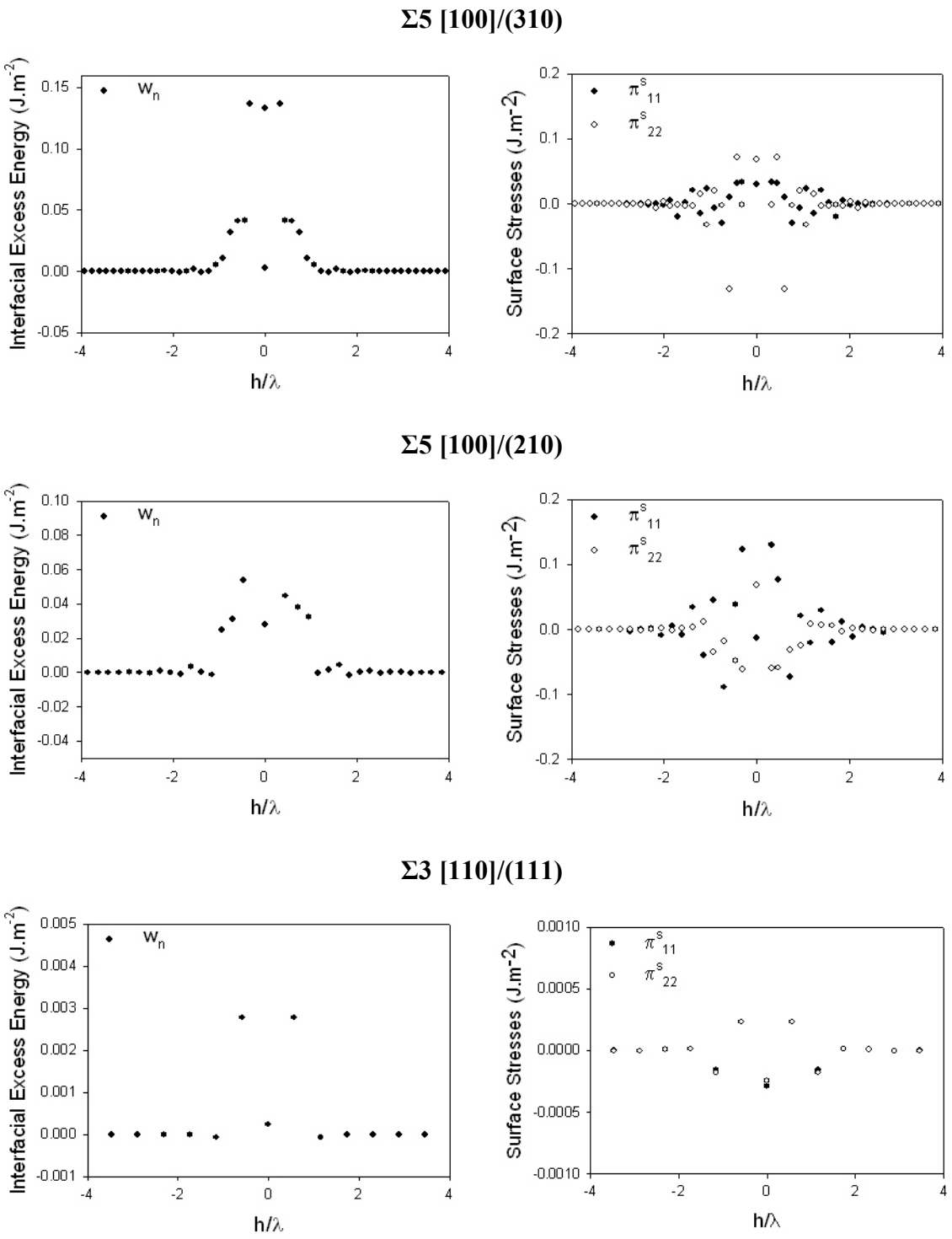

Figure 4.14 Layer decomposition of (a) the surface energy Γ_0 and (b) residual surface stress $\pi^s_{\alpha\alpha}$ for Σ5 [001]/(310), Σ5 [001]/(210) and Σ3 [110]/(210) symmetric tilt grain boundaries in copper

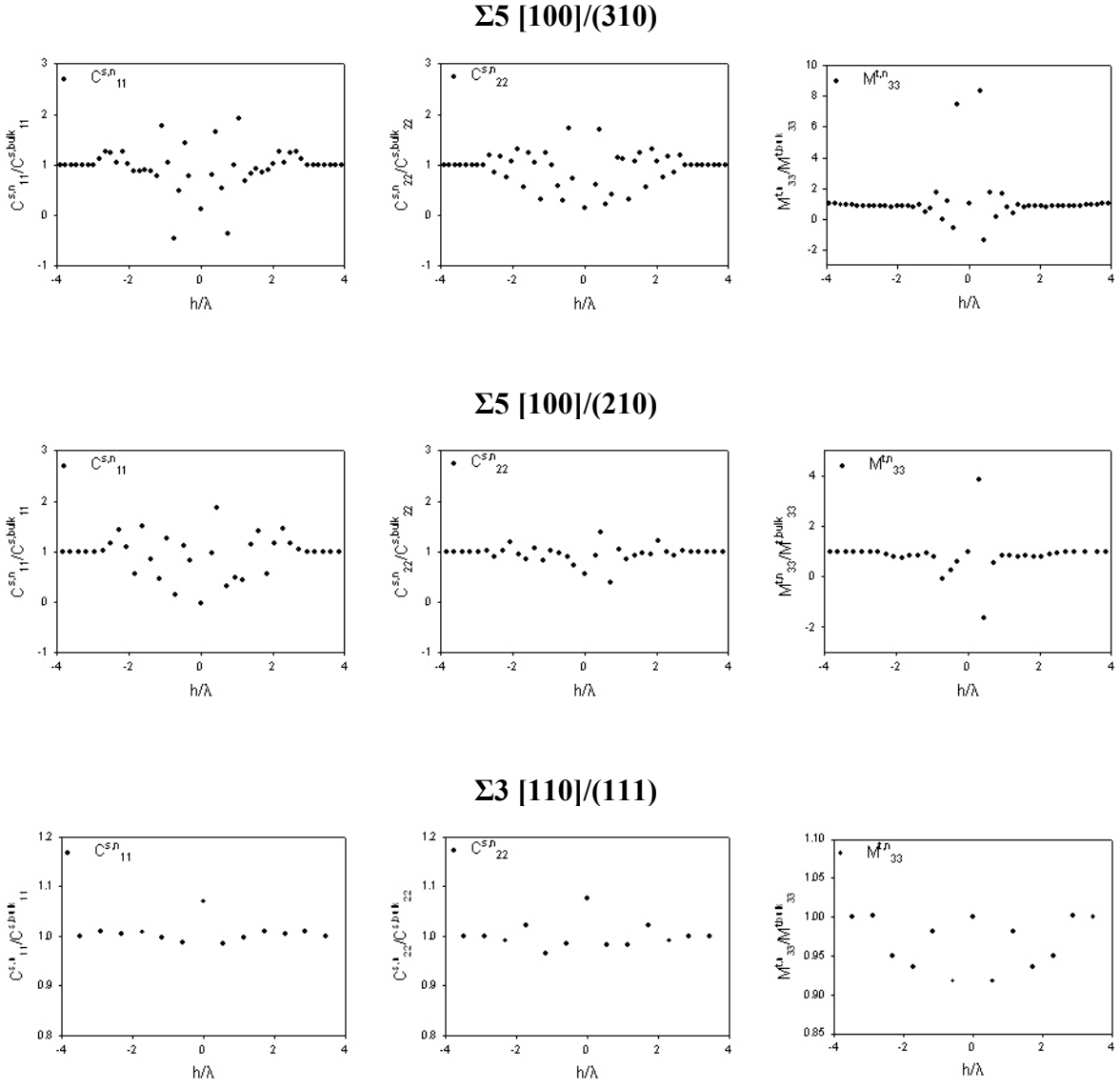

Figure 4.15 Normalized diagonal elements of the tensor of the atomic elastic moduli for Σ5 [001]/(310), Σ5 [001]/(210) and Σ3 [110]/(210) symmetric tilt grain boundaries in copper, (a) $C^{s,n}_{1111}/C^{s,bulk}_{1111}$, (b) $C^{s,n}_{2222}/C^{s,bulk}_{2222}$, (c) $M^{t,n}_{3333}/M^{t,bulk}_{3333}$

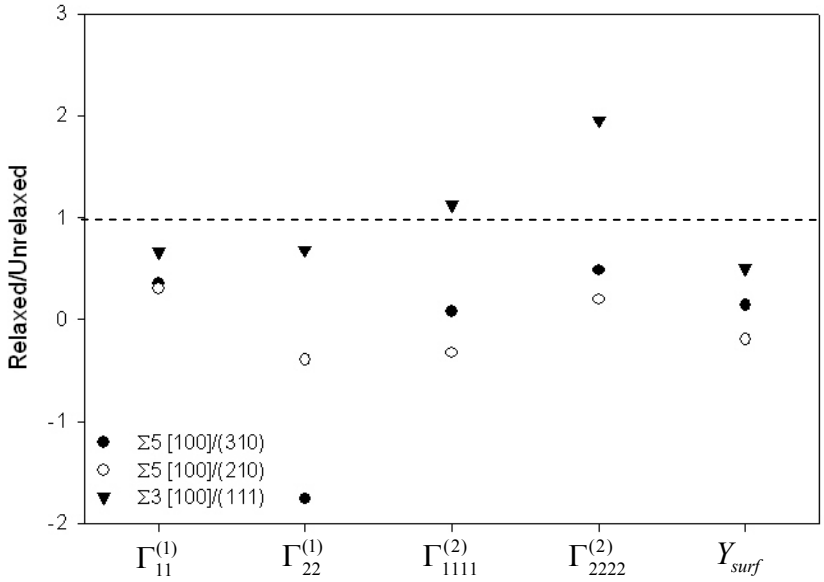

Figure 4.16 Effects of the interface internal relaxation on the elastic properties of low-CSL symmetric tilt grain boundary in copper

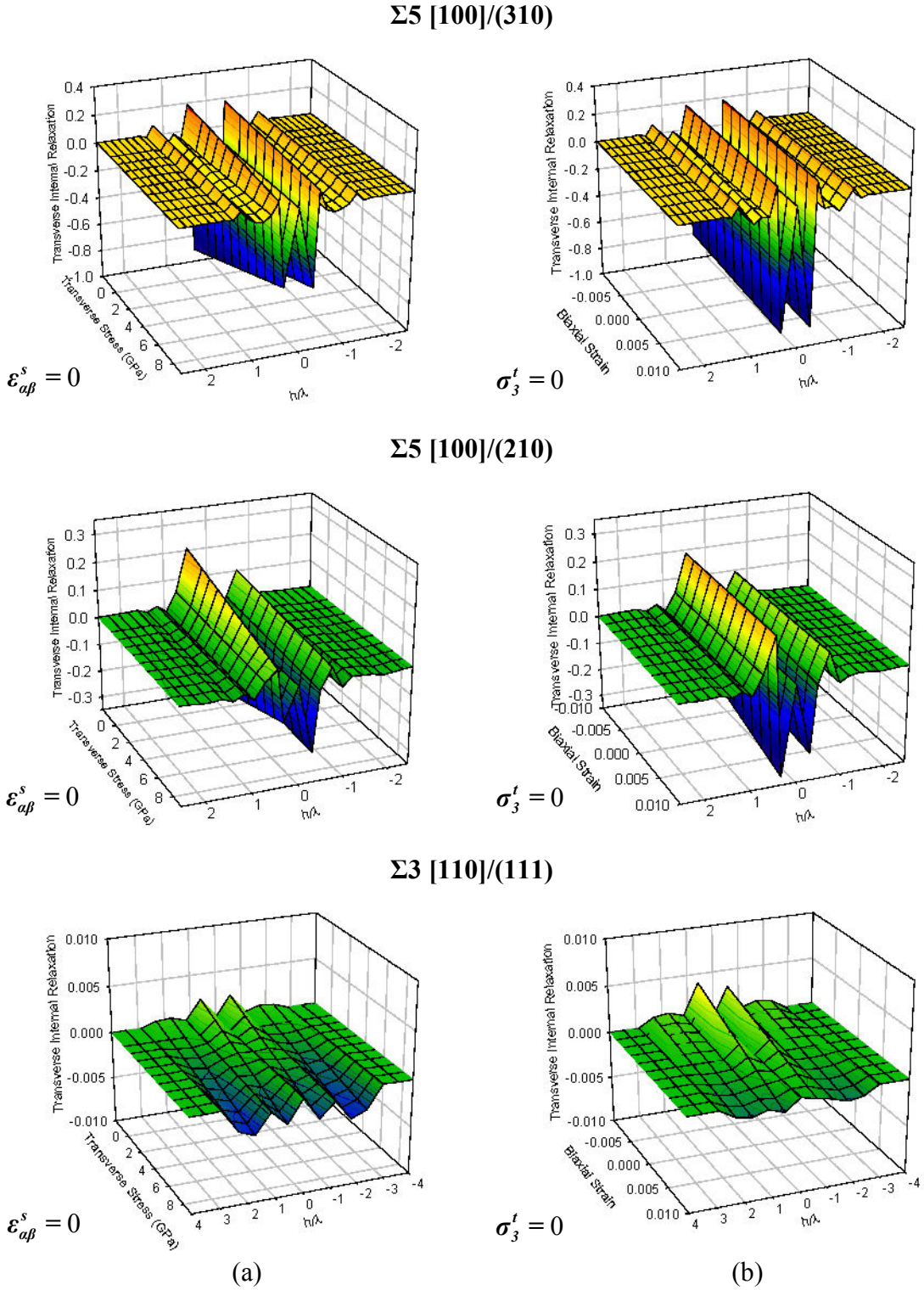

Figure 4.17 Layer decomposition of the transverse internal relaxtion $\tilde{\varepsilon}_3^{t,n}$ for different loading configuration: (a) transverse loading (b) biaxial stretching $\varepsilon^s = \varepsilon^s_{11} = \varepsilon^s_{22}$ for Σ5 [001]/(310), Σ5 [001]/(210) and Σ3 [110]/(210) symmetric tilt grain boundaries in copper

Table 4.1 Calculated surface elastic properties of low-index surfaces for several FCC metals. The unit used is $J.m^{-2}$

		Ni	Cu	Pd	Ag
(111)	Γ_0	1.436 (1.45)[a]	1.181 (1.17)[a]	1.224 (1.22)[a]	0.620 (0.62)[a]
	$\Gamma^{(1)}_{11}$	0.457 (0.43)[b]	0.866 (0.86)[b]	1.848 (3.73)[c]	0.636 (0.64)[b]
	$\Gamma^{(2)}_{1111}$	6.526	2.054	-2.914	0.888
	$\Gamma^{(2)}_{1122}$	3.986	1.086	-1.014	1.194
	$\Gamma^{(2)}_{1212}$	-1.188	-1.071	-2.354	-1.173
(100)	Γ_0	1.572 (1.58)[a]	1.288 (1.28)[a]	1.377 (1.37)[a]	0.703 (0.705)[a]
	$\Gamma^{(1)}_{11}$	1.321 (1.27)[b]	1.396 (1.38)[b]	1.981 (1.58)[e]	0.816 (0.82)[b]
	$\Gamma^{(2)}_{1111}$	-0.865	-0.712	-2.360	-1.245
	$\Gamma^{(2)}_{1122}$	10.722	5.914	2.611	3.343
	$\Gamma^{(2)}_{1212}$	-0.927	-0.992	-3.250	-1.666
(110)	Γ_0	1.721 (1.73)[a]	1.413 (1.40)[a]	1.482 (1.49)[a]	0.768 (0.77)[a]
	$\Gamma^{(1)}_{11}$ [001]	1.054 (0.707)[d]	1.126 (0.957)[d]	1.230 (1.859)[c]	0.492 (0.738)[d]
	$\Gamma^{(1)}_{22}$ [1$\bar{1}$0]	0.706 (0.707)[d]	0.993 (0.957)[d]	1.656 (2.740)[c]	0.684 (0.738)[d]
	$\Gamma^{(2)}_{1111}$	-13.031	-7.798	-4.775	-5.510
	$\Gamma^{(2)}_{2222}$	0.950	-2.263	-6.654	-2.246
	$\Gamma^{(2)}_{1122}$	-5.045	-3.600	-2.086	-2.332
	$\Gamma^{(2)}_{1212}$	-7.827	-4.436	-3.378	-3.296

[a] Reference (Foiles *et al.*, 1986) ; [b] Reference (Gumbsch and Daw, 1991)
[c] Reference (Feibelman, 1995) ; [d] Reference (Ackland *et al.*, 1987).

Table 4.2 Surface elastic properties of (100) surfaces for several FCC metals calculated by the strain meshing of the energy. The unit used is $J.m^{-2}$

	Ni	**Cu**	**Ag**
Γ_0	1.572	1.288	0.703
$\Gamma_{11}^{(1)}$	1.634	1.396	0.813
$\Gamma_{1111}^{(2)}$	-0.788	-1.280	-1.344
$\Gamma_{1122}^{(2)}$	13.383	6.384	3.699

Table 4.3 Bulk lattice constant (λ) and bulk cohesive energy (E_c)

	Ni	**Cu**	**Pd**	**Ag**
λ **(Å)**	3.52	3.615	3.89	4.09
E_c **(eV)**	-4.45	-3.54	-3.91	-2.85

Table 4.4 Surface relaxation for several FCC metals (in %)

		Ni	Cu	Ag	Pd
(111)	**Layer 1 (top layer)**	-0.54 (-2.1)[a]	-1.33 (-2.1)[a]	-1.34 (-1.1)[a]	-3.24 (-1.5)[a]
	Layer 2	-0.06	-0.06	0.01	0.24
	Layer 3	0.01	0.02	0.01	0.00
	Total	-0.20	-0.48	-0.44	-1.00
(100)	**Layer 1 (top layer)**	-0.25 (-2.9)[a]	-1.23 (-2.9)[a]	-1.85 (-1.1)[a]	-4.31 (-2.3)[a]
	Layer 2	-0.07	-0.21	-0.01	0.07
	Layer 3	0.03	0.12	0.05	0.20
	Total	-0.11	-0.44	-0.60	-1.35
(110)	**Layer 1 (top layer)**	-2.35 (-7.9)[a]	-4.73 (-7.9)[a]	-5.17 (-4.3)[a]	-11.37 (-5.8)[a]
	Layer 2	0.08	0.16	0.37	1.10
	Layer 3	-0.19	-0.52	-0.28	-0.79
	Total	-0.82	-1.70	-1.69	-3.68

[a] Reference (Todd and Lynden-Bell, 1993)

Table 4.5 Calculated surface elastic properties of low-index unrelaxed surfaces for several FCC metals. The unit used is $J.m^{-2}$

		Ni	Cu	Pd	Ag
(111)	Γ_0	1.4376	1.186	1.283	0.621
	$\Gamma_{11}^{(1)}$	0.477	0.888	1.966	0.665
	$\Gamma_{1111}^{(2)}$	6.868	2.310	-3.920	1.095
	$\Gamma_{1122}^{(2)}$	4.212	1.293	-1.330	1.386
	$\Gamma_{1212}^{(2)}$	-1.310	-1.285	-3.069	-1.424
(100)	Γ_0	1.572	1.291	1.446	0.708
	$\Gamma_{11}^{(1)}$	1.324	1.395	2.085	0.833
	$\Gamma_{1111}^{(2)}$	-1.038	-1.171	-3.988	-1.919
	$\Gamma_{1122}^{(2)}$	11.325	7.311	4.495	4.753
	$\Gamma_{1212}^{(2)}$	-0.907	-0.965	-3.979	-1.818
(110)	Γ_0	1.725	1.427	1.601	0.778
	$\Gamma_{11}^{(1)}$ [001]	0.888	1.184	2.010	0.886
	$\Gamma_{22}^{(1)}$ $[1\bar{1}0]$	1.254	1.350	1.614	0.695
	$\Gamma_{1111}^{(2)}$	0.381	-3.714	-19.554	-3.772
	$\Gamma_{2222}^{(2)}$	-16.727	-12.921	-16.125	-10.246
	$\Gamma_{1122}^{(2)}$	-6.909	-6.475	-11.560	-4.987
	$\Gamma_{1212}^{(2)}$	-9.593	-6.545	-6.966	-5.407

Table 4.6 Crystallographic characteristics of the symmetric tilt grain boundaries studied in this work

Σ	Misorientation Axis	Boundary Plane	Misorientation Angle
5	[001]	(310)	36.9º
5	[001]	(210)	53.1º
3	$[1\bar{1}0]$	(111)	109.5º

Table 4.7 Calculated interface elastic properties of low-CSL symmetric tilt grain boundaries for copper

	Σ5 [100]/(310)	**Σ5 [100]/(210)**	**Σ3 [110]/(111)**
In-plane (Units in $J.m^{-2}$)			
Γ_0	0.911	0.962	0.023
$\Gamma_{11}^{(1)}$ (tilt axis)	3.609	3.759	-0.004
$\Gamma_{22}^{(1)}$	-0.9888	-3.712	-0.004
$\Gamma_{1111}^{(2)}$	-10.679	-9.342	1.484
$\Gamma_{2222}^{(2)}$	-10.510	-15.931	0.465
$\Gamma_{1122}^{(2)}$	-14.908	-11.678	-0.120
$\Gamma_{1212}^{(2)}$	-2.489	0.862	1.472
Transverse (Units in nm for $\Lambda_3^{(1)}$ nm; $(100Gpa)^{-1}$ for $\Lambda_{22}^{(2)}$)			
$\Lambda_3^{(1)}$	-0.086	-0.012	0.001
$\Lambda_{11}^{(2)}$	0.494	0.243	0.080
$\Lambda_{22}^{(2)}$	-0.185	0.674	0.080
$\Lambda_{33}^{(2)}$	0.121	-0.193	-0.046
Poisson's Effect (Units in nm)			
H_{111}	0.0003	0.0002	0.000
H_{122}	0.0002	0.000	0.000
H_{211}	0.046	0.239	0.178
H_{222}	0.057	0.458	-0.089
H_{311}	0.350	0.364	0.039
H_{322}	0.618	0.904	0.168

Table 4.8 Calculated interface elastic properties of low-CSL symmetric tilt grain boundaries for copper without the effect of internal relaxation

	Σ5 [100]/(310)	**Σ5 [100]/(210)**	**Σ3 [110]/(111)**
In-plane (Units in $J.m^{-2}$)			
$\Gamma^{(1)}_{11}$ (tilt axis)	1.266	1.123	-0.003
$\Gamma^{(1)}_{22}$	1.737	1.452	-0.003
$\Gamma^{(2)}_{1111}$	-0.854	3.067	1.669
$\Gamma^{(2)}_{2222}$	-5.092	-3.158	0.908
$\Gamma^{(2)}_{1122}$	-0.657	4.758	-0.860
$\Gamma^{(2)}_{1212}$	-2.489	0.862	1.472

CHAPTER 5

FROM AN ATOMISTIC DESCRIPTION TO A CONTINUUM FRAMEWORK: SIZE-DEPENDENT ELASTICITY

In this chapter, we focus on developing a continuum framework that incorporates the surface properties into the analysis of the macroscopic deformation of nanostructured materials. In particular, we study the effects of surface properties on the effective modulus of nano-particles, nano-wires and nano-films as well as nanostructured crystalline materials. Based on this approach, it is demonstrated that the overall elastic behavior of structural elements (such as particles, wires and films) is size-dependent. Although such size-dependency is negligible for conventional structural elements, it is shown that the size effect becomes significant when at least one of the dimensions of the element shrinks to the nanometer range. Numerical examples are given to illustrate quantitatively the effects of the surface on the elastic properties of nano-size particles. Furthermore, the continuum model developed here clearly shows the influence of the third order elastic constants on the effective elastic stiffness of the nanostructural elements. Subsequently, the interfacial thermodynamic properties introduced in chapter 4 are used to formulate the interfacial conditions in a mesoscopic framework of polycrystals and nano-composites.

5.1 Introduction

Nanometer-scale / nanostructured materials are of great technological interest due to their potential applications in miniaturized electrical, optical, thermal and mechanical systems. A wide variety of micro-electromechanical systems (MEMS) and nano-

electromechanical (NEMS) devices, which use (or will use) these nanostructured materials, depend on the stiffness and strength of components with dimensions on the order of the nanometer. In these kinds of applications, it is important to understand and characterize the mechanical properties of the constituent structures. Many researchers (Hall *et al.*, 1991; Alber *et al.*, 1992; Kondo and Takayanagi, 1997; Cuenot *et al.*, 2004; Diao, 2004; Duan *et al.*, 2005) have demonstrated, through both experiments and modeling, that the structure and properties of these nanostructured materials can be significantly different compared to more conventional and bulk materials, attributing these differences to the effects of surfaces.

The previous works most relevant to these observations are studies of surface and interface stress effects in thin films. It has been found (Banerjea and Smith, 1987; Cammarata and Sieradzki, 1989; Kosevich, 1989; Nix, 1998) that the surface energy could increase the apparent in-plane bi-axial modulus of a Cu (100) free standing film of 2 nm thick by about 15 ~ 25%. Several researchers have examined the elastic properties of thin films grown along selected crystallographic orientations. Young's modulus in the [001] direction for (100) oriented Cu and Au films is found to decrease with a decrease of the film thickness while the Young's modulus in the [110] or in [112] direction for the (111) Cu and Au films is found to increase as the thickness of the film decreases (Cammarata and Sieradzki, 1989; Wolf, 1991; Streitz, 1994; Streitz *et al.*, 1994). More recently, Miller and Shenoy (2000) developed a simple model to incorporate surface stress in determining the size-dependent elastic modulus of plates and rods. Using atomistic simulations, Liang and coworkers (Liang *et al.*, 2005) studied the elasticity of copper nanowires along [001], [110], and [111] crystallographic directions. They observed a size-dependence in the elastic response of the different nanowires studied. By doing a self-consistent comparison with the bulk response, they qualitatively showed that the overall nanowire elasticity is primarily due to nonlinear response of the nanowire core.

Nevertheless, few researchers have proposed a model incorporating the surface behavior into a continuum model. Cammarata and Sieradzki (1989) proposed a simple surface stress model that explicitly introduced surface energy and surface stress into the equations for equilibrium of a thin film but that neglected the change of the film thickness caused by the surface relaxations.

The effect of the surface properties on the mechanical properties of nanocomposite and nanocrystalline materials can also be very significant but it has scarcely been studied. Although Wu and coworkers (Wu *et al.*, 2004) have studied the stress concentration near a nanohole and its influence on the elastic properties of a single crystal Ag from both atomistic and continuum viewpoints, they failed to consider surface effects in the continuum formulation. Researchers like Sharma, Duan, or Huang (Sharma and Ganti, 2003; Sharma *et al.*, 2003; Sharma and Ganti, 2004; Duan *et al.*, 2005; Duan *et al.*, 2005; Duan *et al.*, 2005; Huang, 2006) addressed the issue of the size dependence of nanostructured materials and nanocomposites. All of their works revisited the Eshelby solution and include the surface energy and interfacial stresses but assume that the same relationship between surface energy (or interfacial energy in this case) and surface stress exists for free surfaces and for bicrystal surfaces.

5.2 Effective Modulus of Nanoparticle

Conventionally, the elastic modulus of a material is an intensive property. It is defined as a point-wise quantity that relates the stresses and strains at each point in the material. When a material is not homogeneous, such as a composite material, its elastic modulus may vary from point to point. In this case, the concept of effective modulus can be introduced. For example, effective modulus is used to characterize the overall

stiffness of a fiber reinforced composite, where the fiber and matrix have different elastic modulus.

Now consider a particle made of a single phase material. On or near the particle surface, the atomistic structure is somewhat different from that of the bulk. Therefore, a particle of a single phase material, strictly speaking, is not a homogeneous body. The overall stiffness of the particle needs to be characterized by its effective modulus. However, when the particle size is large enough, the surface region is negligible in comparison to the particle volume. In this case, the surface region can be neglected and the particle can be considered as a homogenous body. Therefore, its elastic modulus is uniform and is the same as that of the material from which the particle is made. This is no longer the case when the particle size shrinks to the nanometer range, where the surface region becomes significant in comparison to the particle size. Consequently, the particle must be viewed as an inhomogeneous body, and the effective modulus of the particle needs to be used to characterize the stiffness of the particle. Although the discrete atomistic nature of particles becomes important at small scales, nanostructural elements can be modeled using a continuum mechanics framework following the idea that *"nanostructure=bulk+surface"*. In this section, a formulation is developed to compute the effective modulus of a particle that incorporates the effect of its surface.

To this end, consider a perfect crystal of infinite extent. Within the infinite crystal, let Ω be an ellipsoidal region consisting of a certain number of atoms. Let the initial volume of Ω be V_0, and its surface area be S_0. Now imagine that Ω is removed from the infinite crystal to become a stand-alone particle, as shown in Figure 5.1. The newly created surface of the particle gives rise to surface stresses. Consequently, the particle may deform. The self-equilibrium state of the particle will be discussed later in this section. For now, simply let $\hat{V}$ and $\hat{S}$ be the volume and surface area, respectively, of the particle in its self-equilibrium state.

To describe the deformation of the particle, let us introduce a uniform strain ε_{ij} in the bulk of the particle; ε_{ij} is measured from the perfect lattice of an undeformed crystal of infinite extent. For an ellipsoidal particle, see Figure 5.2, the surface strain is related to the absolute bulk strain within the particle through a coordinate transformation

$$\varepsilon^{s}_{\alpha\beta} = t_{\alpha i} t_{\beta j} \varepsilon_{ij}\Big|_{S} \quad , \tag{5.1}$$

where the transformation tensor $t_{\alpha i}$ for the ellipsoidal surface is derived in Appendix D.

The total strain energy of the particle corresponding to ε_{ij} can be decomposed as a bulk phase bounded by a surface phase such that it can written as,

$$U = U_{bulk} + U_{surface} \quad , \tag{5.2}$$

where U_{bulk} is the total strain energy in the bulk of the particle,

$$U_{bulk} = \int_{V_0} \int_{0}^{\varepsilon_{ij}} \frac{\partial U}{\partial e_{ij}} de_{ij} dV_0 = \int_{V_0} \Big[U(\varepsilon_{ij}) - U(0) \Big] dV_0 \quad , \tag{5.3}$$

where U is the bulk elastic potential, which can be expanded into a series of the bulk strain tensor,

$$U = \frac{1}{2} C_{ijkl} \varepsilon_{ij} \varepsilon_{kl} + \frac{1}{6} C^{(3)}_{ijklmn} \varepsilon_{ij} \varepsilon_{kl} \varepsilon_{mn} + \cdots \quad , \tag{5.4}$$

where C_{ijkl} and $C^{(3)}_{ijklmn}$ are, respectively, the tensors of second and third order elastic constants of the perfect crystal lattice. Substituting (5.4) into (5.3) and neglecting higher order in strains leads to

$$U_{bulk} = V_0 \left[\frac{1}{2} C_{ijkl} \varepsilon_{ij} \varepsilon_{kl} + \frac{1}{6} C^{(3)}_{ijklmn} \varepsilon_{ij} \varepsilon_{kl} \varepsilon_{mn} \right] \quad . \tag{5.5}$$

The total surface free energy on the entire particle surface follows from equation (4.19)

$$U_{surface} = \int_{S_0} \left[\int_{0}^{\varepsilon^{s}_{\alpha\beta}} \Sigma^{s}_{\alpha\beta}(e_{\kappa\lambda}) de_{\alpha\beta} \right] dS_0 \quad . \tag{5.6}$$

Substituting equation (4.24) with into (5.6) yields,

$$U_{surface} = \int_{S_0} \left[\int_0^{\varepsilon^s_{\alpha\beta}} \frac{d\Gamma}{de_{\alpha\beta}} de_{\alpha\beta} \right] dS_0 = \int_{S_0} \left[\Gamma(\varepsilon^s_{\alpha\beta}) - \Gamma(0) \right] dS_0 \quad , \tag{5.7}$$

Note that in the case of free standing particles, no transverse load is applied. Making use of the expansion equation (4.14) into (5.7), one has

$$U_{surface} = \int_{S_0} \left[\Gamma^{(1)}_{\alpha\beta} \varepsilon^s_{\alpha\beta} + \frac{1}{2} \Gamma^{(2)}_{\alpha\beta\kappa\lambda} \varepsilon^s_{\alpha\beta} \varepsilon^s_{\kappa\lambda} + \frac{1}{6} \Gamma^{(3)}_{\alpha\beta\kappa\lambda\gamma\eta} \varepsilon^s_{\alpha\beta} \varepsilon^s_{\kappa\lambda} \varepsilon^s_{\gamma\eta} \right] dS_0 \quad , \tag{5.8}$$

where the surface strain is related to the bulk strain within the particle through the coordinate transformation.

$$\varepsilon^s_{\alpha\beta} = t_{\alpha i} t_{\beta j} \varepsilon_{ij} \Big|_S \quad . \tag{5.9}$$

Substitution of (5.9) into (5.8) yields the strain energy stored in the surface of the ellipsoidal particle Ω when it is subjected to the bulk strain ε_{ij},

$$U_{surface} = \frac{V_0}{a} \tau_{ij} \varepsilon_{ij} + \frac{V_0}{2a} Q_{ijkl} \varepsilon_{ij} \varepsilon_{kl} + \frac{V_0}{6a} P_{ijklmn} \varepsilon_{ij} \varepsilon_{kl} \varepsilon_{mn} \quad , \tag{5.10}$$

where *a* is the smallest of the three semi-axes of the ellipsoid and

$$\tau_{ij} = \frac{a}{V_0} \int_{S_0} \Gamma^{(1)}_{\alpha\beta} t_{\alpha i} t_{\beta j} dS_0 \quad , \tag{5.11}$$

$$Q_{ijkl} = \frac{a}{V_0} \int_{S_0} \Gamma^{(2)}_{\alpha\beta\kappa\lambda} t_{\alpha i} t_{\beta j} t_{\kappa k} t_{\lambda l} dS_0 \quad , \tag{5.12}$$

$$P_{ijklmn} = \frac{a}{V_0} \int_{S_0} \Gamma^{(3)}_{\alpha\beta\kappa\lambda\gamma\eta} t_{\alpha i} t_{\beta j} t_{\kappa k} t_{\lambda l} t_{\gamma m} t_{\eta n} dS_0 \quad . \tag{5.13}$$

The fourth order tensor Q_{ijkl} can be viewed as the *surface rigidity tensor*. It represents the combined effect of the surface stiffness, $\Gamma^{(2)}_{\alpha\beta\kappa\lambda}$, and the surface geometry. Note that the surface rigidity tensor has the dimension of force per unit length. It possesses the usual symmetry of stiffness tensors, $Q_{ijkl} = Q_{klij} = Q_{jikl} = Q_{ijlk}$. The integrals in (5.11) – (5.13) can be further written as

$$\tau_{ij} = \frac{3}{4\pi}\int_0^{2\pi}\left[\int_0^{\pi}\Gamma^{(1)}_{\alpha\beta}t_{\alpha i}t_{\beta j}\rho d\phi\right]d\theta \quad , \tag{5.14}$$

$$Q_{ijkl} = \frac{3}{4\pi}\int_0^{2\pi}\left[\int_0^{\pi}\Gamma^{(2)}_{\alpha\beta\kappa\lambda}t_{\alpha i}t_{\beta j}t_{\kappa k}t_{\lambda l}\rho d\phi\right]d\theta \quad , \tag{5.15}$$

$$P_{ijklmn} = \frac{3}{4\pi}\int_0^{2\pi}\left[\int_0^{\pi}\Gamma^{(3)}_{\alpha\beta\kappa\lambda\gamma\eta}t_{\alpha i}t_{\beta j}t_{\kappa k}t_{\lambda l}t_{\gamma m}t_{\eta n}\rho d\phi\right]d\theta \quad , \tag{5.16}$$

where

$$\rho = \sin\phi\sqrt{\sin^2\phi\cos^2\theta + \frac{a^2}{b^2}\sin^2\phi\sin^2\theta + \frac{a^2}{c^2}\cos^2\phi} \quad . \tag{5.17}$$

It is important to observe that these tensors depend on the shape of the ellipsoid, but not the size.

It then follows from substituting (5.10) and (5.5) into (5.2) that

$$U = \frac{V_0}{a}\tau_{ij}\varepsilon_{ij} + \frac{V_0}{2}\left(C_{ijkl} + \frac{1}{a}Q_{ijkl}\right)\varepsilon_{ij}\varepsilon_{kl} + \frac{V_0}{6}\left(C^{(3)}_{ijklmn} + \frac{1}{a}P_{ijklmn}\right)\varepsilon_{ij}\varepsilon_{kl}\varepsilon_{mn} \quad . \tag{5.18}$$

This gives the total strain energy of the particle when it deforms relative to the undeformed perfect crystal lattice of an infinite extent.

Because of surface stresses, the self-equilibrium state of the particle is different from the perfect crystal lattice of an infinite extent. The strain tensor, $\hat{\varepsilon}_{ij}$, that describes the deformation from the perfect crystal lattice to the self-equilibrium state of the particle can be found by minimizing the total strain energy. To this end, consider

$$\left.\frac{\partial U}{V_0\partial\varepsilon_{ij}}\right|_{\varepsilon_{ij}=\hat{\varepsilon}_{ij}} = \left(C_{ijkl} + \frac{1}{a}Q_{ijkl}\right)\hat{\varepsilon}_{kl} + \frac{1}{2}\left(C^{(3)}_{ijklmn} + \frac{1}{a}P_{ijklmn}\right)\hat{\varepsilon}_{kl}\hat{\varepsilon}_{mn} + \frac{1}{a}\tau_{ij} = 0 \quad . \tag{5.19}$$

This is a set of six quadratic equations which, in general, need to be solved numerically for the six components of self-equilibrium strain tensor $\hat{\varepsilon}_{ij}$. Once $\hat{\varepsilon}_{ij}$ is found, the effective modulus tensor of the particle at the state of self-equilibrium can be defined as

$$\bar{C}_{ijkl} = \frac{\partial^2}{\partial\varepsilon_{ij}\partial\varepsilon_{kl}}\left(\frac{U}{V_0}\right)\Bigg|_{\boldsymbol{\varepsilon}=\hat{\boldsymbol{\varepsilon}}} = C_{ijkl} + \frac{1}{a}Q_{ijkl} + \left(C^{(3)}_{ijklmn} + \frac{1}{a}P_{ijklmn}\right)\hat{\varepsilon}_{mn} \quad . \tag{5.20}$$

Note that in deriving (5.20), it had to be assumed that the strain in the ellipsoid bulk is uniform. Consequently, the effective modulus tensor given by (5.20) is generally an upper bound.

When the self-equilibrium strain is small, i.e., $\hat{\varepsilon}_{ij} \ll 1$, the quadratic term in (5.19) can be neglected. This yields the self-equilibrium strain,

$$\hat{\varepsilon}_{ij} \approx -\frac{1}{a}\left(C_{ijkl} + \frac{1}{a} Q_{ijkl} \right)^{-1} \tau_{kl} \quad . \tag{5.21}$$

Substitution of (5.21) into (5.20) leads to

$$\bar{C}_{ijkl} = C_{ijkl} + \frac{1}{a} Q_{ijkl} - \frac{1}{a}\left(C^{(3)}_{ijklmn} + \frac{1}{a} P_{ijklmn} \right)\left(C_{mnkl} + \frac{1}{a} Q_{mnkl} \right)^{-1} \tau_{kl} \quad . \tag{5.22}$$

This is the effective elastic modulus tensor of the particle. Further, if one assumes

$$C_{ijkl} \gg \frac{1}{a} Q_{ijkl}, \;\; C^{(3)}_{ijklmn} \gg \frac{1}{a} P_{ijklmn} \quad , \tag{5.23}$$

equations (5.21)-(5.22) can be simplified to obtain the explicit expressions of the self-equilibrium strain and the effective elastic modulus tensor,

$$\hat{\varepsilon}_{ij} \approx -\frac{1}{a} C^{-1}_{ijkl} \tau_{kl} = -\frac{1}{a} M_{ijkl} \tau_{kl} \quad , \tag{5.24}$$

$$\bar{C}_{ijkl} = C_{ijkl} + \frac{1}{a}\left(Q_{ijkl} - C^{(3)}_{ijklmn} M_{mnpq} \tau_{pq} \right) \quad , \tag{5.25}$$

where $M_{ijkl} = C^{-1}_{ijkl}$ is the compliance tensor of the bulk crystal.

As mentioned earlier, Q_{ijkl} and P_{ijklmn} are independent of the particle size a. Therefore, the assumptions made in (5.23), for a given material, effectively place a lower limit on the particle size for which the explicit expressions (5.24) – (5.25) are valid. All of our numerical experiments have shown that (5.23) is met for values of a as small as a few nanometers.

It is seen that the contribution of the surface energy to the effective modulus of the particle is inversely proportional to the particle size. It will be shown later

numerically that the surface energy contribution is negligible unless the particle size approaches the nanometer range. It is worth mentioning that if the surface stiffness tensor is independent of the location, i.e., the surface is homogeneous, then the tensor Q_{ijkl} can be obtained analytically for spherical particles ($a = b = c$), wires, fibers and thin films. Their expressions are given in Appendix F.

5.2.1 Special Cases

5.2.1.1 Thin Films

Consider a thin film made of a single crystal with cubic symmetry. Further, it is assumed that the top and bottom surfaces of the film are isotropic (for simplicity of the expressions derived in the following). In the crystallographic coordinate system shown in Figure 5.3, the second and third order elasticity tensors of the crystal are denoted by C_{ijkl} and $C^{(3)}_{ijklmn}$, respectively. Using the Voigt notations, the non-zero, independent components of these tensors are C_{11}, C_{12} and C_{44} for C_{ijkl}, and C_{111}, C_{112}, C_{123}, C_{144}, C_{155} and C_{456} for $C^{(3)}_{ijklmn}$. The relationship between indices of the Voigt and tonsorial notations is given in Appendix E. For example, $11 \to 1$, $23 \to 4$, thus, $C_{1123} = C_{14}$ and $C^{(3)}_{112323} = C_{144}$.

In this particular case, the integrals in (5.11) can be easily evaluated to yield the non-zero components of τ_{ij} and Q_{ijkl}

$$\tau_{11} = \tau_{22} = \Gamma_{11} \quad , \tag{5.26}$$

$$Q_{1111} = Q_{2222} = K^s + \mu^s, \;\; Q_{1122} = K^s - \mu^s, \; Q_{1212} = \mu^s \quad , \tag{5.27}$$

where Γ_{11}, K^s and μ^s are related to $\Gamma^{(1)}_{\alpha\beta}$ and $\Gamma^{(2)}_{\alpha\beta\kappa\lambda}$ as indicated in Appendix E. Substituting the above into (5.25) yields the effective modulus tensor. Non-zero

components of the effective modulus tensor for the thin film in terms of the Voigt notation are given in Appendix F.

It is seen from these expressions that the effective modulus tensor no longer has cubic symmetry. It becomes orthotropic. The quantities of interest are the two in-plane unidirectional Young's modulus in the X_1 and X_2 direction,

$$\bar{E}_{X_1} = \bar{E}_1 = \bar{C}_{11} + \frac{\bar{C}_{33}\bar{C}_{12}^2 + \bar{C}_{22}\bar{C}_{13}^2 - 2\bar{C}_{12}\bar{C}_{13}\bar{C}_{23}}{\bar{C}_{23}^2 - \bar{C}_{22}\bar{C}_{33}} \quad , \tag{5.28}$$

and,

$$\bar{E}_{X_2} = \bar{E}_2 = \bar{C}_{22} + \frac{\bar{C}_{33}\bar{C}_{12}^2 + \bar{C}_{11}\bar{C}_{23}^2 - 2\bar{C}_{12}\bar{C}_{13}\bar{C}_{23}}{\bar{C}_{13}^2 - \bar{C}_{11}\bar{C}_{33}} \quad . \tag{5.29}$$

Substituting Appendix (F5) – (F11) into (5.28) and keeping terms only up to (5.30) $1/a$ yields

$$\bar{E}_{X_1} = E_{X_1} + \frac{1}{a}\left(K^s\kappa + \Gamma_{11}\chi\right) \quad , \tag{5.31}$$

$$\bar{E}_{X_2} = E_{X_2} + \frac{1}{a}\left(K^s\kappa + \Gamma_{22}\chi\right) \quad , \tag{5.32}$$

where

$$E_{X_1} = E_1 = C_{11} + \frac{C_{33}C_{12}^2 + C_{22}C_{13}^2 - 2C_{12}C_{13}C_{23}}{C_{23}^2 - C_{22}C_{33}} \tag{5.33}$$

and,

$$E_{X_2} = E_2 = C_{22} + \frac{C_{33}C_{12}^2 + C_{11}C_{23}^2 - 2C_{12}C_{13}C_{23}}{C_{13}^2 - C_{11}C_{33}} \tag{5.34}$$

are the unidirectional Young's moduli of the bulk crystal in the X_1 and X_2 directions respectively and

$$\kappa = \frac{\mu^s}{K^s}\left(\frac{C_{33} + 2C_{13}}{C_{33} + C_{13}}\right)^2 + \left(\frac{C_{33}}{C_{33} + C_{13}}\right)^2 \quad , \tag{5.35}$$

$$\chi = \frac{\eta}{(C_{33}+C_{13})^2}\left[\left(\frac{2C_{13}^3 - C_{33}^3 - 2C_{13}C_{33}^2 - 2C_{13}^2C_{33}}{C_{33}C_{13}}\right)C_{333}\right.$$
$$\left. + \left(6C_{11} - \frac{C_{11}^2}{C_{12}} + \frac{4C_{12}^2}{C_{11}}\right)C_{112} + 2\left(C_{11} - 2C_{12} - \frac{2C_{12}^2}{C_{11}}\right)C_{123}\right] \quad . \tag{5.36}$$

Clearly, κ and χ are due to surface stress combined with the non linear elastic behavior of the core of the film through its third order elastic constants.

Another quantity of interest is the in-plane biaxial Young's modulus defined as

$$\overline{Y}_b = \frac{1}{2}\left[\overline{C}_{11} + \overline{C}_{22} + 2\overline{C}_{12} - \frac{\left(\overline{C}_{13} + \overline{C}_{23}\right)^2}{\overline{C}_{33}}\right] \quad . \tag{5.37}$$

Substituting Appendix (F5) – (F11) into (5.37) and keeping terms only up to $1/a$ yields

$$\overline{Y}_b = Y_b + \frac{1}{a}\left(2K^s + \Gamma_{11}\chi\right) \quad , \tag{5.38}$$

where

$$Y_b = \frac{1}{2}\left[C_{11} + C_{22} + 2C_{12} - \frac{\left(C_{13} + C_{23}\right)^2}{C_{33}}\right] \tag{5.39}$$

the biaxial Young's modulus of the bulk crystal in the X_1X_2-plane and,

$$\chi = \eta\left[\left(\frac{4C_{13}^2}{C_{33}^3} - \frac{1}{C_{13}}\right)C_{333} + 3\left(\frac{2}{C_{33}} - \frac{1}{C_{13}} - \frac{4C_{13}}{C_{33}^2}\right)C_{331} + \frac{6}{C_{33}}C_{123}\right] \quad . \tag{5.40}$$

Clearly, χ is due to surface stress and third order elastic constants.

Under the biaxial loading, $\sigma_{11} = \sigma_{22}$ and $\sigma_{33} = 0$, one can define an effective biaxial Poisson's ratio, $\overline{\nu}_b = -\varepsilon_{33}/\varepsilon$, where $\varepsilon = \varepsilon_{11} = \varepsilon_{22}$ because of the cubic symmetry in the X_1X_2-plane of the film. Making use of the above equations in conjunction with Appendix (F5) – (F11), one arrives at

$$\overline{\nu}_b = \frac{\left(C_{13} + C_{23}\right)}{C_{33}} + \frac{2\Gamma_{11}\eta}{aC_{33}C_{13}}\left[\left(\frac{4C_{13}}{C_{33}} - 1\right)C_{331} - \frac{2C_{13}^2}{C_{33}^2}C_{333} - C_{123}\right] \quad , \tag{5.41}$$

where the first term of this sum is the biaxial Poisson's ratio for a bulk crystal. It is noted here that when $\bar{\nu}_b$ is assumed to be independent of the film thickness, i.e., neglecting the second term in (5.41), the effective biaxial Young's modulus (5.38) reduces to the effective biaxial modulus derived by Streitz *et al* (1994).

The self-equilibrium strain of the film follows directly from (5.24),

$$\hat{\boldsymbol{\varepsilon}} = \frac{\Gamma_{11}\eta}{a}\begin{bmatrix} 2/C_{33} & 0 & 0 \\ 0 & -1/C_{13} & 0 \\ 0 & 0 & -1/C_{13} \end{bmatrix} . \tag{5.42}$$

Clearly the sign of Γ_{11} determines whether there is a negative (contraction) or positive (dilatation) relaxation of the film in the plane directions. For $C_{13} > 0$, positive Γ_{11} would yield negative compressive in-plane strain and positive transverse stain. The same result for the in-plane self-equilibrium $\hat{\varepsilon}_{11} = \hat{\varepsilon}_{22}$ has been obtained by Streitz *et al.* (1994).

5.2.1.2 Thin Wire of Square Cross-section

Now, consider a thin wire of square cross-section made of a single crystal with cubic symmetry as shown in Figure 5.4. Again, assume that the surfaces of the wire are isotropic. The corresponding effective modulus tensor of the wire can be directly computed from the general formulas given by (5.24) – (5.25) . The non-zero components of the effective modulus tensor are given in Appendix F, see (F21) – (F26).

It is seen from (F20) – (F25) that, just like in the case of the film, the effective modulus tensor becomes orthotropic. The unidirectional Young's modulus in the axial direction is given by

$$\bar{E}_{X_3} = E_{X_3} + \frac{1}{a}\left(K^s\kappa + \Gamma_{11}\chi\right) , \tag{5.43}$$

where

$$E_{X_3} = E_L = C_{33} + \frac{C_{11}C_{23}^2 + C_{22}C_{13}^2 - 2C_{12}C_{13}C_{23}}{C_{12}^2 - C_{11}C_{22}} \tag{5.44}$$

is the unidirectional Young's modulus of the bulk crystal in the X_3 directions and

$$\kappa = \frac{\mu^s}{K^s}\left(\frac{C_{11}+2C_{12}}{C_{11}+C_{12}}\right)^2 + \frac{C_{11}^2+4C_{12}^2}{\left(C_{11}+C_{12}\right)^2} \quad , \tag{5.45}$$

$$\chi = \frac{\eta}{(C_{11}+C_{12})^2}\left[3\left(2C_{11}-4C_{12}-\frac{C_{11}^2}{C_{12}}\right)C_{112}\right. \\ \left. + \left(\frac{4C_{12}^2}{C_{11}} - \frac{C_{11}^2}{C_{12}}\right)C_{111} + 6C_{11}C_{123}\right] \quad . \tag{5.46}$$

The Poisson's ratios are given by

$$\overline{\nu}_{13} = \nu_{13} + \frac{1}{a}\left(K^s\kappa + \Gamma_{11}\chi\right) \quad , \tag{5.47}$$

and,

$$\overline{\nu}_{23} = \nu_{23} + \frac{1}{a}\left(K^s\kappa + \Gamma_{22}\chi\right) \quad , \tag{5.48}$$

where

$$\nu_{13} = \frac{C_{22}C_{13} - C_{23}C_{12}}{C_{11}C_{22} - C_{12}^2} \quad , \tag{5.49}$$

and,

$$\nu_{23} = \frac{C_{11}C_{23} - C_{13}C_{12}}{C_{11}C_{22} - C_{12}^2} \quad , \tag{5.50}$$

are the Poisson's ratio of the bulk crystal and

$$\kappa = \frac{C_{11}}{(C_{11}+C_{12})^2} - \frac{\mu^s}{K^s}\frac{C_{11}+2C_{12}}{(C_{11}+C_{12})^2} \quad , \tag{5.51}$$

$$\chi = \frac{\eta}{(C_{11}+C_{12})^2}\left[\left(1-2\frac{C_{12}}{C_{11}}\right)C_{111}\right.$$
$$\left.+\left(4-\frac{3C_{11}}{C_{12}}-\frac{4C_{12}}{C_{11}}\right)C_{112}+\left(3-\frac{C_{11}}{C_{12}}+\frac{2C_{12}}{C_{11}}\right)C_{123}\right] . \quad (5.52)$$

The self-equilibrium strain is given by

$$\hat{\boldsymbol{\varepsilon}} = \frac{-\Gamma_{11}\eta}{a}\begin{bmatrix} \frac{C_{11}-2C_{12}}{C_{11}C_{12}} & 0 & 0 \\ 0 & \frac{C_{11}-2C_{12}}{C_{11}C_{12}} & 0 \\ 0 & 0 & \frac{2}{C_{12}} \end{bmatrix} . \quad (5.53)$$

5.2.1.3 Spherical Particles

Consider a spherical particle made of an isotropic elastic solid. Furthermore, assume that the particle's surface is homogeneous and isotropic. Clearly, this is an idealized case, for in reality a curved crystal surface inevitably involves different crystallographic surfaces, and thus becomes non-homogeneous and anisotropic. It is nevertheless interesting to study such an idealized case because of the simplicity of the solution.

Under such assumptions, the tensors Q_{ijkl} and $R_{ijkl} = C^{(3)}_{ijklmn} M_{mnpq} \tau_{pq}$ can be easily obtained analytically by setting $a = b = c$ in the equations derived earlier. Their expressions are given in Appendix F, see (F27) – (F29).

Making use of equations (F27) – (F29), one can easily find that the effective stiffness tensor is still isotropic for an isotropic spherical particle with isotropic surface. For such a particle of radius a, the effective bulk and shear moduli are

$$\bar{K} = K + \frac{4}{3a}\left[K^s - \frac{\Gamma_1}{K}\left(\frac{3}{2}L + 3M + \frac{4}{3}N\right)\right] \quad , \tag{5.54}$$

$$\bar{\mu} = \mu + \frac{1}{a}\left[\frac{1}{5}\left(K^s + 6\mu^s\right) - \frac{2\Gamma_1}{3K}\left(3M + 4N\right)\right] \quad , \tag{5.55}$$

where K and μ are, respectively, the bulk and shear moduli of the bulk material, L, M and N are the third order elastic constants related to C_{ijk}, see Appendix E.

Making use of (5.24), one can compute the self-equilibrium strain of the spherical particle,

$$\hat{\varepsilon}_{ij} = -\frac{1}{a} M_{ijkl}\tau_{kl} = -\frac{2\Gamma_{11}}{3aK}\delta_{ij} \quad . \tag{5.56}$$

Clearly, a positive Γ_{11} would mean a contraction of the sphere due to surface stress.

5.2.2 Atomistic Calculation for Computing the Effective Elastic Constants of Nanoparticles

As a partial validation of the model developed above, we performed atomistic calculations using a semi-analytical method for evaluating and analyzing the elastic properties of nanostructures such as nanowires and thin films.

The essence of the method is based on the Taylor expansion of an interatomic potential about the equilibrium (or relaxed) state of the studied nanostructure. When subjected to a uniform strain field ε_{ij}, we showed in chapter 4 that the elastic stiffness tensor C_{ijkl} of the nanostructure measured at the relaxed state is given by

$$C_{ijkl} = \frac{1}{N}\sum_{n=1}^{N}\frac{1}{\Omega_n}A_{ijkl}^{(n)} = \frac{1}{N}\sum_{n=1}^{N}\sum_{p\neq n}\sum_{q\neq n}\frac{1}{\Omega_n}\frac{\hat{r}_j^{pn}\hat{r}_l^{qn}\partial^2 E^{(n)}\left(r^{mn}\right)}{\partial r_i^{pn}\partial r_k^{qn}}\bigg|_{r^{mn}=\hat{r}^{mn}} \quad , \tag{5.57}$$

where $E^{(n)}$ is a generic interatomic potential function for an atom n, $\mathbf{r}^{mn}$ is the position vector between atoms m and n, $\Omega^{(n)}$ is the volume of the Voronoi polyhedron associated

with atom *n*. More details of the methods are described in chapter 4, section 3. This analysis implicitly accounts for the effects of that specific nanostructure's shape and size, including the effects of surfaces which play an important role at the nanoscale.

Note that the elastic constants are defined with respect to the relaxed configuration of the nanostructures. The method described here is not limited to wires and films. It can be used to deal with nanostructures of more complex shapes and the sizes. Obviously, this approach implicitly accounts for the surface effects that influence the properties of the structure. It is therefore important to choose an appropriate interatomic potential function in order to have an accurate description of the properties of the material studied.

Furthermore, in the present case, the physical nature of the surface atoms is different from that in the bulk, and deviations from the bulk elastic behavior in small scale systems can be considered as manifestations of Gibbs-Thomson effects. It had been shown in chapter 4 that the EAM potential used in this work adequately display the proper surface properties such as surface energy and surface stress. Hence it ensures that surface properties are being modeled correctly so that their influence on small size solids are properly being taken into account when determining how the surface effects are causing changes in the elastic properties.

We extended the methodology to the characterization of the size-dependence of the elastic moduli of thin films and nanowires grown along the [001], [110], and [111] crystallographic directions for group 10-11 transition metals (Cu, Ni, Pd, and Ag). Figure 5.5 shows the orientations of the lateral surfaces of these nanostructures. This homologous series of metals is chosen because they have similar atomic bonding characteristics that are different from those in ionic or covalent crystals. Here, the full set of effective elastic constants for Cu, Ni, Ag and Pd nanowires and thin films are calculated.

Nanostructures of different sizes are obtained by considering a top down fabrication approach (Gruber *et al.*, 1999) by "cutting" them from bulk crystals in the desired crystallographic orientations. Periodic boundary conditions (PBCs) are applied along the longitudinal direction and the lateral surfaces are kept free. For nanowires, PBCs are applied along the X_3 axis, illustrated in Figure 5.5. For nanofilms, PBCs are applied in the X_1 and X_2 directions. It is found that computational cell lengths of at least 6 nm for wires and in-plane widths of at least 4 nm for films are sufficient to ensure results which are independent of the choices of computational cell sizes. Therefore, a cell length of 20 nm used for all the nanowires and a cross-sectional size of 8 nm × 8 nm is used for all films. The embedded atom method (EAM) potential developed by Daw and Baskes (Daw and Baskes, 1984; Foiles *et al.*, 1986) is used in this work. The atomic interactions are calculated up to the third nearest neighbor by truncating the EAM potential at the appropriate distance. The reduced coordination of atoms near free surfaces induces a redistribution of electronic charges which alters the binding situation. Consequently, atoms near surfaces relax or move away from their perfect lattice positions and, as a result, their energy is different from the values in bulk. The nonlinear conjugate gradient method is used to minimize the energy of the system and to obtain the relaxed configuration. Contractions in the longitudinal direction are observed upon relaxation. This self-equilibrium state is characterized by the relaxation-induced strain field $\hat{\varepsilon}_{ij}$ given by equation (5.24) and the average stress over the entire structure, which is equal to zero since the structure is in a free-standing state.

In order to verify and validate those calculations, we have also performed a strain meshing of the calculation cell with strains in the two planar directions ranging from -1% to 1% and incremented by ±0.01% strain steps. The meshing procedure used to calculate the elastic properties of interest is quite similar to the one described previously for surface properties: after the initial geometry is defined, depending on the dimensionality of the element, different boundary conditions are applied. Periodic boundary conditions

are used in the two planar directions with free surfaces in the vertical direction to mimic a thin film (2D). Periodic boundary conditions are used in the longitudinal direction with free surfaces in the two other directions to mimic nanowires in the longitudinal direction (1D). No periodic boundary conditions are used to represent a free standing sphere (0D). After the initial relaxation of the nanoparticle, the element can be loaded in the desired direction(s) using the same methodology described earlier in this section and therefore we can obtain a meshing of the change of strain energy during the loading process with respect to the reference configuration as shown in Figure 5.6(a) for a thin film for example. The general steps of the calculation can be outlined as follows,

(a) Create the initial assembly using the given material properties (atomic weight, lattice spacing, EAM potential, crystallographic orientation, etc.).

(b) Equilibrate the assembly to find the self equilibrium state.

(c) Apply a small strain field, $\varepsilon^s_{\alpha\beta}$, to the assembly and re-equilibrate.

(d) Compute the strain energy density corresponding to this given strain field.

(e) Increase the magnitude of $\varepsilon^s_{\alpha\beta}$ and repeat steps (c) and (d).

After repeating steps (c) – (d) a sufficient number of times, we obtain a mesh of the total energy of the atomic assembly. After curve fitting, the effective elastic constants of the particle at the state of self-equilibrium $\hat{\boldsymbol{\varepsilon}}$ can be identified using the expression of the effective modulus tensor defined as,

$$\bar{C}_{ijkl} = \frac{\partial^2}{\partial\varepsilon_{ij}\partial\varepsilon_{kl}}\left(\frac{U}{V_0}\right)\Bigg|_{\boldsymbol{\varepsilon}=\hat{\boldsymbol{\varepsilon}}} \quad . \tag{5.58}$$

The results obtained using this method agree well with the semi-analytical method and the continuum model as seen from Figure 5.6.

The effective Young's moduli of thin films and wires of various thickness obtained from the semi-analytical model were compared with those calculated using a continuum model described earlier in section 5.2.

5.2.3 Numerical Results for Thin Films, Nanowires and Nanospheres

In this section, several numerical examples for the effective modulus and effective Poisson's ratio of spherical particles, wires of square cross-section and films are presented for four FCC materials (Cu, Ni, Ag and Pd) in three different crystallographic orientations. The discussion here focuses on the elastic properties of these homologous materials and the underlying trends in the effects of surface orientations. The values for the cubic (second order) and third order elastic constants of the single crystals and the surface properties required for the continuum model are taken from chapter 3 and chapter 4 and are listed in Table 4.1, Table 3.2 and Table 3.3. All the results discussed in this section are for unreconstructed surfaces. As reported by several researchers (Ackland and Finnis, 1986; Diao, 2004; Liang *et al.*, 2005), for certain orientations and materials, phase transformation and surface and structure reconstruction can occur when the characteristic size is sufficiently small. Examples include [100]-oriented gold nanowires with cross-sectional areas smaller than 1.83 nm × 1.83 nm. The sizes considered in this paper are larger than the critical sizes associated with lattice reorientation phenomena; therefore, issues related to structural changes are neglected in the analysis.

Figure 5.7 and Figure 5.8 respectively show the self-equilibrium strains during the initial relaxation of nickel nanowires as a function of wire thickness and the self-equilibrium strains during the initial relaxation of silver thin films as a function of film thickness. The results computed via equation (5.24) from the continuum model are also shown. For the three crystallographic orientations and for all materials studied, the self-equilibrium strains obtained from the atomistic calculations agree well with the values calculated using the model. As seen from the continuum and semi-analytical model results, we can observe longitudinal contractions and lateral expansions that increase as the size of the wires decreases. For a given wire size grown in the [110] and [111]

directions, the axial contractions have similar magnitudes but, they are much larger in the case of wires grown in the [100] direction. For example, for a 2 nm wire, the equilibrium strain is approximately -2% for [100] wires and is around -1% for [110] and [111] wires. Table 4.2 shows that for all the metals studied, the intrinsic surface stress $\Gamma_{\alpha\alpha}^{(1)}$ of (100) surfaces is greater than the surface stresses of the two other surfaces, while they are similar for the (111) and (110) surfaces. Due to the higher moduli in the [111] and [110] directions and smaller intrinsic surface stresses on the lateral surfaces, the relaxation strain is smaller for [110] and [111] nanowires than for [100] wires at a given thickness. Similar observations can be made for thin films. Clearly, in both cases, the intrinsic residual surface stresses directly influence the magnitude of the self equilibrium strain. This observation is analytically confirmed by equation (5.24).

The effective unidirectional and biaxial moduli for single crystal Ni wires and Cu films of various thicknesses are plotted in Figure 5.9 and Figure 5.10, respectively. For the Ni wires, the axial modulus for the [110] orientation increases as the wire diameter decreases, while an opposite trend is seen for the [100] orientation. For a wire size of 2 nm, the axial modulus for the [100] orientation is approximately 15% smaller than for its bulk counterpart (we calculated a reduction up to 35% compared to the bulk value in the case of 2nm Cu nanowires), while in the case of the wire grown in the [110] orientation, the axial modulus for a 2nm wire is approximately 23% higher than the value obtained in the bulk. As seen from Figure 5.9, as the wire size is decreased from 8 nm to 2 nm, the axial Young's modulus decreases by 28% for [100] wires and by only 2% for [111] wires, while it increases by 15% for [110] wires. Similar trends are seen for the uniaxial modulus of Cu films since a film can be viewed as an array of wires placed side-by-side.

In the case of the biaxial Young's modulus of Cu thin films, as seen in Figure 5.10, we nevertheless observe opposite trends as compared with the uniaxial Young's modulus of the nanowires. Specifically, for a 2 nm film, the biaxial modulus for the (100) orientation is almost 33% higher than its bulk value. We can see from Figure 5.10 that when the thickness of the film is reduced from 8 nm to 2 nm, the biaxial Young's modulus increases by 22% and 4% with respect to its bulk value for the (100) and (111) films, respectively, while it is decreases by 4% for the (110) wires.

Another interesting observation is the similarity between the size-dependences of the uniaxial Young's modulus for nanowires in the [100] direction and the uniaxial Young's modulus in the (001) direction of the [110] films. This can be qualitatively explained by considering the surface attributes for the (110) plane. In particular, the trough and ridge structure of (110) surface results of atoms along the $\left[1\bar{1}0\right]$ direction separated by relatively wide troughs. The nearest neighbors of the atoms in a row are other atoms in the same row and atoms in the layers underneath. The only nearest neighbor bonds of the surface layers atoms that have components transverse to the $\left[1\bar{1}0\right]$ row are those that connect them to the atoms in the second layer resulting in a higher uniaxial Young's modulus in the $\left[1\bar{1}0\right]$ direction than in the $\left[100\right]$. The Poisson's ratio for the wire and the biaxial Poisson's ratio for the film are plotted in Figure 5.11 for wires and films of various thicknesses. The dashed lines indicate the bulk values without the effect of free surfaces. It is seen that the bi-axial Poisson's ratio of the film decreases with decreasing film thickness, while the axial Poisson's ratio of the wire increases with decreasing wire thickness. In both cases, a sharp change occurs around thickness of 2

nm. It is interesting to note that molecular dynamic simulations by Diao, *et al*, (2003) have shown that single crystal gold wires undergo a phase transformation from face center cubic symmetry to body center tetragonal symmetry when the wire diameter reduces to around 2 nm due to surface stress, giving rise to a significant increase in Poisson's ratio (Diao *et al*, 2004).

Finally before closing this section, Figure 5.12 presents the results for all the materials studied and compares the uniaxial Young's modulus for nanowires, uniaxial and biaxial Young's modulus for thin films as a function of their characteristic sizes. The Young's modulus decreases for [100] wires, increases for [110] wires and remains essentially constant for [111] wires as the cross-sectional size is decreased (Figure 5.12(a)). For the thin films (Figure 5.12(b)), the biaxial Young's modulus shows exactly the opposite trend to those seen in the nanowires for all the materials studied. The size dependence trends observed for the uniaxial moduli of thin films grown in various orientations are also consistent among the materials analyzed. Such a consistency in the elastic response is expected since the surface and bulk properties are quite similar for the materials in this homologous series.

5.2.4 Influence of Non-Linear Elasticity of the Bulk Core and Surface Elasticity

Given the excellent correlation between the atomistic calculations from section 5.2.2 and the model developed in section 5.2.1 we can go a step further in our reasoning and study the influence of several parameters on the size-dependence elasticity stiffness of the nanostructures in order to qualitatively and quantitatively understand their contribution to the elastic response.

As seen from equation (5.24) and based on the observations and remarks made in the previous section concerning the self-equilibrium strain, the intrinsic (or residual) surface stresses clearly drive the relaxation behaviors of nanostructural elements.

Therefore we can conclude that the knowledge of the intrinsic surface stress completely defines the relaxed state of nanostructural elements such as the wires and films studied here and it is characterized by equation (5.24).

Based on equation (5.25), two material properties clearly influence the softening or stiffening of nanoparticles: (i) the surface elasticity represented through the tensor Q_{ijkl} (which is a function of the surface elastic behavior and the shape of the nanostructural element) and (ii) the non-linear behavior of the core of the nanostructure. In Figure 5.13 – Figure 5.17, we show the influence of the surface elasticity and the influence of non-linear behavior of the bulk on the effective properties of films and wires. To study the influence of the nonlinear elastic behavior of the bulk, we plotted the ratio between the Young's moduli of the nanostructural elements and the bulk moduli of the material studied when the surface stresses are held constant (surface stresses do not depend on the stretching of the surface and are equal to the intrinsic tensile surface stresses). In this circumstance only the non-linear elastic behavior of the core of the nanoparticles is artificially taken into account. On the other hand, to study the influence of surface elasticity, we plotted the ratio between the Young's moduli of the nanoparticles and the bulk moduli when the non-linear elastic behavior of the bulk is neglected in equation (5.25). Therefore in this case only the elastic behavior of the surfaces is expected to influence the effective properties. In both cases, ratios greater than unity imply that the particular parameter considered contributes to the stiffening of the actual nanoparticles while ratios smaller than unity imply a softening induced on the structure studied. Based on such a decomposition of surface and bulk effects, we can clearly identify several trends in the effective elastic responses of the nanowires and thin films.

5.2.4.1 Parameters Influencing the Size-Dependence of Nanowires

In the case of nanowires, we studied the influence of the non-linearity of the cores and the effect of the surface elasticity on the size-dependence for wires grown in the three basal crystallographic directions. First, as seen from Figure 5.13 and Figure 5.16(a), we can observe that for the [100] crystallographic direction, the neglect of non-linear elastic behavior of the bulk or the invariance of the surface stresses with respect to surface strains makes the wire softer than its bulk counterpart. For example, for a 2nm thick copper wire, the elastic behavior of the surfaces by itself softens the wire's uniaxial Young's modulus by 22%, while the non linear elastic behavior of its core reduces it by 18%. Therefore the non-linear elasticity of the bulk as well as the surface elasticity contribute to the softening of the nanowires grown in the [100] direction equally, which in turn is reflected in the overall decrease in the Young's modulus with decrease in size.

On the contrary, when we consider wires grown in the [110] direction, the influence of surface elasticity on its effective modulus is rather negligible (a few percent for a 2nm thick wire for example) and only the non-linear elasticity of the bulk influences significantly the effective elastic stiffness of the wire. As seen from Figure 5.13, the modulus ratio for the third order constants in the [110] orientation is greater than unity and therefore contributes to the stiffening of the nanowires (~20% increase in modulus with respect to the bulk for a 2nm wire). Thus, the contribution of the surface elasticity on [110] nanowires is considerably smaller than the contribution of the non-linear elasticity of their core and as a result the effective modulus of the nanowire is larger than the bulk.

Finally, in the case of the nanowires grown in the [111] direction we notice that the non-linear elastic behavior of the bulk counteracts the effects of surface elasticity. As seen from Figure 5.13, for a 2nm thick wire, the effect of the non-linearity increases the uniaxial Young's modulus by approximately 6% with respect to the bulk modulus while the elasticity of the surface decreases it by 11% i.e the non-linear elasticity of the stiffens

and the elastic behavior of the surface softens the nanoparticle. However, as seen from the changes in moduli, the contributions of the surface and the core acting individually are minimal.

For all three nanowire orientations and for all the studied materials, surface elasticity always contributes to the softening of the wires as compared to their respective bulk values. This softening is moderate (7-22%) in the case of the (100) and (110) nanowires while it is negligible in the case of the [111] nanowires. The non linear elastic behavior of the core of the wire, however, influences the size dependent softening or stiffening depending on the orientation. These conclusions concur with the observations already made with atomistic simulations by Liang (2005) for copper nanowires.

5.2.4.2 Parameters Influencing the Size-Dependence of Thin Films

In the case of thin films, we analyzed the effects of the surface and the core of the nanostructural elements on the uniaxial and biaxial Young's modulus for the three basal crystallographic orientations. As seen from Figure 5.14, for (100) films (Ni or Cu), the influence of the parameters on the size-dependence for the uniaxial Young's modulus is opposite to that of the biaxial Young's modulus. The biaxial Young's modulus of a film is greater than the bulk value when considering either the constant surface stresses or when the non-linearity of the core is neglected or when both are acting simultaneously. For example, as illustrated in Figure 5.14 for a 2 nm thick film of nickel, the effect of the surface elasticity increases the modulus by 6% compared with the bulk modulus while the non linear elastic behavior of its core increases it by 15%. On the contrary, when we examine the uniaxial behavior of that same thin film, the uniaxial Young's modulus is smaller than its bulk value when either or both parameters are considered. For a 2 nm copper thick film, the surface effects decrease the modulus by 12% and the third order elastic constants of the core decrease the modulus by 14% with respect to the Bulk

biaxial Young's modulus. Therefore, both, the non-linear elasticity of the bulk as well as the surface elasticity, are driving factors in the stiffening or softening of (100) thin films depending on the modulus considered.

For (110) and (111) films, while the influence of the non-linear elastic behavior on the biaxial modulus seems irrelevant (decrease of 4% of the biaxial modulus for 2 nm-thick films of nickel), the elastic behavior of the surface appears to be the most influential parameter on the size dependent elastic biaxial modulus of the thin film. Interestingly enough, we notice that for the uniaxial Young's modulus of (110) films, both the non linear elasticity of the films' cores as well as surface elasticity play a part in the size dependent softening of the film (for 2 nm-thick films of copper we notice a decrease of 9% with the surface elasticity effect and a decrease of 8% caused by the non linear elastic behavior of the core). As already noted in the previous section, the trough-and-ridge structure results in a greater softening of uniaxial Young's modulus in the $[100]$ direction than in the $[1\bar{1}0]$ direction.

For the three thin films'orientations and all the materials studied, the surface elasticity and the non linear elasticity within the core of the thin film have an effect on the size dependent softening or stiffening which highly depends on the orientation and elastic constants considered. Furthermore, as expected, the trends observed for each orientation are consistent within the homologous series of metals.

Figure 5.16 and Figure 5.17 compare the effects of surface and core elasticity on the nanowire and thin film responses for all the materials considered in this work. As seen from the figures, the trends observed for each orientation are consistent within the homologous series of metals. Irrespective of the orientation considered, the surface elastic behavior is seen to soften the nanowires for each material (Figure 5.16(a)). We note that in the case of palladium, the effect of the surface on the size-dependence elasticity of the [110] wire is slightly different from the rest of the materials studied.

While for copper, nickel and silver, the influence of surface elasticity on its effective modulus is rather negligible, we can observe that the contribution of the surface elasticity on [110] palladium nanowires makes the wire softer than the bulk. For example, as seen from Figure 5.16(a), for a 2nm thick [110] palladium wire, the surface effects decrease the modulus by approximately 10%. Using equation (5.25), we can show that this observation is primarily explained by the fact that the term $\Gamma_{2222}^{(100)} + \Gamma_{2222}^{(110)}$ drives surface effect on the size dependent elasticity of [110] wires. In the case of (111) palladium thin film, while the effects of the surface are still negligible (less than 1% for a 2nm thick film), its sensitivity to the surface elasticity is different from the rest of the studied materials. As seen from Figure 5.16(b) and Figure 5.16(c), while for copper, nickel and silver, the effects of the surface stiffen the (111) films for very small thicknesses, the surface actually softens the (111) palladium thin films. This trend can be simply identified by looking more closely at Table 1. Indeed (111) palladium surface has negative surface elastic constants while these for copper, nickel and silver are positive. From a physics point of view, this simply means that (111) palladium surface stresses are relaxed upon stretching. The effect of core non-linearity is also similar for the materials resulting in consistency in the overall behavior also seen in Figure 5.17(a). Similar observations can also be made for the uniaxial and biaxial moduli of thin films (Figure 5.17(b) and Figure 5.17(c)).

5.3 Eshelby nano-inclusion problem

5.3.1 Interphase versus Interface

In the preceding chapter, when dealing with surface excess stress and surface excess strain, we have intentionally limited ourselves to continuum media. Therefore,

there is no microstructure, thus no characteristic length involved, and the interface is a mathematical surface with zero-thickness. For realistic bimaterials, there typically exist two distinctive length parameters, namely, the atomic spacing (lattice parameter) d, and the radius of curvature of the interface D, where D is generally several order of magnitude greater than d for most of the problems of engineering interest.

For example, in a bicrystal, the equilibrium position and energy of atoms near the grain boundary are, in general, different from those of the atoms in the bulk of the crystals that constitute the bicrystal. The transition from one bulk values to the other may take place over a few layers of atoms (Blakely, 1973; Dingreville and Qu, 2007; Dingreville and Qu, 2007). Therefore, in the framework of continuum mechanics, an interface between two dissimilar materials may be considered as a region over which the material properties changes gradually from the bulk property of one material to the other. This transition region is regarded as the *interphase* of thickness h. Field quantities in the continuum framework such as stress, strain and strain energy density may all vary continuously across the interphase. Specifically, the displacement and traction are continuous across any surface (including the interface) within the interphase when measured by the microscopic length scale h. It is in such length scale that the continuity of displacement and traction is specified that leads to, $\boldsymbol{\sigma}_{+}^{t} = \boldsymbol{\sigma}_{-}^{t}$ and $\boldsymbol{\varepsilon}_{+}^{s} = \boldsymbol{\varepsilon}_{-}^{s}$.

In many engineering materials like polycrystals and composites, in addition to discrete atoms, there might also be inhomogeneities, such as precipitates, grains, fibers, etc. Let the characteristic length of these inhomogeneities be measured by D, the radius of curvature of the interface between an inhomogeneity and its surrounding medium. Since D is typically much greater than the atomic spacing h, in the mesoscopic framework of mechanics of materials where the focus is on the material's macroscopic behavior, the discrete atomic structure of the material is smeared (homogenized) into a continuum (Sharma *et al.*, 2003; Sharma and Ganti, 2004; Duan *et al.*, 2005; Zhang and Sharma, 2005; Lim *et al.*, 2006). In other words, the mesoscopic approach simply

implies that $h/D \approx 0$. Intuitively, this is like observing the interface from a far distance so that one cannot see the atomic structure, nor the thickness of the interphase. All one sees is that the properties jump from one bulk value to the other across the interface. Consequently, one may perceive that field quantities are discontinuous at the interface when measured by the mesoscopic length scale *D*. Figure 5.18 illustrates schematically the two different views based on two different length scales.

The results from chapter 4 allow us to establish the relationship between microscopic properties (measured by *h*) and mesoscopic jumps of these properties across the interface measured by *D*.

5.3.2 Mesoscopic Interfacial Conditions

In this section, our attention is given to equations valid at the mesoscopic length scale *D*. The practical interest of this length scale arises from nano-grain crystalline materials, nano-particles reinforced composite materials, multi-layer nano-films, etc. The main objective here is to develop the interfacial conditions for the displacement, strain and stress fields across the interface.

When the inclusion is large enough so that the interface excess energy is negligible, the problem is called the Eshelby inclusion problem (Eshelby, 1957) and the solution is called the Eshelby solution. Eshelby solved the general problem of the elastic state of an inhomogeneity containing eigenstrains located within a foreign material and subjected to an applied external stress. In Eshelby's work, inhomogeneities are defined as embedded particles with material properties differing from the surrounding host material or matrix while eigenstrains are stress-free strains such as lattice parameter mismatch, thermal expansion, inelastic strains, etc. In its present form, Eshelby's formalism does not include the effects of the elastic surface properties (residual surface

tension, surface moduli) of inhomogeneities and their elastic state is entirely based on bulk properties.

When the inclusion approaches nano-size, the interfacial excess energy becomes more prominent and needs to be taken into account in the Eshelby problem. Although various solutions for the Eshelby nano-inclusion problems have appeared in the literature recently (Sharma *et al.*, 2003; Sharma and Ganti, 2004; Duan *et al.*, 2005; Duan *et al.*, 2005; Duan *et al.*, 2005), none has taken the interface effects fully into account. In this section, we will present the interfacial conditions for such Eshelby nano-inclusion problem, accounting the full interface effects.

To this end, we assume that the size of the inclusion D is small enough so that the effect of interface must be considered, but D is still large enough such that $h/D \approx 0$. Typically, this means that the inclusion size is between a few nanometers and a few hundreds nanometers for most crystalline materials / nanocomposites.

5.3.2.1 Kinematic Interfacial Conditions: Displacement Fields Near the Interphase

First, consider the kinematic conditions. Consider an interface S separating two dissimilar linearly elastic solids. Without loss of generality, for any given point on the interface, a reference Cartesian coordinate system x_i $(i = 1,2,3)$ can be chosen so that $x_3 = 0$ is the tangent plane of the interface at $x_1 = x_2 = 0$. Thus, near the neighborhood coordinate origin, the interface can be described by the following equation,

$$F(x_1, x_2, x_3) = f(x_1, x_2) - x_3 = 0 \quad , \tag{5.59}$$

where it is assumed that $f(x_1, x_2)$ is a twice-differentiable function of x_α $(\alpha = 1,2)$ near $x_\alpha = 0$. Thus, Taylor expansion of $f(x_1, x_2)$ near $x_\alpha = 0$ leads to

$$x_3 = f(x_1, x_2) = \frac{1}{2}\kappa_{\alpha\beta} x_\alpha x_\beta + \mathrm{O}(x_\alpha^2) \quad , \tag{5.60}$$

where κ_{11} and κ_{22} are the two curvatures of the interface, and $\kappa_{12} = \kappa_{21} = 0$, provided that x_1 and x_2 are in the directions of the two major curvature lines of the interface at $x_\alpha = 0$.

A parametric form of the surface can be written as

$$x_1 = y_1 \quad , \quad x_2 = y_2 \quad , \quad x_3 = \frac{1}{2}\kappa_{\alpha\beta} y_\alpha y_\beta \quad , \tag{5.61}$$

where y_α are the coordinates of the interface, for a pair of y_α uniquely determines a point on the interface. The metric tensor of the interface is thus given by,

$$a_{\alpha\beta} = \frac{\partial x_i}{\partial y_\alpha}\frac{\partial x_i}{\partial y_\beta} \quad . \tag{5.62}$$

In particular

$$a_{11} = 1 + \kappa_{11}^2 y_1^2 \quad , \quad a_{22} = 1 + \kappa_{22}^2 y_2^2 \quad . \tag{5.63}$$

The unit tangent vector in y_α-axis is given by

$$\mathbf{e}_1 = \frac{1}{\sqrt{a_{11}}}\frac{\partial x_k}{\partial y_1}\mathbf{i}_k = \frac{\mathbf{i}_1 + \kappa_{11} y_1 \mathbf{i}_3}{\sqrt{1 + \kappa_{11}^2 y_1^2}} \quad , \quad \mathbf{e}_2 = \frac{1}{\sqrt{a_{22}}}\frac{\partial x_k}{\partial y_2}\mathbf{i}_k = \frac{\mathbf{i}_2 + \kappa_{22} y_2 \mathbf{i}_3}{\sqrt{1 + \kappa_{22}^2 y_2^2}} \quad , \tag{5.64}$$

where $\mathbf{i}_k$ are the three unit vectors in the Cartesian system x_k. The normal of the interface can the be defined by,

$$\mathbf{e}_3 = \mathbf{e}_1 \times \mathbf{e}_2 = \frac{-\kappa_{11} y_1 \mathbf{i}_1 - \kappa_{22} y_2 \mathbf{i}_2 + \mathbf{i}_3}{\sqrt{1 + \kappa_{11}^2 y_1^2}\sqrt{1 + \kappa_{22}^2 y_2^2}} \quad . \tag{5.65}$$

We are now ready to introduce an orthogonal rectilinear system y_k so that a point in the Cartesian coordinate system x_i can be written as $x_i = y_k \mathbf{e}_k \cdot \mathbf{i}_i$. This allows us to compute the metric tensor g_{ij} between these two systems. At $y_\alpha = 0$ (equivalently $x_\alpha = 0$), we have,

$$\mathbf{g}=\begin{bmatrix}(1-\kappa_{11}y_3)^2 & 0 & 0\\ 0 & (1-\kappa_{22}y_3)^2 & 0\\ 0 & 0 & 1\end{bmatrix} \quad . \tag{5.66}$$

The corresponding Christoffel symbol of the second kind is given by,

$$\begin{Bmatrix} i \\ k \quad j \end{Bmatrix} = g_{il}\frac{\partial^2 x_m}{\partial y_k \partial y_j}\frac{\partial x_m}{\partial y_l} \quad . \tag{5.67}$$

The small strain tensor is thus given by,

$$\varepsilon_{ij}=\frac{1}{2}\left(\frac{\partial u_i}{\partial y_j}+\frac{\partial u_j}{\partial y_i}\right)+\begin{Bmatrix} i \\ k \quad j \end{Bmatrix}u_k \quad , \tag{5.68}$$

where $u_m = u_m(y_1, y_2, y_3)$ are the displacement components in the y_k coordinate system. Specifically at $y_\alpha = 0$, the two coordinate systems x_k and y_k coincide, and we have,

$$\boldsymbol{\varepsilon}=\begin{bmatrix} \frac{\partial u_1}{\partial x_1}-\kappa_{11}u_3 & \frac{1}{2}\left(\frac{\partial u_1}{\partial x_2}+\frac{\partial u_2}{\partial x_1}\right) & \frac{1}{2}\left(\frac{\partial u_1}{\partial x_3}+\frac{\partial u_3}{\partial x_1}+\kappa_{11}u_1\right) \\ \frac{1}{2}\left(\frac{\partial u_1}{\partial x_2}+\frac{\partial u_2}{\partial x_1}\right) & \frac{\partial u_2}{\partial x_2}-\kappa_{22}u_3 & \frac{1}{2}\left(\frac{\partial u_2}{\partial x_3}+\frac{\partial u_3}{\partial x_2}+\kappa_{22}u_2\right) \\ \frac{1}{2}\left(\frac{\partial u_1}{\partial x_3}+\frac{\partial u_3}{\partial x_1}+\kappa_{11}u_1\right) & \frac{1}{2}\left(\frac{\partial u_2}{\partial x_3}+\frac{\partial u_3}{\partial x_2}+\kappa_{22}u_2\right) & \frac{\partial u_3}{\partial x_3} \end{bmatrix} \quad . \tag{5.69}$$

It thus follows (5.69) and (B.4) that the transverse strain $\boldsymbol{\varepsilon}^t$ is given by

$$\boldsymbol{\varepsilon}^t = \mathbf{P}\cdot\left(\nabla u_3+\frac{\partial \mathbf{u}}{\partial x_3}\right)+\frac{\partial u_3}{\partial x_3}\mathbf{n}+\boldsymbol{\kappa}\cdot\mathbf{P}\cdot\mathbf{u}=\frac{\partial \mathbf{u}}{\partial x_3}+\mathbf{P}\cdot\nabla u_3+\boldsymbol{\kappa}\cdot\mathbf{P}\cdot\mathbf{u} \quad . \tag{5.70}$$

where $\mathbf{n}$ is the normal of the interface, and $\mathbf{P}=\mathbf{I}-\mathbf{n}\otimes\mathbf{n}$ is called the surface projection tensor. Furthermore it follows from (5.65) for y_α near $y_\alpha = 0$, here the normal vector of the interface $\mathbf{n}=\mathbf{e}_3$ can be written as

$$n_i = \delta_{3i}-\kappa_{\alpha\beta}y_\beta\delta_{i\alpha} \quad . \tag{5.71}$$

Thus, we have the relationship at $x_\alpha = 0$,

$$\kappa_{\alpha\beta} = -\frac{\partial n_\alpha}{\partial y_\beta} \text{ , or } \boldsymbol{\kappa} = -\nabla_s \mathbf{n} \quad . \tag{5.72}$$

The surface gradient operator ∇_s is defined through the regular three-dimensional gradient operator ∇ by,

$$\nabla_s = \nabla - \mathbf{n}\frac{\partial}{\partial(\mathbf{x}\cdot\mathbf{n})} \quad . \tag{5.73}$$

By making use of the above, the transverse interfacial excess strain can be written as,

$$\boldsymbol{\Delta}^t = \int_{-h}^{h}\left(\mathbf{P}\cdot\nabla u_3 + \frac{\partial \mathbf{u}}{\partial x_3} + \boldsymbol{\kappa}\cdot\mathbf{P}\cdot\mathbf{u}\right)dx_3 - h(\boldsymbol{\varepsilon}_+^t + \boldsymbol{\varepsilon}_-^t) \quad , \tag{5.74}$$

where $\boldsymbol{\varepsilon}_+$ and $\boldsymbol{\varepsilon}_-$ are uniform strain fields in the two materials, respectively, see chapter 4 equation (4.6). Carrying out the integral leads to,

$$\boldsymbol{\Delta}^t = \mathbf{u}(x_1, x_2, h) - \mathbf{u}(x_1, x_2, -h) + \int_{-h}^{h}\left(\mathbf{P}\cdot\nabla u_3 + \boldsymbol{\kappa}\cdot\mathbf{P}\cdot\mathbf{u}\right)dx_3 - h(\boldsymbol{\varepsilon}_+^t + \boldsymbol{\varepsilon}_-^t) \quad . \tag{5.75}$$

When measured by the mesoscopic length scale *D*, i.e., $h/D \approx 0$, and accounting for the uniformity of the strain fields $\boldsymbol{\varepsilon}_+$ and $\boldsymbol{\varepsilon}_-$ (and therefore the uniformity of the displacement field) the above equations reduce to,

$$\boldsymbol{\Delta}^t = \mathbf{u}(x_1, x_2, h) - \mathbf{u}(x_1, x_2, -h) + O\left(h/D\right) \approx \mathbf{u}(x_1, x_2, h) - \mathbf{u}(x_1, x_2, -h/D) \approx [\![\mathbf{u}]\!] \quad . \tag{5.76}$$

where $[\![\mathbf{u}]\!]$ is simply the jump in displacement across the interface in the mesoscopic length scale. It is seen that, although the displacement is continuous everywhere within the interphase when measured by the microscopic length scale *d*, it is not continuous across the interface when measured by the mesoscopic length scale *D*. The jump is nothing but the transverse interfacial excess strain which was computed in the microscopic length scale. Thus equation (5.76) provides a bridge between the microscopic and mesoscopic length scales. It transfers the atomistic information to the mesoscopic behavior. Since $\boldsymbol{\Delta}^t$ is known from equation (4.22) as a function of the applied load $\boldsymbol{\varepsilon}^s$ and $\boldsymbol{\sigma}^t$, equation (5.76) gives the condition for the displacement jump

across the inclusion-matrix interface in the Eshelby nano-inclusion problem. Note that the interface considered here is still a coherent one, i.e., the displacements are continuous across the interfacial region between the inclusion and matrix. The displacement jump in (5.76) is purely an artifact of vanishing thickness of the interfacial region. In other words, if one uses a magnifying glass to zoom in a small (~ d) region near the interface, one would find that the displacement is continuous across the interfacial region. However, if one uses a telescope to view the entire inclusion (~ D), details of the interfacial region becomes invisible and the displacement will appear to be discontinuous across the interface.

To close this section, we mention that in all the above derivations, we have neglected the difference between contravariant and covariant components to simplify the notations. The special choices of the coordinate systems make such simplification possible.

5.3.2.2 Kinetic Interfacial Conditions: Traction Across the Interface

To obtain the kinetic conditions at the interface, consider an interface of area A_0 with normal $\mathbf{n}$. Let the area be bounded by the curve ∂A_0. The outward normal vector of ∂A_0 that is tangent to A_0 is denoted by $\mathbf{m}$. Again, measured by the mesoscopic length scale D, the "thickness" of the interface can be considered zero. The traction vector on the top and bottom of the interface is therefore given by $\boldsymbol{\sigma}\cdot\mathbf{n}$ and $-\boldsymbol{\sigma}\cdot\mathbf{n}$, respectively, while the traction along the edge of the interface is given by $\boldsymbol{\Sigma}^s\cdot\mathbf{m}$. In this case, the static equilibrium of the interface requires,

$$\int_{A_0}[\![\boldsymbol{\sigma}]\!]\cdot\mathbf{n}dA+\int_{\partial A_0}\boldsymbol{\Sigma}^s\cdot\mathbf{m}ds=\mathbf{0}\quad . \tag{5.77}$$

Applying the surface divergence theorem (Gurtin *et al.*, 1998) to the line integral above yields,

$$\int_{A_0} [\![\boldsymbol{\sigma}]\!] \cdot \mathbf{n} + \mathrm{div}_s \left(\boldsymbol{\Sigma}^s \right) dA = \mathbf{0} \quad , \tag{5.78}$$

where $\mathrm{div}_s(\ )$ denotes the surface divergent operator as introduced in (Gurtin *et al.*, 1998).

Since equation (5.78) holds for any surface area A_0, we have immediately,

$$[\![\boldsymbol{\sigma}]\!] \cdot \mathbf{n} + \mathrm{div}_s \left(\boldsymbol{\Sigma}^s \right) = \mathbf{0} \quad \text{on the interface.} \tag{5.79}$$

This is the same equation derived in (Gurtin *et al.*, 1998) by a variational principle approach. A more convenient form of (5.79) is,

$$\mathbf{n} \cdot [\![\boldsymbol{\sigma}]\!] \cdot \mathbf{n} + \boldsymbol{\Sigma}^s : \boldsymbol{\kappa} = 0, \quad \mathbf{P} \cdot [\![\boldsymbol{\sigma}]\!] \cdot \mathbf{n} + \nabla_s \boldsymbol{\Sigma}^s = \mathbf{0} \quad \text{on the interface,} \tag{5.80}$$

The derivation from (5.79) to (5.80) is straightforward by using the following

$$\mathbf{P} \cdot \boldsymbol{\Sigma}^s = \boldsymbol{\Sigma}^s \quad , \quad \mathbf{n} \cdot \boldsymbol{\Sigma}^s = \mathbf{0}, \quad \mathrm{div}_s \left(\mathbf{n} \cdot \boldsymbol{\Sigma}^s \right) = \mathbf{n} \cdot \mathrm{div}_s \left(\boldsymbol{\Sigma}^s \right) + \left(\nabla_s \mathbf{n} \right) : \boldsymbol{\Sigma}^s \quad . \tag{5.81}$$

Summarizing, the interfacial conditions across the inclusion-matrix interface for the Eshelby nano-inclusion problem consist of the following equations on the interface at the continuum length scale,

$$\begin{cases} \mathbf{n} \cdot [\![\boldsymbol{\sigma}]\!] \cdot \mathbf{n} + \boldsymbol{\Sigma}^s : \boldsymbol{\kappa} = 0 \\ \mathbf{P} \cdot [\![\boldsymbol{\sigma}]\!] \cdot \mathbf{n} + \nabla_s \boldsymbol{\Sigma}^s = \mathbf{0} \\ \boldsymbol{\Delta}^t = [\![\mathbf{u}]\!] \end{cases} , \tag{5.82}$$

5.3.3 Inhomogeneity problem

In this section, our attention is given to formulating the Eshelby inhomogeneity problem incorporating the effect of interface properties.

Consider an elastic body/matrix D with elastic modulus $\mathbf{C}_0$ containing an ellipsoidal inhomogeneity Ω with elastic modulus tensor $\mathbf{C}_1$. Let S be the interface between the matrix D and the inhomogeneity Ω. Next, assume D is subjected to surface

traction $\mathbf{p}^0 = \boldsymbol{\sigma}^0 \cdot \mathbf{n}$ on the outer boundary of *D*, as shown in Figure 5.19. We are to find the stress fields in $D \cup \Omega$. If the effect of interface is neglected, the above is referred to as the Eshelby inhomogeneity problem. When the material properties of the inhomogeneity and the matrix are the same, i.e., $\mathbf{C}_1 = \mathbf{C}_0$ the above problem is often referred to as Eshelby's inclusion problem (Mura, 1987).

The equilibrium equation for the stress field is given by,

$$div(\boldsymbol{\sigma}) = 0 \quad , \ \mathbf{x} \subset D \cup \Omega \quad . \tag{5.83}$$

The stresses are related to the strains through the Hooke's law

$$\boldsymbol{\sigma} = \mathbf{C}_0 : \boldsymbol{\varepsilon} , \quad \mathbf{x} \subset D \quad , \tag{5.84}$$

$$\boldsymbol{\sigma} = \mathbf{C}_1 : \boldsymbol{\varepsilon} , \quad \mathbf{x} \subset \Omega \quad . \tag{5.85}$$

In the classical Eshelby problem, the inhomogeneity is assumed perfectly bonded to the matrix and the interfacial excess energy is neglected. In this case, the traction and displacement are continuous across the interface,

$$[\![\boldsymbol{\sigma}]\!] = \mathbf{0} \ , \quad [\![\mathbf{u}]\!] = \mathbf{0} \quad , \tag{5.86}$$

where $[\![\boldsymbol{\sigma}]\!] \equiv \boldsymbol{\sigma}(\mathbf{x})\big|_{\mathbf{x} \subset S^+} - \boldsymbol{\sigma}(\mathbf{x})\big|_{\mathbf{x} \subset S^-}$.

The above problem was solved by Eshelby in 1957. Since then, the Eshelby's solution has played a critical role in developing mesomechanics of heterogeneous media. It is not an over statement that the Eshelby solution is the corner stone of modern mechanics of materials.

However, in many cases, the condition of perfect bonding at the inhomogeneity/matrix interface is inadequate for the description of the physical nature and mechanical behavior of the interface region. Grain boundary sliding in polycrystals and granular materials are common phenomena. Several models incorporate some of the interface properties into the solution of the inclusion properties.

Free sliding models for example allow for free tangential slip at an interface but exclude relative normal displacement. Physically speaking, free sliding models may represent grain boundary sliding in polycrystal behavior of precipitates at high temperature. Free sliding models have been used for example to analyze the local elastic fields and effective properties of composites by Gharemani (Ghahremani, 1980), Jasiuk *et al.* (Jasiuk *et al.*, 1987) among others. In this model the normal traction and displacement are assumed to be continuous across an interface, and the shear traction is assumed to be zero, i.e.

$$\begin{cases} \mathbf{n}\cdot[\![\boldsymbol{\sigma}]\!]\cdot\mathbf{n}=0 \\ \mathbf{P}\cdot\boldsymbol{\sigma}\cdot\mathbf{n}=0 \\ [\![\mathbf{u}]\!]\cdot\mathbf{n}=0 \end{cases} . \tag{5.87}$$

In the linear spring model case, the interface tractions are assumed to be continuous, but the displacements can be discontinuous across an interface, and the displacement discontinuities are proportional to the interface tractions.

$$\begin{cases} [\![\boldsymbol{\sigma}]\!]\cdot\mathbf{n}=0 \\ \mathbf{P}\cdot\boldsymbol{\sigma}\cdot\mathbf{n}=\alpha\mathbf{P}\cdot[\![\mathbf{u}]\!] \\ \mathbf{n}\cdot\boldsymbol{\sigma}\cdot\mathbf{n}=\beta[\![\mathbf{u}]\!]\cdot\mathbf{n} \end{cases} , \tag{5.88}$$

where α and β are interfacial elastic parameters in the tangential and normal direction respectively. Linear spring model has been used to study the stress fields in composites by many researchers such as Qu (Qu, 1993) or Lipton (Lipton and Vernescu, 1996) for example . It was shown for example, that in the case of slightly weakened interfaces, the modified Eshelby tensor would write in the form,

$$\boldsymbol{\varepsilon}=\left(\mathbf{S}+\mathbf{T}(\mathbf{x}):\left(\mathbf{I}-\mathbf{S}\right)\right):\boldsymbol{\varepsilon}^{*} , \tag{5.89}$$

where $\mathbf{T}(\mathbf{x})$ accounts for the displacement jump condition given by the spring stiffness constants. Equation (5.89) provides the first-order asymptotic solution for the total strain

field inside an ellipsoidal inclusion with slightly weakened interface. It is seen that the strains are no longer uniform inside the inclusion.

Recent works (Sharma *et al.*, 2003; Sharma and Ganti, 2004; Duan *et al.*, 2005; Zhang and Sharma, 2005; Lim *et al.*, 2006) revisited the Eshelby solution including the surface energy and interfacial stresses such that the boundary condition transforms into,

$$\begin{cases} \mathbf{n}\cdot[\![\boldsymbol{\sigma}]\!]\cdot\mathbf{n} = -\boldsymbol{\Sigma}^s : \boldsymbol{\kappa} \\ \mathbf{P}\cdot[\![\boldsymbol{\sigma}]\!]\cdot\mathbf{n} = -\nabla_s\boldsymbol{\Sigma}^s \\ [\![\mathbf{u}]\!] = 0 \end{cases} . \tag{5.90}$$

It was shown for example, that in the case of spherical inhomogeneities, assuming that the same relationship between surface energy (or interfacial energy in this case) and surface stress exist for free surfaces and bicrystal surfaces and by neglecting the transverse interfacial behavior, the modified Eshelby tensor would write in the form,

$$\boldsymbol{\varepsilon} = \mathbf{S} : \boldsymbol{\varepsilon}^* - \left(2\kappa s\right)\mathbf{C}^{-1} : \left(\mathbf{S} : \mathbf{I}\right) \ , \tag{5.91}$$

,where κ is the curvature of the interface, the scalar s is related to the in-plane surface stress. As a consequence, the elastic state of inclusions is rendered size-dependent.

The mesoscopic boundary conditions described by equation (5.90) does not account the interfacial excess energy fully. This is because equation (5.90) neglects the transverse deformation of the interface. As discussed in section 5.3.2, when the transverse deformation of the interface is accounted for, the mesoscopic interfacial condition should be

$$\begin{cases} \mathbf{n}\cdot[\![\boldsymbol{\sigma}]\!]\cdot\mathbf{n} = -\boldsymbol{\Sigma}^s : \boldsymbol{\kappa} \\ \mathbf{P}\cdot[\![\boldsymbol{\sigma}]\!]\cdot\mathbf{n} = -\nabla_s\boldsymbol{\Sigma}^s \\ [\![\mathbf{u}]\!] = \boldsymbol{\Delta}^t \end{cases} . \tag{5.92}$$

The boundary value problem described by the governing equations (5.83) – (5.85) and boundary conditions (5.92) has not been solved. As stated in the future recommendation

in chapter 6, its solution is being investigated and the results will be presented in the near future.

5.4 Summary and Conclusions

The main purpose of this chapter is to develop a continuum framework that casts the atomic level information into continuum quantities that can be subsequently used to analyze, model and simulate the macroscopic behavior of nanostructured materials, bridging the gap between discrete systems (atomic level interactions) and continuum mechanics.

In particular, we studied the effects of surface free energy on the effective modulus of nano-particles, nano-wires and nano-films as well as nanostructured crystalline materials and we propose analytical expressions valid for any shape of nanostructural elements / nano-inclusions (integral forms). Explicit expressions of the effective elasticity tensors were obtained for thin films, wires and spherical particles. The solutions derived here show that the overall elastic properties of structural elements (such as particles, wires, films) are size-dependent. Although such size-dependency is negligible for conventional structural elements, it becomes significant when at least one of the dimensions of the structural element shrinks to nanometers. Numerical examples for a variety of materials were given in the chapter to quantitatively illustrate the effects of surface free energy on the elastic properties of nano-sized particles, wires and films. It is found that the effect of surface energy on the elastic behavior becomes significant when one of the characteristic dimensions is below about 15 nm.

Also, similarly to what has been presented in chapter3, and in order to corroborate the above mentioned framework, a semi-analytical method for computing the elastic

properties of nanostructural elements has been developed. This method is semi-analytical in that it expresses the elastic properties explicitly in terms of the inter-atomic potential. It requires only one molecular statics calculation to obtain the self-equilibrium state (relaxed state) of the nanostructural elements. Compared with existing methods, this method has several advantages including (i) it does not require extensive computational resources (~90% reduction in CPU time as compared to full atomistic techniques); (ii) it directly gives the full set of elastic properties; (iii) it is very general and applies to any inter-atomic potential, although an EAM potential was used in this paper in the numerical examples; and (iv) it implicitly accounts for the effects of the shape and size of the nanostructure studied. Nanostructures of different geometric shapes and sizes such as nanowires, nanofilms, and nanoparticles have been studied using this method in a uniform manner without modifications to the formulation. In addition to its efficiency and simplicity, this method yields results which are in excellent agreement with those measured from experiments and predicted by other atomistic methods.

By using the both of the methods mentioned previously, the size-dependence of the elastic properties of nanowires and nanofilms of Cu, Ni, Ag and Pd with the [111], [100] and [110] crystallographic orientations has been investigated. The results show that the size, orientation and shape of the nanostructures influence elastic constants in different manners. Specifically, for the materials studied, decreasing the characteristic size of the nanowires from 8 to 2 nm results in decreases of the elastic modulus of up to 80% for [100] oriented wires and up to 8% for [111] oriented wires and increases between 15% and 37% for [110] oriented wires. In the case of nanofilms, as the film thickness is decreased from 8 to 2 nm, the biaxial modulus can change by up to 50%, 7% and -5% for [100], [111], and [110] films, respectively. Among the materials in this homologous series analyzed, similar trends in elastic properties are observed, consistent with what is reported in the literature.

The continuum framework mentioned above clearly enables the study of the influence of (i) the surface elasticity and (ii) the non-linear behavior of the core of the nanostructure on the softening or stiffening of nanoparticles. Several interesting conclusions were found. First, it was uncovered that the knowledge of the tensile residual surface stress completely defines the relaxed state of nanostructural elements. Second, for the three nanowires' basal orientations and for all the studied materials, the influence of the surface elasticity always contributes to the softening of the wires compared to their equivalent bulk (up to 22% compared with bulk values) while the non linear elastic behavior of the core of the wire affects the size dependence by either softening or stiffening it depending on its orientation. Finally, in the case of the thin films, we demonstrated that, depending on the crystallographic orientation and the modulus considered, the surface elasticity as well as the non linear elasticity of the core of the thin film can contributes to either a size dependence softening or stiffening of the thin films. These results put light on the fact that the knowledge and the clear understanding of the surface elastic behavior and the non linear elastic behavior of the bulk are crucial for accurately predicting the elastic properties of nanostructural elements.

Finally the extension of the Shuttleworth relation presented in chapter 4, enables us to establish the relationship between microscopic properties and mesoscopic jumps of these properties across the interface. More specifically, we derived the kinematic and kinetic interfacial conditions. In turn, these boundary conditions can be used in the formulation of the Eshelby inhomogeneity problem incorporating the effect of interface properties.

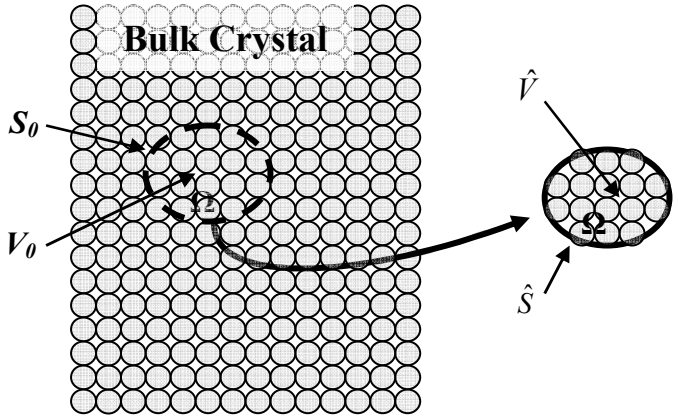

Figure 5.1 A particle is created by removing it from a bulk crystal

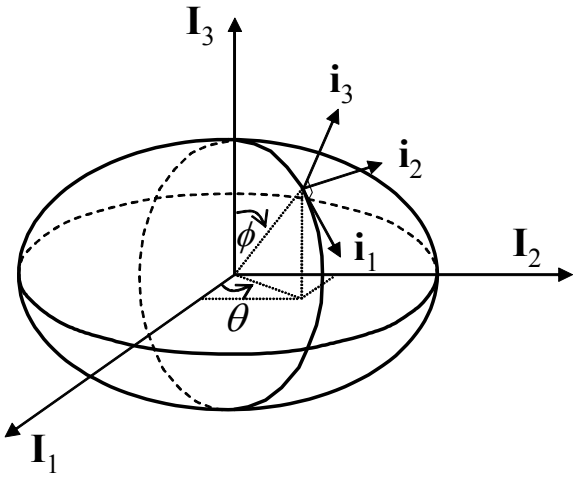

Figure 5.2 An ellipsoidal particle

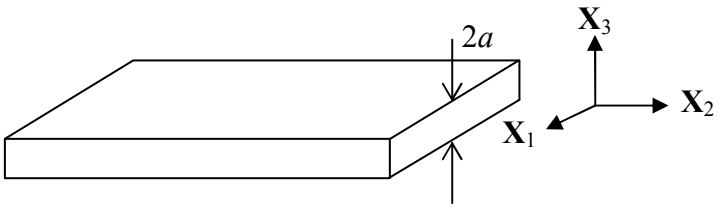

Figure 5.3 A single crystal thin film

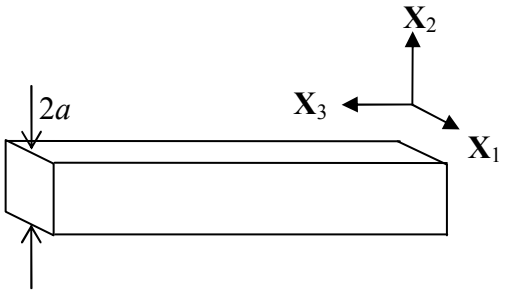

Figure 5.4 A thin wire of square cross-section

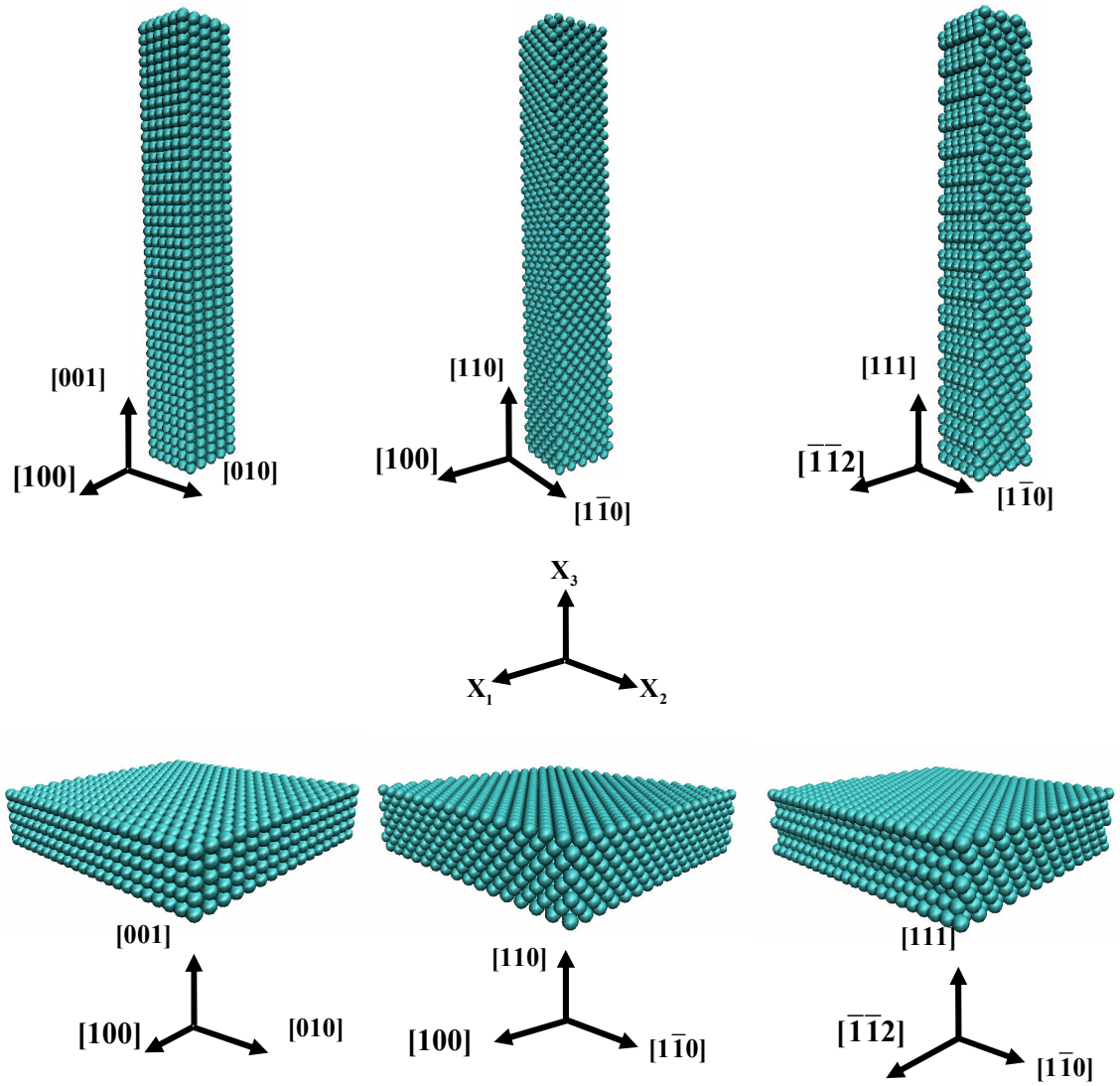

Figure 5.5 Atomistic structures and the crystallographic orientations used in the simulation cells. Periodic boundary conditions are applied in the longitudinal directions (X_3 axis in the case of nanowires, X_1 and X_2 axis in the case of thin films). The transversal directions are kept traction free

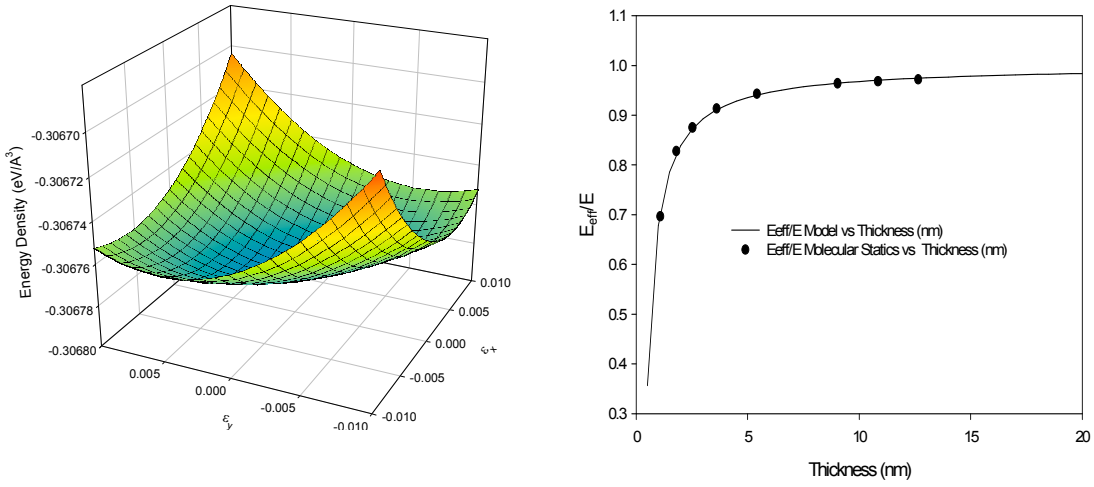

(a) (b)

Figure 5.6 (a) Strain energy density meshing as a function of in-plane strains for Cu thin film (b) Comparison of the in-plane uniaxial Young's modulus of Cu films between meshing method and continuum model presented in section 5.2.1

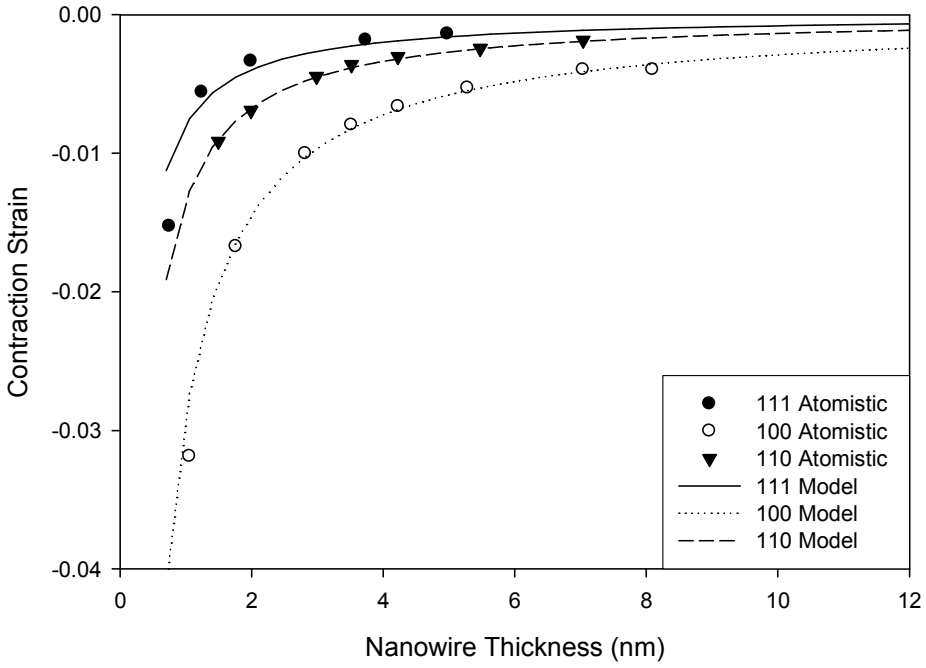

Figure 5.7 Self Equilibrium strain of nickel nanowires as a function of the nanowires thickness for different crystallographic orientations calculated using the EAM potential after energy minimization and compared with self equilibrium strain calculated from equation (5.24)

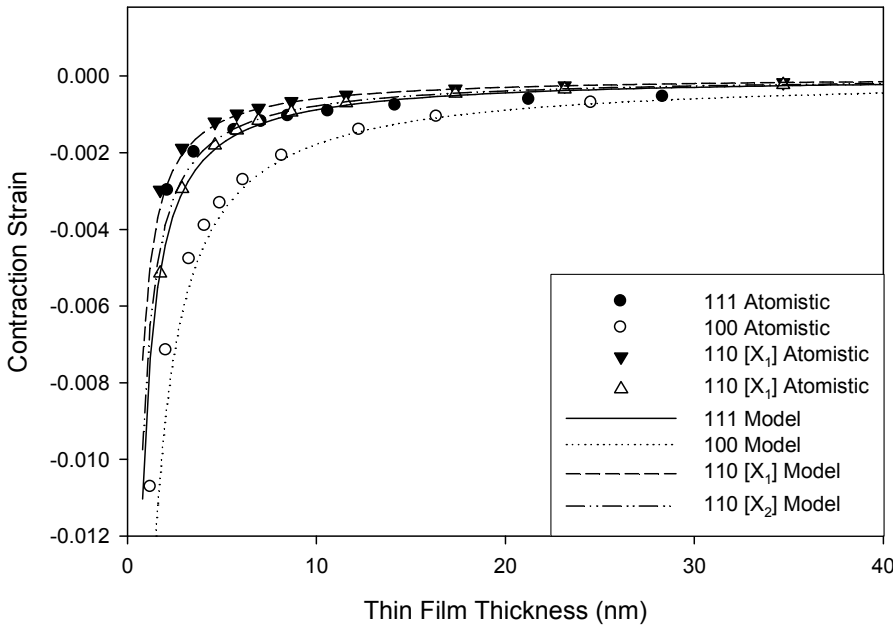

Figure 5.8 Self Equilibrium strain of silver thin films as a function of the films thickness for different crystallographic orientations calculated using the EAM potential after energy minimization and compared with self equilibrium strain calculated from equation (5.24)

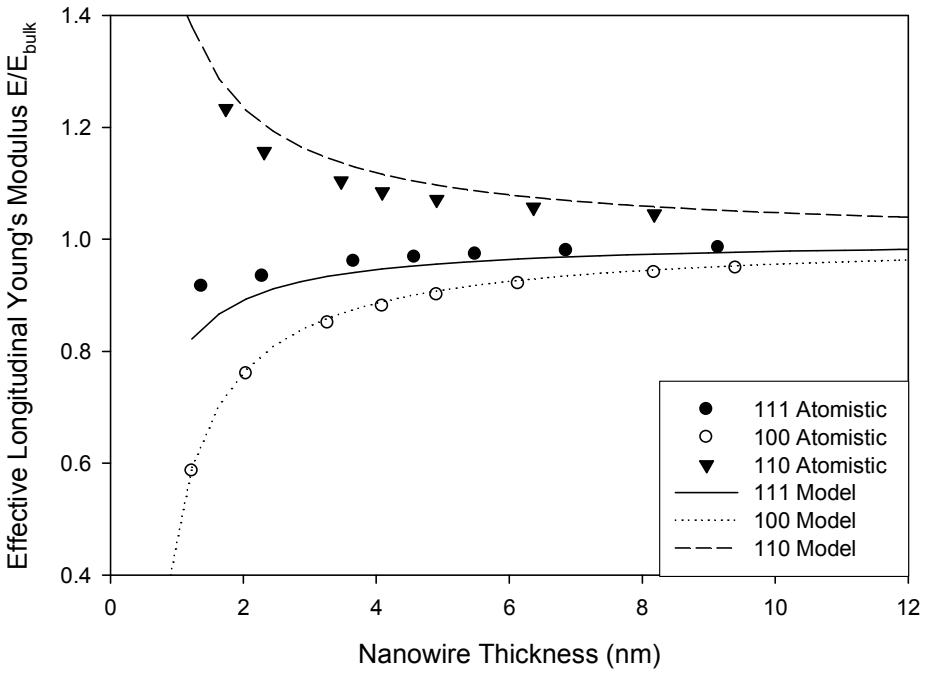

Figure 5.9 Effective longitudinal Young's modulus of silver nanowires as a function of the nanowires thickness calculated using the semi analytical method and compared to the effective longitudinal Young's modulus calculated from equation (5.43)

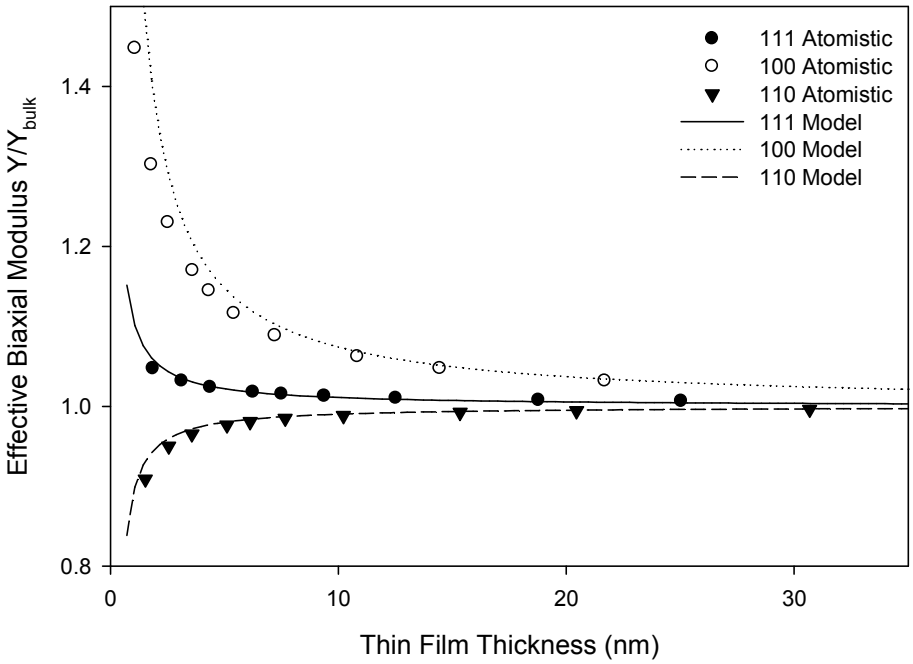

Figure 5.10 Effective biaxial Young's modulus of copper thin films as a function of the film thickness calculated using the semi analytical method and compared to the effective longitudinal Young's modulus calculated from equation (5.38)

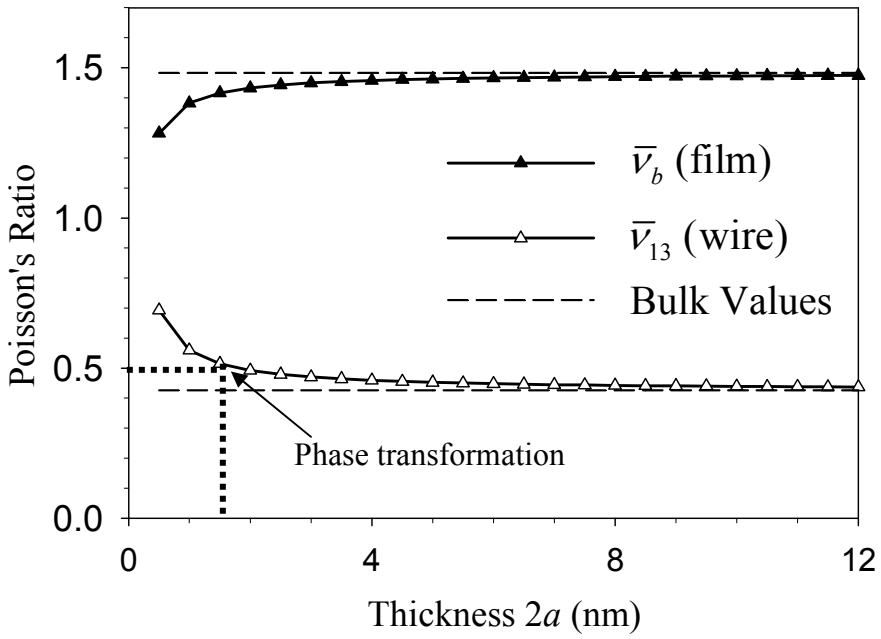

Figure 5.11 Poisson's ratio for the films and the wires of various sizes

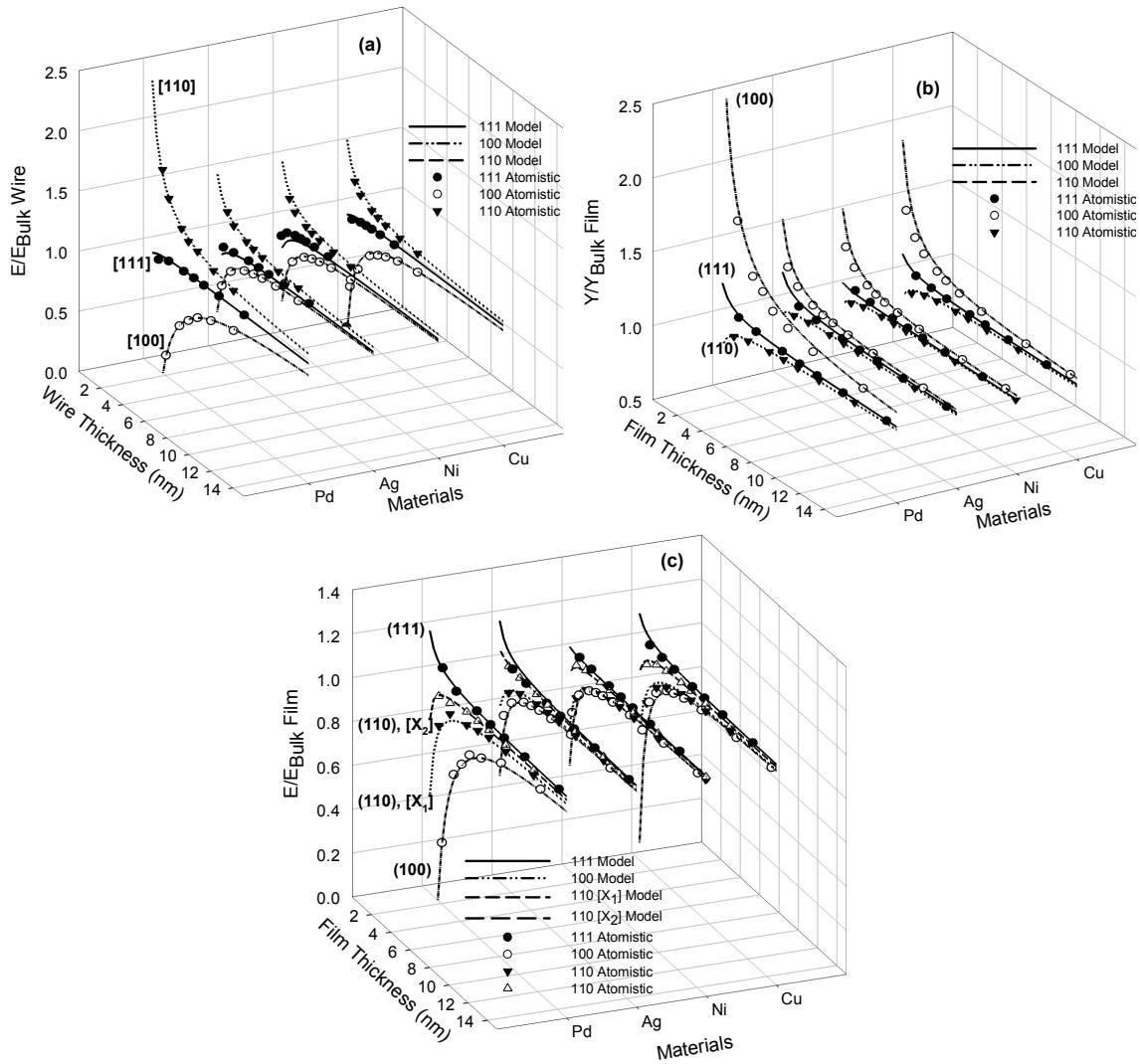

Figure 5.12 Comparison of elastic responses of nanowires and thin films for Cu, Ni, Ag and Pd; (a) Effective longitudinal Young's modulus of nanowires, (b) Effective biaxial Young's modulus of thin films and (c) Effective uniaxial Young's modulus of thin films as a function of the film thickness for various orientations for the studied materials. Atomistic calculation results are compared to the effective longitudinal Young's modulus calculated from section 5.2.1

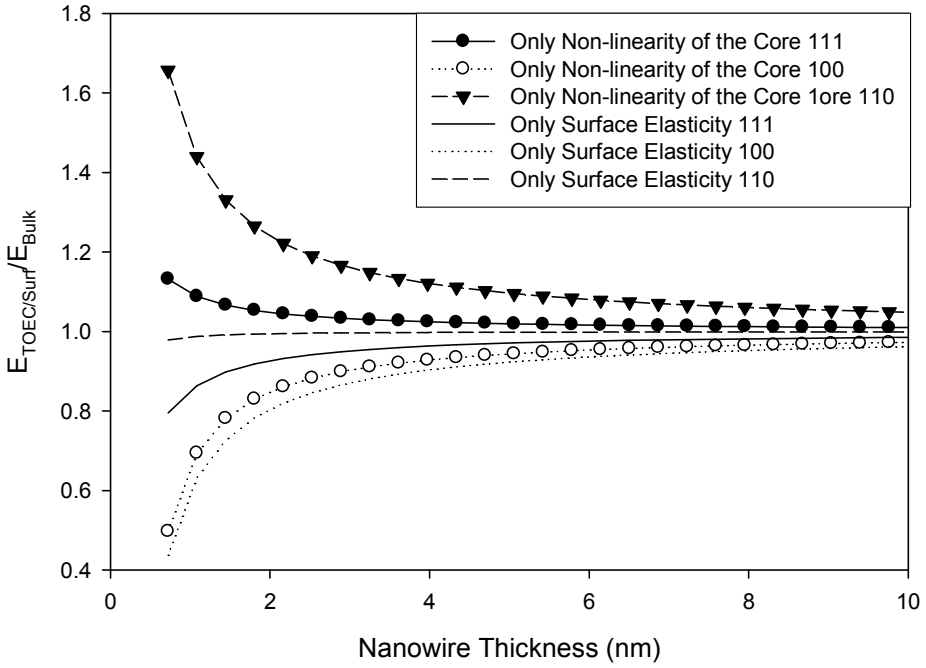

Figure 5.13 Relative effects of surface elasticity and third order elastic constants for copper nanowires

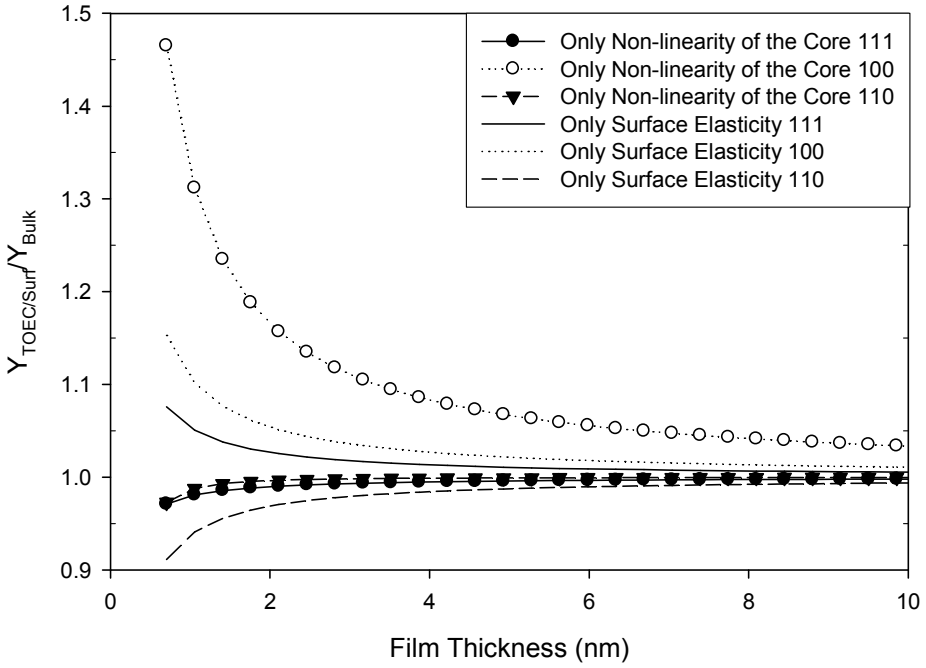

Figure 5.14 Relative effects of the surface elasticity and third order elastic constants for nickel thin films on the biaxial modulus

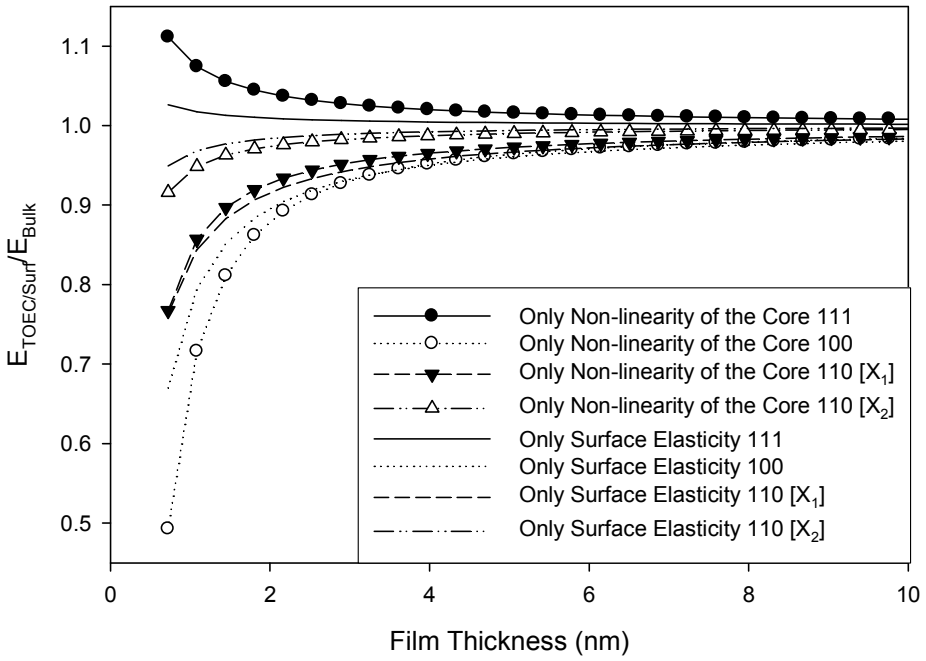

Figure 5.15 Relative effects of the surface elasticity and third order elastic constants for copper thin films on the uniaxial Young's modulus

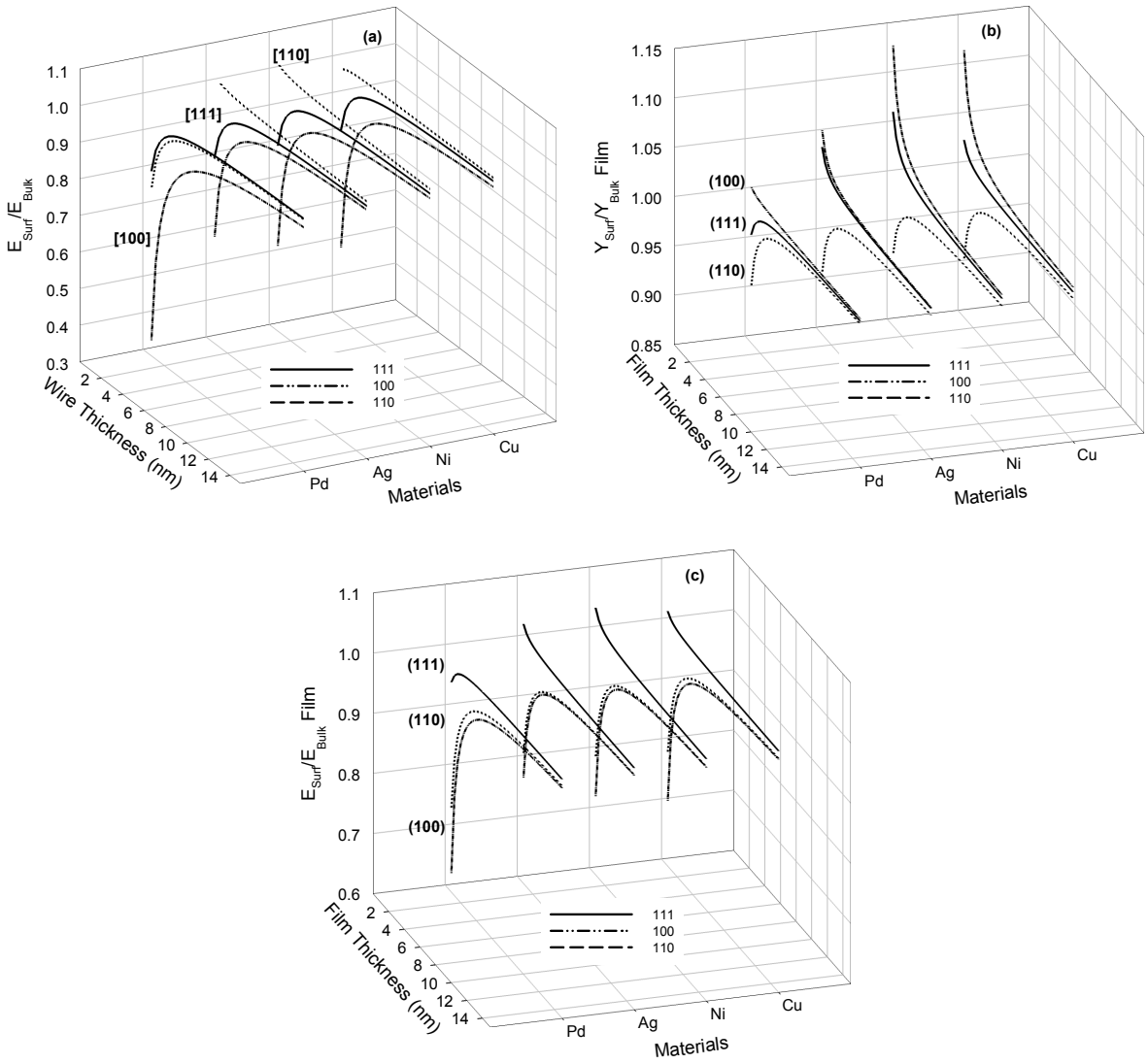

Figure 5.16 Comparison of the effects of surface elasticity on (a) uniaxial Young's modulus of nanowires, (b) biaxial Young's modulus of thin films and (c) uniaxial Young's modulus of thin films as a function of the film thickness and orientation for Cu, Ni, Ag, and Pd

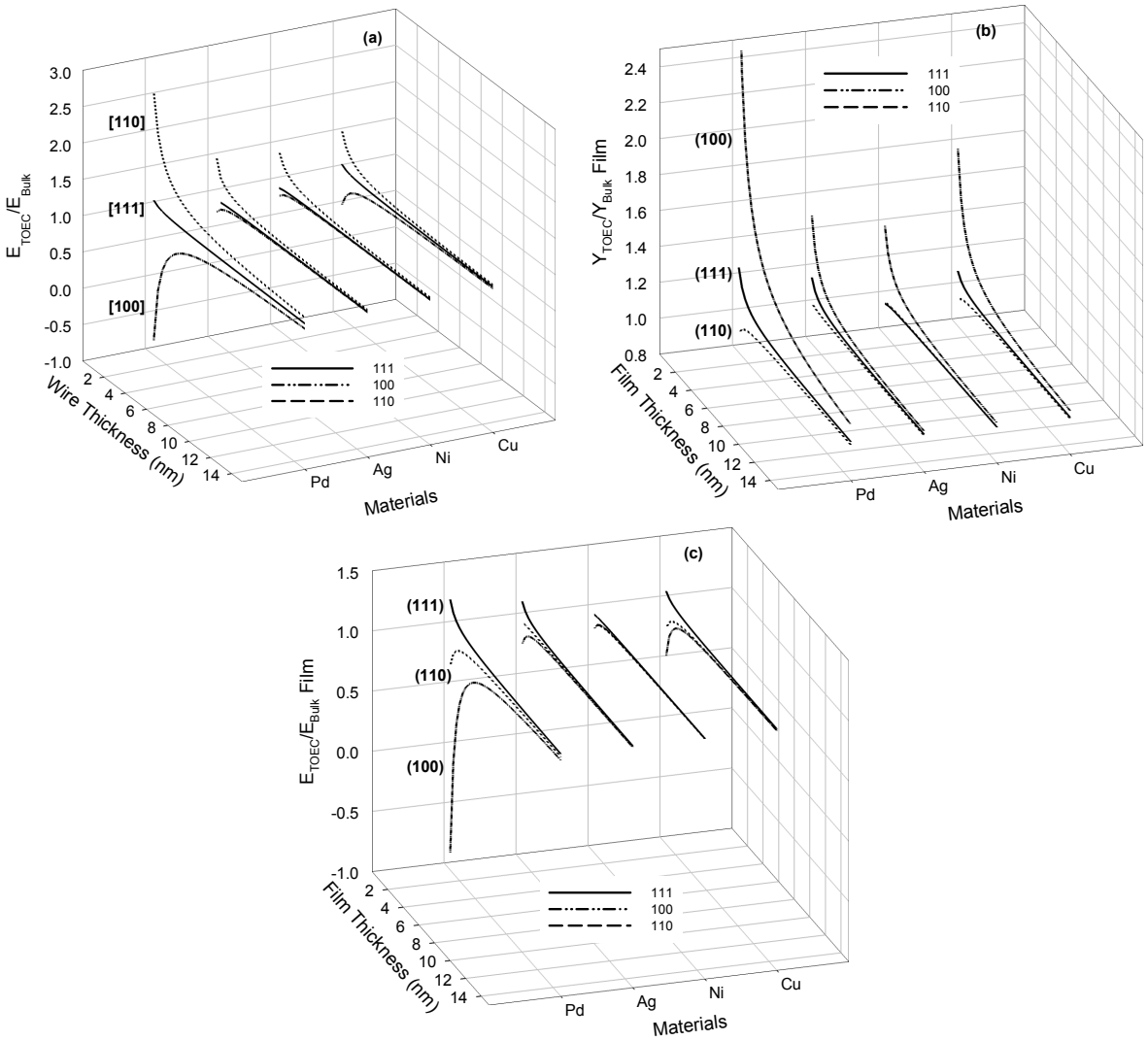

Figure 5.17 Comparison of the effects of core elasticity on (a) uniaxial Young's modulus of nanowires, (b) biaxial Young's modulus of thin films and (c) uniaxial Young's modulus of thin films as a function of the film thickness and orientation for Cu, Ni, Ag, and Pd

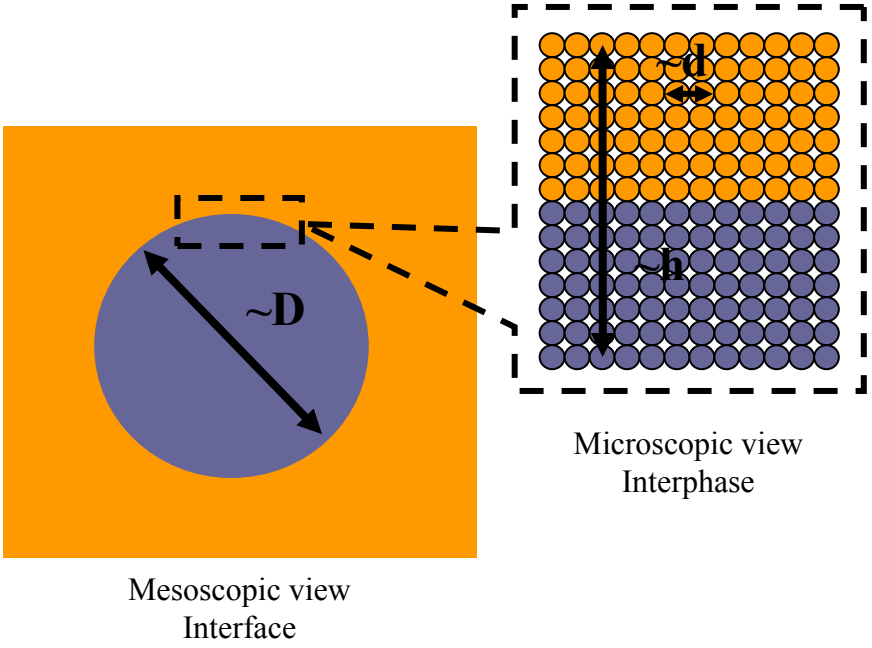

Figure 5.18 Interphase vs. interface: different views based on different length scales

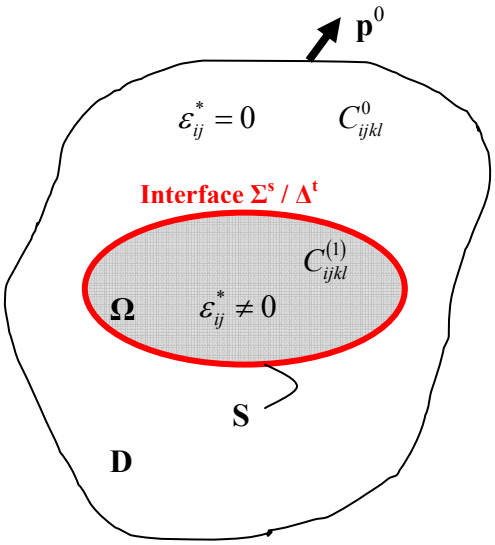

Figure 5.19 Schematic of the inhomogeneity problem

CHAPTER 6

CONCLUSIONS AND RECOMMENDATIONS

6.1 Summary of Significant Contributions

The work presented in this dissertation proposes an innovative approach that combines continuum mechanics and atomistic calculations to develop nanomechanics theories for modeling and predicting the macroscopic behavior of nanomaterials. The discrete atomic structures are cast into thermodynamic quantities and used in a continuum framework. The methodology itself can be used to determine a wide range of effective properties including effective thermal expansion, effective conductivity, effective dielectric constants, etc., as long as the appropriate thermodynamic variables are selected. Furthermore, the process of including surface/interface energy into a continuum mechanics formulation is an innovative approach to link discrete molecular level microstructure to continuum level modeling.

In terms of fundamental science, this approach provides useful information on interfacial mechanics and on how interfacial structure affects macroscopic material behavior. In terms of engineering applications, this methodology proves to be a useful tool for multi-scale modeling of heterogeneous materials with nanometer scale microstructures. The results from this research will make the following fundamental contributions:

(a) Providing surface elastic behavior for several material systems. These data are very useful in many fields including surface science, tribology, fracture mechanics, adhesion science and engineering, etc.

(b) Providing a tool to model and predict the effective properties of nanostructured materials. This will accelerate the insertion of nano-size structural elements, nano-composite and nanocrystalline materials into engineering applications.

We recall the four main objectives to this dissertation: (i) to understand the general behavior of interfaces considered as dividing surfaces; (ii) to provide atomistic tools in order to efficiently determine the behavior of interfaces and surfaces; (iii) to develop, a continuum framework that accounts for the interface effects by casting the atomic level information into continuum quantities and that can be used to analyze, model and simulate macroscopic behavior of nanostructured materials; (iv) to understand the effects of surfaces on the overall behavior of nano-size structural elements (particles, films, fibers, etc.) and nanostructured materials. It is clear that each of these objectives has been addressed by the work presented in this dissertation. In particular, the significant contributions of this work are summarized as follows:

- An easy and simple unified analytical method has been developed for calculating the full set of third order elastic (TOE) constants for single crystal materials based on their interatomic potentials. The method developed here requires only the construction of the crystal of interest. Once the atomic coordinates of the atoms are known, higher order elastic properties can be expressed analytically based on the interatomic potential and its spatial derivatives. Although EAM was used in the present work, the methodology can be applied to any interatomic potential. The method is analytical in that it involves only numerical evaluation of the interatomic potential and its derivatives. The TOE constants of single crystal Cu, Ni, Au, Ag, Pt, Pd and Al were calculated using this method. The comparison of

our results with available literature data shows good agreement with existing experimental data.

- The effective TOE constants of Cu, Ni, Au, Ag, Pt, Pd and Al polycrystals were obtained from their single crystal data using micromechanics tools such as the self-consistent method as well as Voigt and Reuss-type estimates. Although some data are available in the open literature, it is believed that the method presented in Chapter 3 is the only simple unified analytical method to evaluate the TOE constant for single crystals and isotropic aggregates. Compared with other existing methods, this method has several advantages including (i) it does not require extensive computational resources (~99% reduction in CPU time as compared to full atomistic techniques); (ii) it directly gives the full set of elastic properties for both single crystals and polycrystals; (iii) it is very general and applies to any inter-atomic potential, although an EAM potential was used in this work in the numerical examples. Therefore, it constitutes a valuable tool to characterize anharmonicity properties of single crystal and polycrystal materials (such as thermal expansion, Grüneisen parameters, specific heat, interactions of thermal and acoustic phonons, or defects' properties of crystals for example).

- Similarly to the method developed to evaluate the TOE, a semi-analytical method for computing the elastic properties of nanostructural elements (such as nanowires, nanotubes and nanofilms) has been developed. This method is based on the Taylor series expansion of an interatomic potential about the relaxed state of a nanostructure and implicitly accounts for the effects of shape, size and surface of the nanostructures. Calculations were carried out to quantify the size-dependence of the elastic moduli of nanofilms and nanowires with [001], [110], and [111] crystallographic growth orientations for groups 10 and 11 transition metals (Cu, Ni, Pd, and Ag). This method is semi-analytical in that it expresses

the elastic properties explicitly in terms of the inter-atomic potential. It requires only one molecular statics calculation to obtain the self-equilibrium state (relaxed state) of the nanostructural elements. Compared with existing methods, this method has several advantages including (i) it does not require extensive computational resources (~90% reduction in CPU time as compared to full atomistic techniques); (ii) it directly gives the full set of elastic properties; (iii) it is very general and applies to any inter-atomic potential, although an EAM potential was used in this work in the numerical examples; and (iv) it implicitly accounts for the effects of the shape and size of the nanostructure studied. Nanostructures of different geometric shapes and sizes such as nanowires, nanofilms, and nanoparticles can be studied using this method in a uniform manner without modifications to the formulation. In addition to its efficiency and simplicity, this method yields results which are in excellent agreement with those measured from experiments and predicted by other atomistic methods.

- A general framework has been developed to incorporate the surface free energy into the continuum theory of mechanics. Analytical expressions were derived for the effective elastic modulus tensor of nano-sized structural elements that account for the effects of surface free energy. Explicit expressions of the effective elasticity tensors were obtained for thin films, wires and spherical particles. The solutions derived show that the overall elastic properties of structural elements (such as particles, wires, films) are size-dependent. Although such size-dependency is negligible for conventional structural elements, it becomes significant when at least one of the dimensions of the structural element shrinks to nanometers. Numerical examples for nanospheres, nanofilms and nanowires with [001], [110], and [111] crystallographic growth orientations for groups 10 and 11 transition metals (Cu, Ni, Pd, and Ag) were given in to quantitatively illustrate the

effects of surface free energy on the elastic properties of nano-sized particles, wires and films. The results are in excellent agreement with atomistic calculations performed separately. It is found that the effect of surface energy on the elastic behavior becomes significant when one of the characteristic dimensions is below about 15 nm.

- By using both of the methodologies mentioned above, the size-dependence of the elastic properties of nanowires and nanofilms of Cu, Ni, Ag and Pd with the [111], [100] and [110] crystallographic orientations has been investigated. The results show that the size, orientation and shape of the nanostructures influence elastic constants in different manners. Specifically, for the materials studied, decreasing the characteristic size of the nanowires from 8 to 2 nm results in decreases of the elastic modulus of up to 80% for [100] oriented wires and up to 8% for [111] oriented wires and increases between 15% and 37% for [110] oriented wires. In the case of nanofilms, as the film thickness is decreased from 8 to 2 nm, the biaxial modulus can change by up to 50%, 7% and -5% for [100], [111], and [110] films, respectively. Among the materials in this homologous series analyzed, similar trends in elastic properties are observed, consistent with what is reported in the literature.

- The continuum framework mentioned earlier clearly enables the study of the influence of (i) the surface elasticity and (ii) the non-linear behavior of the core of the nanostructure on the softening or stiffening of nanoparticles. First it is shown that the knowledge of the tensile intrinsic surface stress completely defines the relaxed state of nanostructural elements. Second, for the three nanowires' basal orientations and for all the studied materials, the influence of the surface elasticity always contributes to the softening of the wires compared to their equivalent bulk

(up to 22% compared with bulk values) while the non linear elastic behavior of the core of the wire affects the size dependence by either softening or stiffening it depending on its orientation. In the case of thin films, the surface elasticity and the non linear elasticity of the core of the thin film contribute to either the size dependence softening or stiffening of the thin films depending on the crystallographic orientation and the modulus considered. These results put light on the fact that clear understanding of the surface elastic behavior and the non linear elastic behavior of the bulk are crucial for accurately predicting the elastic properties of nanostructural elements.

- We derived in this work a new relationship between the interfacial excess energy and interfacial excess stress for coherent interfaces that is applicable to interfaces in elastic solids under general loading conditions. It is shown that the well-known Shuttleworth relationship between the interfacial excess energy and interfacial excess stress is valid only when the interface is free of transverse stresses. The new formulation accounts for both in-plane and transverse deformation of the interface, and naturally introduces the interfacial stiffness and compliance tensors, as well as the transverse interfacial excess strain. Dually, the concept of transverse interfacial excess strain is also introduced, and the complementary Shuttleworth equation is derived that relates the interfacial excess energy to the newly introduced transverse interfacial excess strain. Such new formulation of interfacial excess stress and excess strain naturally leads to the definition of an in-plane residual stresses tensor $\boldsymbol{\Gamma}^{(1)}$, an in-plane interfacial stiffness tensor $\boldsymbol{\Gamma}^{(2)}$, a transverse interfacial compliance tensor $\boldsymbol{\Lambda}^{(2)}$, and a coupling tensor $\mathbf{H}$ that accounts for the Poisson's effect of the interface, and fully characterizes the elastic behavior of coherent solid bimaterial interfaces upon deformation. It was shown that when both constituents of the bimaterial are isotropic, the interface is

transversely isotropic. Explicit expressions of the interfacial tensors were derived for such transversely isotropic interface in terms of five elastic constants of the interface.

- We proposed in this work semi-analytical methods to evaluate and calculate interfacial elastic properties. The methods presented in this dissertation are based on the idea of expanding the atomic energy and atomic stress into power series of surface strains and transverse stresses and accounting for internal relaxation by appropriately incorporating the equilibrium and traction conditions across the interface. The theoretical framework of the generalized Shuttleworth relationship helps us to subsequently obtain analytical expressions for the interface elastic properties, such as the surface density, intrinsic surface stress and surface elastic stiffness and compliance. Basal free surfaces and low order CSL grain boundaries have been studied using this method in a uniform manner without modifications to the formulation. To evaluate these analytical expressions, one only needs to know the relaxed configuration of the atomic assembly of interest. In comparison with other existing methods, the semi-analytical methods developed here reduce the amount of computation significantly (~95% reduction in CPU time as compared to full atomistic techniques). They also directly give the full set of elastic properties and can be applied to any inter-atomic potential, although an EAM potential was used in this work in the numerical examples. More importantly, because of the analytical nature of these methods, they provide a much better understanding of the interface characteristics and enable us to analytically evaluate the elastic response of a certain interface under any given load without any further computation.

- By using the aforementioned methods, surface elastic properties of low-index surfaces (111), (100) and (110) of Cu, Ni, Ag and Pd were obtained. The results show the presence of a tensile surface stress in all the surface orientations considered, which indicates that these surfaces tend to contract within the surface plane. Comparison of our results with available literature data on Γ_0 and $\Gamma_{\alpha\beta}^{(1)}$ shows good agreement. The surface elastic stiffness data for these materials are believed to be new to the literature. The semi-analytical method presented in section 4.3.1 also enabled us to study the effects of relaxation on the surface elastic constants of free surfaces. These results clearly uncovered the importance of accounting for the surface relaxation and its impact on the surface elastic properties. It is found that, on one hand, the relaxation effects do not or moderately affect the intrinsic surface energy and intrinsic surface stresses (few percents). But on the other hand, the elastic constants are strongly influenced by the relaxation.

- Finally, the extension of the interface theory allows us to establish the relationship between microscopic properties and mesoscopic jumps of these properties across the interface. More specifically, we derived the kinematic and kinetic interfacial conditions. We showed that the jump in displacement across the interface is directly linked to the interfacial strain and the curvature of the interface considered. Similarly, the jump in stress across the interface is directly linked to the surface stresses lying on the interface and its curvature.

6.2 Recommendations for Future Work

One of the fundamental issues addressed in modeling macroscopic mechanical behavior of nano-structured materials based on their discrete structure is the large difference in time and length scales. On the opposite ends of the time and length scale spectrum are atomistic simulation and continuum mechanics, each of which consists of highly developed and reliable modeling methods.

Both the continuum models and the atomistic methods developed in this work provide a mine of information on the link between the atomic-level elastic constants and the macroscopic response of the systems studied. The basic geometries (wires, thin films) and atomic assemblies (free surfaces, low CSL grain boundaries) studied in this dissertation were chosen because they constitute the building-blocks of simple nanostructures and show the path for more complex systems. Consequently, there are a number of issues that are not addressed in this work.

- Based on the previously discussed observation that in nanostructured materials a significant number of atoms reside in the grain boundary region, a micromechanics composite model could be developed to evaluate the yield stress as a function of the grain size. This model could be developed based on the approach described in chapter 5 and in conjunction with the concept of secant moduli of the different constituent (Weng, 1981) and field theory (Khachaturyan, 1995). The constituent nanostructure (either nanocomposites or nanostructural elements) would be modeled with a grain-size dependence plasticity that incorporates the interfacial properties concept developed in this work. Similarly to the approach developed in this work, the overall stress-strain relation of the nanostructure could be calculated in terms of the secant modulus C_{ijkl}^{secant} such that

$\sigma_{ij} = C_{ijkl}^{\text{secant}} \varepsilon_{ij}$. Note that, in this context the secant modulus C_{ijkl}^{secant} would not only be a function of the given state of plastic stress and plastic strain but would also depended on surface behavior. This model would enable the characterization of the overall elasto-plastic behavior of diverse nanostructures and their yield strength as the grain size decreases.

- Since the semi-analytical method presented in chapter 4 section 4.3.2 is written in a general form, calculation should be performed on more complex systems. Ionic free surfaces could constitute such system, since it would be of great interest to calculate surface properties for these type of materials as size dependence of the mechanical properties of ZnO nanobelts as been uncovered experimentally (Lucas *et al.*, 2007) as well as through Molecular Dynamics calculations (Kulkarni *et al.*, 2005; Kulkarni and Zhou, 2006). Knowledge of these surface properties could be subsequently used in the continuum framework presented in chapter 5 to correlate with those experiments.

- The use of this semi-analytical method could also help uncover abnormal phenomena such as the elastic structural transition mentioned in chapter 4. Indeed, by studying the evolution of the excess energy of interfacial system for different grain boundaries with close structures, we could construct a viability space (defined by 7 dimensions: 3 in-plane strains, 3 transverse stresses and the interfacial excess energy) that would predict the evolution of the interface structure in that loading space.

- As suggested in the summary and conclusion of chapter 3, some efforts should address the variational estimates and derivation of possible bounds for the TOEC.

The existing results for nonlinear heterogeneous solids, already considered in the literature (Willis, 1990), may be of significant help. Similarly, another extension of this work would carry on efforts to present a unified method to determine the effective TOEC for transversely isotropic and orthotropic aggregates of cubic crystals estimates and assess bounds for the overall moduli.(Qu and Cherkaoui, 2006). Furthermore, parallel to the analytical method presented here, a thorough experimental study measuring the TOEC for single crystals and polycrystalline would greatly complement this work.

- Based on the discussions presented in chapter 5 section 5.3.3, the classical formulation of Eshelby for embedded inclusions needs to be revisited and modified by incorporating the previously excluded interface stresses, interface strains and interface energies. The extension of the interface theory provides us with both the discontinuity boundary conditions across the interface and the governing equation of interface. It is expected that, in this generalized micromechanic framework, stresses and strains fields would be functions of the interface properties and the size of the inhomogeneities. The dependence of the elastic moduli on the size of the inhomogeneities will highlights the importance of the surface/interface in analysing the deformation of nano-scale structures which in turn would be applicable to analysis of the properties of nano-composites and nanocrystalline materials.

APPENDIX A

TAYLOR EXPANSION OF THE EAM POTENTIAL

The many-body EAM potential postulates that the total energy of an atom *n* can be written as

$$E^{(n)} = G(\rho^{(n)}) + \frac{1}{2}\sum_{m\neq n} V(r^{mn}) \quad , \tag{A.1}$$

where the first term on the right hand side is the embedding energy and the second term is the pair interaction energy. The variable r^{mn} represents the scalar distance between atom *m* and atom *n*. The electron density $\rho^{(n)}$ at the site of atom *n* is taken as a linear superposition of the contributions from all neighboring atoms which are assumed to be spherically symmetric, i.e.,

$$\rho^{(n)} = \sum_{m\neq n} \rho(r^{mn}) \quad . \tag{A.2}$$

Throughout this work, we use the Taylor expansion of the potential energy with respect to the strain such as,

$$E_n = A^{(n)} + A_{ij}^{(n)}\varepsilon_{ij} + \frac{1}{2}A_{ijkl}^{(n)}\varepsilon_{ij}\varepsilon_{kl} + \frac{1}{6}A_{ijklmn}^{(n)}\varepsilon_{ij}\varepsilon_{kl}\varepsilon_{mn} \quad , \tag{A.3}$$

with the quantities $A^{(n)}$, $A_{ij}^{(n)}$, $A_{ijkl}^{(n)}$ and $A_{ijklmn}^{(n)}$ defined by,

$$A^{(n)} = E_n\left(\hat{r}^{mn}\right) \quad , \tag{A.4}$$

$$A_{ij}^{(n)} = \sum_{p\neq n} \left.\frac{r_j^{pn}\partial E_n\left(r^{mn}\right)}{\partial r_i^{pn}}\right|_{r^{mn}=\hat{r}^{mn}} \quad , \tag{A.5}$$

$$A_{ijkl}^{(n)} = \sum_{p\neq n}\sum_{q\neq n} \left.\frac{\hat{r}_j^{pn}\hat{r}_l^{qn}\partial^2 E_n\left(r^{mn}\right)}{\partial r_i^{pn}\partial r_k^{qn}}\right|_{r^{mn}=\hat{r}^{mn}} , \; A_{ijkluv}^{(n)} = \sum_{p\neq n}\sum_{q\neq n}\sum_{s\neq n} \left.\frac{\hat{r}_j^{pn}\hat{r}_l^{qn}\hat{r}_v^{sn}\partial^3 E_n\left(r^{mn}\right)}{\partial r_i^{pn}\partial r_k^{qn}\partial r_u^{sn}}\right|_{r^{mn}=\hat{r}^{mn}} . \tag{A.6}$$

It follows from (A.4) – (A.6) that, for the EAM potential given by (A.1)

$$A^{(n)} = G\left(\sum_{m\neq n}\rho\left(\hat{r}^{mn}\right)\right) + \frac{1}{2}\sum_{m\neq n} V\left(\hat{r}^{mn}\right) \quad , \tag{A.7}$$

$$A_{ij}^{(n)} = \left[\sum_{p \neq n} \hat{r}_j^{pn} \left(\frac{\partial G^{(n)}}{\partial r_i^{pn}} + \frac{\partial V^{(n)}}{2\partial r_i^{pn}} \right) \Bigg|_{r^{mn}=\hat{r}^{mn}} \right]_{<i,j>} , \tag{A.8}$$

$$A_{ijkl}^{(n)} = \left[\sum_{p \neq n} \sum_{q \neq n} \hat{r}_j^{pn} \hat{r}_l^{qn} \left(\frac{\partial^2 G^{(n)}}{\partial r_i^{pn} \partial r_k^{qn}} + \frac{\partial^2 V^{(n)}}{2\partial r_i^{pn} \partial r_k^{qn}} \right) \Bigg|_{r^{mn}=\hat{r}^{mn}} \right]_{<i,j>,<k,l>} , \tag{A.9}$$

$$A_{ijkluv}^{(n)} = \sum_{p \neq n} \sum_{q \neq n} \sum_{s \neq n} \hat{r}_j^{pn} \hat{r}_l^{qn} \hat{r}_v^{sn} \left(\frac{\partial^3 G^{(n)}}{\partial r_i^{pn} \partial r_k^{qn} \partial r_u^{sn}} + \frac{\partial^3 V^{(n)}}{\partial r_i^{pn} \partial r_k^{qn} \partial r_u^{sn}} \right) \Bigg|_{r^{mn}=\hat{r}^{mn}} . \tag{A.10}$$

Making use of the chain rule of differentiation, the derivatives can be carried out explicitly for the pair interaction potential,

$$\frac{\partial V^{(q)}}{\partial r_i^{mn}} = V'(r^{mn}) \frac{r_i^{mn}}{r^{mn}} \left(\delta_{qm} + \delta_{qn} \right) , \tag{A.11}$$

$$\frac{\partial^2 V^{(q)}}{\partial r_i^{mn} \partial r_k^{pn}} = \left[V''(r^{pn}) \frac{r_i^{pn} r_k^{pn}}{(r^{pn})^2} + V'(r^{pn}) \left(\frac{\delta_{ik}}{r^{pn}} - \frac{r_i^{pn} r_k^{pn}}{(r^{pn})^3} \right) \right] \delta_{pm} \left(\delta_{qp} + \delta_{qn} \right) , \tag{A.12}$$

$$\begin{aligned} \frac{\partial^3 V^{(q)}}{\partial r_i^{pn} \partial r_k^{mn} \partial r_u^{sn}} = & \frac{1}{2} \left[\frac{r_i^{pn} r_k^{pn} r_u^{pn}}{\left(r^{pn} \right)^3} \left(V'''\left(r^{pn} \right) - \frac{3}{r^{pn}} \left\{ V''\left(r^{pn} \right) - \frac{V'\left(r^{pn} \right)}{r^{pn}} \right\} \right) \right] \delta_{pm} \delta_{ps} \\ & + \frac{1}{\left(r^{pn} \right)^2} \left(V''\left(r^{pn} \right) - \frac{V'\left(r^{pn} \right)}{r^{pn}} \right) \left(r_i^{pn} \delta_{ku} + r_k^{pn} \delta_{iu} + r_u^{pn} \delta_{ik} \right) \delta_{pm} \delta_{ps} \end{aligned} , \tag{A.13}$$

where a prime, double primes and triple primes on the function indicate the first, second and third derivatives, respectively, with respect to the argument of the function. For example, $V''(r) = d^2V/dr^2$.

In the case of the embedding energy we have,

$$\frac{\partial \rho^{(q)}}{\partial r_i^{mn}} = \rho'(r^{mn}) \frac{r_i^{mn}}{r^{mn}} \left(\delta_{qm} + \delta_{qn} \right) , \tag{A.14}$$

$$\frac{\partial^2 \rho^{(q)}}{\partial r_i^{mn} \partial r_k^{pn}} = \left[\rho''(r^{pn}) \frac{r_i^{pn} r_k^{pn}}{(r^{pn})^2} + \rho'(r^{pn}) \left(\frac{\delta_{ik}}{r^{pn}} - \frac{r_i^{pn} r_k^{pn}}{(r^{pn})^3} \right) \right] \delta_{pm} \left(\delta_{qp} + \delta_{qn} \right) , \tag{A.15}$$

$$\frac{\partial^3\rho^{(q)}}{\partial r_i^{pn}\partial r_k^{mn}\partial r_u^{sn}}=\frac{1}{2}\left[\frac{r_i^{pn}r_k^{pn}r_u^{pn}}{\left(r^{pn}\right)^3}\left(\rho'''\left(r^{pn}\right)-\frac{3}{r^{pn}}\left\{\rho''\left(r^{pn}\right)-\frac{\rho'\left(r^{pn}\right)}{r^{pn}}\right\}\right)\right]\delta_{pm}\delta_{ps}$$
$$+\frac{1}{\left(r^{pn}\right)^2}\left(\rho''\left(r^{pn}\right)-\frac{\rho'\left(r^{pn}\right)}{r^{pn}}\right)\left(r_i^{pn}\delta_{ku}+r_k^{pn}\delta_{iu}+r_u^{pn}\delta_{ik}\right)\delta_{pm}\delta_{ps} \quad .(A.16)$$

For the background electron density and,

$$\frac{\partial G^{(q)}}{\partial r_i^{mn}}=G'\left(\sum_{p\neq q}\rho(r^{pq})\right)\rho'(r^{mn})\frac{r_i^{mn}}{r^{mn}}\left(\delta_{qm}+\delta_{qn}\right) \quad , \quad (A.17)$$

$$\frac{\partial^2 G^{(q)}}{\partial r_i^{mn}\partial r_k^{pn}}=G''\left(\sum_{u\neq q}\rho(r^{uq})\right)\left(\frac{\partial\rho}{\partial r_i^{mn}}\right)\left(\frac{\partial\rho}{\partial r_k^{pn}}\right)\delta_{pm}\left(\delta_{qp}+\delta_{qn}\right)$$
$$+G'\left(\sum_{u\neq q}\rho(r^{uq})\right)\left(\frac{\partial^2\rho}{\partial r_i^{pn}\partial r_k^{qn}}\right)\delta_{pm}\left(\delta_{qp}+\delta_{qn}\right) \quad , \quad (A.18)$$

$$\frac{\partial^3 G^{(q)}}{\partial r_i^{pn}\partial r_k^{mn}\partial r_u^{sn}}=G'''\left(\sum_{m\neq n}\rho\left(r^{mn}\right)\right)\left(\frac{\partial\rho}{\partial r_i^{pn}}\right)\left(\frac{\partial\rho}{\partial r_k^{mn}}\right)\left(\frac{\partial\rho}{\partial r_u^{sn}}\right)$$
$$+G''\left(\sum_{m\neq n}\rho\left(r^{mn}\right)\right)\left[\left(\frac{\partial\rho}{\partial r_i^{pn}}\right)\left(\frac{\partial^2\rho}{\partial r_k^{mn}\partial r_u^{sn}}\right)+\left(\frac{\partial\rho}{\partial r_k^{mn}}\right)\left(\frac{\partial^2\rho}{\partial r_i^{pn}\partial r_u^{sn}}\right)\right. \quad . \quad (A.19)$$
$$\left.+\left(\frac{\partial\rho}{\partial r_u^{sn}}\right)\left(\frac{\partial^2\rho}{\partial r_i^{pn}\partial r_k^{mn}}\right)\right]+G'\left(\sum_{m\neq n}\rho\left(r^{mn}\right)\right)\left(\frac{\partial^3\rho}{\partial r_i^{pn}\partial r_k^{mn}\partial r_u^{sn}}\right)$$

APPENDIX B

"T" STRESS DECOMPOSITION

Consider an inhomogeneous, linearly elastic solid with strain energy density per unit undeformed volume given by

$$w = w_0 + \tau_{ij}\varepsilon_{ij} + \frac{1}{2}C_{ijkl}\varepsilon_{ij}\varepsilon_{kl} \quad , \tag{B.1}$$

where ε_{ij} is the Lagrangian strain tensor. Note that all the material constants in (B.1) have the proper symmetry and may depend on the spatial coordinate x_i, but are not necessarily positive definite. The corresponding second Piola-Kirchhoff stress tensor is thus given by

$$\sigma_{ij} = \frac{\partial W}{\partial \varepsilon_{ij}} = \tau_{ij} + C_{ijkl}\varepsilon_{kl} \quad . \tag{B.2}$$

It can be easily shown that (B.2) is equivalently to

$$\sigma^s_{\alpha\beta} = \tau^s_{\alpha\beta} + C_{\alpha\beta\kappa\lambda}\varepsilon^s_{\kappa\lambda} + C_{\alpha\beta 3k}\varepsilon^t_k \quad , \quad \sigma^t_j = \tau^t_j + C_{3j\kappa\lambda}\varepsilon^s_{\kappa\lambda} + C_{3j3k}\varepsilon^t_k \quad , \tag{B.3}$$

where the summation convention is implied, and the lower case Roman subscripts go from 1 to 3 and the lower case Greek subscripts go from 1 to 2, and

$$\sigma^s_{\alpha\beta} = \sigma_{\alpha\beta} \, , \quad \varepsilon^s_{\kappa\lambda} = \varepsilon_{\kappa\lambda} \, , \quad \sigma^t_j = \sigma_{3j} \, , \quad \varepsilon^t_\alpha = 2\varepsilon_{\alpha 3} \, , \quad \varepsilon^t_3 = \varepsilon_{33} \, , \quad \tau^s_{\alpha\beta} = \tau_{\alpha\beta} \, , \quad \tau^t_j = \tau_{3j} \quad . \tag{B.4}$$

Making use of the above notation conventions, we may write (B.1) in an alternative form

$$w = w_0 + \frac{1}{2}\tau^s_{\alpha\beta}\varepsilon^s_{\alpha\beta} + \frac{1}{2}\tau^t_j\varepsilon^t_j + \frac{1}{2}\sigma^s_{\alpha\beta}\varepsilon^s_{\alpha\beta} + \frac{1}{2}\sigma^t_j\varepsilon^t_j \quad . \tag{B.5}$$

If C_{3j3k} as a second order tensor is invertible, then it follows from the second of (B.3) that

$$\varepsilon_k^t = -M_{kj}\tau_j^t + M_{kj}\sigma_j^t - \gamma_{k\alpha\beta}\varepsilon_{\alpha\beta}^s \quad , \tag{B.6}$$

where

$$M_{kj} = C_{3k3j}^{-1} \ , \ \gamma_{j\alpha\beta} = M_{jk}C_{3k\alpha\beta} \quad . \tag{B.7}$$

Substituting (B.6) into the first of (B.3) yields

$$\sigma_{\alpha\beta}^s = \hat{\tau}_{\alpha\beta}^s + C_{\alpha\beta\kappa\lambda}^s\varepsilon_{\kappa\lambda}^s + \gamma_{j\alpha\beta}\sigma_j^t \quad , \tag{B.8}$$

where

$$\hat{\tau}_{\alpha\beta}^s = \tau_{\alpha\beta}^s - \tau_j^t\gamma_{j\alpha\beta} \ , \ C_{\alpha\beta\kappa\lambda}^s = C_{\alpha\beta\kappa\lambda} - C_{\alpha\beta3j}\gamma_{j\kappa\lambda} \quad . \tag{B.9}$$

Substituting (B.6) – (B.8) into (B.5) yields

$$w = \hat{w}_0 + \hat{\tau}_{\alpha\beta}^s\varepsilon_{\alpha\beta}^s + \frac{1}{2}C_{\alpha\beta\kappa\lambda}^s\varepsilon_{\kappa\lambda}^s\varepsilon_{\alpha\beta}^s + \frac{1}{2}\sigma_j^t M_{kj}\sigma_k^t \quad , \tag{B.10}$$

where

$$\hat{w}_0 = w_0 - \frac{1}{2}M_{kj}\tau_k^t\tau_j^t \quad . \tag{B.11}$$

In matrix notations, (B.6), (B.8) and (B.10) can be written, respectively, as

$$\boldsymbol{\varepsilon}^t = -\mathbf{M}\cdot\boldsymbol{\tau}^t + \mathbf{M}\cdot\boldsymbol{\sigma}^t - \boldsymbol{\gamma}:\boldsymbol{\varepsilon}^s \quad , \tag{B.12}$$

$$\boldsymbol{\sigma}^s = \hat{\boldsymbol{\tau}}^s + \mathbf{C}^s:\boldsymbol{\varepsilon}^s + \boldsymbol{\sigma}^t:\boldsymbol{\gamma} \quad , \tag{B.13}$$

$$w = \hat{w}_0 + \hat{\boldsymbol{\tau}}^s:\boldsymbol{\varepsilon}^s + \frac{1}{2}\boldsymbol{\varepsilon}^s:\mathbf{C}^s:\boldsymbol{\varepsilon}^s + \frac{1}{2}\boldsymbol{\sigma}^t\cdot\mathbf{M}\cdot\boldsymbol{\sigma}^t \quad . \tag{B.14}$$

If the material is isotropic, i.e,

$$C_{ijkl} = \lambda\delta_{ij}\delta_{kl} + \mu\left(\delta_{ik}\delta_{jl} + \delta_{il}\delta_{jk}\right) \quad , \tag{B.15}$$

where λ and μ are the Lamé constants. It thus follows from (B.7), (B.9), and (B.15)that

$$C_{3k3j} = (\lambda + \mu)\delta_{3k}\delta_{3j} + \mu\delta_{kj} \quad , \tag{B.16}$$

$$M_{kj} = -\frac{\lambda + \mu}{(\lambda + 2\mu)\mu}\delta_{3k}\delta_{3j} + \frac{1}{\mu}\delta_{kj} \ , \ \gamma_{i\alpha\beta} = \frac{\lambda}{\lambda + 2\mu}\delta_{3i}\delta_{\alpha\beta} \quad , \tag{B.17}$$

$$C^s_{\alpha\beta\kappa\lambda} = \frac{2\lambda\mu}{\lambda + 2\mu}\delta_{\alpha\beta}\delta_{\kappa\lambda} + \mu\left(\delta_{\alpha\kappa}\delta_{\beta\lambda} + \delta_{\alpha\lambda}\delta_{\beta\kappa}\right) \quad , \tag{B.18}$$

$$\hat{\tau}^s_{\alpha\beta} = \tau^s_{\alpha\beta} - \tau^t_j\gamma_{j\alpha\beta} = \tau^s_{\alpha\beta} - \tau^t_3\frac{\lambda}{\lambda + 2\mu}\delta_{\alpha\beta} \quad . \tag{B.19}$$

APPENDIX C

ATOMIC LEVEL STRESS AND INTERNAL RELAXATION

Atomic Level Mapping

In order to account for the inner displacements, we first define an atomic level mapping between the undeformed and deformed configuration by

$$r_i^m - \hat{r}_i^m = \left(\overline{\varepsilon}_{ij}^{\pm} + \tilde{\varepsilon}_{ij}^m\right)\hat{r}_j^m \quad , \tag{C.1}$$

where $\overline{\varepsilon}_{ij}^{\pm}$ corresponds to a homogeneous deformation of atom *m* and $\tilde{\varepsilon}_{ij}^m$ describes the "inner" relaxation (or additional "non-homogeneous" deformation) of atom *m* with respect to a homogeneous deformation. The positive (or negative) sign should be selected if atom *m* is in the upper (or lower) crystal. The atomic position of atom *m* is measured from a fixed reference point.

The homogeneous deformation of the bicrystal assembly can be described by an in-plane deformation $\varepsilon_{\alpha\beta}^s$ and a transverse loading σ_i^t ("T" stress). Derivations and detailed expressions are presented in the Appendix. The homogeneous deformation is expressed as a function of these two global variables such that (C.1) transforms into,

$$r_i^m - \hat{r}_i^m = \left(A_{ij\alpha\beta}^{\pm}\varepsilon_{\alpha\beta}^s + B_{ijk}^{\pm}\sigma_k^t\right)\hat{r}_j^m + \tilde{\varepsilon}_{ij}^m\hat{r}_j^m \quad , \tag{C.2}$$

with,

$$A_{ij\alpha\beta}^{\pm} = \delta_{i\alpha}\delta_{j\beta} - \frac{1}{2}\left(\gamma_{j\alpha\beta}^{\pm}\delta_{3i} + \gamma_{i\alpha\beta}^{\pm}\delta_{3j}\right) \quad , \tag{C.3}$$

$$B_{ijk}^{\pm} = \frac{1}{2}\left(M_{jk}^{\pm}\delta_{3i} + M_{ik}^{\pm}\delta_{3j}\right) \quad ,$$

where $\gamma_{j\alpha\beta}^{\pm}$ and $M_{jk}^{\pm}$ are given in the Appendix B. Note that $A_{ij\alpha\beta}^{\pm}$ and $B_{ijk}^{\pm}$ are known tensors and characterize the homogeneous behavior of the bicrystal.

The difference in position of two atoms near their relaxed state is therefore given by,

$$r_i^{mn} - \hat{r}_i^{mn} = A_{i\alpha\beta}^{mn}\varepsilon_{\alpha\beta}^{s} + B_{ik}^{mn}\sigma_k^{t} + \left(\tilde{\varepsilon}_{ij}^{m}\hat{r}_j^{m} - \tilde{\varepsilon}_{ij}^{n}\hat{r}_j^{n}\right) \quad , \tag{C.4}$$

where,

$$A_{i\alpha\beta}^{mn} = \left(A_{ij\alpha\beta}^{\pm,m} + A_{ij\alpha\beta}^{\pm,n}\right)\hat{r}_j^{mn} - \left(A_{ij\alpha\beta}^{\pm,n}\hat{r}_j^{m} - A_{ij\alpha\beta}^{\pm,m}\hat{r}_j^{n}\right) \quad , \tag{C.5}$$

and,

$$B_{ik}^{mn} = \left(B_{ijk}^{\pm,m} + B_{ijk}^{\pm,n}\right)\hat{r}_j^{mn} - \left(B_{ijk}^{\pm,n}\hat{r}_j^{m} - B_{ijk}^{\pm,m}\hat{r}_j^{n}\right) \quad . \tag{C.6}$$

Total Energy of the Atomic Assembly

As reported by Johnson (1972), one can expand the energy density of an atom *n* about its equilibrium configuration.

$$w^n = \frac{1}{\Omega_n}\sum_{\substack{m=1\\m\neq n}}^{N}\left[E^{(n)}\left(r^{nm}\right)\Big|_{r^{nm}=\hat{r}^{nm}} + \frac{\partial E^{(n)}}{\partial r_i^{nm}}\Big|_{r^{nm}=\hat{r}^{nm}}\left(r_i^{nm} - \hat{r}_i^{nm}\right) + \frac{1}{2}\sum_{\substack{p=1\\p\neq n}}^{N}\frac{\partial E^{(n)}}{\partial r_i^{nm}r_k^{np}}\Big|_{r^{nm}=\hat{r}^{nm}}\left(r_i^{nm} - \hat{r}_i^{nm}\right)\left(r_k^{np} - \hat{r}_k^{np}\right) + \cdots\right] . \tag{C.7}$$

The total strain energy density of the system, *E*, is defined by the sum $\sum_n w^n$. Substituting equation (C.4) into equation (C.7) yields for the total strain energy of the atomic assembly,

$$E = E_0 + \overline{A}_{\alpha\beta}^{(1)}\varepsilon_{\alpha\beta}^{s} + \overline{B}_k^{(1)}\sigma_k^{t} + \frac{1}{2}\overline{A}_{\alpha\beta\kappa\lambda}^{(2)}\varepsilon_{\alpha\beta}^{s}\varepsilon_{\kappa\lambda}^{s} + \frac{1}{2}\overline{B}_{uv}^{(2)}\sigma_u^{t}\sigma_v^{t} + \overline{Q}_{\alpha\beta u}\varepsilon_{\alpha\beta}^{s}\sigma_u^{t} + \sum_{n=1}^{N-1}\left(K_{ij}^{n} + D_{ij\alpha\beta}^{n}\varepsilon_{\alpha\beta}^{s} + G_{ijk}^{n}\sigma_k^{t}\right)\tilde{\varepsilon}_{ij}^{n} + \frac{1}{2}\sum_{n=1}^{N-1}\sum_{m=1}^{N-1}L_{ijkl}^{mn}\tilde{\varepsilon}_{ij}^{n}\tilde{\varepsilon}_{kl}^{m} \quad , \tag{C.8}$$

with,

$$E_0 = \sum_n \frac{1}{\Omega_n}\sum_{m\neq n}E^{(n)}\left(r^{nm}\right)\Big|_{r^{mn}=\hat{r}^{mn}} \quad , \tag{C.9}$$

$$\overline{A}_{\alpha\beta}^{(1)} = \sum_n \frac{1}{\Omega_n}\sum_{m\neq n}\frac{\partial E^{(n)}}{\partial r_i^{nm}}\Big|_{r^{mn}=\hat{r}^{mn}} A_{i\alpha\beta}^{mn} \quad , \tag{C.10}$$

$$\overline{B}_k^{(1)} = \sum_n \frac{1}{\Omega_n} \sum_{m \neq n} \left. \frac{\partial E^{(n)}}{\partial r_i^{nm}} \right|_{r^{mn} = \hat{r}^{mn}} B_{ik}^{mn} \quad , \tag{C.11}$$

$$\overline{A}_{\alpha\beta\kappa\lambda}^{(2)} = \sum_n \frac{1}{\Omega_n} \sum_{m \neq n} \left. \frac{\partial^2 E^{(n)}}{\partial r_i^{nm} \partial r_k^{nm}} \right|_{r^{mn} = \hat{r}^{mn}} A_{i\alpha\beta}^{mn} A_{k\kappa\lambda}^{mn} \quad , \tag{C.12}$$

$$\overline{B}_{jl}^{(2)} = \sum_n \frac{1}{\Omega_n} \sum_{m \neq n} \left. \frac{\partial^2 E^{(n)}}{\partial r_i^{nm} \partial r_k^{nm}} \right|_{r^{mn} = \hat{r}^{mn}} B_{ij}^{mn} B_{kl}^{mn} \quad , \tag{C.13}$$

$$\overline{Q}_{\alpha\beta j} = \sum_n \frac{1}{\Omega_n} \sum_{m \neq n} \left. \frac{\partial^2 E^{(n)}}{\partial r_i^{nm} \partial r_k^{nm}} \right|_{r^{mn} = \hat{r}^{mn}} A_{i\alpha\beta}^{mn} B_{kj}^{mn} \quad , \tag{C.14}$$

which describe the homogeneous behavior of the assembly upon a deformation configuration $\left(\varepsilon_{\alpha\beta}^s,\ \sigma_k^t\right)$ while,

$$\begin{aligned} K_{ij}^n = & \frac{1}{2\Omega_n} \hat{r}_j^n \left(\sum_{p \neq n} \left. \frac{\partial E^{(p)}}{\partial r_i^{pn}} \right|_{r^{pn} = \hat{r}^{pn}} - \left. \frac{\partial E^{(n)}}{\partial r_i^{pn}} \right|_{r^{pn} = \hat{r}^{pn}} \right) \\ & + \frac{1}{2\Omega_n} \hat{r}_i^n \left(\sum_{p \neq n} \left. \frac{\partial E^{(p)}}{\partial r_j^{pn}} \right|_{r^{pn} = \hat{r}^{pn}} - \left. \frac{\partial E^{(n)}}{\partial r_j^{pn}} \right|_{r^{pn} = \hat{r}^{pn}} \right) \end{aligned} \quad , \tag{C.15}$$

$$\begin{aligned} D_{ij\alpha\beta}^n = & \frac{1}{2\Omega_n} \hat{r}_j^n \sum_{p \neq n} \sum_{q \neq n} \left[\left(\left. \frac{\partial^2 E^{(p)}}{\partial r_i^{pn} \partial r_k^{qn}} \right|_{r^{mn} = \hat{r}^{mn}} - \left. \frac{\partial^2 E^{(n)}}{\partial r_i^{pn} \partial r_k^{qn}} \right|_{r^{mn} = \hat{r}^{mn}} \right) A_{k\alpha\beta}^{pn} \right] \\ & + \frac{1}{2\Omega_n} \hat{r}_i^n \sum_{p \neq n} \sum_{q \neq n} \left[\left(\left. \frac{\partial^2 E^{(p)}}{\partial r_j^{pn} \partial r_l^{qn}} \right|_{r^{mn} = \hat{r}^{mn}} - \left. \frac{\partial^2 E^{(n)}}{\partial r_j^{pn} \partial r_l^{qn}} \right|_{r^{mn} = \hat{r}^{mn}} \right) A_{l\alpha\beta}^{pn} \right] \end{aligned} \quad , \tag{C.16}$$

$$\begin{aligned} G_{iju}^n = & \frac{1}{2\Omega_n} \hat{r}_j^n \sum_{p \neq n} \sum_{q \neq n} \left[\left(\left. \frac{\partial^2 E^{(p)}}{\partial r_i^{pn} \partial r_k^{qn}} \right|_{r^{mn} = \hat{r}^{mn}} - \left. \frac{\partial^2 E^{(n)}}{\partial r_i^{pn} \partial r_k^{qn}} \right|_{r^{mn} = \hat{r}^{mn}} \right) B_{ku}^{pn} \right] \\ & + \frac{1}{2\Omega_n} \hat{r}_i^n \sum_{p \neq n} \sum_{q \neq n} \left[\left(\left. \frac{\partial^2 E^{(p)}}{\partial r_j^{pn} \partial r_l^{qn}} \right|_{r^{mn} = \hat{r}^{mn}} - \left. \frac{\partial^2 E^{(n)}}{\partial r_j^{pn} \partial r_l^{qn}} \right|_{r^{mn} = \hat{r}^{mn}} \right) B_{lu}^{pn} \right] \end{aligned} \quad , \tag{C.17}$$

$$
\begin{aligned}
L_{ijkl}^{mn} = & \frac{1}{2\Omega_n}\left(\sum_{p\neq n}\frac{\partial^2 E^{(p)}}{\partial r_i^{pn}\partial r_k^{pn}}\bigg|_{r^{mn}=\hat{r}^{mn}} + \frac{\partial^2 E^{(n)}}{\partial r_i^{pn}\partial r_k^{pn}}\bigg|_{r^{mn}=\hat{r}^{mn}}\right)\hat{r}_j^n\hat{r}_l^n\delta_{mn} \\
& + \frac{1}{2\Omega_n}\left(\sum_{p\neq n}\frac{\partial^2 E^{(p)}}{\partial r_j^{pn}\partial r_l^{pn}}\bigg|_{r^{mn}=\hat{r}^{mn}} + \frac{\partial^2 E^{(n)}}{\partial r_j^{pn}\partial r_l^{pn}}\bigg|_{r^{mn}=\hat{r}^{mn}}\right)\hat{r}_i^n\hat{r}_k^n\delta_{mn} \\
& - \frac{1}{4\Omega_n}\frac{\partial^2 E^{(n)}}{\partial r_i^{nm}\partial r_k^{nm}}\bigg|_{r^{mn}=\hat{r}^{mn}}\left(\hat{r}_j^n\hat{r}_l^m + \hat{r}_j^m\hat{r}_l^n\right)\left(1-\delta_{mn}\right) \\
& - \frac{1}{4\Omega_n}\frac{\partial^2 E^{(n)}}{\partial r_j^{nm}\partial r_l^{nm}}\bigg|_{r^{mn}=\hat{r}^{mn}}\left(\hat{r}_i^n\hat{r}_k^m + \hat{r}_i^m\hat{r}_k^n\right)\left(1-\delta_{mn}\right)
\end{aligned}
, \qquad \text{(C.18)}
$$

represent the components of perturbation response of the system introduced by the non-equivalency of the atomic ensemble such as in grain boundaries or multi-species compounds.

Atomic Level Stress

The virial stress on atom *n* is given by,

$$
\sigma_{ij}^n = \frac{1}{2\Omega_n}\sum_{\substack{m=1\\ m\neq n}}^{N}\frac{\partial E}{\partial r_i^{mn}}r_j^{mn} \quad . \qquad \text{(C.19)}
$$

Expanding the atomic level stress $\sigma_{ij}^{(n)}$ with respect to r_i^{mn} near $\hat{r}_i^{mn}$, where $\hat{r}_i^{mn}$ is the equilibrium configuration of the bi-crystal, gives

$$
\sigma_{ij}^n = \sigma_{ij}^n\Big|_{r^{mn}=\hat{r}^{mn}} + \sum_{\substack{m=1\\ m\neq n}}^{N}\frac{\partial\sigma_{ij}^n}{\partial r_k^{mn}}\bigg|_{r^{mn}=\hat{r}^{mn}}\left(r_k^{mn}-\hat{r}_k^{mn}\right) \ , \qquad \text{(C.20)}
$$

where

$$
\frac{\partial\sigma_{ij}^n}{\partial r_k^{mn}}\bigg|_{r^{mn}=\hat{r}^{mn}} = \frac{1}{2\Omega_n}\sum_{\substack{p=1\\ p\neq n}}^{N}\frac{\partial}{\partial r_k^{mn}}\left(\frac{\partial E}{\partial r_i^{pn}}r_j^{pn}\right)\bigg|_{r^{pn}=\hat{r}^{pn}} \quad . \qquad \text{(C.21)}
$$

Substituting the mapping of equation (C.4) into equation (4.81) gives,

$$\sum_{\substack{m=1\\m\neq n}}^{N}\left.\frac{\partial\sigma_{ij}^{n}}{\partial r_{k}^{mn}}\right|_{r^{mn}=\hat{r}^{mn}}\left(r_{k}^{mn}-\hat{r}_{k}^{mn}\right)=\left(\sum_{\substack{m=1\\m\neq n}}^{N}\left.\frac{\partial\sigma_{ij}^{n}}{\partial r_{k}^{mn}}\right|_{r^{mn}=\hat{r}^{mn}}\left(A_{k\alpha\beta}^{mn}\varepsilon_{\alpha\beta}^{s}+B_{kl}^{mn}\sigma_{l}^{t}\right)\right)$$
$$+\sum_{\substack{m=1\\m\neq n}}^{N}\left.\frac{\partial\sigma_{ij}^{n}}{\partial r_{k}^{mn}}\right|_{r^{mn}=\hat{r}^{mn}}\hat{r}_{l}^{m}\tilde{\varepsilon}_{kl}^{m}-\left(\sum_{\substack{p=1\\p\neq n}}^{N}\left.\frac{\partial\sigma_{ij}^{n}}{\partial r_{k}^{pn}}\right|_{r^{pn}=\hat{r}^{pn}}\right)\hat{r}_{l}^{n}\tilde{\varepsilon}_{kl}^{n} \quad , \tag{C.22}$$

Consequently, when substituting equation (C.22) into equation (4.81), we obtain for the atomic level stress,

$$\sigma_{ij}^{n}=\tau_{ij}^{n}+\bar{C}_{ij\alpha\beta}^{s,n}\varepsilon_{\alpha\beta}^{s}+\bar{M}_{kij}^{t,n}\sigma_{k}^{t}+\sum_{m=1}^{N-1}T_{ijkl}^{nm}\tilde{\varepsilon}_{kl}^{m} \quad , \tag{C.23}$$

where, τ_{ij}^{n}, $\bar{C}_{ij\alpha\beta}^{s,n}$, $\bar{M}_{kij}^{t,n}$ and T_{ijkl}^{nm} are known constants given in terms of the interatomic potential E and its partial derivative with respect to the interatomic distance r, with,

$$\tau_{ij}^{n}=\sigma_{ij}^{n}\Big|_{r^{mn}=\hat{r}^{mn}}=\frac{1}{2\Omega_{n}}\sum_{\substack{m=1\\m\neq n}}^{N}\left.\frac{\partial E}{\partial r_{i}^{mn}}\right|_{r^{mn}=\hat{r}^{mn}}\hat{r}_{j}^{mn} \quad , \tag{C.24}$$

$$\bar{C}_{ij\alpha\beta}^{s,n}=\sum_{\substack{m=1\\m\neq n}}^{N}\left.\frac{\partial\sigma_{ij}^{n}}{\partial r_{k}^{mn}}\right|_{r^{mn}=\hat{r}^{mn}}A_{k\alpha\beta}^{mn} \quad , \tag{C.25}$$

$$\bar{M}_{kij}^{t,n}=\sum_{\substack{m=1\\m\neq n}}^{N}\left.\frac{\partial\sigma_{ij}^{n}}{\partial r_{l}^{mn}}\right|_{r^{mn}=\hat{r}^{mn}}B_{lk}^{mn} \quad , \tag{C.26}$$

$$T_{ijkl}^{mn}=\left.\frac{\partial\sigma_{ij}^{n}}{\partial r_{k}^{mn}}\right|_{r^{mn}=\hat{r}^{mn}}\hat{r}_{l}^{m}\left(1-\delta_{mn}\right)-\left(\sum_{\substack{p=1\\p\neq n}}^{N}\left.\frac{\partial\sigma_{ij}^{n}}{\partial r_{k}^{pn}}\right|_{r^{pn}=\hat{r}^{pn}}\hat{r}_{l}^{n}\right)\delta_{mn} \quad , \tag{C.27}$$

Considering that the total energy of the system containing N atoms is $E=\sum_{n=1}^{N}E^{(n)}$, we can evaluate equation (C.22) and equation (C.24) such that,

$$\tau_{ij}^{n}=\frac{1}{2\Omega_{n}}\sum_{\substack{m=1\\m\neq n}}^{N}\hat{r}_{j}^{mn}\left(\sum_{q=1}^{N}\left.\frac{\partial E^{(q)}}{\partial r_{i}^{mn}}\right|_{r^{mn}=\hat{r}^{mn}}\right) \quad , \tag{C.28}$$

$$\left.\frac{\partial \sigma_{ij}^{n}}{\partial r_{k}^{mn}}\right|_{r^{mn}=\hat{r}^{mn}} = \frac{1}{2\Omega_n}\sum_{\substack{p=1 \\ p\neq n}}^{N}\left[\hat{r}_{j}^{pn}\left(\sum_{q=1}^{N}\left.\frac{\partial^2 E^{(q)}}{\partial r_{i}^{mn}\partial r_{k}^{pn}}\right|_{r^{mn}=\hat{r}^{mn}}\right)+\delta_{pm}\delta_{jk}\left(\sum_{q=1}^{N}\left.\frac{\partial E^{(q)}}{\partial r_{i}^{mn}}\right|_{r^{mn}=\hat{r}^{mn}}\right)\right] \quad .(C.29)$$

Finding the Internal Relaxations

The conditions of mechanical equilibrium and traction continuity across the interface yield,

$$\sigma_{j}^{t,n} = \sigma_{j}^{t} \quad . \tag{C.30}$$

Substituting equation (4.84) into equation (4.83) gives a system of 3*N* equations for the 6*N* unknowns $\tilde{\varepsilon}_{ij}^{n}$.

$$\sigma_{i}^{t} = \tau_{i}^{t,n} + \bar{C}_{3i\alpha\beta}^{s,n}\varepsilon_{\alpha\beta}^{s} + \bar{M}_{k3i}^{t,n}\sigma_{k}^{t} + \sum_{m=1}^{N-1} T_{3ikl}^{nm}\tilde{\varepsilon}_{kl}^{m} \quad . \tag{C.31}$$

Using equation (4.85), one can express the transverse relaxation $\tilde{\varepsilon}_{i}^{t,n}$ as a function of the in-plane relaxation strain $\tilde{\varepsilon}_{\alpha\beta}^{s,n}$, in the in-plane homogeneous strains $\varepsilon_{\alpha\beta}^{s}$ and the transverse stretching σ_{i}^{t}.

$$\tilde{\varepsilon}_{i}^{t,n} = \varsigma_{i}^{t,n} + X_{ij}^{n}\sigma_{j}^{t} - Y_{i\alpha\beta}^{n}\varepsilon_{\alpha\beta}^{s} - \sum_{m=1}^{N-1} Z_{i\alpha\beta}^{nm}\tilde{\varepsilon}_{\alpha\beta}^{s,m} \quad , \tag{C.32}$$

with,

$$\varsigma_{i}^{t,n} = -\sum_{m=1}^{N-1} S_{3j3i}^{nm}\tau_{j}^{t,m} \quad , \tag{C.33}$$

$$X_{ij}^{n} = \sum_{m=1}^{N-1} S_{3j3k}^{nm}\left(\delta_{ik} - \bar{M}_{3ik}^{t,m}\right) \quad , \tag{C.34}$$

$$Y_{i\alpha\beta}^{n} = \sum_{m=1}^{N-1} S_{3j3i}^{nm}\bar{C}_{3j\alpha\beta}^{s,m} \quad , \tag{C.35}$$

$$Z_{i\alpha\beta}^{nm} = \sum_{p=1}^{N-1} S_{3j3i}^{np}T_{3j\alpha\beta}^{pm} \quad , \tag{C.36}$$

and,

$$S^{nm}_{3j3k} = \left[\mathrm{T}^{nm}_{3j3k} \right]^{-1} \quad \text{, or } \sum_{m=1}^{N-1} S^{nm}_{3i3j} T^{mp}_{3j3k} = \delta_{ik}\delta_{np} \quad . \tag{C.37}$$

In order to solve for the 6*N* unknowns of equation (4.85), we furthermore need to consider that the application of a prescribed "mixed" loading configuration (in-plane prescribed deformation and transverse prescribed traction) to the bicrystal produces a finite strain and a minimization of strain energy density by internal relaxation. In other words, once we substitute the transverse relaxation from equation (4.86) into equation (C.8), the total strain energy must be minimum with respect to any arbitrary spontaneous in-plane relaxation strain, i.e.,

$$\frac{\partial E}{\partial \tilde{\varepsilon}^{s,n}_{\alpha\beta}} = 0 \quad ; \quad \forall n \in \Omega \quad , \tag{C.38}$$

where Ω is the total bicrystal assembly. It is seen that equation (4.87) is now a system of 3*N* equations for the 3*N* unknowns $\tilde{\varepsilon}^{s,n}_{\alpha\beta}$.

Then, we solve for the internal in-plane relaxation,

$$\tilde{\varepsilon}^{s,n}_{\alpha\beta} = \eta^{s,n}_{\alpha\beta} - M^{s,n}_{i\alpha\beta}\sigma^{t}_{i} + Q^{s,n}_{\alpha\beta\kappa\lambda}\varepsilon^{s}_{\kappa\lambda} \quad , \tag{C.39}$$

with,

$$\eta^{s,n}_{\alpha\beta} = \sum_{m=1}^{N-1} J^{nm}_{\alpha\beta\kappa\lambda} \left(K^{m}_{\kappa\lambda} - \sum_{p=1}^{N-1} \left\{ K^{p}_{3i} Z^{pm}_{i\kappa\lambda} - \left[\left(\sum_{q=1}^{N-1} L^{<pq>}_{<3i3j>} Z^{qm}_{i\kappa\lambda} \right) - L^{<pm>}_{<\kappa\lambda 3j>} \right] \varsigma^{t,p}_{j} \right\} \right) \quad , \tag{C.40}$$

$$M^{s,n}_{i\alpha\beta} = -\sum_{m=1}^{N-1} J^{nm}_{\alpha\beta\kappa\lambda} \left(G^{m}_{\kappa\lambda i} - \sum_{p=1}^{N-1} \left\{ G^{p}_{3ji} Z^{pm}_{j\kappa\lambda} - \left[\left(\sum_{q=1}^{N-1} L^{<pq>}_{<3j3k>} Z^{qm}_{j\kappa\lambda} \right) - L^{<pm>}_{<\kappa\lambda 3k>} \right] X^{p}_{ki} \right\} \right) \quad , \tag{C.41}$$

$$Q^{s,n}_{\alpha\beta\kappa\lambda} = \sum_{m=1}^{N-1} J^{nm}_{\alpha\beta\mu\nu} \left(D^{m}_{\mu\nu\kappa\lambda} - \sum_{p=1}^{N-1} \left\{ D^{p}_{3i\kappa\lambda} Z^{pm}_{i\mu\nu} + \left[\left(\sum_{q=1}^{N-1} L^{<pq>}_{<3j3i>} Z^{qm}_{j\mu\nu} \right) - L^{<pm>}_{<\mu\nu 3i>} \right] Y^{p}_{i\kappa\lambda} \right\} \right) \quad , \tag{C.42}$$

and,

$$J^{mn}_{\alpha\beta\kappa\lambda} = \left[-L^{<mn>}_{<\alpha\beta\kappa\lambda>} + \sum_{p=1}^{N-1} \left(L^{<mp>}_{<3i\kappa\lambda>} Z^{pn}_{i\alpha\beta} + Z^{pm}_{i\kappa\lambda} L^{<pn>}_{<\alpha\beta 3i>} - \sum_{q=1}^{N-1} Z^{pm}_{j\kappa\lambda} L^{<pq>}_{<3i3j>} Z^{qn}_{i\alpha\beta} \right) \right]^{-1} \quad . \tag{C.43}$$

Substituting equation (4.88) back into equation (4.86) leads to the internal transverse relaxation,

$$\tilde{\varepsilon}_i^{t,n} = \eta_i^{t,n} + M_{ij}^{t,n}\sigma_j^t - Q_{i\alpha\beta}^{t,n}\varepsilon_{\alpha\beta}^s \quad , \tag{C.44}$$

with,

$$\eta_i^{t,n} = \varsigma_i^{t,n} + \sum_{m=1}^{N-1} Z_{i\alpha\beta}^{nm}\eta_{\alpha\beta}^{s,m} \quad , \tag{C.45}$$

$$M_{3j3k}^{t,n} = X_{ij}^n - \sum_{m=1}^{N-1} Z_{i\alpha\beta}^{nm} M_{j\alpha\beta}^{s,m} \quad , \tag{C.46}$$

$$Q_{i\alpha\beta}^n = Y_{i\alpha\beta}^n - \sum_{m=1}^{N-1} Z_{i\kappa\lambda}^{nm} Q_{\kappa\lambda\alpha\beta}^{s,m} \quad , \tag{C.47}$$

Atomic Level In-plane Stress

The in-plane virial stress on atom *n* can be extracted from equation (4.83),

$$\sigma_{\alpha\beta}^{s,n} = \tau_{\alpha\beta}^n + \bar{C}_{i\alpha\beta\kappa\lambda}^{s,n}\varepsilon_{\kappa\lambda}^s + \bar{M}_{k\alpha\beta}^{t,n}\sigma_k^t + \sum_{m=1}^{N-1} T_{\alpha\beta kl}^{nm}\tilde{\varepsilon}_{kl}^m \quad . \tag{C.48}$$

Substituting the internal relaxations from equation (4.88) and equation (C.44) yields for the in-plane stress

$$\sigma_{\alpha\beta}^{s,n} = \pi_{\alpha\beta}^n + C_{\alpha\beta\kappa\lambda}^{s,n}\varepsilon_{\kappa\lambda}^s + Q_{i\alpha\beta}^n\sigma_i^t \quad , \tag{C.49}$$

with,

$$\pi_{\alpha\beta}^n = \tau_{\alpha\beta}^n + \sum_{m=1}^{N-1} \mathrm{T}_{\alpha\beta 3k}^{nm}\eta_k^{t,m} + \sum_{m=1}^{N-1} \mathrm{T}_{\alpha\beta\kappa\lambda}^{nm}\eta_{\kappa\lambda}^{s,m} \quad , \tag{C.50}$$

$$C_{\alpha\beta\kappa\lambda}^{s,n} = \bar{C}_{\alpha\beta\kappa\lambda}^{s,n} - \sum_{m=1}^{N-1} \mathrm{T}_{\alpha\beta 3i}^{nm} Q_{i\kappa\lambda}^{t,m} + \sum_{m=1}^{N-1} \mathrm{T}_{\alpha\beta\mu\nu}^{nm} Q_{\mu\nu\kappa\lambda}^{s,m} \quad , \tag{C.51}$$

$$Q_{i\alpha\beta}^n = \bar{M}_{i\alpha\beta}^{t,n} + \sum_{m=1}^{N-1} \mathrm{T}_{\alpha\beta 3j}^{nm} M_{ji}^{t,m} - \sum_{m=1}^{N-1} \mathrm{T}_{\alpha\beta\kappa\lambda}^{nm} M_{i\kappa\lambda}^{s,m} \quad . \tag{C.52}$$

APPENDIX D

COORDINATE TRANSFORMATION

Consider the ellipsoid Ω shown in Figure 5.2. When the ellipsoid is subjected to a uniform strain field, ε_{ij}, the surface of the ellipsoid deforms accordingly. Let the two-dimensional surface strain tensor, $\varepsilon^s_{\alpha\beta}$, be defined in a local coordinate system $(\mathbf{i}_1, \mathbf{i}_2, \mathbf{i}_3)$, where $\mathbf{i}_1$ and $\mathbf{i}_2$ are tangent to the surface, and $\mathbf{i}_3$ is normal to the surface. Clearly, the choice of $\mathbf{i}_1$ and $\mathbf{i}_2$ is not unique. The following approach is taken to uniquely define the local coordinate system on the ellipsoidal surface.

In the spherical coordinate system,

$$\mathbf{X}_1 = r\cos\theta\sin\phi,\ \mathbf{X}_2 = r\sin\theta\sin\phi,\ \mathbf{X}_3 = r\cos\phi,\ 0 \le \theta \le 2\pi,\ 0 \le \phi \le \pi. \quad \text{(D.1)}$$

A point on the surface of the ellipsoid can be represented by the vector,

$$\mathbf{R}(\theta,\phi) = a\cos\theta\sin\phi\mathbf{I}_1 + b\sin\theta\sin\phi\mathbf{I}_2 + c\cos\phi\mathbf{I}_3 \quad . \quad \text{(D.2)}$$

A local coordinate system at this point may be introduced by the following three unit vectors,

$$\mathbf{i}_3 = \frac{1}{d_1}\left(\cos\theta\sin\phi\mathbf{I}_1 + \frac{a}{b}\sin\theta\sin\phi\mathbf{I}_2 + \frac{a}{c}\cos\phi\mathbf{I}_3\right) \quad , \quad \text{(D.3)}$$

$$\mathbf{i}_2 = \frac{\partial\mathbf{R}}{\partial\theta}\Big/\left\|\frac{\partial\mathbf{R}}{\partial\theta}\right\| = \frac{1}{d_2}\left(-\frac{a}{b}\sin\theta\mathbf{I}_1 + \cos\theta\mathbf{I}_2\right) \quad , \quad \text{(D.4)}$$

$$\mathbf{i}_1 = \mathbf{i}_2 \times \mathbf{i}_3 = \frac{a}{cd_1d_2}\cos\theta\cos\phi\mathbf{I}_1 + \frac{a^2}{bcd_1d_2}\sin\theta\cos\phi\mathbf{I}_2 - \frac{d_2}{d_1}\sin\phi\mathbf{I}_3 \quad , \quad \text{(D.5)}$$

where,

$$d_1 = \sqrt{\cos^2\theta\sin^2\phi + \frac{a^2}{b^2}\sin^2\theta\sin^2\phi + \frac{a^2}{c^2}\cos^2\phi} \quad , \quad \text{(D.6)}$$

$$d_2 = \sqrt{\frac{a^2}{b^2}\sin^2\theta + \cos^2\theta} \quad . \quad \text{(D.7)}$$

The transformation matrix between the global ($\mathbf{I_1}$, $\mathbf{I_2}$, $\mathbf{I_3}$) and the local $(\mathbf{i}_1, \mathbf{i}_2, \mathbf{i}_3)$ coordinate systems is thus given by,

$$\left[t_{ij}\right] = \begin{bmatrix} \frac{a}{cd_1d_2}\cos\theta\cos\phi & \frac{a^2}{bcd_1d_2}\sin\theta\cos\phi & -\frac{d_2}{d_1}\sin\phi \\ -\frac{a}{bd_2}\sin\theta & \frac{1}{d_2}\cos\theta & 0 \\ \frac{1}{d_1}\cos\theta\sin\phi & \frac{a}{bd_1}\sin\theta\sin\phi & \frac{a}{cd_1}\cos\phi \end{bmatrix} . \tag{D.8}$$

Therefore, according to the tensor transformation rule, the surface strain in the local coordinate system can be written as

$$\varepsilon^s_{\alpha\beta} = t_{\alpha i} t_{\beta j} \varepsilon_{ij} \quad . \tag{D.9}$$

For a spherical particle ($a = b = c$), the transformation matrix reduces to

$$\left[t_{ij}\right] = \begin{bmatrix} \cos\theta\cos\phi & \sin\theta\cos\phi & -\sin\phi \\ -\sin\theta & \cos\theta & 0 \\ \sin\phi\cos\theta & \sin\phi\sin\theta & \cos\phi \end{bmatrix} . \tag{D.10}$$

APPENDIX E

BULK AND SURFACE ELASTICITY TENSORS

For isotropic solids, the number of independent elastic constants is reduced to only two independent constants for C_{ijkl}. They are

$$C_{11} = C_{22} = C_{33} = K + \frac{4\mu}{3} \quad , \quad C_{12} = C_{13} = C_{23} = K - \frac{2\mu}{3} \quad , \tag{E.1}$$

$$C_{44} = C_{55} = C_{66} = \mu \quad , \tag{E.2}$$

where *K* is called the bulk modulus, μ the shear modulus.

For isotropic solids, $C^{(3)}_{ijklmn}$ has three independent non-zero constants *L*, *M*, *N*. They are related to C_{ijk} (in the Voigt notation) by

$$C_{111} = C_{222} = C_{333} = L + 6M + 8N \quad , \tag{E.3}$$

$$C_{144} = C_{255} = C_{366} = M \quad , \tag{E.4}$$

$$C_{112} = C_{113} = C_{122} = C_{133} = C_{223} = C_{233} = L + 2M \quad , \tag{E.5}$$

$$C_{155} = C_{166} = C_{244} = C_{266} = C_{344} = C_{355} = M + 2N \quad , \tag{E.6}$$

$$C_{123} = L \quad , \quad C_{456} = N \quad . \tag{E.7}$$

In terms of the Kronecker delta δ_{ij}, these elasticity tensors can be written conveniently as,

$$C_{ijkl} = K\delta_{ij}\delta_{kl} + \mu\left(\delta_{ik}\delta_{jl} + \delta_{il}\delta_{jk} - \frac{2}{3}\delta_{ij}\delta_{kl}\right) \quad , \tag{E.8}$$

$$\begin{aligned} C^{(3)}_{ijklmn} &= L\delta_{ij}\delta_{kl}\delta_{mn} \\ &+ M\left(\delta_{ij}\delta_{km}\delta_{ln} + \delta_{ij}\delta_{kn}\delta_{lm} + \delta_{im}\delta_{jn}\delta_{kl} + \delta_{in}\delta_{jm}\delta_{kl} + \delta_{ik}\delta_{jl}\delta_{mn} + \delta_{il}\delta_{jk}\delta_{mn}\right) \\ &+ N\left(\delta_{ik}\delta_{jm}\delta_{ln} + \delta_{im}\delta_{jk}\delta_{ln} + \delta_{il}\delta_{jm}\delta_{kn} + \delta_{im}\delta_{jl}\delta_{kn} + \delta_{ik}\delta_{jn}\delta_{lm} + \delta_{in}\delta_{jk}\delta_{lm}\right. \\ &\left. + \delta_{il}\delta_{jn}\delta_{km} + \delta_{in}\delta_{jl}\delta_{km}\right) \end{aligned} \quad . \tag{E.9}$$

Next, consider the surface elasticity tensors $\Gamma^{(1)}_{\alpha\beta}$ and $\Gamma^{(2)}_{\alpha\beta\kappa\lambda}$. Again, it follows from the definition equation (4.14) that certain symmetry conditions must be met,

$$\Gamma^{(1)}_{\alpha\beta} = \Gamma^{(1)}_{\beta\alpha},\ \Gamma^{(2)}_{\alpha\beta\kappa\lambda} = \Gamma^{(2)}_{\kappa\lambda\alpha\beta} = \Gamma^{(2)}_{\beta\alpha\kappa\lambda} \quad . \tag{E.10}$$

In general, $\Gamma^{(1)}_{\alpha\beta}$ and $\Gamma^{(2)}_{\alpha\beta\kappa\lambda}$ can be anisotropic in the surface (where they are defined). For isotropic surfaces, both $\Gamma^{(1)}_{\alpha\beta}$ and $\Gamma^{(2)}_{\alpha\beta\kappa\lambda}$ should be isotropic. It can be shown (Aris, 1962) that $\Gamma^{(1)}_{\alpha\beta}$ is isotropic if and only $\Gamma^{(1)}_{12} = \Gamma^{(1)}_{21} = 0$ and $\Gamma^{(1)}_{11} = \Gamma^{(1)}_{22}$, and $\Gamma^{(2)}_{\alpha\beta\kappa\lambda}$ is isotropic if and only $\Gamma^{(2)}_{1112} = \Gamma^{(2)}_{1222} = 0$, and $\Gamma^{(2)}_{1111} = \Gamma^{(2)}_{2222} = \Gamma^{(2)}_{1122} + 2\Gamma^{(2)}_{1212}$. This is the case if the surface has a rotation axis of three-fold or higher symmetry (Buerger, 1963). Therefore, for a (111) surface, which has three-fold symmetry, and for a (100) surface, which has four-fold symmetry, the surface stiffness tensors can be written as

$$\Gamma^{(1)}_{\alpha\beta} = \Gamma_{11}\delta_{\alpha\beta} \ ,\ \Gamma^{(2)}_{\alpha\beta\kappa\lambda} = K^s\delta_{\alpha\beta}\delta_{\kappa\lambda} + \mu^s\left(\delta_{\alpha\kappa}\delta_{\beta\lambda} + \delta_{\alpha\lambda}\delta_{\beta\kappa} - \delta_{\alpha\beta}\delta_{\kappa\lambda}\right) \ . \tag{E.11}$$

APPENDIX F

EFFECTIVE ELASTIC PROPERTIES OF NANOPARTICLES: SPECIAL CASES

Films

For the film shown in Figure 5.3, the integrals in (5.11) – (5.12) can be written as integrals on the top and bottom surfaces of the film. On these surfaces, the integrands in both integrals are constants. Thus, they can be easily carried out to yield (5.26) and (5.27). Consequently, the non-zero components of the fourth order tensor $R_{ijkl} = C^{(3)}_{ijklmn} M_{mnpq} \tau_{pq}$ are obtained as

$$R_{3333} = 2\Gamma_{11}\eta\left(\frac{C_{112}}{C_{12}} - \frac{C_{111}}{C_{11}}\right) , \tag{F.1}$$

$$R_{1133} = R_{2233} = \Gamma_{11}\eta\left(\frac{C_{123}+C_{112}}{C_{12}} - \frac{2C_{112}}{C_{11}}\right) , \tag{F.2}$$

$$R_{1111} = R_{2222} = \Gamma_{11}\eta\left(\frac{C_{111}+C_{112}}{C_{12}} - \frac{2C_{112}}{C_{11}}\right) , \tag{F.3}$$

$$R_{1122} = 2\Gamma_{11}\eta\left(\frac{C_{112}}{C_{12}} - \frac{C_{123}}{C_{11}}\right) , \tag{F.4}$$

where C_{ijk} are related to their third order elastic constants as indicated in Appendix E and η is defined by (F.11). The non-zero components of the effective elasticity tensor for the thin film in terms of the Voigt notation can then be obtained from (5.25),

$$\bar{C}_{33} = C_{11} + \frac{2\Gamma_{11}\eta}{a}\left(\frac{C_{111}}{C_{11}} - \frac{C_{112}}{C_{12}}\right) , \tag{F.5}$$

$$\bar{C}_{13} = \bar{C}_{23} = C_{12} + \frac{\Gamma_{11}\eta}{a}\left(\frac{2C_{112}}{C_{11}} - \frac{C_{123}+C_{112}}{C_{12}}\right) , \tag{F.6}$$

$$\bar{C}_{11} = \bar{C}_{22} = C_{11} + \frac{1}{a}\left[\left(K^s + \mu^s \right) + \Gamma_{11}\eta \left(\frac{2C_{112}}{C_{11}} - \frac{C_{111} + C_{112}}{C_{12}} \right) \right] \ , \tag{F.7}$$

$$\bar{C}_{12} = C_{12} + \frac{1}{a}\left[(K^s - \mu^s) + 2\Gamma_{11}\eta \left(\frac{C_{123}}{C_{11}} - \frac{C_{112}}{C_{12}} \right) \right] \ , \tag{F.8}$$

$$\bar{C}_{44} = C_{44} + \frac{1}{a}\left[\mu^s + 2\Gamma_{11}\eta \left(\frac{C_{144}}{C_{11}} - \frac{C_{155}}{C_{12}} \right) \right] \ , \tag{F.9}$$

$$\bar{C}_{55} = \bar{C}_{66} = C_{44} + \frac{\Gamma_{11}\eta}{a} \left(\frac{2C_{155}}{C_{11}} - \frac{C_{144} + C_{155}}{C_{12}} \right) \ , \tag{F.10}$$

where η is a non-dimensional constant given by

$$\eta = \frac{C_{11}C_{12}}{\left(C_{11} + 2C_{12} \right)\left(C_{11} - C_{12} \right)} \ . \tag{F.11}$$

Note that the positive definiteness of the strain energy density requires $C_{11} > \left| C_{12} \right|$. Thus, $\eta \geq 0$ if $C_{12} \geq 0$.

Wires

For the wire shown in Figure 5.4, the integrals in (5.11) – (5.12) can be written as integrals on the lateral surfaces of the wire. On these surfaces, the integrands in both integrals are constants. Thus, they can be easily carried out to yield,

$$\tau_{11} = \tau_{22} = \Gamma_{11} \ , \ \ \tau_{33} = 2\Gamma_{11} \ , \tag{F.12}$$

$$Q_{1111} = Q_{2222} = K^s + \mu^s \ , \ \ Q_{3333} = 2(K^s + \mu^s) \ , \tag{F.13}$$

$$Q_{1133} = Q_{2233} = K^s - \mu^s \ , \ Q_{2323} = Q_{1313} = \mu^s \ . \tag{F.14}$$

Consequently, the non-zero components of the fourth order tensor $R_{ijkl} = C^{(3)}_{ijklmn} M_{mnpq} \tau_{pq}$ are obtained as

$$R_{1111} = R_{2222} = \Gamma_{11}\eta \left(\frac{C_{111} + 3C_{112}}{C_{12}} - \frac{2(C_{111} + C_{112})}{C_{11}} \right) \ , \tag{F.15}$$

$$R_{3333} = 2\Gamma_{11}\eta\left(\frac{C_{111}+C_{112}}{C_{12}} - \frac{2C_{112}}{C_{11}}\right) \ , \tag{F.16}$$

$$R_{1122} = 2\Gamma_{11}\eta\left(\frac{C_{112}+C_{123}}{C_{12}} - \frac{2C_{112}}{C_{11}}\right) \ , \tag{F.17}$$

$$R_{1133} = R_{2233} = \Gamma_{11}\eta\left(\frac{C_{123}+3C_{112}}{C_{12}} - \frac{2(C_{112}+C_{123})}{C_{11}}\right) \ , \tag{F.18}$$

$$R_{2323} = R_{1313} = \Gamma_{11}\eta\left(\frac{C_{144}+3C_{155}}{C_{12}} - \frac{2(C_{144}+C_{155})}{C_{11}}\right) \ , \tag{F.19}$$

$$R_{1212} = 2\Gamma_{11}\eta\left(\frac{C_{144}+C_{155}}{C_{12}} - \frac{2C_{155}}{C_{11}}\right) \ . \tag{F.20}$$

The non-zero components of the corresponding effective elasticity tensor are thus given by

$$\overline{C}_{11} = \overline{C}_{22} = C_{11} + \frac{1}{a}\left[\left(K^s + \mu^s\right) + \Gamma_{11}\eta\left(\frac{2(C_{111}+C_{112})}{C_{11}} - \frac{C_{111}+3C_{112}}{C_{12}}\right)\right] \ , \tag{F.21}$$

$$\overline{C}_{33} = C_{11} + \frac{1}{a}\left[2\left(K^s + \mu^s\right) + 2\Gamma_{11}\eta\left(\frac{2C_{112}}{C_{11}} - \frac{C_{111}+C_{112}}{C_{12}}\right)\right] \ , \tag{F.22}$$

$$\overline{C}_{12} = C_{12} + \frac{2\Gamma_{11}\eta}{a}\left(\frac{2C_{112}}{C_{11}} - \frac{C_{123}+C_{112}}{C_{12}}\right) \ , \tag{F.23}$$

$$\overline{C}_{13} = \overline{C}_{23} = C_{12} + \frac{1}{a}\left[\left(K^s - \mu^s\right) + \Gamma_{11}\eta\left(\frac{2(C_{112}+C_{123})}{C_{11}} - \frac{3C_{112}+C_{123}}{C_{12}}\right)\right] \ , \tag{F.24}$$

$$\overline{C}_{44} = \overline{C}_{55} = C_{44} + \frac{1}{a}\left[\mu^s + \Gamma_{11}\eta\left(\frac{2(C_{144}+C_{155})}{C_{11}} - \frac{C_{144}+3C_{155}}{C_{12}}\right)\right] \ , \tag{F.25}$$

$$\overline{C}_{66} = C_{44} + \frac{2\Gamma_{11}\eta}{a}\left(\frac{2C_{155}}{C_{11}} - \frac{C_{144}+C_{155}}{C_{12}}\right) \ , \tag{F.26}$$

Spherical Particles

For spherical particles, the integrals in (5.11) – (5.12) reduced to spherically symmetric tensors. Thus, they can be easily carried out to yield,

$$Q_{ijkl} = \frac{4}{3} K^s \delta_{ij}\delta_{kl} + \frac{1}{5}\left(K^s + 6\mu^s\right)\left(\delta_{ik}\delta_{jl} + \delta_{il}\delta_{jk} - \frac{2}{3}\delta_{ij}\delta_{kl}\right) \quad , \tag{F.27}$$

$$\tau_{ij} = 2\Gamma_{11}\delta_{ij} \quad . \tag{F.28}$$

Consequently, the fourth order tensor $R_{ijkl} = C^{(3)}_{ijklmn} M_{mnpq} \tau_{pq}$ is obtained as

$$R_{ijkl} = \frac{2\Gamma_{11}}{3K}\left(3L + 6M + \frac{8}{3}N\right)\delta_{ij}\delta_{kl} + \frac{2\Gamma_{11}}{3K}\left(3M + 4N\right)\left(\delta_{ik}\delta_{jl} + \delta_{il}\delta_{jk} - \frac{2}{3}\delta_{ij}\delta_{kl}\right) \quad . \tag{F.29}$$

REFERENCES

Ackland, G. J. and M. W. Finnis (1986). "Semi-empirical calculation of solid surface tensions in body-centered cubic transistion metals." *Philosophical Magazine A* **54**(2): 301-315.

Ackland, G. J., G. Tichy, V. Vitek and M. W. Finnis (1987). "N-body potentials for the noble metals and nickel." *Philosophical Magazine A* **56**(6): 735-756.

Adams, J. B., W. G. Wolfer and S. M. Foiles (1989). "Elastic properties of grain boundaries in copper and their relationship to bulk elastic constants." *Physical Review B* **40**(14): 9479-9484.

Alber, I., J. L. Bassani, M. Khantha, V. Vitek and G. J. Wang (1992). "Grain boundaries as heterogeneous systems: Atomic and continuum elastic properties." *Philosophical Transactions: Physical Sciences and Engineering* **339**(1655): 555-586.

Alymov, M. I. and M. K. Shorshorov (1999). "Surface tension of ultrafine particles." *Nanostructured Materials* **12**(1-4): 365-368.

Andreev, A. F. and Y. A. Kosevich (1981). *Soviet Physics-JETP* **54**: 761.

Aris, R. (1962). Vectors, tensors, and basic equations of fluid mechanics. New Jersey.

Bachurin, D. V., R. T. Murzaev and A. A. Nazarov (2003). "Atomistic computer and disclination simulation of [001] tilt boundaries in nickel and copper." *Fizika Metallov i Mettallovedenie* **96**(11): 128–134.

Baker, S. P., M.K. Small, , B. J. Vlassak, B. J., Daniels, B.J. and W. D. Nix (1993). "The search for the supermodulus effect" in Mechanical properties and deformation behavior of materials having ultra-fine microstructures. Netherlands, Kluwer Academic Publishers.

Banerjea, A. and J. R. Smith (1987). "Continuum elasticity analysis of the enhanced modulus effect in metal-alloy superlattice films." *Physical Review B* **35**(11): 5413-5420.

Barsh, G. R. (1968). "Relation between third-order elastic constants of single crystals and polycrystals." *Journal of Applied Physics* **39**(8): 3780-3793.

Baskes, M. I. (1992). "Modified embedded-atom potentials for cubic materials and impurities." *Physical Review B* **46**(5): 2727-2742.

Bassani, J. L., V. Vitek and I. Alber (1992). "Atomic-level elastic properties of interfaces and their relation to continua." *Acta Metallurgica et Materialia* **40**(S1): S307-S320.

Blakely, J. M. (1973). Introduction to the properties of crystal surfaces. New York, Pergamon Press.

Borchers, C. and R. Bormann (2005). "Determination of low-temperature interfacial energies from a pair interaction model." *Acta Materialia* **53**(13): 3695-3701.

Born, M. and K. Huang (1954). Dynamical theory of crystal lattices. Oxford, Clarendon Press.

Brugger, K. (1965). "Pure modes for elastic waves in crystals." *Journal of Applied Physics* **36**(3): 759-768.

Buerger, M. J. (1963). Elementary crystallography. New York, Willey.

Çağin, T. and J. R. Ray (1988). "Third-order elastic constants from molecular dynamics: Theory and an example calculation." *Physical Review B* **38**(12): 7940-7946.

Cahn, J. W. and F. Larché (1982). "Surface stress and chemical equilibrium of small crystals -2. Solid particles embedded in a solid matrix." *Acta Metallurgica* **30**(1): 51-56.

Cammarata, R. C. (1997). "Surface and interface stress effects on interfacial and nanostructured materials." *Materials Science and Engineering A* **237**(2): 180-184.

Cammarata, R. C. and K. Sieradzki (1989). "Effects of surface stress on the elastic moduli of thin films and superlattices." *Physical Review Letters* **62**(17): 2005-2008.

Cammarata, R. C. and K. Sieradzki (1994). "Surface and interface stresses." *Annual Review of Materials Science* **24**: 215-234.

Cammarata, R. C., T. M., Trimble, and D. J. Srolovitz (2000). "Surface stress model for intrinsic stresses in thin films." *Journal of Materials Research* **15**(11): 2468-22774.

Capolungo, L., C. Jochum, M. Cherkaoui and J. Qu (2005). "Homogenization method for strength and inelastic behavior of nanocrystalline materials." *International Journal of Plasticity* **21**(1): 67-82.

Capolungo, L., D. E. Spearot, M. Cherkaoui, D. L. McDowell, J. Qu and K. I. Jacob (2007). "Dislocation nucleation from bicrystal interfaces and grain boundary

ledges: Relationship to nanocrystalline deformation." *Journal of the Mechanics and Physics of Solids* **In Press**.

Carlsson, A. E. (1990). "Beyond pair potentials in elemental transition metals and semiconductors." *Solid State Physics* **43**: 1-90.

Catlin, A., and W. P. Walter (1960). "Mechanical properties of thin single-crystal gold films." *Journal of Applied Physics* **31**: 2135 - 2139.

Chen, D. L. and T. C. Chen (2005). "Mechanical properties of Au nanowires under uniaxial tension with high strain-rate by molecular dynamics." *Nanotechnology* **16**: 2972–2981.

Collins, P. C., M. S. Arnold and P. Avouris (2001). "Engineering carbon nanotubes and nanotube circuits using electrical breakdown." *Science* **292**(5517): 706-710.

Cuenot, S., C. Frétigny, S. Demoustier-Champagne and B. Nysten (2004). "Surface tension effect on the mechanical properties of nanomaterials measured by atomic force microscopy." *Physical Review B* **69**: 165410-1–165410-5.

Daw, M. S. and M. I. Baskes (1983). "Semiempirical, quantum mechanical calculation of hydrogen embrittlement in metals." *Physical Review Letters* **50**(17): 1285-1288.

Daw, M. S. and M. I. Baskes (1984). "Embedded-atom method: Derivation and application to impurities, surfaces, and other defects in metals." *Physical Review B* **29**(12): 6443-6453.

de Boer, F., R. Boom, W. C. M. Mattens, A. R. Miedema and A. K. Niessen (1988). Cohesion in Metals. Amsterdam, North-Holland.

Diao, J., K. Gall, and M. L. Dunn (2004). "Atomistic simulation of the structure and elastic properties of gold nanowires." *Journal of the Mechanics and Physics of Solids* **52**(9): 1935-1962.

Digilov, R. M., V. K. Kumykov and K. B. Khokonov (1976). "Measurement of the surface tension of refractory metals in the solid state." *Physics of Metals and Metallography* **41**(5): 68-71.

Dingreville, R. and J. Qu (2007). "A semi-analytical method to compute surface elastic properties." *Acta Materialia* **55**: 141-147.

Dingreville, R., J. Qu and M. Cherkaoui (2005). "Surface free energy and its effect on the elastic behavior of nano-size particles, wires and films." *Journal of the Mechanics and Physics of Solids* **53**: 1827-1854.

Duan, H. L., J. Wang, Z. P. Huang and B. L. Karihaloo (2005). "Eshelby formalism for nano-inhomogeneities." *Proceedings of the Physical Society A* **461**: 3335–3353.

Duan, H. L., J. Wang, Z. P. Huang and B. L. Karihaloo (2005). "Size-dependent effective elastic constants of solids containing nano-inhomogeneities with interface stress." *Journal of the Mechanics and Physics of Solids* **53**: 1574–1596.

Duan, H. L., J. Wang, Z. P. Huang and Z. Y. Luo (2005). "Stress concentration tensors of inhomogeneities with interface effects." *Mechanics of Materials* **37**: 723–736.

Eshelby, J. D. (1957). "The determination of the elastic field of an ellipsoidal inclusion, and related problems." *Proceedings of the Royal Society of London A* **241**(1226): 376-396.

Fartash, A., E. E. Fullerton, I. K. Schuller, S. E. Bobbin, J. W. Wagner, R. C. Cammarata, S. Kumar, and M. Grimsditch (1991). "Evidence for the supermodulus effect and enhanced hardness in metallic superlattices." *Physical Review B* **44**(24): 13760-13763.

Feibelman, P. J. (1991). "Pulay-type formula for surface stress in a local-density-functional, linear combination of atomic orbitals, electronic-structure calculation." *Physical Review B* **44**(8): 3916–3925.

Feibelman, P. J. (1995). "Anisotropy of the stress on fcc(110) surfaces." *Physical Review B* **51**(24): 17867-17875.

Fiorentini, V., M. Methfessel and M. Scheffler (1993). "Reconstruction mechanism of fcc transition metal (001) surfaces." *Physical Review Letters* **71**(7): 1051-1054.

Fletcher, R. and C. M. Reeves (1964). "Function minimization by conjugate gradients." *Computer Journal* **7**(2): 149-154.

Foiles, S. M., M. I. Baskes and M. S. Daw (1986). "Embedded-atom-method functions for the fcc metals Cu, Ag, Au, Ni, Pd, Pt, and their alloys." *Physical Review B* **33**(12): 7983-7991.

Fougere, G. E., L. Riester, M. Ferber, J. R. Weertman, and R. W. Siegel (1995). "Young's modulus of nanocrystalline Fe measured by nanoindentation." *Materials Science and Engineering A* **204**(1-2): 1-6.

Fumi, F. G. (1951). "Third-order elastic coefficients of crystals." *Physical Review* **83**(6): 1274-1275.

Gamaly, E. G. and T. W. Ebbesen (1995). "Mechanism of carbon nanotube formation in the arc discharge." *Physical Review B* **52**(3): 2083-2089.

Ghahremani, F. (1980). "Effect of grain boundary sliding on an elasticity of polycrystals." *International Journal of Solids and Structures* **16**: 825–845.

Gilmore, C. M. and V. Provenzano (1990). "Embedded-atom-method study of coherency and elastic moduli of Pd-Cu multilayers." *Physical Review B* **42**(11): 6899-6905.

Gleiter, H. (1989). "Nanocrystalline materials." *Progress in Materials Science* **33**(4): 223-315.

Greiner, W., L. Neise and H. Stocker (1995). Thermodynamics and statistical mechanics. New York, Springer.

Gruber, A., J. Gspann and H. Hoffmann (1999). "Nanostructures produced by cluster beam lithography." *Applied Physics A: Materials Science & Processing* **68**(2): 197-201.

Gryaznov, V. G., A. M. Kaprelov and A. E. Romanov (1989). "Size effect of dislocation stability in small particles and microcrystallites." *Scripta Metallurgica* **23**(8): 1443-1448.

Gryaznov, V. G., V. A. Solov'ev and L. I. Trusov (1990). "Peculiarities of initial stages of deformation in nanocrystalline materials (NCMs)." *Scripta Metallurgica et Materialia* **24**(8): 1529-1534.

Gumbsch, P. and M. S. Daw (1991). "Interface stresses and their effects on the elastic moduli of metallic multilayers." *Physical Review B* **44**(8): 3934-3938.

Gurtin, M. E. and A. I. Murdoch (1975). "A continuum theory of elastic material surfaces." *Archive for Rational Mechanics and Analysis* **57**: 291-323.

Gurtin, M. E. and A. I. Murdoch (1978). "Surface stress in solids." *International Journal of Solids and Structures* **14**(6): 431-440.

Gurtin, M. E., J. Weissmuller and F. Larche (1998). "A general theory of curved deformable interfaces in solids at equilibrium." *Philosophical Magazine A* **78**(5): 1093 - 1109.

Hall, B. D., M. Flueli, R. Monot and J. P. Borel (1991). "Multiply twinned structures in unsupported ultra fine silver particles observed by electron diffraction." *Physical Review B* **43**: 3906–3917.

Hamilton, R. A. H. and J. E. Parrott (1968). "The third-order elastic constants of quasi-isotropic materials." *Journal of Physics C* **1**: 829-834.

Harten, U., A. M. Lahee, J. P. Toennies and C. Wöll (1985). "Observation of a soliton reconstruction of Au(111) by high-resolution helium-atom diffraction." *Physical Review Letters* **54**(24): 2619-2622.

Herring, C. (1950). "Diffusional viscosity of a polycrystalline solid." *Journal of Applied Physics* **21**(5): 437-445.

Hiki, Y. and A. V. Granato (1966). "Anharmonicity in noble metals; higher order elastic constants." *Physical Review* **144**(2): 411-419.

Hill, R. (1952). "The elastic behaviour of a crystalline aggregate." *Proceedings of the Physical Society of London A* **65**(5): 349.

Hoover, W. G. (1985). "Canonical dynamics: equilibrium phase-space distributions." *Physical Review A* **31**: 1695-1697.

Huang, Z. P. W. (2006). "A theory of hyperelasticity of multi-phase media with surface/interface energy effect." *Acta Mechanica* **182**: 195–210.

Iijima, S. (1992). "Carbon nanotubes." *Solid State Physics* **27**(6): 39-45.

Iijima, S. and T. Ichihashi (1993). "Single-shell carbon nanotubes of 1-nm diameter." *Nature* **363**(6430): 603-605.

Itozaki, H. (1982). Mechanical properties of composition modulated copper-palladium foils., Northwestern University. **Ph.D. Thesis**.

Jarić, J. P. and D. S. Kuzmanović (2001). "On the elasticty tensor of third order." *Theoretical and Applied Mechanics* **26**: 91-106.

Jasiuk, I., E. Tsuchida and T. Mura (1987). "The sliding inclusion under shear." *International Journal of Solids and Structures* **23**: 1373–1385.

Johnson, R. A. (1972). "Relationship between two-body interatomic potentials in a lattice model and elastic constants." *Physical Review B* **6**(6): 2094-2100.

Johnson, R. A. (1973). "Empirical potentials and their use in the calculation of energies of point defects in metals." *Journal of Physics F: Metal Physics* **3** (2): 295-321.

Johnson, R. A. (1988). "Analytic nearest-neighbor model for fcc metals." *Physical Review B* **37**(8): 3924-3931.

Johnson, R. A. and D. J. Oh (1989). "Analytic embedded atom method model for bcc metals." *Journal of Materials Research* **4**(5): 1195-1201.

Khachaturyan, A. G., S. Semenovskaya, and T. Tsakalakos (1995). "Elastic strain energy of inhomogeneous solids." *Physical Review B* **52**(22): 15909-15919.

Kluge, M. D., D. Wolf, J. F. Lutsko and S. R. Phillpot (1990). "Formalism for the calculation of local elastic constants at grain boundaries by means of atomistic simulation." *Journal of Applied Physics* **67**(5): 2370-2379.

Kondo, Y. and K. Takayanagi (1997). "Gold nanobridge stabilized by surface structure." *Physical Review Letters* **79**: 3455–3458.

Korn, D., R. Birringer, H. Gleiter, A. Morsch and W. Arnold (1988). "Measurements of the elastic constants and the specific heat and the entropy of grain boundaries by means of ultrasound." *Journal of Physics (Paris)* **49**(C5): 769.

Kosevich, Y. A. and A. M. Kosevich (1989). "On the possibility of measuring the tensor of surface stress in thin crystalline plates." *Solid State Communications* **70**(5): 541-543.

Krstic, V., U. Erb and G. Palumbo (1993). "Effect of porosity on Young's modulus of nanocrystalline materials." *Scripta Metallurgica et Materialia* **29**(11): 1501-1504.

Kulkarni, A. J. and M. Zhou (2006). "Surface-effects-dominated mechanical and thermal responses of zinc oxide nanobelts." *Acta Mechanica Sinica* **22**: 217.

Kulkarni, A. J., M. Zhou and F. J. Ke (2005). "Orientation and size dependence of the elastic properties of zinc oxide nanobelts." *Nanotechnology* **16**: 10.

Landolt-Bornstein (1979). Numerical Data and Functional Relationships in Science and Technology. Berlin, Springer-Verlag.

Larché, F. and J. W. Cahn (1978). "Thermochemical equilibrium of multiphase solids under stress." *Acta Metallurgica* **26**(10): 1579-1589.

Lee, Y. W. and H. I. Aaronson (1980). "Anisotropy of coherent interphase boundary energy." *Acta Materialia* **28**(4): 539-548.

Leo, P. H. and M. H. Schwartz (2000). "Energy of semicoherent interfaces." *Journal of the Mechanics and Physics of Solids* **48**(12): 2539-2557.

Liang, H., M. Upmanyu and H. Huang (2005). "Size-dependent elasticity of nanowires: Nonlinear effects." *Physical Review B* **71**(24): 241403(R).

Lim, C. W., Z. R. Li and L. H. He (2006). "Size dependent, non-uniform elastic field inside a nano-scale spherical inclusion due to interface stress." *International Journal of Solids and Structures* **42**(17): 5055-5065.

Lipton, R. and B. Vernescu (1996). "Composites with imperfect interface." *Proceedings of the Royal Society of London A* **452**: 329–358.

Lubarda, V. A. (1997). "New estimates of the third-order elastic constants for isotropic aggregates of cubic crystals." *Journal of the Mechanics and Physics of Solids* **45**(4): 471-490.

Lucas, M., W. Mai, J. H. Song, Z. L. Wang and E. Riedo (2007). "Size dependence of the mechanical properties of ZnO nanobelts." *Philosophical Magazine* **accepted**.

Mansfield, M. and R. J. Needs (1991). "Surface energy and stress of lead (111) and (110) surfaces." *Physical Review B* **43**(11): 8829-8833.

Marinopoulos, A. G., V. Vitek and J. L. Bassani (1998). "Local and effective elastic properties of grain boundaries in silicon." *Physica Status Solidi (a)* **166**(1): 453 - 473.

Martin, J. W. (1975). "Many-body forces in metals and the Brugger elastic constants." *Journal of Physics C* **8**(18): 2837-2857.

Martin, J. W. (1975). "Many-body forces in solids and the Brugger elastic constants. II. Inner elastic constants." *Journal of Physics C* **8**(18): 2858-2868.

Miller, R. E. and V. B. Shenoy (2000). "Size-dependent elastic properties of nanosized structural elements." *Nanotechnology* **11**(3): 139-147.

Mishin, Y., D. Farkas, M. J. Mehl and D. A. Papaconstantopoulos (1999). "Interatomic potentials for Al and Ni from experimental data and ab initio calculations." *Materials Research Society Symposium - Proceedings* **538**: 535-540.

Mishin, Y., D. Farkas, M. J. Mehl and D. A. Papaconstantopoulos (1999). "Interatomic potentials for monoatomic metals from experimental data and ab initio calculations." *Physical Review B* **59**(5): 3393-3407.

Mishin, Y., D. Farkas, M.J. Mehl, D. A. Papaconstantopoulos, A. F. Voter, and J. D. Kress (2001). "Structural stability and lattice defects in copper: Ab initio, tight-binding, and embedded-atom calculations." *Physical Review B* **63**(22): 224106-224122.

Morris, D. G. (1998). Mechanical behavior of nanostructured materials. Endfield, NH, USA, Trans Tech Publishings, Inc.

Müller, P. and A. Saúl (2004). "Elastic effects on surface physics." *Surface Science Reports* **54**(5-8): 157-258.

Mullins, W. W. (1959). "Flattening of a Nearly Plane Solid Surface due to Capillarity." *Journal of Applied Physics* **30**(1): 77-83.

Mura, T. (1987). Micromechanics of defects in solids. Dordrecht / Boston / London, Kluwer Academic Publishers.

Murdoch, A. I. (1976). "Thermodynamical theory of elasticity material interfaces." *Quarterly Journal of Mechanics and Applied Mathematics* **29**(3): 245-275.

Mütschele, T. and R. Kirchheim (1987). "Hydrogen as a probe for the average thickness of a grain boundary." *Scripta Metallurgica* **21**(8): 1101-1104.

Needs, R. J. and M. J. Godfrey (1990). "Surface stress of aluminum and jellium." *Physical Review B* **42**(17): 10933-10939.

Needs, R. J., M. J. Godfrey and M. Mansfield (1991). "Theory of surface stress and surface reconstruction." *Surface Science* **242**(1-3): 215-221.

Nieh, T. G. and J. Wadsworth (1991). "Hall-Petch relation in nanocrystalline solids." *Scripta Metallurgica et Materialia* **25**(4): 955-958.

Nieman, G. W., J. R. Weertman, and R. W. Siegel (1991). "Mechanical behavior of nanocrystalline Cu and Pd." *Journal of Materials Research* **6**(5): 1012-.

Nix, W. D. and H. Gao (1998). "An atomistic interpretation of interface stress." *Scripta Materialia* **39**(12): 1653-1661.

Nosé, S. (1984). "A molecular dynamics method for simulations in the canonical ensemble." *Molecular Physics* **52**(255-268).

Nozières, P. and D. E. Wolf (1988). " Interfacial properties of elastically strained materials. I. Thermodynamics of a planar interface." *Zeitschrift für Physik B Condensed Matter* **70**(3): 399-407.

Oh, D. J. and R. A. Johnson (1988). "Simple embedded atom method model for fcc and hcp metals." *Journal of Materials Research* **3**(3): 471-478.

Palaci, I., S. Fedrigo, H. Brune, C. Klinke, M. Chen and E. Riedo (2005). "Radial elasticity of multiwalled carbon nanotubes." *Physical Review Letters* **94**(17): 1-4.

Phillot, S. R., D. Wolf, and H. Gleiter (1995). "Molecular-dynamics study of the synthesis and characterization of a fully dense, three-dimensional nanocrystalline material." *Journal of Applied Physics* **78** (2): 847-861.

Powell, B. E. and M. J. Skove (1968). "Measurement of higher-order elastic constants, using finite deformations." *Physical Review* **174**(3): 977-983.

Qu, J. (1993). "The effect of slightly weakened interfaces on the overall elastic properties of composites." *Mechanics of Materials* **14**: 269–281.

Qu, J. (2003). Comprehensive structure integrity – Fracture of materials from nano to macro. W. Gerberich and W. Yang, Elsevier Science**:** 219.

Qu, J. (2003). Thermomechanical reliability of microelectronic packaging. comprehensive structure integrity – Fracture of materials from nano to macro. W. Gerberich and W. Yang, Elsevier Science**:** 219 - 240.

Qu, J. and J. L. Bassani (1993). "Interfacial fracture-Mechanics for anisotropic bimaterials." *Journal of Applied Mechanics* **60**(2): 422-431.

Qu, J. and M. Cherkaoui (2006). Fundamentals of micromechanics of solids. Hoboken, NJ, John Wiley & Sons, Inc.

Ray, J. R. and M. C. Moody (1985). "Molecular dynamics calculation of elastic constants for a crystalline system in equilibrium." *Physical Review B: Condensed Matter and Materials Physics* **32**(2): 733-735.

Riley, M. W. and M. J. Skove (1973). "Higher-order elastic constants of copper and nickel whiskers." *Physical Review B* **8**(2): 466-474.

Rittner, J. D. and D. N. Seidman (1996). "<110> symmetric tilt grain-boundary structures in fcc metals with low stacking-fault energies." *Physical Review B* **54**(10): 6999-7015.

Salama, K. and G. A. Alers (1967). "Third-order elastic constants of copper at low temperature." *Physical Review* **161**(3): 673-680.

Sander, D. (2003). "Surface stress: implications and measurements." *Current Opinion in Solid State and Materials Science* **7**(1): 51-57.

Sandy, A. R., S. G. J. Mochrie, D. M. Zehner, G. Grübel, K. G. Huang and D. Gibbs (1992). "Reconstruction of the Pt(111) surface." *Physical Review Letters* **68**(14): 2192-2195.

Sanfeld, A., and A. Steinchen (2000). "Surface energy, stress, capillary-elastic pressure and chemical equilibrium constant in nanoparticles." *Surface Science* **463**(3): 157-173.

Schiøtz, J., F. D. Di Tolla, and K.W. Jacobsen (1998). "Softening of nanocrystalline metals at very small grain sizes." *Nature* **391**(6667).

Schmid, M., W. Hofer, P. Varga, P. Stoltze, K. W. Jacobsen and J. K. Nørskov (1995). "Surface stress, surface elasticity, and the size effect in surface segregation." *Physical Review B* **51**(16): 10937-10946.

Seeger, A. and O. Buck (1960). "Die experimetelle Ermittlung der elastischen Konstanten höherer Ordnung." *Zeitschrift fur Naturforschung* **15a**: 1056-1067.

Sharma, P. and S. Ganti (2003). "On the grain-size-dependent elastic modulus of nanocrystalline materials with and without grain-boundary sliding." *Journal of Materials Research* **18**(8): 1823-1826.

Sharma, P. and S. Ganti (2004). "Size-dependent Eshelby's tensor for embedded nano-inclusions incorporating surface/interface energies." *Journal of Applied Mechanics* **71**: 663-671.

Sharma, P., S. Ganti and N. Bhate (2003). "Effect of surfaces on the size-dependent elastic state of nano-inhomogeneities." *Applied Physics Letters* **82**(4): 535-537.

Shenoy, V. B. (2005). "Atomistic calculations of elastic properties of metallic fcc crystal surfaces." *Physical Review B* **71**(9): 094104.

Shenoy, V. B., R. Miller, E. B. Tadmor, R. Phillips and M. Ortiz (1998). "Quasicontinuum models of interfacial structure and deformation." *Physical Review Letters* **80**(4): 742-745.

Shewchuk, J. R. (1994). An introduction to the conjugate gradient method without the agonizing pain. Pittsburgh, PA, USA, Carnegie Mellon University.

Shuttleworth, R. (1950). "The surface tension of solids." *Proceedings of the Royal Society of London A* **63**: 444-457.

Spearot, D. E. (2005). Atomistic calculations of nanoscale interface behavior in FCC metals. Ph. D. Dissertation, Georgia Institute of Technology.

Srinivasan, R. (1966). "Lattice Theory of Third-Order Elastic Constants of Nonprimitive, Nonpiezoelectric Lattices." *Physical Review* **144**(2): 620-628.

Streitz, F. H., R. C. Cammarata and K. Sieradzki (1994). "Surface-stress effects on elastic properties. I. Thin metal films." *Physical Review B* **49**(15): 10699-10706.

Streitz, F. H., R. C. Cammarata and K. Sieradzki (1994). "Surface-stress effects on elastic properties. II. Metallic multilayers." *Physical Review B* **49**(15): 10707-10716.

Suryanarayana, C. (1995). "Nanocrystalline materials." *International Materials Reviews* **40**(2): 41-64.

Sutton, A. P. and R. W. Balluffi (1987). "Overview no. 61 On geometric criteria for low interfacial energy." *Acta Metallurgica* **35**(9): 2177-2201.

Sutton, A. P. and V. Vitek (1983). "On the structure of tilt grain-boundaries in cubic metals. I. Symmetrical tilt boundaries." *Philosophical Transactions of the Royal Society of London A* **309**: 1-68.

Sutton, A. P. and V. Vitek (1983). "On the Structure of tilt grain boundaries in cubic metals II. Asymmetrical tilt boundaries." *Philosophical Transactions of the Royal Society of London A* **309**(1506): 37-54.

Sutton, A. P. and V. Vitek (1983). "On the structure of tilt grain boundaries in cubic metals. III. Generalizations of the structural study and implications for the properties of grain boundaries." *Philosophical Transactions of the Royal Society of London A* **309**(1506): 55-68.

Tartaglino, U., D. Passerone, E. Tosatti and F. Di Tolla (2001). "Bent surface free energy differences from simulation." *Surface Science* **482-485**(2): 1331-1336.

Thurston, R. N. and K. Brugger (1964). "Third-Order Elastic Constants and the Velocity of Small Amplitude Elastic Waves in Homogeneously Stressed Media." *Physical Review* **133**(A6): A1604–A1610.

Todd, B. D. and R. M. Lynden-Bell (1993). "Surface and bulk properties of metals modelled with Sutton - Chen potentials." *Surface Science* **281**(1-2): 191-206.

Tyson, W. R. and W. A. Miller (1977). "Surface free energies of solid metals: Estimation from liquid surface tension measurements." *Surface Science* **62**(1): 267-276.

Verlet, L. (1967). "Computer "experiments" on classical fluids. I. Thermodynamical properties of Lennard-Jones molecules." *Physical Review* **159**(1): 98-103.

Vitek, V., G. J. Wang, E. S. Alber and J. L. Bassani (1994). "Relationship between modeling of the atomic structure of grain boundaries and studies of mechanical properties." *Journal of Physics and Chemistry of Solids* **55**(10): 1147-1156.

Voter, A. F. (1994). Intermetallic compounds: Principles and practice, John Wiley and Sons, Ltd.

Wasserbach, W. (1990). "Third-order constants of a cubic quasi-isotropic solid." *Physica Status Solidi B* **159**: 689-697.

Weng, G. J. (1981). "Constitutive relations of metal crystals at arbitrary strain." *Acta Mechanica* **41**: 217-232.

Willis, J. R. (1990). Variational estimates for the overall behavior of a nonlinear matrix inclusion composite. Micromechanics and Inhomogeneities. New York, Springer-Verlag.

Wolf, D. (1990). "Structure-energy correlation for grain boundaries in F.C.C metals. III. Symmetrical tilt boundaries." *Acta Metallurgica et Materialia* **38**: 781-790.

Wolf, D. (1991). "Surface-stress-induced structure and elastic behavior of thin films." *Applied Physics Letters* **58**(13): 2081–2083.

Wolf, D., P. Keblinski, S. R. Phillpot and J. Eggebrecht (1999). "Exact method for the simulation of Coulombic systems by spherically truncated, pairwise r^{-1} summation." *The Journal of Chemical Physics* **110**(17): 8254-8282.

Wolf, D. and K. Kluge (1990). "Relationship between shear resistance and local atomic structure at grain boundaries in fcc metals." *Scripta Metallurgica et Materialia* **24**(5): 907-912.

Wolf, D. and J. F. Lutsko (1989). "Structurally-induced elastic anomalies in a superlattice of (001) twist grain boundaries." *Journal of Materials Research* **4**(6): 1427-1443.

Wolf, D., J. F. Lutsko, and M. Kluge (1989). "Physical properties of grain-boundary materials: Comparison of EAM and central-force potentials" in Atomistic Simulation of Materials: Beyond pair potentials. New York, Plenum Press.

Wu, H. A. (2006). "Molecular dynamics study on mechanics of metal nanowire." *Mechanics Research Communications* **33**: 9–16.

Wu, H. A., G. R. Liu and J. S. Wang (2004). "Atomistic and continuum simulation on extension behaviour of single crystal with nano-holes." *Modelling and Simulation in Materials Science and Engineering* **12**: 225–233.

Wulf, G. (1901). "X. betrage zur krystallstructurtheorie." *Zeitschrift für Krystallographie und Mineralogie.* **34**: 449.

Yang, Z.-G., T.-J. Wang, S. Zhong, G. Yang and G.-C. Wang (2005). "Coherent interfacial energy and composition profiles in ternary FCC systems by a discrete lattice plane analysis." *Journal of Materials Science* **40**(3): 701-709.

Zhang, X. and P. Sharma (2005). "Inclusions and inhomogeneities in strain gradient elasticity with couple stresses and related problems." *International Journal of Solids and Structures* **42**(13): 3833-3851.

Zhou, L. G. and H. Huang (2004). "Are surfaces elastically softer or stiffer?" *Applied Physics Letters* **84**(11): 1940-1942.